Investigations of Planar n^+-in-n ATLAS Silicon Sensors with Modified Pixel Implantations

Dissertation
zur Erlagung des akademischen Grades
Doktor der Naturwissenschaften

vorgelegt von

Mareike Wagner

geboren in Leer

Lehrstuhl für Experimentelle Physik IV
Fakultät Physik

technische universität
dortmund

– November 2020 –

Diese Dissertation wurde der Fakultät Physik der Technischen Universität Dortmund zur Erlangungdes akademischen Grades eines Doktors der Naturwissenschaften vorgelegt.

Erstgutachter:	Prof. Dr. K. Kröninger
Zweitgutachter:	Prof. Dr. Dr. W. Rhode
Vorsitzender der Prüfungskommission:	Prof. Dr. C. Westphal
Vertretung der wiss. Mitarbeiter:	Dr. A. Savitsky
Datum des Einreichens der Arbeit:	16. November 2020
Datum der mündlichen Prüfung:	19. Januar 2021

Abstract

In high energy physics experiments new conditions require continuously improved sensors and modules for particle detection. The REINER pixel modules were developed featuring different pixel designs to improve the sensor performance, especially after irradiation. The results for laboratory and test beam measurements for several of these modules are presented in this thesis.
In total nine modules have been irradiated with protons and neutrons to study their performance at the end-of-lifetime of a sensor in the ATLAS Pixel Detector and investigate the intended charge multiplication effect. While all non-irradiated pixel designs showed similar charge collection and hit detection efficiency results, their behavior differs after irradiation. The irradiated standard pixel design measured highest hit detection efficiencies at low bias voltages except for one highly neutron irradiated module ($5 \times 10^{15}\,\mathrm{n_{eq}/cm^2}$). For this module, a pixel design with narrowed $\mathrm{n^+}$-implantation (V5) reached significantly higher particle detection efficiencies at low bias voltages. The results of ensuing annealing studies of a different highly neutron irradiated module showed that the observed higher particle detection efficiencies for pixel design V5 are an annealing effect: An increase in generated charge and hit detection efficiency was observed for this design after long annealing times.
In addition, an existing TCT measurement setup was modified in this thesis to measure the laser induced charge collection efficiency in the laboratory with sub-pixel resolution. First promising results of this setup are consistent with in-pixel maps from test beam measurements: The increased charge collection and hit detection efficiency of pixel design V5 after irradiation and annealing are likely caused by electric field strength maxima at the corners and edges of the $\mathrm{n^+}$-implantation. This higher electric field broadens the depletion zone and a charge multiplication effect is achieved.

Contents

1 Introduction

The fundamental particles and forces are described in particle physics theories. To gain a better understanding of matter and the origin of the universe these theories are confirmed or dispelled through research at particle physics experiments. Among other experiments, particle accelerator facilities like CERN or DESY provide a good basis for this fundamental research by colliding high energetic particles. To maximize the available energy, opposing particle beams are collided so that heavy particles can be produced. The particles decay shortly after their creation and the characteristics of the decay products are measured with detectors located around the interaction point. From these detector measurements conclusions on the produced particle, its decay processes and underling physics phenomena can be drawn. Higher beam energies and more collisions per time are beneficial to find new particles since an increase in statistics improves the probability of rare processes. With increasing beam energies new requirements arise for all detector components. The ATLAS experiment at CERN is a $4\,\pi$ general-purpose detector located around the interaction point and is composed of several sub-detector systems. For the innermost component, the Inner Detector, hybrid pixel detectors are used to track particles. These sensors and modules detecting traversing particles need to be fast and radiation tolerant as they are exposed to higher particle fluences close to the interaction point. For this reason, the development of new materials and new sensor designs is a continuous process in this field of research.
The sensors and modules studied in this work are based on the planar pixel sensors of the current innermost detector component of the ATLAS detector, the IBL. Due to their position close to the interaction point, these modules must be radiation hard and are designed to withstand a radiation fluence of $5 \times 10^{15}\,\mathrm{n_{eq}/cm^2}$. In addition, the modules provide a good signal-to-noise ratio, low leakage currents, high breakdown voltages and a homogeneous electric field inside the sensor bulk for particle detection. However, with increasing radiation damage the depletion voltage increases and the signal amplitudes are reduced. To counteract this reduction in signal amplitude the so-called REINER pixel modules were developed in Dortmund and are extensively studied in this work. They are designed to create electric field strength maxima inside the sensor volume so that higher signal amplitudes and detection efficiency are reached at low bias voltages due to charge multiplication effects. Six pixel designs with different implantation and metal shapes are placed together with the IBL standard pixel design on one sensor. Guard ring structures

and individual HV pads for each group with different pixel designs allow for independent investigation of the designs. Furthermore, the performance of the different designs can be compared directly to the standard design and with each other.
Since the investigated sensors are based on the sensor design of the ATLAS IBL detector of the Large Hadron Collider at CERN and to illustrate the application of pixel detectors, the collider and the experiment including its components are described in Chapter 2. The working principle of silicon particle detectors to measure traversing particles is a crucial point which is explained in Chapter 3. The sensors and modules can get damaged by radiation. The damaging processes and consequences for the sensor characteristics are described in more detail in Chapter 4. To achieve a better performance after irradiation compared to an IBL standard module, the REINER pixel modules were developed. In Chapter 5 the general composition of hybrid pixel modules are described along with the characteristics of these new REINER pixel modules. They have been tested extensively in laboratory and test beam measurements in this thesis. The individual setups, analysis steps and results are presented for non-irradiated modules in Chapter 6, for irradiated modules in Chapter 7 and for annealed irradiated modules in Chapter 8. Finally, in Chapter 9 a resume on the best performing pixel composition is drawn and an outlook on future studies is given.

2 The Large Hadron Collider and the ATLAS Experiment

The world's largest and most powerful particle accelerator is the Large Hadron Collider (LHC) [1] located at the European Organization for Nuclear Research (CERN) near Geneva. With more than 12 200 associated scientists of 110 nationalities, CERN is the biggest organization in particle physics world wide [2]. CERN's focus is fundamental research to understand the universe and the origin of matter. Our current understanding of fundamental particles and their interactions is described in the Standard Model (SM). A recently verified hypothesis of the SM is the existence of the Higgs boson which gives mass to elementary particles [3]. However, the standard model leaves some unanswered questions: What are the particles or phenomena that are responsible for dark energy and dark matter? Why is there more matter than anti matter? Are there more fundamental particles that we do not know yet?
To investigate these questions highly energetic particle beams are collided producing an environment with an energy density similar to the one existing a few moments after the Big Bang. In these collisions massive particles like the Higgs boson, τ-leptons, B-hadrons and others are produced. Their decay products can be investigated with particle detectors around the interaction point. This way conclusions about the properties of the produced particles are drawn and the fundamental particles are examined in detail.

2.1 The CERN Accelerator Complex and the LHC

At CERN, a particle beam of protons or lead ions is accelerated in a chain of pre-accelerators before their injection into the LHC. Experiments using lower energy beams are supplied by pre-accelerators which are arranged in a chain as illustrated in Figure 2.1.

For a proton beam the process starts by injecting hydrogen gas into a Duoplasmatron [4] to separate protons and electrons in an electrical field. The first accelerator, the Linac 2, accelerates the protons to an energy of 50 MeV. In the following accelerator chain of Proton Synchrotron Booster (Booster), Proton Synchrotron (PS)

and Super Proton Synchrotron (SPS) the protons are boosted successively to an energy of 450 GeV. Finally, the bunches of protons are injected into the LHC.
In the first of two beam pipes the particles circulate clockwise, in the second anticlockwise. Superconducting magnets guide the beams in the 26.7 km ring while accelerating structures increase the protons' energy up to 7 TeV. The particle beams are collided at four interaction points where the particle detectors ATLAS (A Toroidal LHC Apparatus) [5], CMS (Compact Muon Solenoid) [6], ALICE (A Large Ion Collider Experiment) [7] and LHCb (LHC beauty) [8] are located. Each detector is designed differently to study other physical phenomena from particle collisions. ATLAS and CMS are multi-purpose detectors searching for new physics and perform precision measurements of "old" physics. ALICE is a general-purpose detector but specialized in lead-lead or lead-proton collisions. The research at LHCb is focused on hadronic decays with beauty or charm quarks to investigate CP violating processes.

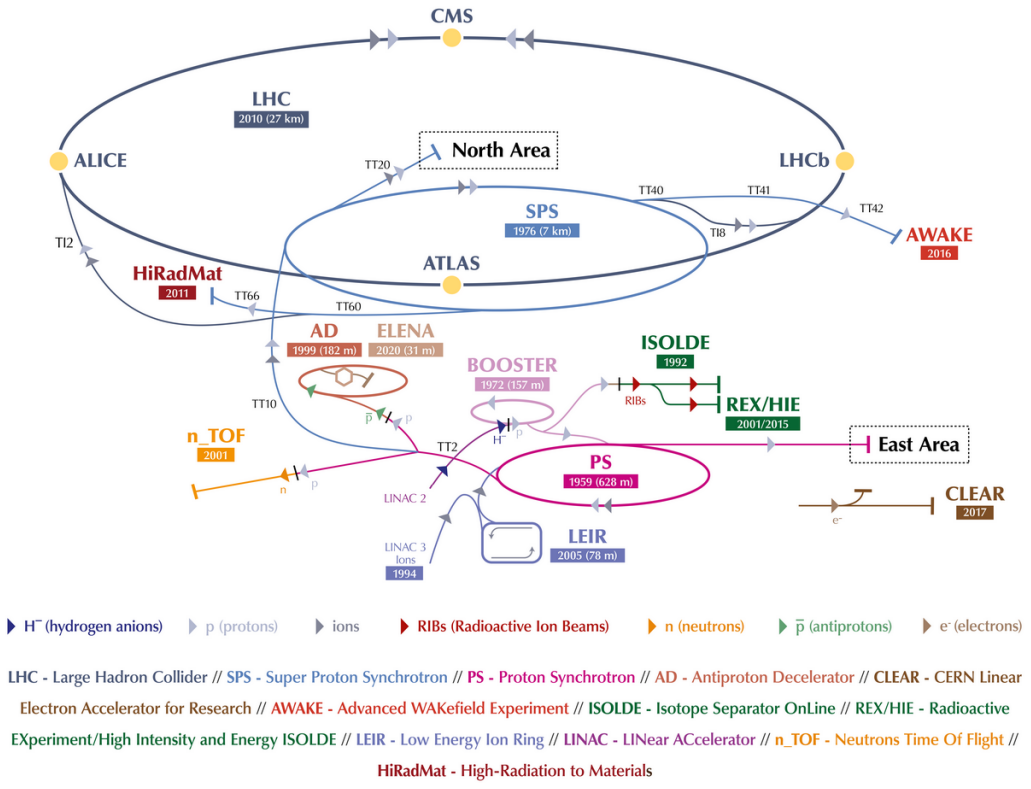

Figure 2.1: The CERN accelerator complex. [9] (modified)

Apart from the energy of the colliding particle beams the luminosity is an important parameter of particle colliders. The number of collisions in the detector given in $\mathrm{cm}^{-2}\,\mathrm{s}^{-1}$ is characterized by the instantaneous luminosity $\mathcal{L}$. It is defined as

$$\mathcal{L} = f \cdot N_b \frac{N_1 N_2}{4\pi\sigma_x\sigma_y} \tag{2.1}$$

with the revolution frequency f, the number of bunches N_b, the number of particles per bunch $N_{1,2}$ and $\sigma_{x,y}$ the Gaussian transversal beam dimension in x and y [10]. The LHC is designed to operate at a center of mass energy of $\sqrt{s} = 14\,\mathrm{TeV}$ and a luminosity of $1 \times 10^{34}\,\mathrm{cm}^{-2}\,\mathrm{s}^{-1}$. The integrated luminosity is then defined as the integral of the instantaneous luminosity taken over the detector's sensitive time.

With this high center of mass energy heavy particles are produced in collisions at the interaction points of the LHC and their characteristics investigated in surrounding detectors. In addition, the great number of collisions enables the study of very rare processes.

In 2010 the first proton-proton collisions were realized with a center of mass energy of $\sqrt{s} = 7\,\mathrm{TeV}$. Until the end of Run 1 in 2013, the energy was increased to $\sqrt{s} = 8\,\mathrm{TeV}$ and an integrated luminosity of $23.1\,\mathrm{fb}^{-1}$ was delivered to ATLAS and CMS [11]. With the data obtained in this run the discovery of the Higgs boson could be announced on July 4th, 2012 [3] by ATLAS [12] and CMS [13].
After two years of Long Shutdown 1 (LS1) the proton energy was increased to $6.5\,\mathrm{TeV}$ resulting in a center of mass energy of $\sqrt{s} = 13\,\mathrm{TeV}$. For Run 2, from May 2015 until end of 2018, an integrated luminosity of $156\,\mathrm{fb}^{-1}$ could be achieved [14]. In Figure 2.2 the integrated luminosity of proton-proton collisions for Run 1 and Run 2 at center of mass energies of $\sqrt{s} = (7-8)\,\mathrm{TeV}$ and $\sqrt{s} = 13\,\mathrm{TeV}$ delivered to ATLAS and CMS are presented. The image underlines the difference in delivered luminosity between the end of Run 1 and Run 2 (factor of 6.8). In addition, the increase in luminosity is not constant but interrupted by annual winter shutdowns which are used for small replacements and repairs of the infrastructure and detectors.

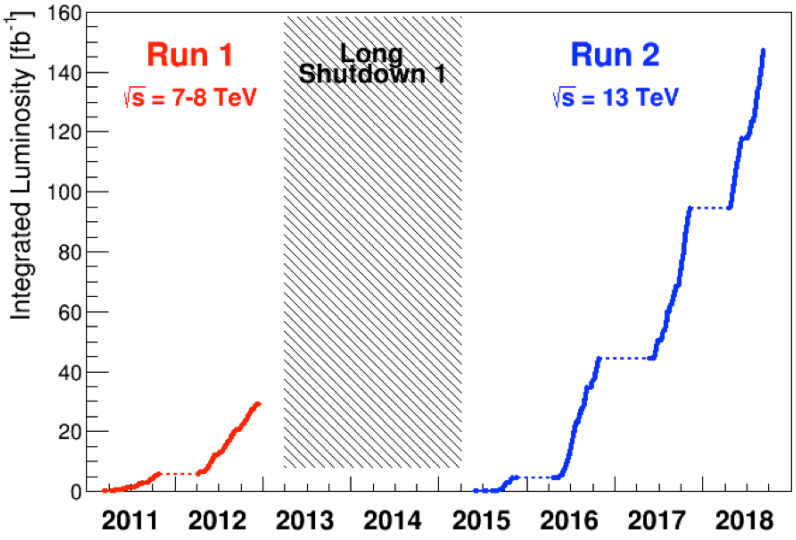

Figure 2.2: Integrated Luminosity of Run 1 and Run 2 delivered to ATLAS and CMS. [15]

2.2 The ATLAS Detector

The cylindrical ATLAS detector with a length of 46 m, a diameter of 25 m and a weight of 7000 t is a general-purpose detector. A schematic overview of the ATLAS detector is shown in Figure 2.3.

To characterize the short-lived particles produced in proton-proton collisions the detector measures the energy, direction, momentum and charge of the decay products: The tracking system close to the interaction point gives information about the path of the particles. The tracks of charged particles are bent due to a magnetic field in the tracking system. Based on the track direction the charge of the particles is determined and the momentum is measured from the curvature of the tracks. Following the tracking system the calorimeter system provides information about the energy and particle type. Finally, the muon system measures properties of produced muons.
In addition, a trigger, data acquisition and computing system is necessary to collect and analyze the information from the different detector components.
The detector components are arranged in cylindrical layers around the interaction point, so-called barrels. At both ends of the barrels, end-caps are located, typically consisting of several disks.

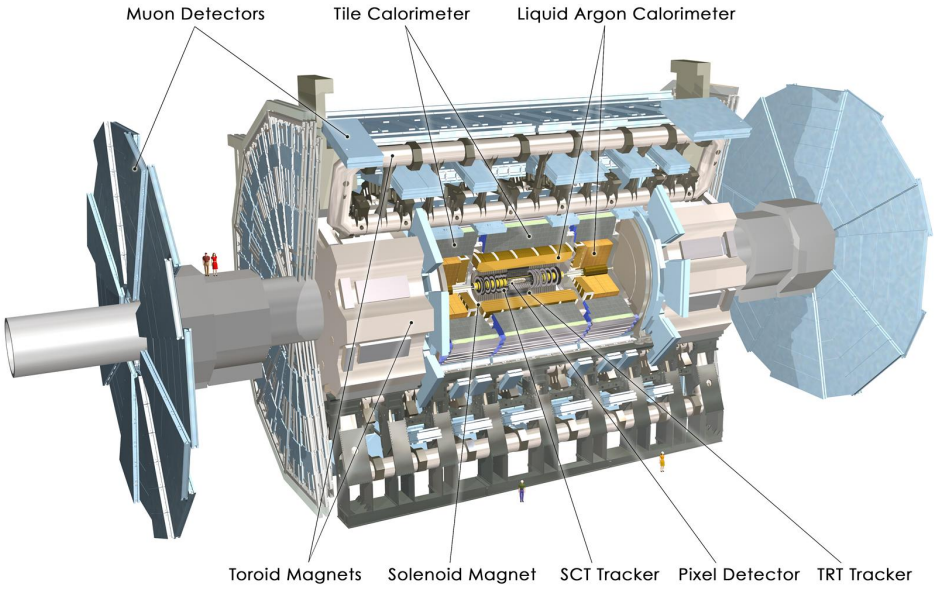

Figure 2.3: Schematic drawing of the ATLAS detector. [16]

The following coordinate system is used to describe positions in the ATLAS detector: The origin of the right handed coordinate system is the interaction point in the center. The beam direction matches the z-axis and is transverse to the xy-plane. The positive x-axis points to the center of the LHC ring, while the positive y-axis points upwards.
In the transverse plane cylindrical coordinates are often used with the radius r and the azimuthal angle ϕ around the beam pipe. In cylindrical coordinates the pseudorapidity η is identified with the polar angle θ (defined from the positive z-axis) as $\eta = -\ln[\tan(\theta/2)]$.

In the following section, the individual sub-detectors of the ATLAS experiment are described: Starting with the magnet system, the sub-detectors are presented from the outermost components to the inside of the detector.

2.2.1 The Magnet System

The magnet system of the ATLAS detector [17] consists of superconducting magnets and provides a magnetic field for different detector parts. This is essential as bent particle tracks are used to determine the particles' momenta.
In the outer region of the detector the barrel toroid magnet is located which has an

open structure to minimize the material budget and thus reduce weight and cost. The barrel toroid and the end-cap toroid produce a maximum 4 T inhomogeneous magnetic field for muon identification. Further inwards, the central solenoid magnet produces a homogeneous 2 T magnetic field along the beam axis for the tracking system.

2.2.2 The Muon Spectrometer

The Muon Spectrometer [18] is the outermost sub-detector of the ATLAS experiment. Muons interact mainly electromagnetically and produce less bremsstrahlung compared to electrons and positrons. They can pass through dense material and only a small ionization signal is generated in the inner detector components and no signal in the calorimeters. To measure these particles, four different technologies of muon chambers are used for detection: Thin Gap Chambers, Resistive Plate Chambers, Monitored Drift Tubes and Cathode Strip Chambers. These precision chambers of the spectrometer cover a large volume and the magnetic field from the toroid is mostly orthogonal to the muons' trajectories. Thus, measurements of the transverse momentum p_T can be performed over a wide energy range of the muons with high precision: For muons with energies between 3 GeV to 100 GeV it is designed to measure the momentum with a relative uncertainty of 4 %, for higher energetic muons ($p_T = 1$ TeV) the resolution increases to 10 %. The four different chamber types cover the area with $|\eta| \leq 1$ at radii from 10 m to 5 m in the barrel and $1 \leq |\eta| \leq 2.7$ in the end-caps. In addition, stand-alone triggering is implemented for $\eta \leq 2.4$.

2.2.3 The Calorimeters

The calorimeter system [19] is installed between the Muon Spectrometer and the solenoid magnet. Its purpose is to measure the particles' energy with high precision by completely stopping the particles. The calorimeters in the ATLAS detector are sampling calorimeters and composed of alternating layers of active and passive materials. They are divided into a hadronic calorimeter in the outer region and an electromagnetic calorimeter in the inner region. The passive materials in the hadronic calorimeter have to have a high hadronic interaction length and a small free path length to increase the number of interactions and to stop hadrons. Electrons, positrons and photons are stopped in the electromagnetic calorimeter by materials with low radiation lengths. A high energy resolution of the calorimeters is necessary to determine parameters like the mass of produced particles more accurately.
The hadronic Tile Calorimeter [20] located in the barrel region is designed to stop

hadrons. It covers a radius of 4.23 m to 2.28 m and has a length of 6.10 m along the beam axis. In the Tile Calorimeter all passive layers are made of steel followed by active scintillator tiles for particle detection. The greater proximity of the hadronic end-caps to the beam line results in a higher particle flux and higher levels of radiation. Therefore, in the hadronic end-caps more radiation hard liquid argon (LAr) is used as active material and copper as passive material.
Further inwards, the electromagnetic calorimeter fills the radii from 2.25 m to 1.15 m and spans 6.65 m along the beam axis. Lead as passive material and LAr as active material are used in the barrel region and in the end-caps.
The Forward Calorimeter contains LAr as active medium and tungsten as passive material in the hadronic part and copper in the electromagnetic part. In technical terms all detector components using LAr as active material are combined as "Liquid Argon Calorimeter" [21].

2.2.4 The Inner Detector

Closest to the interaction point is the ATLAS Inner Detector (ID) [22, 23] which therefore needs a high tolerance to large radiation doses. It is placed inside the 2 T magnetic field of the solenoid magnet. The straw tubes, silicon strips and silicon pixel sensors of this highly sensitive detector enable the track reconstruction of charged particles with a very high spatial resolution even for a large number of tracks. The sensitive area is maximized while for each device a low noise occupancy, high radiation hardness and high tracking efficiency is required. From the reconstructed tracks the charge and momentum of the produced particles can be determined. The detector is constructed with a minimized material budget to reduce multiple scattering and not to distort the energy measurement performed in the calorimeters. In Figure 2.4 a schematic drawing of a part of the barrel region of the Inner Detector with its three complementary sub-detectors is presented. All three sub-detectors are used to maximize the resolution of the momentum measurement. This way the measurement is robust and precise even when a single system does not perform to its full potential.

The Transition Radiation Tracker

The outermost region of the Inner Detector is equipped with the Transition Radiation Tracker (TRT) [25–27]. This gaseous detector with a barrel region and two end-caps is made of 298 304 drift tubes, so-called straws. In the barrel region three cylindrical layers cover a sensitive volume in the radius range of 108 cm to 56 cm and 1.5 m along the beam axis. The first layer consists of 19, the second of 24 and

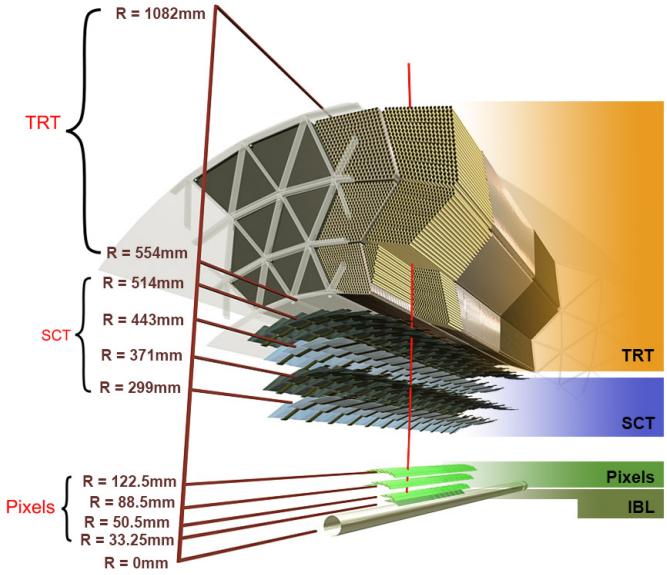

Figure 2.4: Schematic drawing of the Inner Detector. [24]

the third of 30 straw layers. The tubes are arranged in parallel to the beam axis and read out from both sides of the straw. In the end-caps, the 0.4 m long straws are arranged in 18 wheels perpendicular to the beam axis and read out only at the outer end.
Each straw with a diameter of 4 mm is made of Kapton reinforced with thin carbon fibers. An electrical field is applied between the straw and the 30 µm gold plated tungsten wire in the center of each straw. A gas mixture of 70 % xenon, 27 % CO_2 and 3 % O_2 inside the tubes is ionized if a charged particle passes. The electron-hole pairs are separated by the electrical field and the electrons drift into the direction of the wire. The induced charge of the wire is amplified and read out by the electronics at the end of each straw.
In between the straws radiators are installed which produce soft X-ray photons via transition radiation if a highly relativistic charged particle passes through. These photons are absorbed by the xenon gas and a higher electrical signal is produced. The intensity of the transition radiation effect depends on the Lorentz factor $\gamma = \frac{E}{m}$ and is strongest for electrons. This way the signals from electrons can be distinguished from those of other particles. Per straw an intrinsic accuracy of 130 µm per straw in $r\phi$ direction is achieved [5] and a traversing particle produces typically 36 tracking points which allows for a continuous tracking with high accuracy.

The Semiconductor Tracker

The Semiconductor Tracker (SCT) [28, 29] covers the radii between 56 cm and 29.9 cm over a length of approximately 1.5 m in the barrel region. The end-caps extend the coverage of the barrel layer to $|\eta| < 2.5$. A total of 4088 double sided silicon detector modules cover an area of 61 m^2 in 4 cylindrical layers in the barrel region and 18 planar end-cap disks. Thus, four precision measurements per traversing track are obtained with the binary hit information from the modules.
One module consists of four silicon micro-strip sensors: Two micro-strip sensors with a pitch of 80 µm are combined to a pair of sensors with a length of 12.8 cm. Two of these pairs are glued back-to-back onto a holder with an angle of 40 mrad forming a module. With this technique a high tracking precision of 17 µm in $r\phi$ and 580 µm in z-direction can be achieved [5].

The Pixel Detector

The innermost part of the ATLAS detector is the Pixel Detector [30]. Three barrel layers and six disk layers within two end-caps are equipped with in total 1744 silicon pixel modules. The radius region of 15 cm to 5 cm ensures a minimum distance between the first detector layer, so-called B-Layer, and the interaction point. The minimum radius is limited by the diameter of the beam pipe.
Important features are the 3D vertexing capability and identification of short-living particles such as b- or τ-leptons. In addition, a very good resolution for the transverse impact parameter and the pattern recognition in the high multiplicity environment are requirements for the Pixel Detector. Three pixel hits per track are measured for tracks in $\eta < 2.5$. A high granularity is achieved with a small pixel size of 50 µm × 400 µm and 47 232 pixels per module. The high granularity results in an intrinsic accuracy of 10 µm in $r\phi$ and 115 µm in z direction in the barrel and the end cap region [5]. To prevent gaps in particle detection the modules overlap in z-direction. In addition, the modules are mounted tilted in ϕ (15° in the B-Layer, 11° to 16° in the other two barrels) to maximize the collected charge in a single pixel. A module is read out by 16 radiation hard front-ends which are bump bonded to the sensor. A module provides not only binary hit information but also information about the deposited charge with the Time-over-Threshold (ToT) value.
After ten years of operation the total expected fluence of $5 \times 10^{15}\ n_{eq}/cm^2$ would exceed the design values of the innermost B-Layer. Therefore, the B-Layer was designed independently from the other two layers to ensure installation and removal without interfering with other parts. However, the final design and construction of the innermost B-Layer did not allow for a replacement so that a task force in 2008 decided to exchange the beam pipe and add an additional layer to the Pixel

Detector, the Insertable B-Layer (IBL) [31, 32]. The material budget of the IBL is minimized and accounts only for half of the existing B-Layer material budget. The practical experience demonstrated the possibility of narrowing the existing beam pipe since a small beam diameter with a good beam positioning control was accomplished. Therefore, the existing beam pipe was exchanged by a smaller beam pipe with a diameter reduction of 4 mm to gain space for the IBL. The new layer with the new beam pipe was installed during the Long Shutdown 1 in 2013-2014. With the new detector layer the b tagging efficiency can be restored even if modules in the other layers of the Pixel Detector fail, so that a good tracking performance is ensured even at higher peak luminosities. Due to the close position to the interaction point at a radius of 33 mm, the IBL improves vertexing and the b tagging performance. Because the modules are exposed to a high particle fluence they need to be more radiation robust. They are designed to withstand a fluence of $5 \times 10^{15}\,\mathrm{n_{eq}/cm^2}$ and a radiation dose of 2.5 MGy.

Figure 2.5 shows a schematic view of the Pixel Detector with the added IBL. On each of the 14 staves, 20 modules are mounted to achieve full coverage around the beam axis (in ϕ) and a wide coverage along the beam axis ($|\eta| < 3.0$). Two different sensor techniques, 12 planar double chip assemblies and 8 3D single chip assemblies [33], are used per stave. These sensor technologies are explained in more detail in Chapter 5.1. A double chip assembly consists of one sensor that is connected and read out by two readout chips. Compared to the other pixel layers no overlapping of modules for the IBL is possible due to space limitations. Therefore, a slim edge design was developed to reduce the size of inactive edges in z-direction. The $\mathrm{n^+}$-in-n technology of the planar pixel sensors is based on the technology used in the other three layers, but the pixel size is reduced to 50 µm × 250 µm for higher granularity. The 26 880 pixels are organized in a pixel matrix of 80 columns and 336 rows resulting in an active area of $16.8 \times 20.5\,\mathrm{mm^2}$ for a single chip assembly. The planar sensors have a thickness of 200 µm. All sensors are bump bonded and read out with the Front-End I4 readout chip [34] which is described in more detail in Chapter 5.2.

2.2.5 Upgrade Plans

The LHC at CERN will be upgraded to the High-Luminosity LHC (HL-LHC)[36] in the Long Shutdown 3 starting from 2024 to increase the discovery potential after its planned completion by 2027. The goal of the upgrade to HL-LHC is to increase the peak luminosity up to $7.5 \times 10^{34}\,\mathrm{cm^{-2}\,s^{-1}}$ and the integrated luminosity up to $4000\,\mathrm{fb^{-1}}$ in twelve years [37]. With the higher luminosity the number of collisions is increased and rare processes can be studied like the double Higgs production

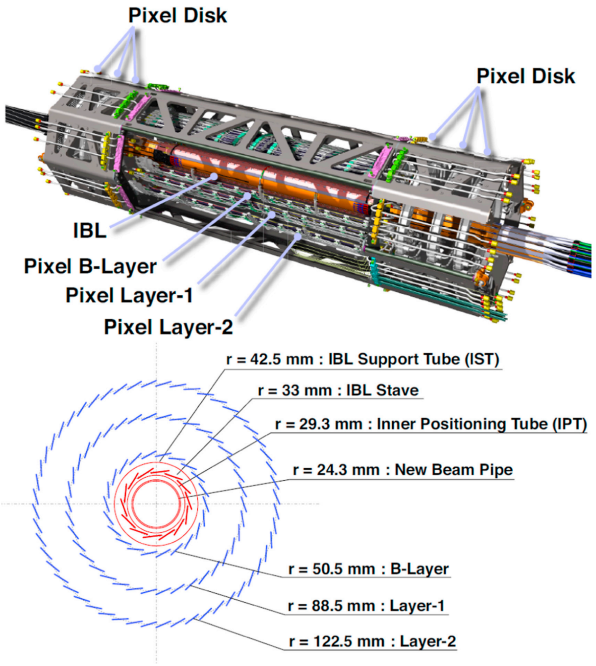

Figure 2.5: Schematic view of the ATLAS 4-Layer Pixel Detector for Run 2. [35]

[38]. More data of known processes allows to study them in more detail and higher precision. In Figure 2.6 the time line for the LHC and HL-LHC is shown.

With the improvement towards the HL-LHC not only the beam infrastructure, but also the experiments need to be partially replaced or upgraded. In the ATLAS detector on average 200 interactions will take place per bunch crossing at a 7 TeV beam each 25 ns [37]. The high density of particle tracks results in high trigger rates, high detector occupancy and challenging data acquisition. Thus, the detector needs to be faster, more radiation hard and more granular. To cope with the new requirements the Inner Detector of the ATLAS experiment will be exchanged completely for the new Inner Tracker (ITk). This all-silicon detector has to provide a robust tracking with very high resolution in an environment with on average 200 pile-up events per bunch crossing (for comparison: in 2018 only about 36 pile-up events per pp collision at 13 TeV took place). The detector is composed of a pixel sub-detector [40] in regions with smaller radii and a strip sub-detector [41] at larger radii. With the combination of pixel and strip detector, the goal is to measure at least nine hits for tracks in the full acceptance of $|\eta| < 4.0$. In addition, the material budget should be as low as possible. Figure 2.7 shows the layout of the ITk as published in reference [42] and fulfills the requirement of nine hits.

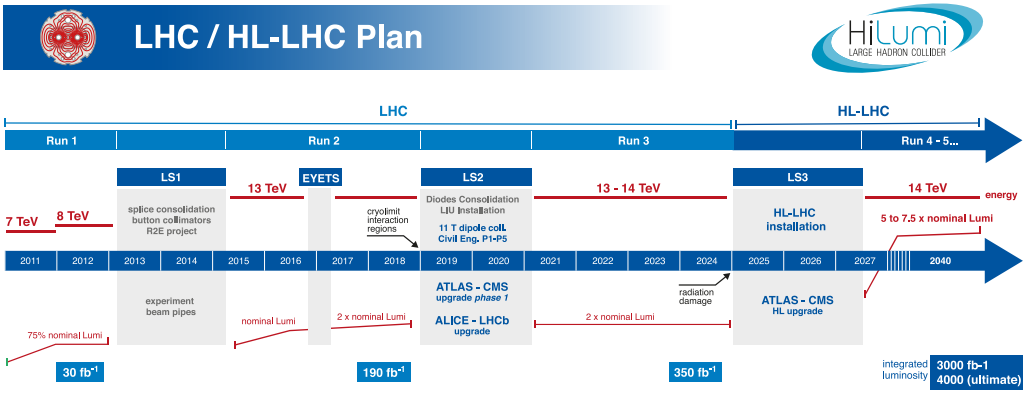

Figure 2.6: Time line of the LHC and HL-LHC. Last updated on January 2020. [39]

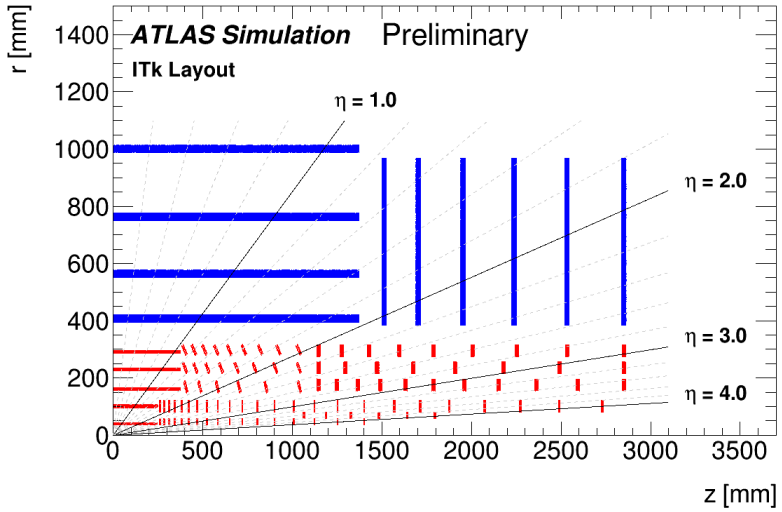

Figure 2.7: Schematic layout of the ITk showing the active detector components in one quadrant of the detector. The active elements of the strip detector are shown in blue, those of the pixel detector in red. The horizontal axis corresponds to the beam line and the vertical represents the radius starting with the interaction point at zero. [42]

The strip detector with four barrel layers and six disks in each end-cap covers the region $|\eta| < 2.7$. On each layer and on each disk strip sensors are mounted on the front and back side with a stereo angle between them to provide information about the z-coordinate of a track. The strip lengths in the barrel and the end-caps vary with position: In the barrel region the strip length is (21.1–48.2) mm with a pitch of 75.5 µm while in the end-caps the strip length is (19.0–60.1) mm with a pitch of (75.0–80.7) µm [41]. The strip detector is exposed to a maximum fluence of $1.6 \times 10^{15}\,\mathrm{n_{eq}/cm^2}$, including a safety factor of 1.5, after an integrated luminosity of $4000\,\mathrm{fb^{-1}}$.
The pixel detector includes the region $|\eta| < 4$ with five barrel layers and several rings in the end-caps. In the center region of the barrel the modules are mounted flat, while they are inclined in the outer region of each barrel. The pixel modules installed in this detector are quad or single modules: For quad modules one sensor with a larger surface is read out by four readout chips, while for single modules only one readout chip per sensor is used. Because the two innermost barrel layers with the corresponding end-caps are exposed to the highest radiation fluences, they can be exchanged after the collection of $2000\,\mathrm{fb^{-1}}$. Thus, the modules in the layers zero and one with the corresponding end-caps need to withstand a maximum fluence of $1.3 \times 10^{16}\,\mathrm{n_{eq}/cm^2}$ after $2000\,\mathrm{fb^{-1}}$ and the remaining modules a fluence of $3.8 \times 10^{15}\,\mathrm{n_{eq}/cm^2}$ after $4000\,\mathrm{fb^{-1}}$ (a safety factor is included for these fluence calculations).
The pixel modules are produced as hybrid pixel detectors meaning that the silicon sensors are bump bonded to the readout chip. The pixel sensors for the ITk are produced in planar (see Chapter 5.1.1) and 3D technology (see Chapter 5.1.2) and read out with the same readout chip. The innermost layer will be equipped with more radiation hard single-chip modules with 3D sensors while the remaining layers will be assembled with single- and quad-chip modules with planar sensors. To increase the track separation capability, the pixel size for the planar sensors is reduced to 50 µm × 50 µm while the pixel matrix is increased to 400 columns and 384 rows. The planar sensors are produced with the n^+-in-p sensor technology. In addition, the sensor thickness is reduced to 100 µm in layer one, 150 µm in the outer layers and the front-end thickness to 150 µm. For the 3D modules two different pixel sizes, 50 µm × 50 µm and 25 µm × 100 µm, are utilized.

This chapter showed the different applications of various sensor technologies of the ATLAS experiment at CERN. Especially the information regarding the current innermost layer of the ATLAS experiment IBL is of great relevance for this thesis: The studied semiconductor sensors are based on the planar pixel sensors of the IBL. In addition, the investigated sensors are irradiated to fluences corresponding to the requirements of sensors of the future ITk.

3 Silicon Particle Detectors

Particle detectors are developed for fundamental research in physics to measure and characterize particles. Depending on the purpose the detectors can be optimized: As an example, highly sensitive photomultiplier tubes are used in astrophysical applications to study rare interactions of particles like neutrinos inside enormous volumes as the $1\,\mathrm{km}^3$ particle detector of the South Pole neutrino observatory IceCube [43]. For high energy physics applications silicon pixel detectors offer high radiation hardness and excellent spatial resolution. In this chapter the physical processes to measure a traversing particle with a silicon semiconductor detector are described. More detailed information can be found in textbooks [44–47].

3.1 Semiconductors

The energy levels of electrons for a single atom in a crystal lattice are influenced by the neighboring atoms. By this, the discrete energy levels are split in several closely spaced levels and form so-called *energy bands* corresponding to different bands of electron orbitals. The highest energy level in the *conduction band* corresponds to an energy level of E_C and the lowest energy level in the *valence band* to an energy of E_V. Depending on the position of the conduction and valence bands, materials can be classified as conductor, insulator or semiconductor.
For conductors the valence band and the conduction band overlap or the conduction band is partially filled leading to free electrons (e) for conduction.
In insulators the valence electrons are strongly bound to the neighboring atoms resulting in a large *band gap* between the valence and conduction band. The electrons' energy in the valence band is less than the band gap energy $E_g = E_C - E_V$ and the electrons cannot overcome the band gap.
For semiconductors thermal excitation or an applied electric field delivers sufficient energy for electrons to get to the conduction band as the band gap of semiconductors is smaller compared to insulators. The now free electrons in the conduction band and the remaining holes (h) in the valence band lead to an electrical current when an electric field is applied. Without thermal energy, at $T = 0\,\mathrm{K}$, all electrons are in the valence band and no current is possible. Furthermore, the resistivity of semiconductors is intermediate to the ones of insulators and conductors in the

range of $1 \times 10^{-3}\,\Omega\,\mathrm{cm}$ to $1 \times 10^{8}\,\Omega\,\mathrm{cm}$ at room temperature [44]. The band gap energy of semiconductors depends on pressure and temperature: At room temperature (300 K) and normal pressure (1 bar) the band gap energy for silicon is 1.12 eV [47].

3.2 Silicon

Most of todays semiconductor detectors for charged particle detection are made of silicon. It is a common element of the earth crust where it is found as silica and silicates since pure silicon is highly reactive. Consequently, silicon is comparatively low-priced material and has beneficial properties for the usage as particle detector: Compared to germanium detectors, silicon has a larger band gap and detectors can be operated at higher temperatures. However, for germanium detectors less energy for the creation of electron-hole pairs is necessary which results in a better sensitivity and energy resolution compared to silicon detectors. Besides the lower price of silicon, one of the main reasons for the application in high energy particle physics is the higher mobility of electrons in silicon resulting in a faster signal formation and a higher tolerance to radiation damage in contrast to germanium detectors. In addition, germanium detectors need to be operated in a cooled environment.
The crystal lattice formed by silicon has a diamond structure with a tetrahedron configuration formed by the four nearest neighboring atoms sharing their four valence electrons. To break this *covalent bond*, extra energy is necessary to change the crystal momentum. Silicon is an indirect semiconductor as this extra energy apart from the band gap energy E_g is needed to lift an electron to the conduction band. When the electron has left the covalent bond, a vacant site with positive net charge, a hole, is created (see Figure 3.1). The free electron and the hole can be seen as free charge carriers with different masses that contribute to the current conduction. The average energy needed to produce an electron-hole pair in silicon is 3.65 eV [44]. For *intrinsic semiconductors* where no foreign atoms are brought into the crystal, the number of free electrons n and the number of holes p is the same. The intrinsic carrier concentration n_i depends on temperature and is described with

$$n_i^2 = n \cdot p. \tag{3.1}$$

For silicon at 300 K the intrinsic carrier concentration is $n_i \approx 1.01 \times 10^{10}\,\mathrm{cm}^{-3}$ [44]. The conductivity for intrinsic silicon σ_i is defined as

$$\sigma_i = n_i e\,(\mu_e + \mu_h) \tag{3.2}$$

with the mobility of the charge carriers $\mu_{e/h}$ and can be calculated for silicon to $\sigma_i \approx 2.8 \times 10^{-4}\,\Omega^{-1}\,\mathrm{m}^{-1}$ [44].

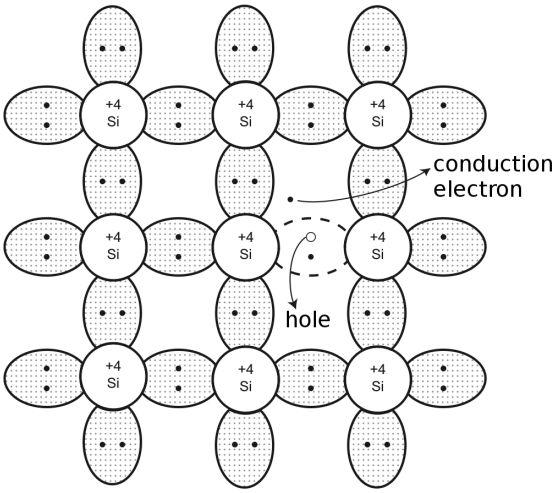

Figure 3.1: Illustration of a split covalent bond and creation of an electron-hole pair in an intrinsic silicon crystal lattice. [44] (modified)

3.3 Doping of Semiconductors

The concept of intrinsic semiconductors is rather hypothetical since a small amount of impurity atoms cannot be eliminated. In contrast, for *extrinsic semiconductors* impurity atoms are brought into the crystal on purpose to achieve certain characteristics. The process is called *doping* and introduces additional energy levels to the band gap. The material stays electrically neutral whereas the electrical conduction properties change. A common doping material from the fifth element group which is added to silicon is phosphorus. The extra valence electron from the phosphorus atom is not in a covalent bond but only weakly bound to the atom via electrostatic forces so it can easily be ionized and used for conduction. If many impurity

atoms are added, a surplus of conducting electrons is created, in which case the impurity atoms are called *donor atoms* or *donors* and the silicon is *n-type* doped. To achieve *p-type* doped silicon, materials from group three, usually boron atoms, are added. These atoms lack one electron compared to silicon atoms, resulting in a hole in one covalent bond. A surplus of conducting holes is formed with many boron atoms in the silicon lattice. These boron atoms are called *acceptor atoms* or *acceptors*. Figure 3.2 shows the bond representation for n-type (a) and p-type (b) silicon semiconductors.

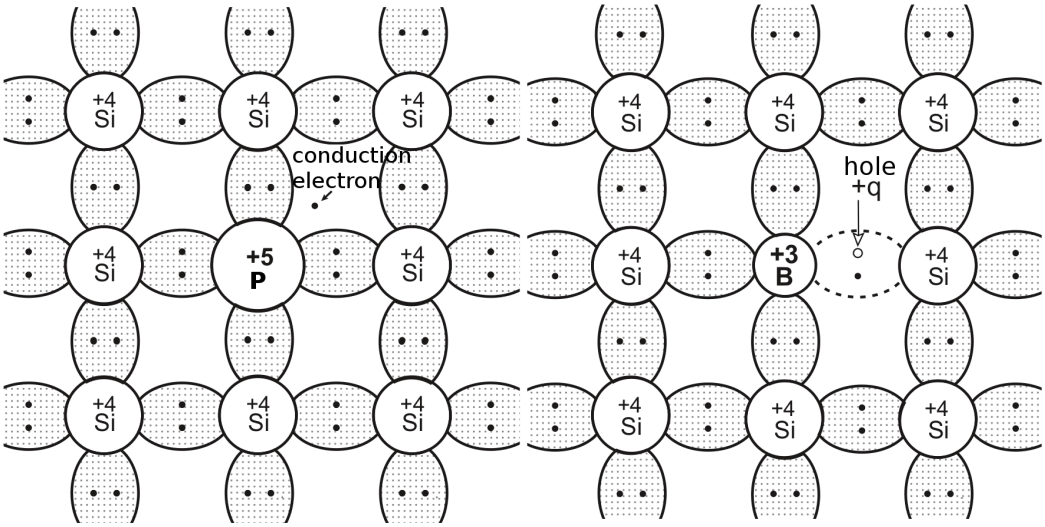

(a) n-doping with a phosphorus atom **(b)** p-doping with a boron atom

Figure 3.2: Illustration of the bond situation in the crystal lattice for n- and p-type doped silicon. [44] (modified)

3.4 p-n Junction

If p- and n-type doped materials are brought into contact, a concentration difference of electrons and holes between the n- and p-type side is created. Thus, the holes from the p-type side diffuse towards the n-type side and the electrons from the n-type region towards the p-type region, forming a diffusion current I_{diff}.
At the junction of the p- and n-doped materials the electrons and holes recombine and produce a space-charge region called *depletion zone*: A positive space charge is present on the p-side and a negative space charge on the n-side of the junction. The resulting electric field generates a drift current I_{drift} which flows from the p-side towards the n-side and in opposite direction to the diffusion current. Without an

external bias voltage the drift and diffusion current are in a thermal equilibrium. The so-called *built-in voltage* U_{bi} of the electric field is about 0.6 V for silicon and depends on the doping concentration [44].
Such a junction can also be generated between layers of the same doping material but at different concentrations. Higher doping concentrations are labeled with n^+ or p^+ ($\approx 10^{20}$ atoms/cm^3) compared to the relative doping concentration n or p ($\geq 10^{13}$ atoms/cm^3) [48]. The concentration difference of electrons and holes at the junction of n^+-n or p^+-p junctions results in an electric field with a diffusion voltage U_{bi} analog to a p-n junction.

The depletion zone can be influenced by an *external bias voltage* U_{ext} depending on the polarity and the voltage. The depletion zone is reduced when a higher potential is applied to the p-side compared to the n-side. In this case the junction is biased in forward direction and the diffusion current exceeds the drift current: More electrons diffuse from the n-side towards the p-side and more holes from the p-side towards the n-side so that the depletion zone is reduced.
The connection of a lower potential on the p-side results in an enlargement of the depletion zone. Semiconductor particle detectors are biased in this *reverse direction* to enlarge the depletion zone. In Figure 3.3 the width of the depletion zone at a p-n junction is indicated as hatched area without external biasing (a), with forward bias (b) and with reverse bias (c).

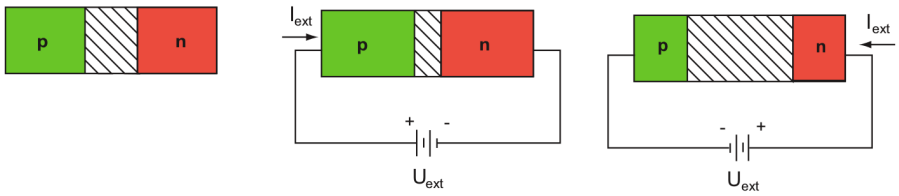

(a) without external bias **(b)** forward bias **(c)** reverse bias

Figure 3.3: Illustration of the width of the depletion zone depending on the external bias voltage. The depletion zone is indicated as hatched area. [44] (modified)

The width of the depletion zone d_{dep} is depends on the doping concentration $N_{D/A}$, the external reverse bias voltage U_{ext}, the built-in voltage U_{bi}, the elementary charge q and the permittivity of vacuum and the material $\epsilon_{0/r}$ and amounts to

$$d_{\mathrm{dep}} = \sqrt{\frac{2\epsilon_0\epsilon_r\left(U_{\mathrm{ext}} + U_{\mathrm{bi}}\right)}{q}\left(\frac{1}{N_D} + \frac{1}{N_A}\right)}. \tag{3.3}$$

The space charge region spreads mainly into the region with lower doping concentration. For further calculations the built-in voltage is neglected as it is significantly lower compared to the external bias voltage. With these assumptions the width of the depletion zone is simplified using the effective doping concentration $N_{\text{eff}} = N_D - N_A$ to

$$d_{\text{dep}} \approx \sqrt{\frac{2\epsilon_0 \epsilon_r U_{\text{ext}}}{q\,|N_{\text{eff}}|}}. \tag{3.4}$$

Electron-hole pairs which are created in the depletion zone do not recombine but drift towards the electrodes and induce a signal. For this reason the aim for semiconductor detectors is to maximize this depleted volume by applying an external bias voltage. The required external bias voltage to achieve the desired depletion of the sensor through the full thickness is called *depletion voltage* U_{dep}. For a fully depleted sensor a high electric field is built up through the full sensor depth.

3.5 Leakage Current

The leakage current of a p-n junction measured at different external bias voltages (*IV measurement*) shows a typical diode characteristic. With a forward biased voltage the current and bias voltage have an exponential relation while for increasing reverse bias the current saturates at the *saturation current* I_S. In Figure 3.4 this *IV characteristic* is presented while the breakdown at higher reverse bias is indicated with a dashed line.
The current measured for a sensor with reverse bias can be divided into a bulk and a surface fraction: In the bulk of the sensor, thermal excitation generates electron-hole pairs. Their contribution to the leakage current, the *generation current* I_{gen}, depends on the volume of the depletion zone and consequently depends on the external bias voltage: The reverse leakage current increases with $I \propto \sqrt{|U_{\text{ext}}|}$ until the bulk is completely depleted (see eq. 3.4). After full depletion the measured current in a sensor is dominated by the generation current which exceeds the constant amount of saturation current.
In addition, the measured reverse current of the bulk is strongly influenced by temperature T:

$$I \propto T^2 e^{-\frac{E_{\text{eff}}}{2k_B T}}. \tag{3.5}$$

In this equation the effective band gap energy E_{eff} is used since the band gap energy depends on the temperature (see reference [49] for information about the relation between E_{eff} and temperature, voltage or irradiation fluence).
Results measured at different temperatures can be compared by temperature scaling. The measured current I_m at the temperature T_m can be normalized to the current I at temperature T by

$$I = I_m \cdot \left(\frac{T}{T_m}\right)^2 \exp\left[\frac{-E_{\text{eff}}}{2k_B}\left(\frac{1}{T} - \frac{1}{T_m}\right)\right]. \tag{3.6}$$

With further increased reverse bias voltage, the electric field reaches a level at which drifting charge carriers are accelerated to high energies and can ionize further atoms. This avalanche effect results in a breakdown of the sensor and is called *avalanche breakdown*. Another breakdown mechanism is the *Zener breakdown*: The electric field due to the external bias voltage is high enough to release electrons from the covalent bond.

The surface contribution to the leakage current is a result of depositions or damages on the surface. It depends on the geometry of surface structures and the external bias voltage. Usually the leakage current is dominated by currents in the bulk.

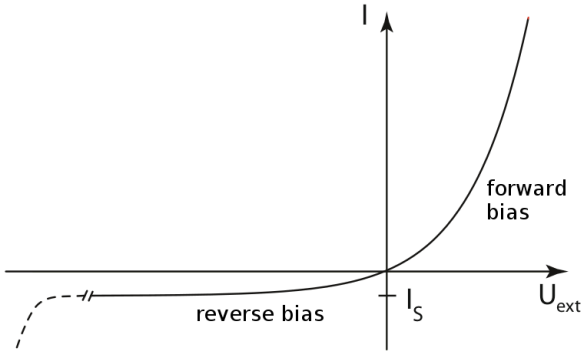

Figure 3.4: IV characteristic of a diode for forward and reverse bias. The breakdown at higher reverse bias is marked with a dashed line. [44] (modified)

3.6 Capacitance

A p-n junction can be seen as a parallel-plate capacitor which is filled with a dielectric. The distance between the plates corresponds to the width of the depletion zone. The capacitance can be calculated with the area A and the width d_{dep} of the depletion zone to

$$\frac{C}{A} = \frac{\epsilon_r \epsilon_0}{d_{\text{dep}}}. \tag{3.7}$$

From *capacitance-voltage (CV) measurements* the doping profile and the depletion voltage can be determined. The depletion voltage is reached when the capacitance, which depends on the width of the depletion zone, reaches a constant value. Moreover, the depletion depth depends on the doping profile (see eq. 3.4) which can be obtained from the slope if $\frac{1}{C^2}$ is measured at different voltages.

3.7 Charge Carrier Generation

Silicon particle detectors in high energy physics use the interaction of charged particles and photons with matter for detection. Electrons and holes are created in the depletion zone and drift towards the electrodes due to the electric field and the resulting signal is measured by the readout electronics. The dominant interaction processes of a traversing charged particle with matter are ionization and excitation of atoms. At higher energies of the traversing particles radiation effects become dominant. The changes due to ionization and excitation in the sensor material are reversible and do not damage the detectors.
To describe the atomic collision process it is necessary to distinguish between heavy charged particles, e.g. muons, pions, protons, α-particles and light charged particles like electrons and positrons. For heavy, relativistic, charged particles the average ionization energy loss in matter is described by the Bethe-Bloch formula [44]:

$$-\left\langle \frac{dE}{dx} \right\rangle = K \frac{Z}{A} \rho \frac{z^2}{\beta^2} \left[\frac{1}{2} \ln \frac{2 m_e c^2 \beta^2 \gamma^2 T_{\max}}{I^2} - \beta^2 - \frac{\delta(\beta\gamma)}{2} - \frac{C(\beta\gamma, I)}{Z} \right] \tag{3.8}$$

with the density correction δ (important for high energies) and the shell correction C/Z (important for small β). Other parameters in this formula are defined as:

- $K = 0.307\,\mathrm{MeV\,cm^2\,mol^{-1}}$.
- Z and A are the atomic number and atomic weight of the medium.
- ρ is the density of the medium.
- z is the charge of the traversing particle.
- m_e is the electron mass.
- $\beta = v/c$ is the velocity of the traversing particle in units of speed of light.
- $\gamma = \frac{1}{\sqrt{1-\beta^2}}$ is the Lorentz factor.
- I is the effective ionization potential averaged over all electrons.
- T_{max} is the maximum energy transfer in a single collision.

The formula describes the stopping power of material due to ionization for a traversing particle and depends on the particle's energy. At an energy range between $3 \leq \gamma\beta \leq 4$ of the traversing particle the minimum amount of energy is deposited in the material. Such a particle is referred to as a *minimal ionizing particle (MIP)*. For particle detection these MIPs generate the lowest signals in the detectors which is why they are often used as benchmark for sensor tests. In silicon the minimum mean energy loss is $1.66\,\mathrm{MeV\,cm^2\,g^{-1}}$ [44].

The main processes responsible for the energy loss of traversing particles are inelastic collisions in which the atom is ionized or excited. Only a small fraction of the particles' energy is transfered per collision while a large number of collisions per unit path length take place. In so-called *soft collisions* excitations happen while in *hard collisions* the material atoms are being ionized.
If the energy transfer to the electron in a hard collision exceeds twice the ionization energy limit the released electron can ionizes further atoms. These electrons are referred to as *δ-electrons* or *knock-on electrons*. In thin materials these δ-electrons add a tail to the deposited energy distribution at higher energies. The energy deposition is described with a *Landau distribution* for thin materials instead of a *Gaussian distribution* for thick materials. The Bethe-Bloch formula (eq. 3.8) describes the *mean* energy loss per path length while these distributions describe the fluctuations around this mean value.
The Landau distribution is mathematically expressed with

$$f_L = \frac{1}{\pi} \int_0^\infty \exp\left(-t \ln t - \lambda t\right) \sin\left(\pi t\right) dt \tag{3.9}$$

while the Gauss distribution is defined as

$$f_G = \frac{1}{\sqrt{2\pi\sigma^2}} \exp\left(-\frac{(x-\mu)^2}{2\sigma^2}\right). \tag{3.10}$$

For the description of the energy loss in silicon detectors with a thickness of 200 µm, which are investigated in this thesis, a convolution of Gauss and Landau distribution is used. This distribution is shown in red along with the Landau distribution (black) in Figure 3.5. To characterize such distributions the *most probable value (MPV)* is used instead of the mean value which is not defined for the asymptotic Landau distribution.

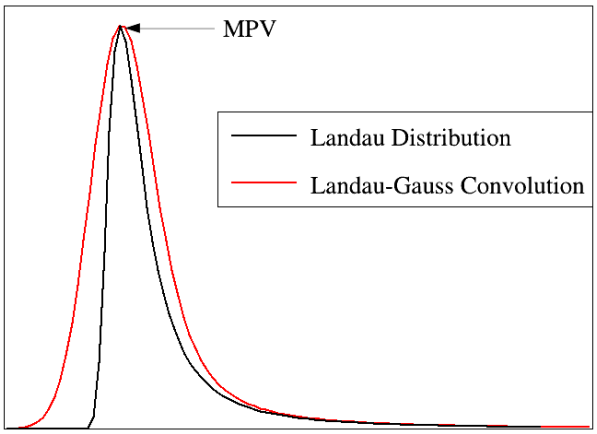

Figure 3.5: Example of a Landau distribution (black) and the convolution of a Landau and Gauss distribution (red). The most probable value (MPV) is indicated. The plot is generated with the adapted C++/ROOT tutorial "Langaus.C" [50].

For relativistic charged particles the amount of produced charge carriers is almost independent from the particles' energy but proportional to the square of the particles' charge. A uniform density of electron-hole pairs is generated along the particles' paths inside the detector. In Figure 3.6 the mean energy loss of protons in silicon as a function of their energy is presented.
However, α particles have a short penetration depth in material: With deceleration of the particles the density of produced electron-hole pairs in material increases as the ionization process depends on the velocity of the traversing particles. At the stopping point of the particles a pronounced maximum of the energy loss, the so-called *Bragg Peak* is reached. This way the α particles are usually stopped completely and their full energy is deposited in the detector.

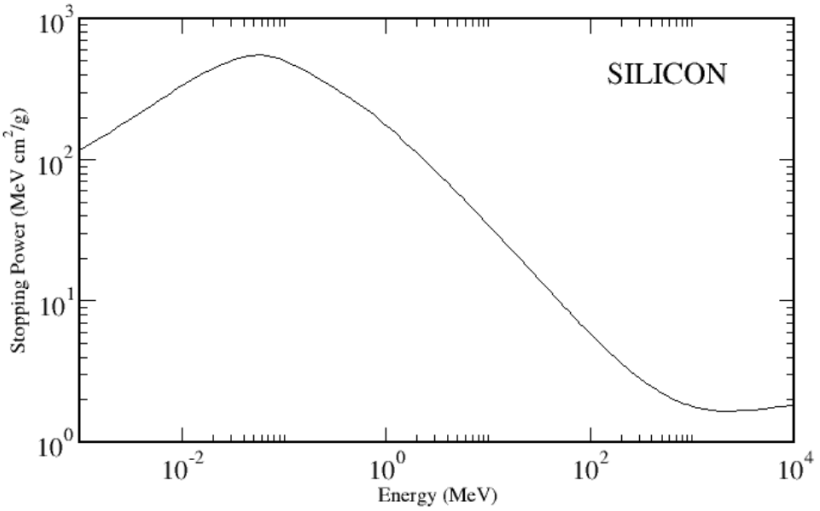

Figure 3.6: Mean energy loss of protons traversing through silicon in dependence of the proton energy. [51]

For electrons and positrons additional effects have to be considered compared to heavy particles as described before. For lower energies electrons and positrons ionize the material by colliding. The Bethe-Bloch Formula (eq. 3.8) needs to be adjusted to describe the energy loss of electrons and positrons in materials since the incident particle is now deflected due to its lower mass and it is not possible to distinguish the colliding particles. For higher energies the probability to generate electromagnetic radiation increases. The particles are deflected in the electric field of the nucleus and bremsstrahlung is produced.
For $\beta^{+/-}$ radiation less ionization takes place compared to the penetration of α particles in matter. As long as the velocity of the β is relativistic, electron-hole pairs are generated uniformly along the path. If the velocity decreases and the particle's energy is less than the energy of a MIP, the density of generated charges increases.

For the detection of neutral photons the following processes are relevant: The photoelectric effect, Compton scattering and pair production. In the lower energy range (1 keV to 60 keV for silicon [44]) the photoelectric effect is the dominant interaction of photons with matter. The complete energy of the photon is transferred to the atom which consequently emits a shell electron. The minimal photon energy for this process is the ionization energy of the material. Additional energy is converted to kinetic energy of the ionized electron which can ionize further atoms. Thus, low energy photons are absorbed close to the surface and the signal amplitude is proportional to photons energy which is completely deposited in the detector.

At higher energies photons interact with matter via the Compton effect. In silicon the Compton effect is dominant for energies between 60 keV to 15 MeV. The photon is scattered elastically with an essentially free shell electron. Many electron-hole pairs are created along the photons' track in a small spatial region.
If the energy of the photon exceeds twice the mass of an electron, the photon can be converted into an electron-positron pair at the nucleus. For this pair production process a minimum energy of 1.022 MeV is necessary. High energetic photons are able to pass several cm of material without interaction. For this reason they can not reliably be detected in the Inner Detector of the ATLAS experiment and are only measured in the calorimeters.

The sensitivity of semiconductor detectors to measure the particles described before is very high but among others limited by the leakage current (noise), trapping of charge carriers in the sensor and the readout electronics. A description on how the signal on the electrodes is generated is given in the following section.

3.8 Signal Formation

After generation in the depletion zone the charges diffuse and drift towards the electrodes attracted by the electric field. They can move freely through the material as their bindings to the lattice is considered in the effective mass $m_{\text{eff}}^{e,h}$ for electrons and holes. The acceleration of the charges towards the electrodes is slowed down by scattering processes and collisions with lattice atoms, impurity atoms or other scattering centers.
The mobility μ of electrons and holes is connected to the velocity and defined as

$$\mu_{e,h} = \frac{q\tau}{m_{\text{eff}}^{e,h}}. \tag{3.11}$$

It depends on the average time between collisions τ and indirectly on the electric field and doping concentration. Furthermore, the mean collision time τ is temperature dependent and for silicon at 300 K in the range of picoseconds [44]. At these temperatures the mobility in silicon of electrons is 1450 $\frac{\text{cm}^2}{\text{V s}}$ and about three times higher compared to the mobility of holes of 500 $\frac{\text{cm}^2}{\text{V s}}$ [44]. The goal in most particle detector applications is to measure the signals of traversing particles fast for which reason mostly the electron signal is read out by the readout electronics and not the hole signal. The detection material silicon provides a faster signal formation compared to other technologies like gaseous detectors: The mobility of ions in gas is about 1000 times lower than the mobility of electrons in silicon [44].

The relation between the drift velocity $v_{e,h}$ and the mobility of the charges in the electric field (generated by the external bias voltage) is linear for electric fields $E < 1 \times 10^3\,\mathrm{V\,cm^{-1}}$.
On their way towards the electrodes, the electrons and holes can recombine or get trapped which results in a reduction of the free path length and the lifetime. For intrinsic silicon semiconductors only indirect recombination like the reverse process to the production of electron-hole pair generation is possible which is very rare because the electrons and holes have a different crystal momentum. The main recombination process occurs at *recombination centers* which are impurity atoms in the lattice. Charge carriers can get captured and released after a certain time. However, if the opposite charge carrier is trapped as well, both charge carriers are annihilated. These recombination centers are the main source for the generation current I_{gen} (see Chapter 3.5). Another process which results from impurities in the crystal lattice is *trapping*. These impurities are only capable of capturing either holes or electrons: The charge carrier is trapped and released after a characteristic time.
The described processes can be explained by extra energy levels in the band gap which are added by the impurity atoms. It is distinguished between *shallow levels* which are located close to the conduction or valence band and *deep levels* in the central region of the band gap. In these deep levels the electrons and holes are trapped for longer periods, while in the shallow levels they can easily be excited and released shortly thereafter. Shallow levels are also introduced in the doping process of the crystals (see Chapter 3.3) in which impurity atoms are brought into the material on purpose. The different energy levels added to the band gap of silicon by the dopants and impurities is illustrated in Figure 3.7.

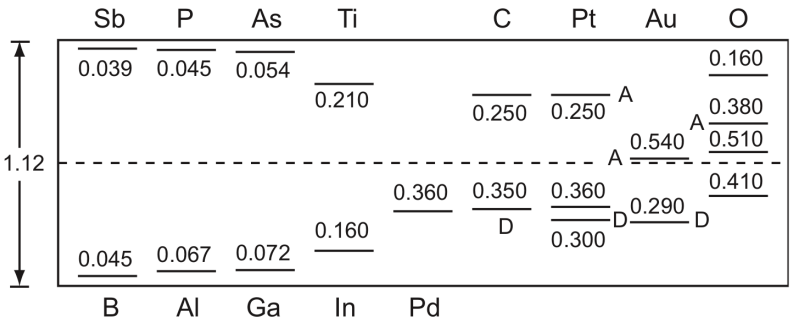

Figure 3.7: Energy levels added to the band gap of silicon by dopants (n-doping: antimony (Sb), phosphorus (P), arsenic (As) and p-doping: boron (B), aluminum (Al), gallium (Ga)) and impurity atoms. The unit of the y-axis is in eV. [44]

The movement of the generated charge carriers towards the electrodes induces charge on the electrodes and the readout signal is formed. The longer the free path length the higher the signal. If charges are trapped and the trapping times are longer compared to the collection time in the readout system, charges will not be registered. As a result, the signal amplitude is lower and the energy resolution of the particle detection is reduced. Therefore, highly purified crystals are required for particle detection.

The signal measured by the electrodes can be determined via the Shockley-Ramo theorem. Detailed information about the theorem can be found in [52, 53]. In accordance to the theorem the measured signal amplitude on the electrodes is independent from the electric field and the applied bias voltage when the device is fully depleted. However, the movement direction and the velocity of the charge carriers are influenced by the electric field which therefore influences the signal shape. In addition, the Shockley-Ramo theorem allows the prediction of the induced charge at the electrodes in the presence of stationary space charges.
In the top of Figure 3.8 an example of an absorbed gamma ray generating n electron-hole pairs at the interaction depth Z in an externally biased semiconductor is presented. The semiconductor diode has a thickness of 1 in z- and an infinite expansion in x- and y-direction. The Shockley-Ramo theorem describes the electrostatic coupling of the charges to the electrodes with the weighting field and weighting potential which is only dependent on the geometry of the electrodes.
The weighting potential ϕ_R for such a planar diode is given by

$$\phi_R(z) = z,\ 0 \leq z \leq 1. \tag{3.12}$$

The electric field separates the charge carriers and the electrons drift from $z = Z$ to $z = 1$ and the holes from $z = Z$ to $z = 0$. The drifting charges induce charge in the electrodes similar to the concept of mirror charges. If no charge carriers are lost, the total change in induced charge ΔQ measured at the anode is calculated with

$$\Delta Q = -(ne)(0 - Z) + (ne)(1 - Z) = ne. \tag{3.13}$$

The induced charge is proportional to the number of generated charge carries and consequently to the deposited energy but independent from the interaction depth Z. In the center of Figure 3.8 the weighting potential of the anode is depicted and the normalized signal components from the electron and hole movements are marked. For a traversing particle with a deposited energy E_γ, charge carriers are produced along the track randomly in all depth of the detector. The energy spectra of the detector output is a constant and presented in the bottom of Figure 3.8 (solid line). Under the assumption that the holes move only a short distance compared to the

detector thickness, the total change in induced charge becomes dependent on the position Z of the charge carrier production and varies between 0 and ne:

$$\Delta Q \approx ne(1 - Z). \tag{3.14}$$

The resulting energy spectrum of the detector without movement of holes is illustrated in the bottom of Figure 3.8 (dashed line).

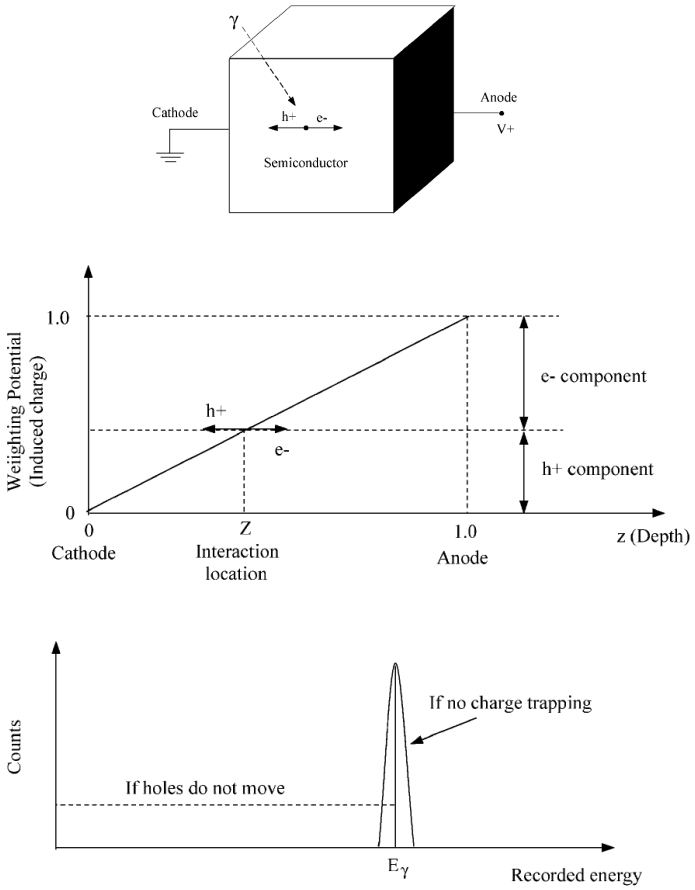

Figure 3.8: Schematic of a detector with planar infinite electrodes. Top: Illustration of a γ-ray semiconductor detector with planar electrodes. Middle: The weighting potential of the anode for charge generation at interaction depth Z. Bottom: Energy spectra for a uniform γ-ray interaction through the full depth of this detector with a fixed energy deposition E_γ without movement of holes (dashed line) and with movement of holes (solid line). [52] (modified)

Detectors like pixel or strip sensors have segmented electrodes which changes the weighting potential as presented on the left side of Figure 3.9. The weighting potential for segmented sensors is highest directly beneath the strip implant and decreases with depth. It expands not only in vertical but also in horizontal direction beneath the neighboring strips. If a charge carrier far away from the strip anode begins to move towards the electrode, a signal charge is induced not only in the closest strip (strip 1) but a similar charge is also in induced in the neighboring strips (strip 2). With decreasing distance between the moving charge and the closest strip, more charge is induced in both, the closest and the neighboring electrodes. When the moving charge is in the close vicinity of the strip the induced charge increases rapidly on the closest electrode, while decreasing at neighboring electrodes. The smaller the pixel or strip width of the electrode compared to the sensor depth, the steeper the rapid increase in induced charge on the closest electrode. This effect is called *small pixel effect*.
The induced charge in dependence on the distance of the moving charge is shown for the closest strip in the upper right part and for the neighboring strip in the lower right part of Figure 3.9. The strip width a is here normalized to the sensor thickness.

The small pixel effect becomes more relevant when the mobilities of electrons and holes differ greatly and charge carriers are influenced by trapping: At the beginning of the charge movement from the center of the sensor depth towards the electrodes the same amount of charges are induced in the closest and the neighboring strip. If the electrons are then trapped on their way it is not possible to distinguish the closest and neighboring electrode. Therefore, the position of the interaction of the incident particle is unclear resulting in a poor spatial resolution.

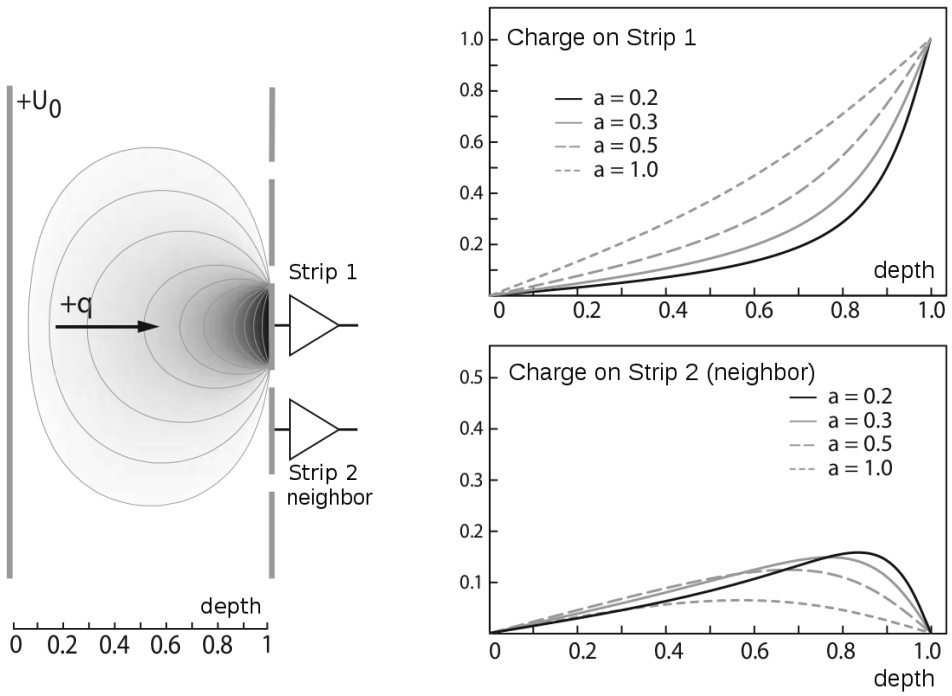

Figure 3.9: Weighting field and resulting charge signal for a strip or pixel detector. Left: Weighting field for a charge q moving towards the signal electrode strip 1 and the neighboring strip electrode 2. Right: Charge signal in dependence of the depth of the moving charge q for the signal strip 1 (b, top) and the neighboring electrode strip 2 (b, bottom). The charge signal is presented for different ratios a between the strip width and the sensor thickness. [44] (modified)

The described signal formation can be investigated in laser induced charge measurements with the so-called *Transition Current Technique (TCT)*: A laser is used to generate electron-hole pairs close to the surface of the sensor. One type of produced charge carrier, either the electrons or the holes, drifts only a short distance to the electrode while the other crosses almost the sensor's full thickness. The induced signal of the former charge carrier is too fast for the readout electronics and neglected. The total signal is dominated by the charge carrier that drifts through the sensor bulk towards the electrode on the opposite side. This way either an electron or a hole signal can be investigated depending on the sensor side that is illuminated by the laser. In Figure (3.10) the close-to-surface injection of charge carriers with a laser is shown for an n^+-in-n sensor. If the charges due to the laser injection are generated close to the surface of the p-type electrode, the electrons drift through the n-type bulk and induce the dominant signal on the electrode on the n^+-side while the hole signal is neglected. For a laser illumination from the n^+-side the holes drift through the sensor bulk. Therefore, the hole movement induces the dominant signal on the electrode of the p-side. For more information about the TCT setup and results of laser induced charge collection measurements see Chapter 8.4.

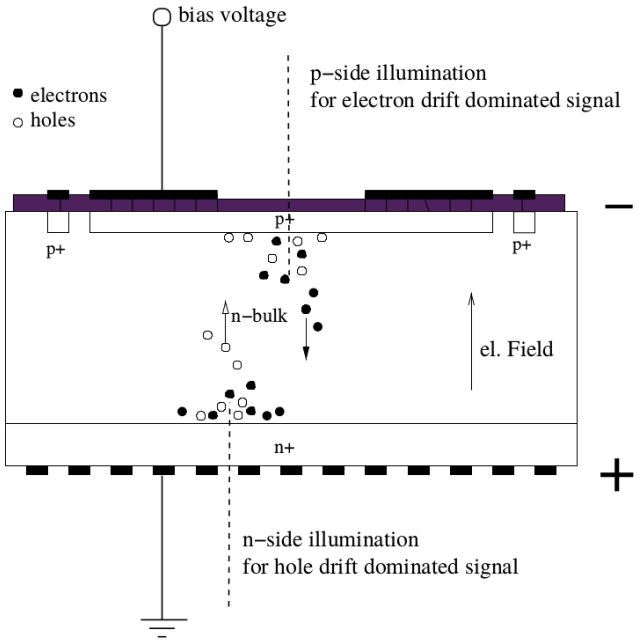

Figure 3.10: Close-to-surface injection of charge carriers for an n^+-in-n sensor. One charge carrier type drifts only a short distance towards the target electrode while the other drifts through the whole sensor. The resulting signal is dominated by the longer distance drifting charge. [53]

4 Radiation Damage in Silicon

The ionizing processes of particles passing through silicon devices, described in Chapter 3.7, are reversible processes and do not change the sensor's properties. They are referred to as *ionizing energy loss (IEL)*. Besides these processes, defects in the crystal lattice can be formed which become more significant at a high particle fluence (*non-ionizing energy loss, NIEL*): Among other defects, crystal atoms are shifted from their regular lattice sides creating holes and interstitials in the lattice. They influence the sensor properties like effective doping concentration, leakage current and signal formation. These effects created by NIEL are irreversible in contrast to the IEL processes.
The damaging effect of various particles is commonly scaled to the impact of neutrons with an energy of 1 MeV. This way the particle fluence passing through material is measured in n_{eq}/cm^2 (neutron equivalent per square centimeter). In experiments like ATLAS the highest fluences are reached at the innermost layers. Typical expected fluences close to the interaction point, as mentioned in Chapter 2.2.4/2.2.5, are $5 \times 10^{15}\, n_{eq}/cm^2$ for the IBL (the current innermost layer of the ATLAS detector) and $1.3 \times 10^{16}\, n_{eq}/cm^2$ for the innermost layer of the ITk (the future innermost detector part of the ATLAS detector after LS3).
The crystal defects influence the sensor properties, especially the mobility of charge carriers and their free path length. Thus, sensors are designed and tested to achieve good performances even after high radiation fluences.
In this chapter only the radiation damage on silicon and silicon devices is discussed while defects of the surface and the bulk are distinguished. More detailed information on radiation defects can be found in [44, 46, 54, 55].

4.1 Surface Damage

The radiation damage caused on the surface of the sensor is mainly produced in the outer passivation layer of the device, the silicon oxide layer or at the boundary layer between silicon and silicon oxide. At the surface the radiation damage is dominated by holes created by IEL while the influence of displacement damage by NIEL can be neglected: The crystal structure in this area is already highly irregular and a displacement of further atoms by NIEL can be ignored. However, the mobility of

holes is about a factor of 10^6 times lower compared to the mobility of electrons because of trapping [44]. In these layers the trapped holes influence the electric properties by building up positive charges. The damage highly depends on the topology of the detector and results in electric field strength maxima and higher surface leakage currents.
The limiting factor for the application of silicon sensors used in high energy physics are radiation defects in the bulk. For this reason bulk damages have been the main focus for studies in this field. More information on radiation damage on the surface can be found in [56].

4.2 Bulk Damage

The silicon lattice of the bulk can among others be changed by radiation via neutron capture and nucleus transmutation. Furthermore, bulk damage is also caused by direct collisions of the incident particle with atoms of the crystal lattice. The so-called *Primary Knock on Atom (PKA)* is displaced from the lattice and moved between regular lattice sites. The remaining *vacancy (V)* and the *interstitial (I)* form a so-called *Frenkel Pair (V-I)* in the lattice which is referred to as *point defect*. About 25 eV are necessary to knock out an atom from the silicon lattice with a displacement probability of 50 % [44]. These point defects are not stable but recombine while moving freely in the lattice. Nevertheless, point defects can also form stable defect complexes either together with other point defects or impurity atoms. Figure 4.1 schematically illustrates different point defects and defect complexes. Examples of well studied stable defect complexes are the double vacancy (V_2), the combination of a vacancy and oxygen, so-called A-center (V-O), and the combination of a vacancy and a donor atom from the fifth element group like phosphor, so-called E-center (V-P).

If the recoil energy of the PKA surpasses 25 eV, it can displace further atoms from the lattice. Depending on the recoil energy point defects or *defect clusters* are generated. A defect cluster is a dense accumulation of point defects with a typical size of 5 nm and about 100 displacements [46]. For recoil energies below 2 keV only point defects will be created while at higher energies between 2 keV to 12 keV one defect cluster and additional point defects are produced. For even higher recoil energies several cluster defects and point defects are generated inside the silicon lattice [46].
The generation of radiation defects in the crystal lattice depends on the type and energy of the impinging radiation. In addition, the kinematic energy transfer to the atom depends on the mass of the radiation particle. The threshold energy of the incident particle to create a Frenkel Pair in silicon is about 175 eV for neutrons

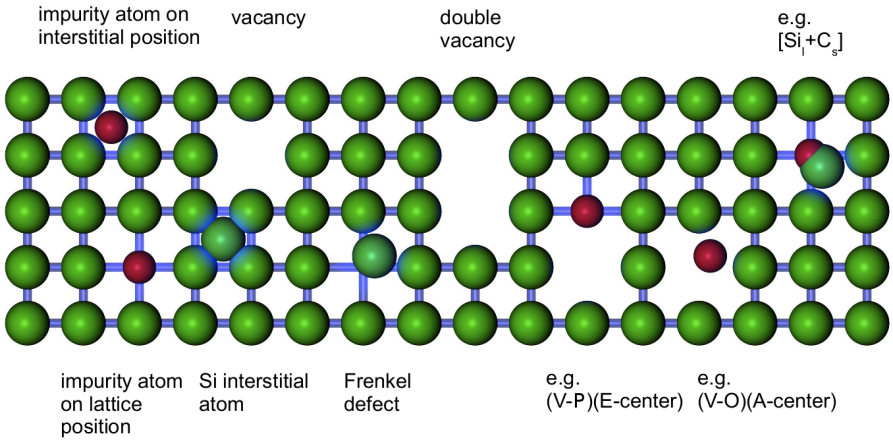

Figure 4.1: Illustration of different crystal defects due to radiation. [57] (modified)

while for electrons a much higher threshold energy of 260 keV is necessary [54]. To compare the radiation damage in silicon generated by one particle type with a specific energy to the impact of another particle the *NIEL-scaling hypothesis* is used. The hypothesis states that all damages in silicon detectors are mainly produced due to cluster and point defects from the PKA. The damage function $D(E)$ takes the impact of different particle types and energies into account and is presented for protons, neutrons, pions and electrons in Figure 4.2. With this damage function the hardness factor κ can be calculated to scale the particle fluence of a certain particle ϕ_x to the fluence of 1 MeV neutrons ϕ_{eq}:

$$\phi_{\text{eq}} = \kappa \cdot \phi_x . \tag{4.1}$$

The hardness factor is calculated with

$$\kappa = \frac{\int_{E_{\min}}^{E_{\max}} D_x(E)\phi_x(E)dE}{D_n(1\,\text{MeV}) \int_{E_{\min}}^{E_{\max}} \phi_x(E)dE}. \tag{4.2}$$

For proton irradiations used in high energy physics the hardness factor κ is determined to 0.6 for 24 GeV and to 1.85 for 25 MeV protons [44]. Even after scaling with the NIEL hypothesis the damage in the silicon lattice depends on the incident particle. Proton irradiation will typically cause cluster defects and isolated single defects while neutron irradiation will typically result in a cascade of interaction with an extended damage region and defect clusters. For the studies herein the approximation of the NIEL scaling hypothesis was applied while its limits are discussed in [58].

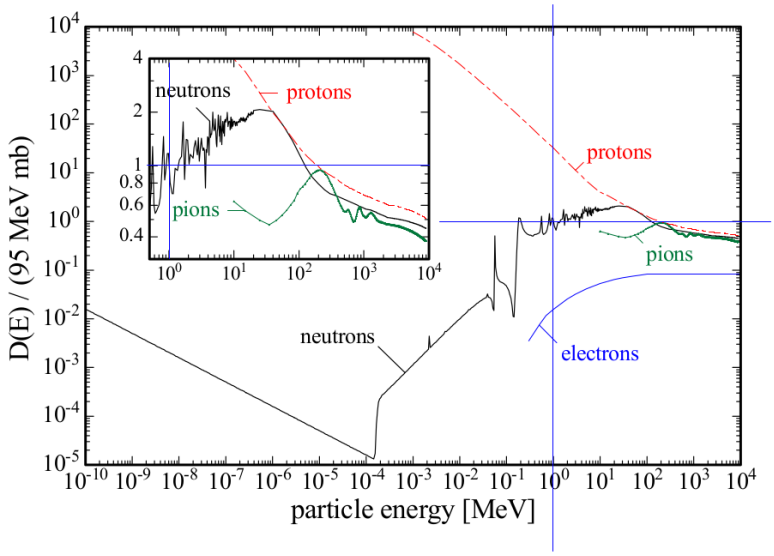

Figure 4.2: Damage function according to the non-ionizing energy loss (NIEL) hypothesis for different particles. [54]

The microscopical defect complexes influence the macroscopic detector properties and depend on their concentration, the energy level and the electron/hole capture cross section. One detector characteristic changing significantly with radiation damage is the effective doping concentration N_{eff}. Donors and acceptors are removed in the space charge region when defect complexes are built of acceptors or donors like vacancy-phosphorus or vacancy-boron complexes. Furthermore, if the complexes have positive or negative charge states, defect complexes can be effective donors or effective acceptors while the production process for acceptor-like complexes is dominating. As stated in Equation 3.4 the depletion depth depends on the voltage and the effective doping concentration. With an increase in doping concentration a higher bias voltage is necessary to reach full depletion of the sensors. As a result, highly irradiated silicon sensors need to be operated at higher bias voltages to maintain a full depletion.
For an n-type semiconductor with increasing particle fluence more phosphorus dopants are captured in defect complexes and the dopants lose their original function. Consequently, the effective doping concentration drops and at a specific fluence the donor and acceptor concentrations reach an equilibrium ($N_{\text{eff}} = N_D - N_A = 0$). At even higher fluences, defects capture valence electrons and function as acceptors, just like a p-doping, which results in a *type inversion* of the originally n-type doped detector. The direction from which the depletion zone starts to grow

is shifted from the front side to the back side of the sensor. The change in effective doping concentration for an n-type semiconductor at different fluences and the required voltage for full depletion are shown in Figure 4.3.

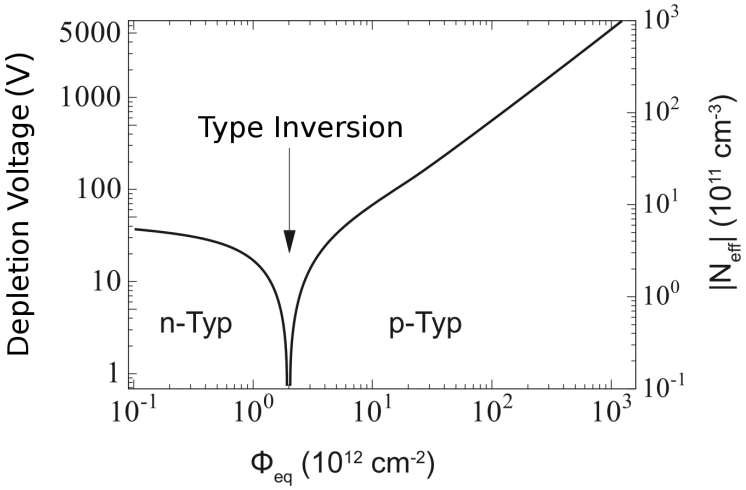

Figure 4.3: Effective doping concentration N_{eff} (right axis) and depletion voltage (left axis) as a function of radiation fluence normalized to 1 MeV neutrons for a sensor with an originally n-type doped bulk. [44] (modified)

The reverse bias current also increases with radiation damage as the defect complexes create deep energy levels in the center of the band gap which function as thermal generation centers. Therefore, an increase in leakage current is observed which is proportional to the radiation fluence:

$$\Delta I_{\text{leak}} = \alpha \cdot \phi_{\text{eq}} \cdot V \tag{4.3}$$

with the depleted volume V, the radiation fluence normalized to 1 MeV neutrons ϕ_{eq} and the damage constant α. This damage constant α is dependent on the particle type and fluence but not influenced by material properties. Therefore, it can be used to monitor the equivalent fluence of particle sources when the change in leakage current ΔI_{leak} is measured [59]. In addition, the damage constant α is strongly temperature dependent and normalized to 20 °C. With higher radiation fluences the leakage current and the power dissipation increase, heating up the sensor. The higher the sensor's temperature rises the more leakage current is generated. This chain reaction is called *thermal runaway* which should be avoided as it has the potential to damage the sensor and the readout electronics: The bias voltage should be kept below the sensors breakdown voltage and readout chips have a limited DC leakage current tolerance (100 nA per pixel for the FE-I4 [60]). By cooling down

the device the leakage current is reduced as it is strongly influenced by temperature (see equation 3.5). For this reason, irradiated sensors which have to be operated at higher bias voltages are always investigated while they are cooled down to temperatures around −20 °C to −40 °C. An operation at lower bias voltage than depletion voltage is possible if necessary, but results in deteriorated detection characteristics. Another consequence resulting from radiation damage is the reduction of the charge collection efficiency: As described in Chapter 3.8 the signal induced into the electrodes depends on the time and distance of the moving charge carriers towards the electrodes. Radiation damage induces crystal defects into the silicon lattice which trap charge carriers and reduce their mean free path. If detrapping takes place when the signal formation time has passed, the signal from the trapped charge carrier is not associated to the correct event. The trapping probability increases linearly with radiation fluence [61].

To produce silicon detectors that are more radiation hard several approaches are pursued: One concept is the enrichment of the silicon bulk with oxygen as described in [59]. After gamma irradiation, which causes mainly point defects, the higher concentration of oxygen suppresses the formation of the V_2O complex by creation of a VO complex. The n-type bulk remains with a positive space charge region and no type inversion takes place at higher fluences. Hadron irradiation produces cluster defects in the material and type inversion is also observed for oxygen enriched n-type bulk material. However, the effective doping concentration N_{eff} of oxygen enriched n-type detectors after type inversion is lower compared to standard material resulting in a lower depletion voltage for oxygen enriched material. Only for the irradiation with neutrons the oxygen enriched materials perform similar to the standard material. Until now this discrepancy is not fully understood and referred to as “p-n puzzle” (more information in [59]). In Figure 4.4 the change in effective doping concentration and depletion voltage for different fluences are presented for sensors produced with the standard and the oxygen enriched float-zone method (FZ) after irradiation with neutrons, pions and hadrons.
Another approach for more radiation hard detectors is the reduction of the charge carrier drift time by either using thinner devices or the 3D sensor technology (see Chapter 5.1.2).
In addition, smaller electrodes like pixel detectors are preferred in the environment of higher radiation fluences compared to large electrodes like strip detectors: With growing radiation damage the leakage current increases which depends on the volume beneath the electrodes (see equation 4.3). With higher leakage current more charge carriers are generated inside the bulk and the noise increases. Therefore, a better signal-to-noise ratio can be achieved with smaller electrodes.

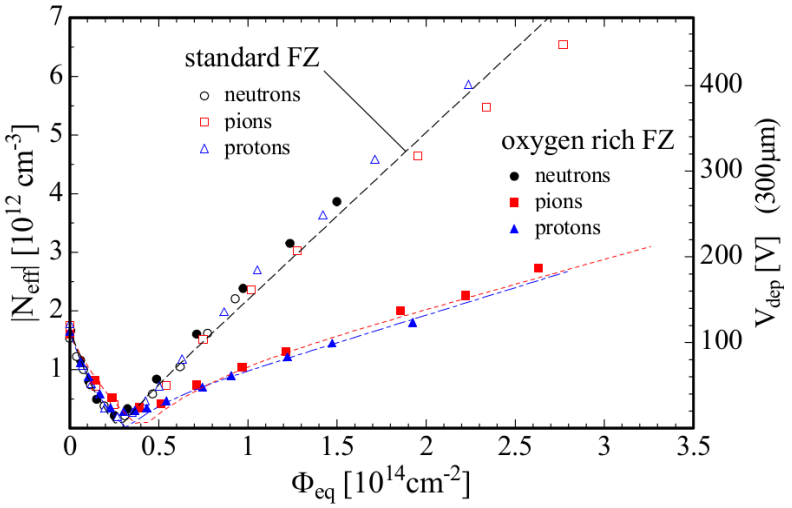

Figure 4.4: Dependence of N_{eff} for standard and oxygen enriched float-zone (FZ) silicon detectors with a thickness of 300 µm after irradiation with 1 MeV neutron equivalent fluence reactor neutrons (Ljubljana), 23 GeV protons (CERN PS) and 192 MeV pions (PSI). [59]

4.3 Annealing

The crystal defects described in the previous section are mobile at high temperatures and thus the number of defects can be changed by controlling the temperature. The exposition of irradiated sensors to room temperatures and higher is referred to as *annealing*. The change in effective doping concentration ΔN_{eff} is described by the *Hamburg Model* [59] which is empirical: A higher temperature after irradiation heals defects during the *beneficial annealing*. For longer periods at higher temperatures other defects form, which worsen the sensor performance in the *reverse annealing*. These annealing effects are influenced by temperature and duration. The effective doping concentration before irradiation (N_{C0}) is changed after irradiation and annealing by

$$\Delta N_{\text{eff}}(\phi_{\text{eq}}, t(T_a)) = N_C(\phi_{\text{eq}}, t(T_a)) + N_A(\phi_{\text{eq}}, t(T_a)) + N_Y(\phi_{\text{eq}}, t(T_a)) \qquad (4.4)$$

with the annealing temperature T_a and the three terms N_A, N_C and N_Y. The first term N_C describes the stable damage part and is determined by the radiation fluence but independent of temperature and annealing time. N_A describes the temperature dependent healing of crystal defects in the short term or beneficial annealing: The effective doping concentration increases resulting in a less negative

N_{eff} for type-inverted detectors and p-type sensors, and a higher positive N_{eff} for n-type sensors (not type-inverted). Consequently, the depletion voltage is lowered for type-inverted detectors and p-type sensors and increased for n-type sensors (not type-inverted). The associated microscopic effects to beneficial annealing are the acceptor removal and/or the creation of donors.
The third term N_Y describes the reverse annealing for long annealing times: Acceptors are created and/or donors annealed and the depletion voltage increases for p-type and type-inverted sensors. For n-type sensors (not type-inverted) the effective doping concentration and the depletion voltage decreases until an equilibrium between acceptor and donor concentration is reached. With a further increase in acceptor concentration the n-type sensor is inverted. In Figure 4.5 the change in effective doping concentration with annealing is displayed for annealing times at 60 °C.

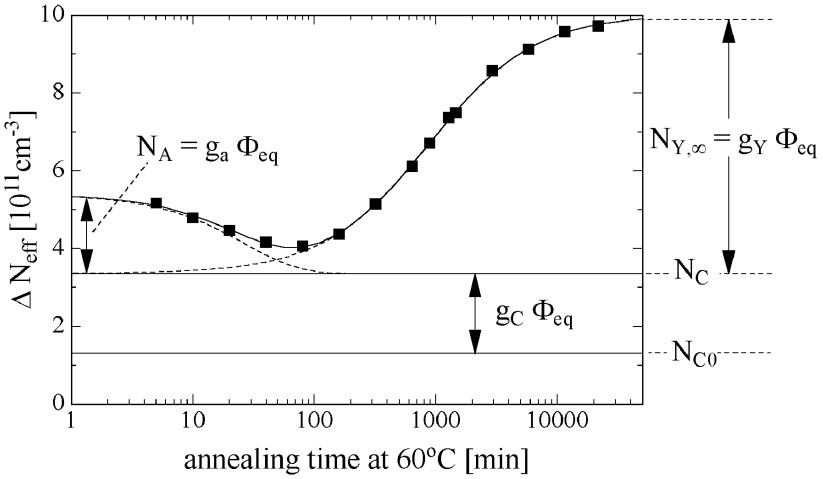

Figure 4.5: Change in doping concentration ΔN_{eff} for different annealing times at 60 °C. [55]

In addition, annealing influences the leakage current and therefore the damage constant α introduced in formula 4.3. With longer annealing times the value for α decreases which is illustrated in Figure 4.6. For this illustration the damage constant α is not normalized to 20 °C and with higher annealing temperatures lower values are measured.

A decrease in trapping probability with annealing is observed for electrons while an increase is measured for holes [53, 61]. In Figure 4.7 the tracking probability for electrons and holes is presented at different annealing times. Hybrid silicon pixel detectors in high energy physics like the ATLAS experiment use the electron signal

as their trapping probability is lower compared to holes and a reduction in trapping probability of electrons after irradiation is beneficial.

In sum, a short time period at room temperature for irradiated installed sensors at the LHC can improve the detector performance in a way that the depletion voltages, the leakage currents and the trapping probability of electrons are reduced. However, the described long term reverse annealing of the effective doping concentration should be avoided.

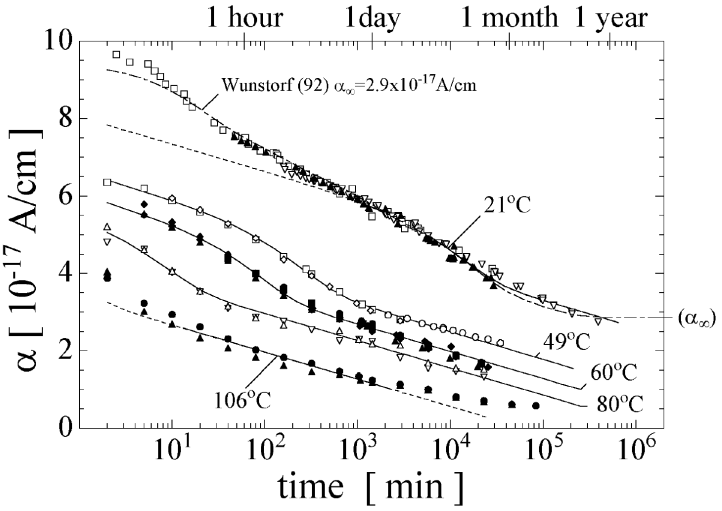

Figure 4.6: Damage rate α as a function of the cumulated annealing time. The annealing is performed at different temperatures with type-inverted and not type-inverted samples. [55]

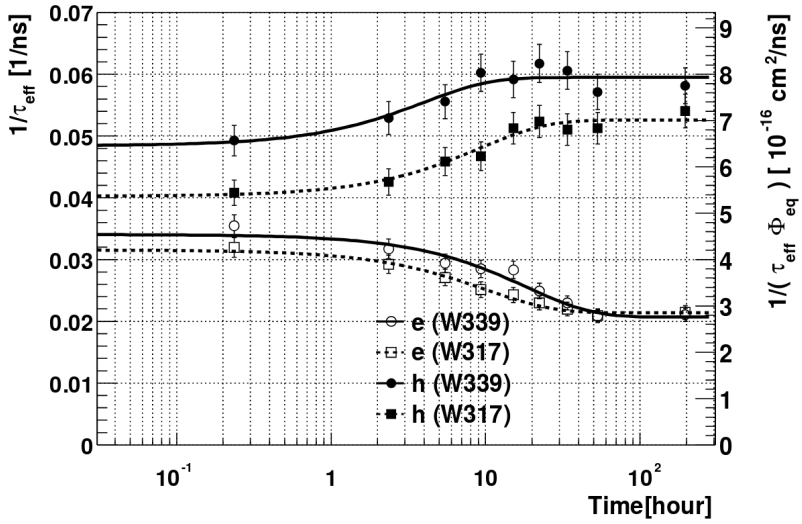

Figure 4.7: Effective trapping probability of electrons and holes as a function of the cumulative annealing time at 60 °C. [61]

5 Hybrid Pixel Modules

As described in the previous chapters, pixel sensors have smaller segmented areas compared to strip detectors and are therefore more radiation hard and provide a better spatial resolution. Two different technologies are currently used for the production of pixel detectors: Hybrid and monolithic.
For hybrid pixel detectors the readout electronics and the silicon sensor are separate components which are produced independently and connected in the *bump bonding* process. This allows to investigate, optimize and test both components independently from each other. However, the bump bonding process is expensive.
For monolithic pixel detectors the sensor and the readout electronics are produced in one piece of silicon. The thickness and hence the material budget can be reduced compared to hybrid pixel detectors. The study of monolithic pixel detectors and their application in high energy physics is a current field of research (see for example [62] and references therein). The application of radiation hard, sophisticated monolithic pixel modules in a large experiment with HL-LHC conditions is missing until know.
Hybrid pixel detectors were used successfully in high radiation environments close to the interaction point like the IBL and will be used in the upgraded pixel detector ITk of the ATLAS detector at CERN. For this thesis hybrid pixel detectors were investigated and the sensor composition, the readout chip and the process to connect both components to a module are presented in the following section. Special attention is payed to the layout of the sensors and modules investigated in this thesis which where developed based on the sensors used for IBL.

5.1 Sensors

The silicon sensors of hybrid pixel modules are composed of a slightly n- or p-doped silicon bulk in which the main interaction for detection of an incident particle with matter takes place. Between the higher n^+- and p^+-doped electrodes the external bias voltage generates a depletion zone and an electric field attracting the generated charge carriers. The movement of the charge carriers induces signal charges in the electrodes which is used for detection. There are two different concepts for the arrangement of the electrodes: Planar and 3D sensors.

5.1.1 Planar Sensors

For planar sensors the electrodes are n^+- and p^+-doped silicon layers on top of and beneath the silicon bulk. This way the depletion zone grows from one surface towards the other and full depletion is reached when the depletion depth matches the bulk thickness. For a depleted device with this electrode arrangement, the maximum distance for the charge carriers to drift towards the electrodes corresponds to the sensor thickness. The bulk material can either be n- or p-type doped and the implantation of the readout electrode (pixel implantation) n^+- or p^+-doped resulting in four different configurations. Since the mobility of electrons in silicon is higher compared to the mobility of holes, a faster signal is generated by electrons. In addition, the trapping probability of electrons is lower and thus the electron signal is used in many high energy physics applications. The doping of the readout electrode defines the signal type and only two different configurations use the electron signal: An n-type silicon bulk with n^+-doped pixel implantations, a so-called *n^+-in-n sensor*, or a p-type silicon bulk with n^+-doped pixel implantations, *n^+-in-p sensor*. The n^+-in-n sensors have segmented layers on either side of the bulk and a double sided wafer processing is necessary which is more expensive than processing only one side of the wafer. For n^+-in-p sensors all segmented layers are on the same side of the wafer reducing their production costs.
This thesis focuses on the investigation of n^+-in-n sensors based on the IBL pixel design for which a schematic cross section is shown in Figure 5.1. Five different layers are placed on the front (pixel side) and back side of a high resistivity slightly doped n-type wafer (with a thickness of 200 µm for IBL). The first layer above the silicon bulk consists of n^+-implantations defining the pixels of the sensor and the segmentation is accomplished with photo-lithography processes. For the IBL sensor design the pixel implantations are arranged in an array of 80 columns and 336 rows with a pixel size of 250 µm × 50 µm. To shield the implantation layer an oxide passivation and an inner nitride passivation layer are superimposed. Subsequently, the moderated p-spray insulating the pixel implantations from each other is injected: Applying the p-spray homogeneously between the implants would result in a junction of n^+- and p-region at the edge of the pixel implant and an area with high electric fields causing an earlier breakdown of the sensor. To avoid these electric field maxima the p-spray is moderated whereby the highest concentration is reached in parts without nitride layer in the middle between two pixels and almost no p-spray is present beneath the nitride layer close to each implant. For more information on moderated p-spray see [63]. Metal contacts on top (*bump pads*) ensure a good connection between the implantation and the readout chip via bump bonds. Except for these bump pads, the sensor is covered by a protective passivation layer on the pixel side.

On the sensor's back side the order of layers is comparable to the front side but instead of pixel implantations only one large p^+-implantation surrounded by 16 *guard rings* exists. While operating, the back side is biased with a negative potential while the edge and the pixel side are on ground potential. The guard rings are supposed to prevent a current flow over the cutting edge. Furthermore, they provide a controlled potential drop between the high voltage pad and the edge of the sensor. This way, the breakdown voltage is increased while the leakage current and thus the noise are reduced. More information on the edge design and guard ring investigations can be found in [64].

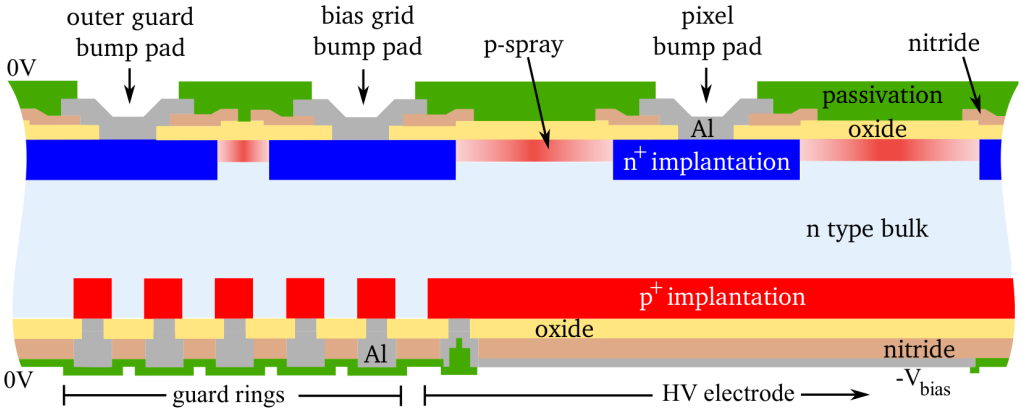

Figure 5.1: Schematic cross section of an n^+-in-n pixel sensor. [64]

The electric field in a non-irradiated n^+-in-n sensor grows from the backside towards the pixel side with increasing bias voltage. Therefore, these detectors can only be operated when they are fully depleted. After exposure to radiation the n-type bulk inverts to a p-type bulk after a certain fluence as explained in Chapter 4.2. Consequently, the growth direction of the electric field in the sensor is inverted and now grows from the pixel side. After irradiation higher bias voltages are necessary to deplete the sensor but power dissipation or leakage current limit the maximum applicable bias voltage. However, the type-inverted sensor can be operated even without full depletion.

For n^+-in-p sensors, n^+-pixel implantations are placed inside a p-type bulk with a large p^+-implant on the backside. For this sensor type the electric field grows from the pixel side towards the backside in the non-irradiated and irradiated case as no type inversion takes place. All segmented areas, like the pixel implants and the guard rings, are located on the same wafer side for n^+-in-p sensors which is why these sensors can be produced in the cheaper single sided process. Hence, this sensor technology is foreseen for the sensors of the future ITk (see Chapter 2.2.5).

For both sensor configurations a metal trace is placed on the pixel side of the sensor between a double column, the so-called *bias rail* which is connected to the *bias dot* of each pixel. The bias dot of each pixel is connected to a small round implantation which is not connected with the pixel implantation. At the rim of the pixel matrix all bias rails are connected to the same bias grid ring which is shielded from the sensor edges by the outer guard ring (see Figure 5.2 (a)). This *bias grid* structure ensures that all pixels are set to the same potential even when no readout electronic is connected with the *punch-through effect*: When the bias voltage U_{B} exceeds the punch through voltages U_{PT} the depletion zones beneath the pixel implantation and the bias dot merge and create a conducting connection (see Figure 5.2 (b)). This way all pixel implantations are held at the same potential.

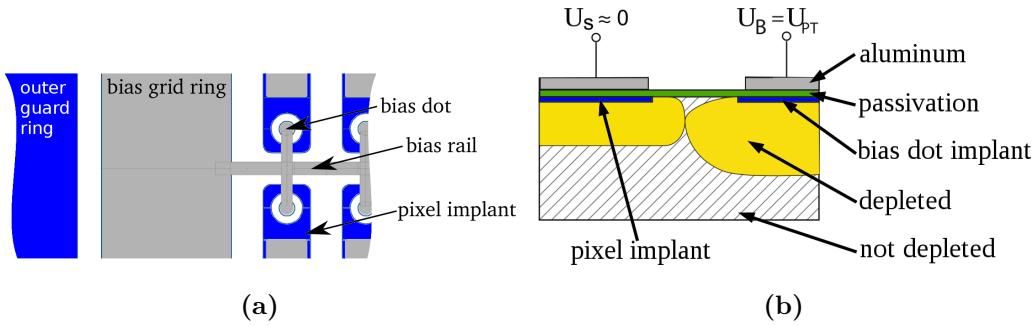

Figure 5.2: The punch through effect. The implantation is shown in blue, metal in gray, passivation in green. Left: Top view of the bias grid for an n^+-in-n sensor. [64] (modified) Right: Cross section of an n^+-in-p sensor. The depletion zone beneath the bias dot and the pixel implant is indicated yellow. The hatched area is not depleted. [44] (modified)

5.1.2 3D Sensors

In contrast to planar sensors with the electrodes implemented on the surface, the electrodes of 3D sensors are made of pillars inside the bulk. This way, a decoupling between the bulk thickness and the drift length of the charge carriers is realized. The short distance between the electrodes (67 µm for IBL 3D sensors) reduces the depletion voltage, the drift length of charge carriers and the charge collection time. Especially after irradiation, the lower depletion voltage and short distance to the electrodes is beneficial for the operation in environments with high particle fluences. The current innermost layer of the ATLAS detector (IBL) is composed to 25 % of 3D modules and they are foreseen to be installed in layer 0 of the future ITk with a reduced pixel size. Nevertheless, 3D sensors are more expensive compared to planar

sensors as extra processing steps are needed in the complex production process. In Figure 5.3 the schematic cross section for a 3D sensor with a p-type bulk is presented. For more information on 3D sensor technology see [33, 65].

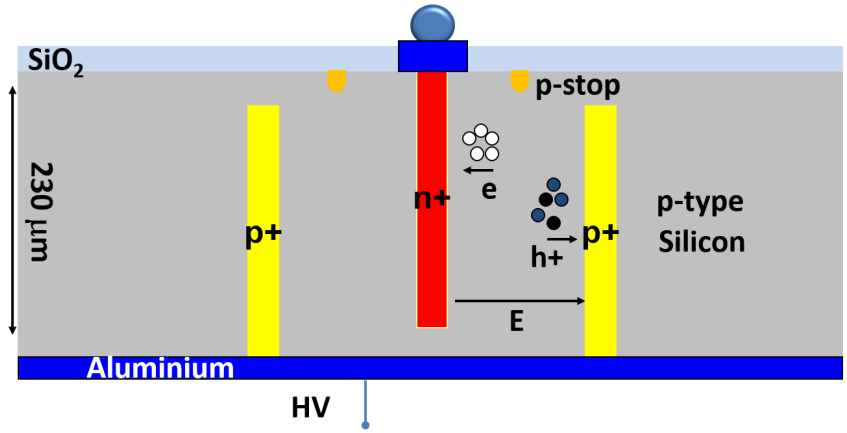

Figure 5.3: Cross section of a 3D sensor. [66] (modified)

5.2 Readout Chip

The induced signal of each pixel electrode is processed afterwards in the DC-coupled readout or *front-end (FE) chip* which amplifies and digitizes the signal. For noise reduction, a *threshold charge* is set in the readout chip to define a signal. Besides the binary hit information the chip provides the time and the amount of measured charge. To compare the measured charges of different pixels, the response to a specific injected charge has to be homogenized for all pixels during the *tuning process* of the chip.

The Inner Detector of the ATLAS Experiment uses the FE-I3 readout chip [67] which has been available since 2003.
The successor of this front-end chip is the FE-I4 readout chip [34, 60] which is used in the IBL detector. The inactive area and the pixel size is reduced to 250 µm × 50 µm while the number of pixels is increased to 26 880 in a matrix of 80 columns and 336 rows. The chip is produced in a 130 nm feature size CMOS process and is thinned down to 150 µm for the application in the IBL [68]. There are two revisions of the chip, the FE-I4A and the successor FE-I4B, which differ only in small design and power supply options. The IBL detector is equipped with the FE-I4B readout chip.

The analog signal from the DC coupled sensor pixel is amplified in two stages in the front-end pixel. The height of the amplified signal and the following discriminator of the front-end can be adjusted to shape the signal. For signal adjustments it is distinguished between local parameters which are configurable for every pixel individually and global parameters which modify a configuration for the complete chip. If the signal exceeds the threshold, the *Time over Threshold (ToT)* is measured in units defined by a 40 MHz (25 ns) clock. This way a value for the measured charge is received and stored together with the firing time. Four analog front-end pixels share one memory and logic block which stores this information and either discards or passes it on if a trigger pulse arrives. The digital circuit is powered with 1.2 V and the analog circuit with 1.5 V for operation which are applied externally. In addition, the chip provides two Shunt-LDO voltage regulators to generate the necessary voltage from a single external support line which was not used during the measurements of this thesis.

For the upgrade of the LHC to the HL-LHC a new pixel front-end chip is required to cope with the increased data rate. For this reason the RD53 collaboration developed the RD53A readout chip [69] as a combined effort of CMS and ATLAS. This prototype chip will not be operated in the experiments but used for testing. The chip is produced in 65 nm CMOS technology and features three different front-end variants. The pixel matrix of 400 columns and 192 rows contains 76 800 pixel cells with a size of 50 µm × 50 µm.

Every module investigated in the course of this theses is read out with FE-I4 readout chip but both variants, the FE-I4A and FE-I4B, were operated. The process of building a module assembly and to attach the sensor to the front-end is described in the following section.

5.3 Module Assembly

In the hybridization process the flip-chip technology is used to connect each pixel of the sensor to a pixel of the readout chip via bump bonds. The modules investigated in this thesis are hybridized with the same methodology as the IBL modules which is described in more detail in [68].
In the first step, *under-bump metalization (UBM)* is placed on the aluminum pads of the sensor and the front-end. This metal layer ensures a good connection, electrically and mechanically, between the solder bumps and the aluminum pads. Afterwards tin-lead solder bumps are placed on the front-end via electroplating. In the following flip-chip operation, a high precision and accuracy is needed to place the front-end exactly above the sensor. Special alignment marks on the sensor and

the readout chip simplify the adjustment of both. By heating up the complete structure the bump bonds are soldered to the sensor and the front-end. The device is now referred to as *bare module*.
This process is the cost driving factor for the production of hybrid pixel modules. For this reason other approaches, like a capacitive coupling between sensor and chip which are glued together [70] or monolithic pixel sensors with the readout chip implemented inside the sensor, are currently under investigation.

To operate the module a *printed circuit board (PCB)* is wire bonded to the front-end chip. For the operation inside the ATLAS detector the PCBs are flexible with an optimized material budget which route the signal and power lines to the sensor and front-end. However, rigid PCBs provide robustness for module tests in the laboratory or in test beam measurements. A bare module glued and wire bonded to a PCB is called *module assembly*. Adjustments to the standard rigid PCB have been made for the investigation of the REINER pixel modules which are described in the following section.

5.4 REINER Pixel Modules

The sensors investigated in this thesis feature various modified pixel designs which are based on the pixel design implemented in IBL sensors. The IBL pixel design is laid out to avoid any electric field strength maxima and to produce homogeneously distributed electric field lines. In Figure 5.4 the standard IBL pixel design (labeled V0) with a pixel size of $250\,\mu m \times 50\,\mu m$ is presented: The composition of significant layers on the pixel side of the bulk on the left and a top view on the right. The n-$^+$-implantation (red) is a uniform sustained pixel layer with a width of $30\,\mu m$ which has a rounded cutout on one side for the bias dot (on the right side in this image). The nitride openings (blue) indicate areas with a higher p-spray concentration. The blue frame is used to insulate the pixel towards neighboring pixels. In addition, three round areas correspond to openings in the nitride layer above the implantation and one at the bias dot to ensure a good connectivity between the implantation and the metal layer (grey) above. The metal layer comprises a uniform $26\,\mu m$ wide band above the homogeneous implantation and the bias grid which connects the bias dot to the bias rail. The bump pad is the connecting point to the metal layer of the pixel and corresponds to the round area of the last layer (green) which marks the opening in the outermost passivation layer.
After irradiation when the depletion voltage of a sensor is increased, electric field strength maxima might have a positive impact on the charge collection by charge multiplication. Such higher charges are reported in other studies and measured for irradiated n$^+$-in-p sensors before [71] and after annealing [72].

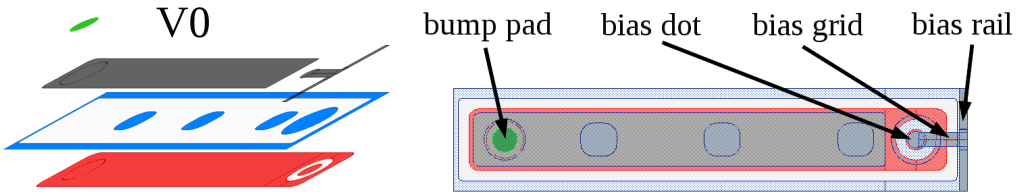

Figure 5.4: Layer composition (left) and top view (right) of the standard IBL pixel design (V0). The n^+-implantation is shown in red, openings in the nitride layer as indication for p-spray in blue, metal in grey and openings in the passivation layer in green.

To investigate the impact of the implantation shape, implantation segmentation, p-spray distribution and metal layer width on the electric field, six different pixel designs are implemented and summarized in the *REINER*[1] *pixel design* by T. Wittig [64]. The six modified pixel designs feature additional implantation segmentations to create more high field regions, narrowed implantations to benefit from the small pixel effect (see Chapter 3.8), variations in the p-spray concentration and metal-overhang. The different pixel designs labeled V1 to V6 are shown in Figure 5.5.
For the pixel designs V1 and V4 the implantation is divided into four parts which are insulated with p-spray. The corners of the implantations are rounded for the design V1 while they are rectangular for the design V4. The width of the metal layer of 26 µm is the same as for the standard design V0.
The n^+-implantation is segmented in additional parts for the pixel designs V2 and V3. Pixel design V2 counts 8 implantation segments and V3 16 parts. Due to space limitations no p-spray is applied between the individual segments. The metal layer above is slightly enlarged to a width of 34 µm.
For the pixel designs V5 and V6 the n^+-implantation is narrowed by a factor of three to a width of 10 µm. These two pixel designs differ in the implementation of p-spray: For pixel design V6 the standard profile at the edges of the pixel design is used, while for design V5 the area with higher p-spray concentration is enlarged towards the pixel center. In addition, the width of the metal layer is reduced for both pixel designs to 14 µm.

[1] **RE**designed, **IN**novative, **E**xciting and **R**ecognizable

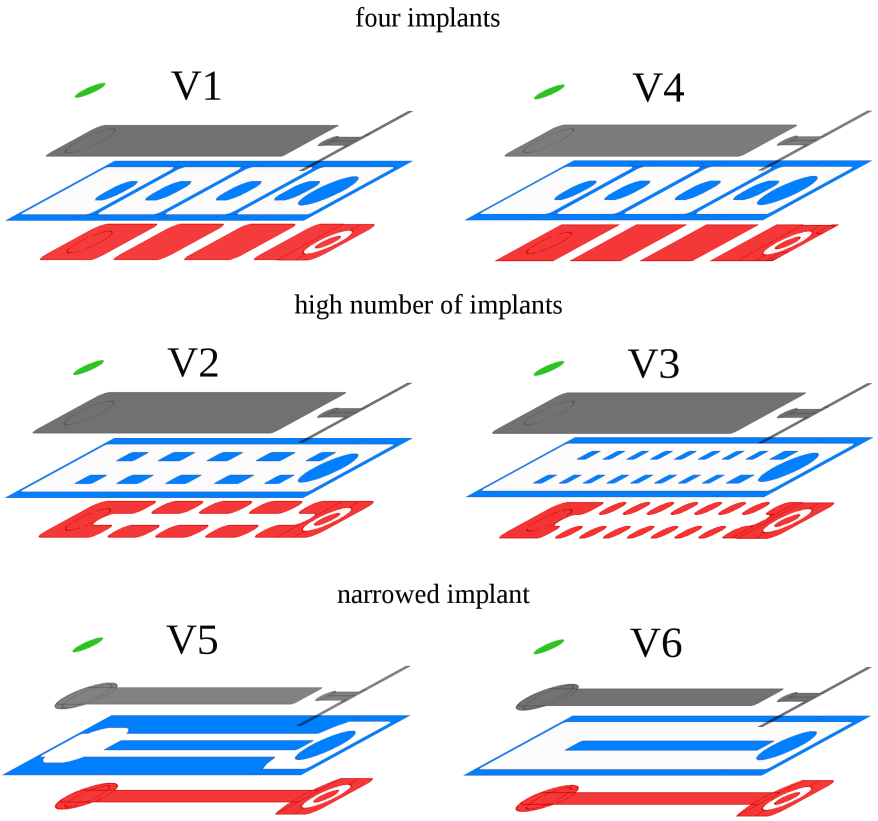

Figure 5.5: Layer composition of the REINER pixel designs V1-V6. The n^+-implantation is shown in red, openings in the nitride layer as indication for p-spray in blue, metal in grey and the opening in the outermost passivation layer in green.

These six modified pixel designs (labeled V1-V6), together with two groups of standard designs pixels (labeled V0 and 05) are placed in *groups* of 10 columns and 336 rows of the same pixel design on an n^+-in-n sensor (see left side of Figure 5.6). The arrangement of the groups on the sensor aims for the maximum distance between related pixel designs. Therefore, the sequence on the sensor from left to right as seen from the p-side is: 05, V6, V4, V2, V3, V1, V5, V0.
The pixels have a size of 250 µm × 50 µm and only the pixels in the first and last column of the sensor (column 0 and 79) are longer pixels with a size of 500 µm × 50 µm. The additional 200 µm of these long pixels are equipped with guard rings on the p-side to reduce the inactive edge of the sensor. For more information on this active edge design see [73]. In total the REINER sensor with a thickness of 200 µm features a size of 20.5 mm × 16.8 mm and matches the size of the FE-I4 readout chip.
On the p-side of the sensor each group is surrounded with individual guard rings to prevent influences from neighboring pixel designs. The 16 guard rings per group are beneath the outermost and the second to last columns of each group. Moreover, two high voltage pads per group enable the powering and investigation of the groups individually. On the right side of Figure 5.6 a schematic view of the border area between two pixel groups is illustrated: The p^+-implantation on the backside of the sensor forming the guard rings is indicated in a darker color.

Several REINER sensors are bump bonded to FE-I4 readout chips. These REINER modules are glued onto a thin aluminum plate which is screwed to a PCB. The PCB has a cutout beneath the module to reduce the material budget in test beam measurements in which a particle beam passes through the module and the thin aluminum plate. For electrical connectivity, the readout chip of the module is wire bonded to the PCB which is displayed in Figure 5.7. The PCB provides an 8-pin Molex connector for low voltage (LV) to operate the readout chip and a high voltage (HV) connector to apply the external bias voltage for the sensor. Special jumpers on the PCB allow the biasing of individual groups of the REINER sensor. In Figure 5.7 the jumpers are set to bias the groups with pixel designs V3, V1, V5 and V0 with the same bias voltage applied via the HV connector. In addition, the communication between the readout system and the readout chip is performed via an Ethernet data connector.

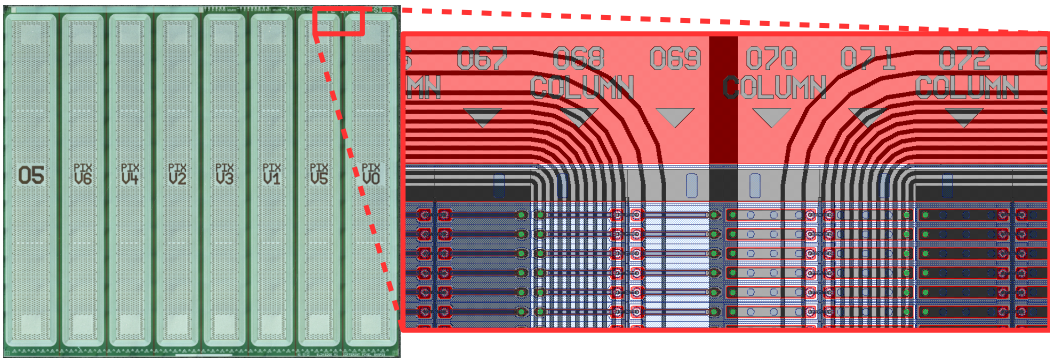

Figure 5.6: The REINER pixel sensor. Left: View of the p-site of the sensor. Right: Schematic zoom into the edge region between two pixel designs. The layers above the bulk are: n^+-implantation in red, openings in the nitride layer as indication for p-spray in blue, metal in grey and the opening in the outermost passivation layer in green. The p-implant forming the guard rings below the bulk is indicated with a darker color.

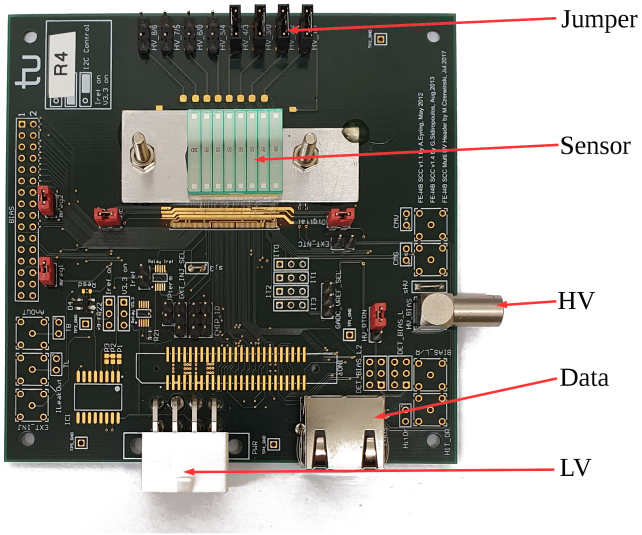

Figure 5.7: REINER module on PCB.

5.5 Readout System and Tuning

A readout system is necessary to communicate with the readout chip and to acquire its recorded data. In addition, with the readout system the module can be *tuned*: In the tuning process global parameters for the complete chip and local parameters for individual pixels can be modified to ensure that all pixels on a module respond to a defined input signal equally. This way the threshold charge and the ToT-response to a specific injected charge are adjusted and unified for all pixels. Otherwise production differences or external effects like temperature differences and/or irradiation of front-ends result in dissimilar output signals for the same input. A tuning to the same parameters and a homogeneous tuning over the full module are essential to compare the performance of pixel areas on the same module and/or the results of different modules.
Two different readout systems, RCE and the USBpix system, are used for measurements performed in this thesis. The RCE system [74] consists of the HSIO II development board, the pixel interface board and its software. Up to 18 FE-I4 chips can be operated with this system at the same time. Predefined scans and primlists (predefined tuning procedures) can be used to tune the configuration of a module. The other system is USBpix [75, 76] which was developed in several iterations in Bonn. The two iterations used in this thesis are an older setup with a multi-IO board (MIO2) connected to a Burn-In card (BIC) and a newer USBpix3 Multi Module Card (MMC3). With the setup of MIO2 plus BIC, up to four front-end chips can be operated at the same time while up to eight readout chips can be linked to the MMC3. Both readout systems use a field programmable gate array (FPGA) to communicate with the readout chip and a micro-controller for communication with the PC. The majority of test beam data and lab measurements presented in this thesis are obtained with the MMC3 readout system shown in Figure 5.8. The connector for the USB3 communication with a computer, the TLU port for external triggering and the RJ45 ports to connect the PCB with the module via Ethernet cables are indicated.

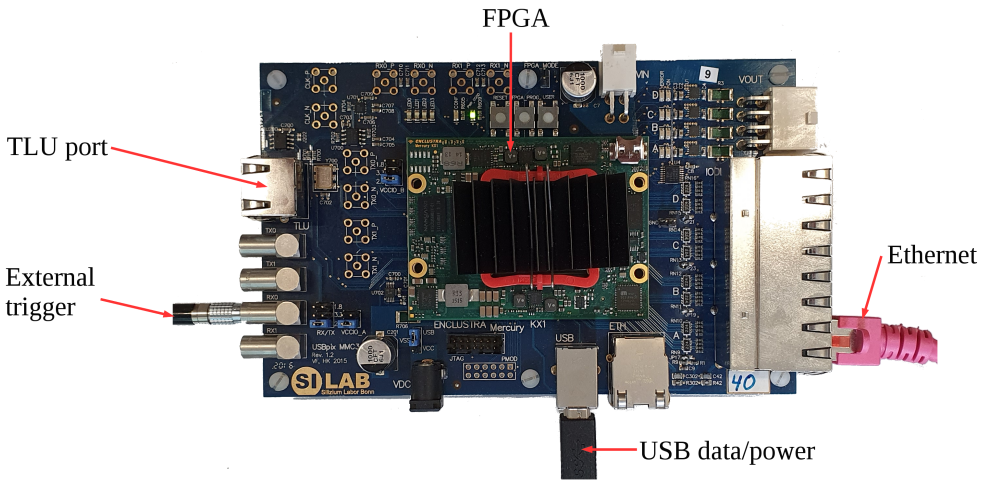

Figure 5.8: MMC3 readout system.

The graphical interface used for the USBpix systems is the C++ and ROOT based software STcontrol [77]. With this software the hardware can be operated, initialized and the firmware updated. STcontrol provides the configuration files for the readout chip in which the configuration parameters are stored. The configuration parameters can be tested and adjusted with scans and tuning algorithms to achieve the desired tuning targets like a specific threshold charge and ToT-response. This is done by changing the amplifier stage and discriminators by modifying various digital-to-analog converters (DACs).
After initialization and configuration of the readout chip, the first step in the tuning procedure is to check the functionality of the readout chip using an *analog scan*: A specific number of hit injections are deposited per pixel according to a mask pattern. For a working pixel the number of measured hits should be similar to the number of injections if the injected charge is above the threshold. This way *noisy pixels* are identified as they measure more hits than the injected number and *dead pixels* measure no hits at all. The results are illustrated in a histogram as presented in Figure 5.9 for the injection of 200 hits per pixel.

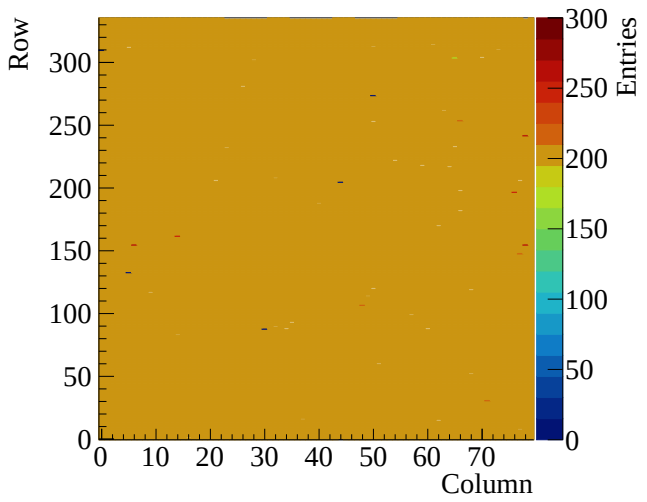

Figure 5.9: Results of the analog scan of STcontrol for a module: Dead and noisy pixels are visible as they measure a different number of hits compared to the 200 injected charges.

The threshold configuration of the module is determined with the so-called *threshold scan*. Test charges are injected per pixel and the discriminator response is recorded. For an ideal discriminator the response with increasing injected charge is described by a step function. However, in reality the response is slightly shifted by electronic noise and is mathematically expressed with an error function (convolution of step and Gauss function). For this reason the same charge is deposited 100 times per pixel and the mean occupancy is calculated. After repetition with increasing injected charge the error function can be fitted. An exemplary plot of the occupancy for different injected charges (VCAL) with a fitted error function for a specific pixel (column 60, row 108) is presented in Figure 5.10.
The threshold value for each pixel is defined as the charge where the occupancy is 50 % and the electronic noise is determined by the width of the distribution. On the left in Figure 5.11 the results for a threshold scan in STcontrol are shown: The module is tuned to a threshold of 1600 electrons.
The ToT response is established with the *ToT verify scan* for which a specific charge is injected several times and the mean response value is calculated. In Figure 5.11 on the right the resulting histograms of the ToT verify scan are depicted: The module is tuned to a ToT response of 10 for a reference charge of 10 000 electrons. In this image two peaks for ToT values of 10 and 11 are visible and an additional ToT adjustment would improve the uniformity of the ToT values.

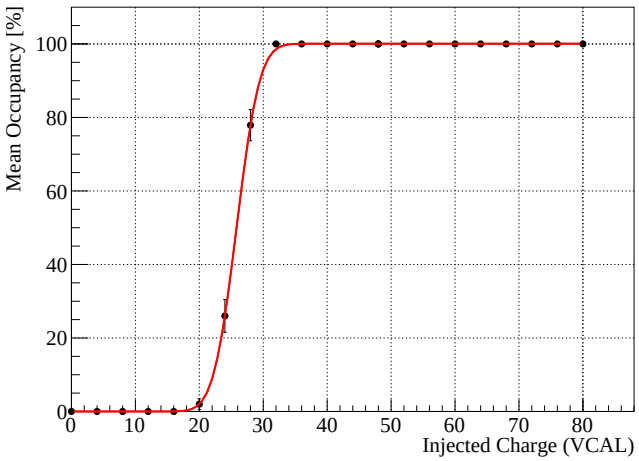

Figure 5.10: Mean occupancy for one pixel for different injected charges (VCAL): The injection is repeated 100 times per charge value and the mean occupancy is calculated. An error function is fitted to determine the threshold value. Data taken from [78].

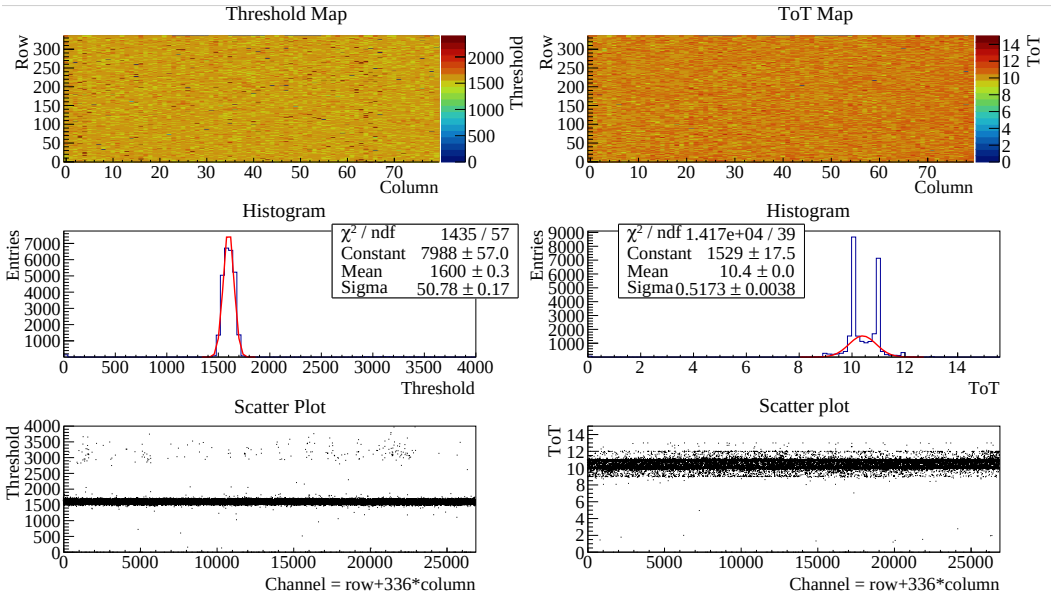

(a) Threshold **(b)** ToT

Figure 5.11: STcontrol results for a threshold scan (left) and a ToT verify scan (right). The results are presented as map in the top, as a histogram in the middle and as a scatter plot in the bottom image. The module is tuned to a threshold value of 1600 e and a ToT response of 10 for a reference charge of 10 ke.

The described scans do not change the configuration parameters but report the module's characteristics with the current parameters. Without tuning the threshold values and ToT responses per pixel show a broad variation for a module. Therefore, global and local parameters have to be adjusted in the tuning procedure to change the threshold and ToT response. More detailed information on the parameters and individual tuning steps can be found in the thesis of A. Gisen [79] or J.-C. Beyer [78] to achieve such small deviations from the targeted values as presented in Figure 5.11. Subsequently, the tuned modules are investigated in laboratory and test beam measurements which are explained in the following chapters.

6 Investigation Methods and Results of non-irradiated REINER Pixel Modules

A sensor passes several production steps and performance checks before it is finally installed as a module in the detector. Even test modules which use new technologies like new readout chips or a new sensor designs undergo similar procedures for characterization: The sensors are produced on wafers and are investigated with IV measurements before cutting. After singularization, the sensors are tested with IV and CV measurements to ensure that they were not damaged in the cutting process. Intact sensors are connected to readout chips in the bump bonding process to obtain modules. The functionality of the module's sensor is afterwards tested by IV measurements and the connection between sensor and readout chip by source and test beam measurements. Charge collection and hit detection efficiency are also significant parameters investigated in these measurements.
In the following section the laboratory and test beam setups are explained in more detail. Moreover, the measurement results obtained with these setups for non-irradiated REINER pixel sensors and modules are outlined. The results of the REINER sensors/modules are compared to the acceptance criteria for sensors/modules to be used for ITk to give a perception on the performance level. However, these REINER sensors are test structures and are never applied in the ITk upgrade.

6.1 Laboratory Measurements

In laboratory measurements the sensors and modules are electrically connected and investigated with IV and source measurements. For bare sensors the CV is additionally measured. These tests are performed in Dortmund in contrast to test beam measurements taking place at the test beam facilities DESY and CERN.

6.1.1 CV Measurements

After receiving the wafer or bare sensor from the supplier, it is visually inspected and measured with contact needles as shown in the setup in Figure 6.1: The n^+-in-n sensor or wafer is placed with the n-side (pixel side) on the grounded vacuum chuck and a negative potential is applied via a needle to the HV pad on the p-side of the sensor. The setup is located inside a box to shield the sensor from light. An automated measurement script is provided by the software e4control [80] which controls and reads the output of the power supplies and/or the LCR meter. The scanned voltage range, current limits, the measurement repetitions per voltage step and a delay time between setting the voltage and starting the measurements can be adjusted. In addition, a temperature and humidity logging is possible during the measurements.

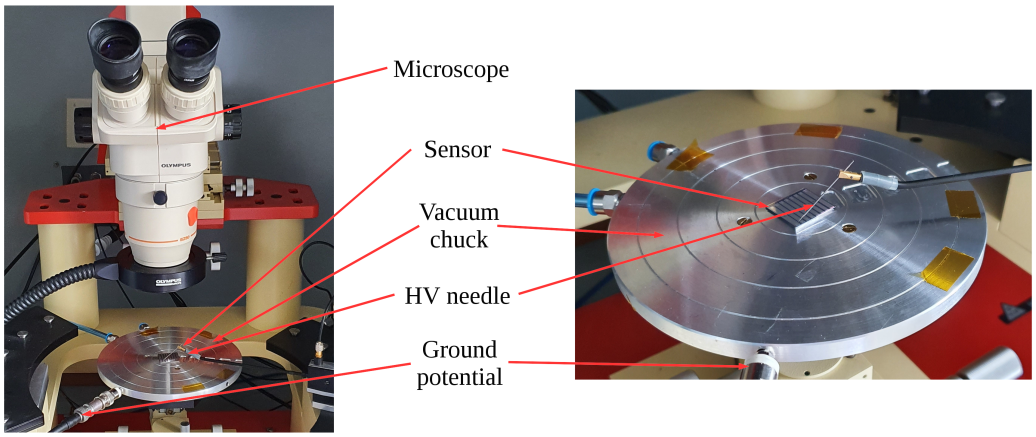

Figure 6.1: Laboratory setup to measure bare sensors inside a dark box (left) [81] and a zoom onto the vacuum chuck of this setup with a bare REINER sensor contacted via needle (right).

For capacitance-voltage (CV) measurements the circuit diagram illustrated in Figure 6.2 is necessary to determine the capacitance between the p- and n-side of the sensor with an LCR meter which is set to an oscillation voltage of 50 mV and a frequency of 10 kHz. As the maximum applicable signal voltage of the LCR meter is 2 V, an external source meter is connected via a bias box providing the bias voltage. For more information on the setup see [82].

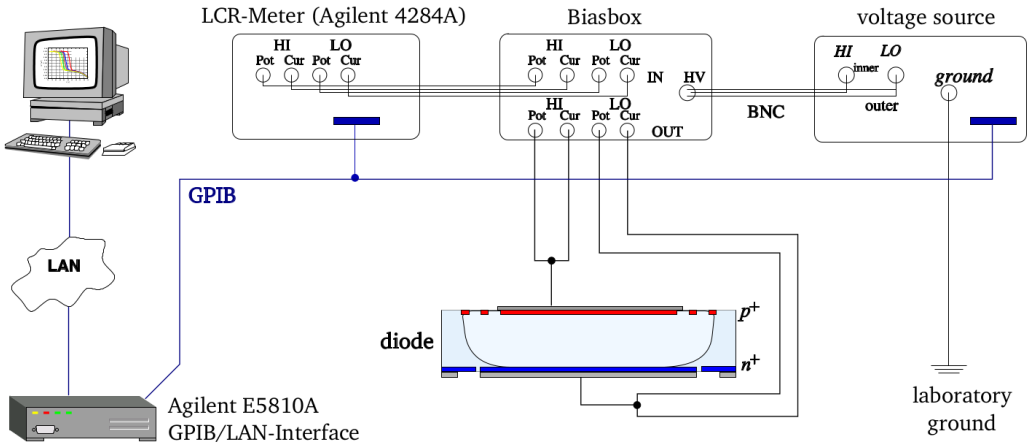

Figure 6.2: Schematic of the CV measurement setup: The high voltage from the source meter is superimposed with a high frequency injected pulse from the LCR meter. The frequency and amplitude can be set and are typically 10 kHz and 50 mV. The n-side of the sensor is laying on a connected vacuum chuck while the p-side is connected via needles. The LCR meter measures the capacitance between the n- and p-side of the sensor. [64] (modified)

The individual groups with different pixel designs of several bare REINER sensors were measured with this setup and the depletion voltages were determined in the theses of S. Di Pede [81], J. Helmig [83] and A.-K. Raytarowski [84]. On average the depletion voltage of the measured REINER sensors is about (30 ± 5) V.

6.1.2 IV Measurements

For current-voltage (IV) measurements of bare sensors the same setup illustrated in Figure 6.1 is used with a simplified circuit scheme: Only a remotely controlled source meter is needed which applies the bias potential between the needle and the grounded vacuum chuck. If a sensor is bump bonded to a readout chip and glued to a PCB, IV measurements are performed via the lemo connection powering the sensor. A special adapter and adapter board (see Figure 6.3) was developed for the characterization of REINER pixel modules on PCB: With this device the pixel groups on the REINER sensor can be biased individually and the adjustment for probed groups is set from outside the box.

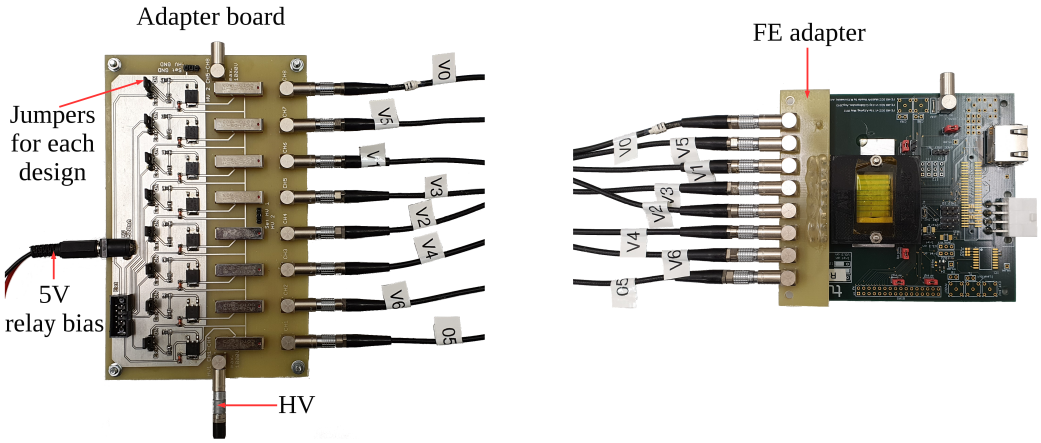

Figure 6.3: Image of the adapter board and FE adapter to bias selected individual pixel designs from outside the measurement setup. 5 V biased relays controlled with jumpers distribute the HV to the selected pixel design groups.

In Figure 6.4 the IV measurements of the REINER module R6 connected to a PCB are presented: The measurements are performed inside a box flushed with dry air at room temperature. For each voltage step the current is measured ten times and the mean and standard error are calculated. Each group with a different pixel design is measured individually (05-V6) while for the full sensor measurement all groups on the module are biased simultaneously. The error bars are included in the image but too small to be seen.
The pixel group with design V6 (narrowed implantation) shows the highest leakage current for all voltages followed by design V5 (narrowed implantation). All other designs can be grouped together and reach a maximum current between 1 µA and 2 µA at 400 V. The measurement for the full module shows a constant increase in leakage current until 150 V. Between 150 V and 180 V a steep increase in leakage current is visible. Interestingly, this increase is also visible for the individual measurements of the pixel designs V6 and V5 and might result from the lateral expansion of the depletion zone reaching the guard rings or neighboring pixel designs. After 180 V the increase in leakage current is constant but with a higher slope than before. The sum of the leakage current measurements of the individual pixel groups is higher than the leakage current measurement of the full sensor. This behavior is unexpected as the sensor and its guard ring structures are designed to feature eight independent parallel groups with different pixel designs. Consequently, the sum of all independent parallel groups should be similar to the full sensor measurement. This feature was studied in the master thesis of J. Helmig in more detail [83] and the functionality of the guard rings in the thesis of S. Di Pede [81].

The *breakdown voltage* is defined in the ITk criteria as an increase in leakage current of more than 20 % over a voltage step of 5 V [85]. The maximum increase in leakage current for the full module R6 is measured between 160 V and 165 V of about 13 %. Consequently, no breakdown is measured for this module for voltages up to 400 V.

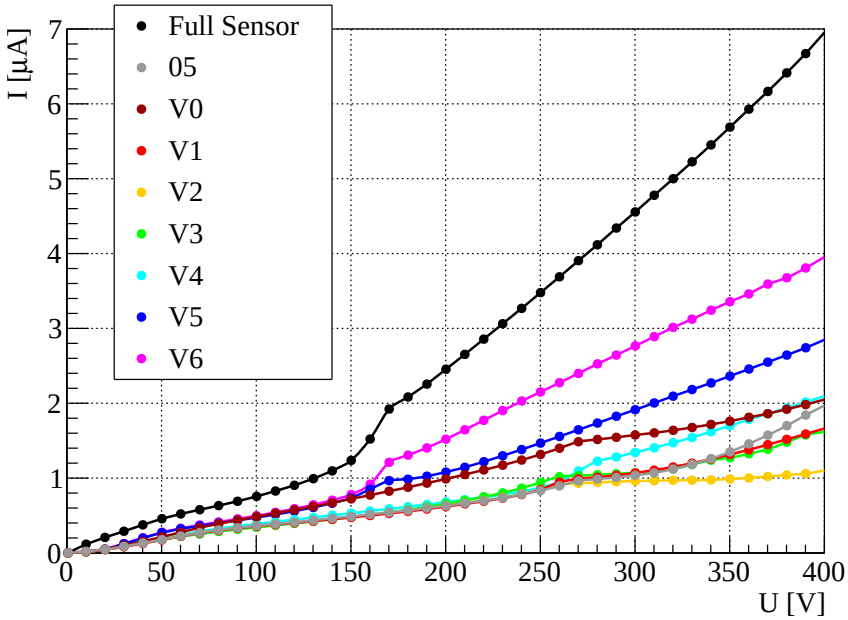

Figure 6.4: IV measurements of module R6 at room temperature. The different pixel groups are biased individually (measurements 05-V6) and all groups are biased at the same time for the full sensor measurement.

Overall, the IV curve characteristics of the individual groups and of the full module R6 are consistent with measurements presented in the master theses of S. Di Pede [81], M. Grothe [86], J. Helmig [83] and A.-K. Raytarowski [84]: For non-irradiated bare REINER sensors and REINER modules the groups with narrowed pixel designs (V5 and V6) always show the highest leakage current compared to all other pixel designs. These increased leakage currents are a first indication for higher intended electric fields of these pixel designs.

6.1.3 Source Measurements

After the bump bonding process modules are checked in the laboratory with source measurements to evaluate the tunability and uniformity of the signals over the pixel array of the module by monitoring collected charge. With the setup pictured in Figure 6.5 the functionality of the sensor and readout chip and connection of both components are investigated: A radioactive source is placed above the module emitting particles which are detected by it. While particles pass through the module energy is deposited in the sensor material producing hits which are read out by the readout chip. The hit information is passed on to the readout system consisting of an MMC3 board operated with the software STcontrol (see Chapter 5.5). The software provides a *self-triggering* mode for which the readout chain is started when the FE detects a particle. However, this mode is error-prone by noisy pixels which give a hit signal independent of passing particles. For this reason a scintillator is placed beneath the sensor generating an *external triggering* signal to the MMC3 to start the readout chain. This way the background of noise and scattered particles is reduced.

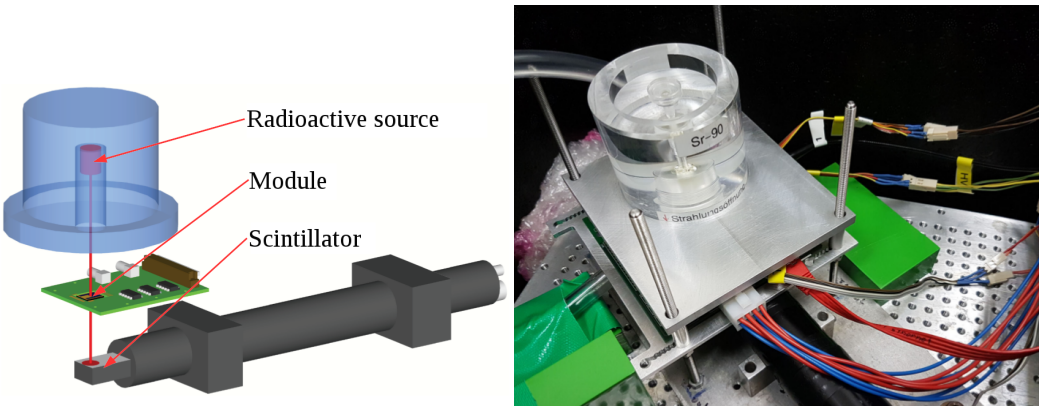

Figure 6.5: Source measurement setup: The radiation source stored in a plastic housing is placed above the module and the scintillator. A schematic layout is presented on the left [87] (modified) and a picture of the setup in the laboratory on the right [86].

A common β-source is the strontium-90 isotope with a half-life of 28.79 years [88] which was used for source measurements presented in this work. It decays in the following chain:

$$^{90}_{38}\mathrm{Sr} \rightarrow ^{90}_{39}\mathrm{Y} + e^- + \bar{\nu_e} \tag{6.1}$$

$$^{90}_{39}\mathrm{Y} \rightarrow ^{90}_{40}\mathrm{Zr} + e^- + \bar{\nu_e} \tag{6.2}$$

The strontium-90 isotope decays with a decay energy of 546.0 keV into yttrium while an electron with a mean energy of 195.8 keV and an electron antineutrino are emitted [88]. The isotope yttrium-90 with a half life of 64.00 hours decays further into the stable zirconium with a decay energy of 2280.1 keV while an electron with a mean energy of 933.7 keV and an electron antineutrino are released [88]. The energy of electrons to be a MIP in silicon is about 1250 keV [51]. For this reason the electron produced in the second process is a good candidate for a MIP. It is investigated whether the module detects these emitted electrons.

The software STcontrol generates the raw file as output that contains the information from the readout chip. The following analysis uses the software tool *fei4Analyzer* [89] which performs a clustering and fits Landau-Gauss convolutions to the measured ToT values. Source measurements of REINER pixel modules have only been performed after irradiation and the results are presented in Chapter 7.2.2.

6.2 Test Beam Measurements

Besides measurements in the laboratory the modules are investigated in test beam measurements. The test beam facilities provide particle beams which pass through the setup consisting of the *beam telescope* and the module. In analogy to source measurements, it is investigated if the traversing particle is detected by the modules. In contrast to source measurements, the presence and position of the passing particle is known precisely for test beam measurements: The trajectory of the particle, the *track*, is reconstructed from the particle hits in the telescope modules and the hit detection and charge collection efficiency of the investigated module can be calculated with high spatial resolution.

6.2.1 Test Beam Facilities

Results of test beam measurements presented in this thesis are recorded at the test beam facilities DESY and CERN. The test beam measurements at DESY were performed at the beam line 22 with an electron beam of 5 GeV. The generation of the beam is illustrated in Figure 6.6. More detailed information on the beam generation and performance of the setup can be found in [90].
The particle beam is produced in a double conversion process: The primary beam of the electron/positron synchrotron DESY II collides with a several µm thick fiber target and a beam of bremsstrahlung photons is produced. Afterwards these photons collide with the secondary target and generate electron-positron pairs in the pair production process. By adjusting the strength and polarity of the following dipole magnet, the momentum and particle type for the test beam can be set. Before entering the test beam area, the beam passes the primary collimator and the beam shutter. Three different beam lines (TB21, TB22 and TB24) with individual test beam areas are available at DESY. Inside each test beam area a secondary collimator allows the user to adjust the beam spot size.

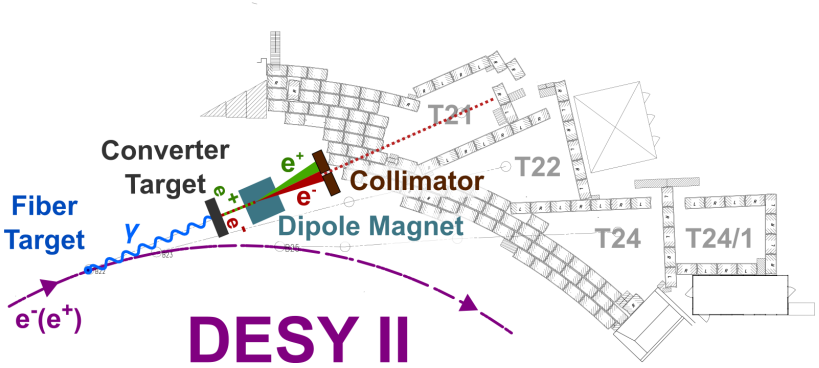

Figure 6.6: Beam generation at the DESY test beam facility. [91] (modified)

At CERN the test beam measurements were performed in the North Area which uses the protons from the SPS as primary beam. The SPS beam is guided to three different targets (T2, T4 and T6) to produce a secondary beam of pions, electrons or muons. The energy of the beam particles can be set by the user via magnets. The secondary particle beams are guided in seven beam lines to the experiments located in three experimental halls (EHN1, EHN2, ECN3). The measurements for this thesis were carried out at the beam line H6 in the areas H6A and H6B with a 120 GeV pion beam. In Figure 6.7 the beam generation and distribution at the CERN North Area is illustrated. For more information on the different test beam lines and areas at CERN see [92].

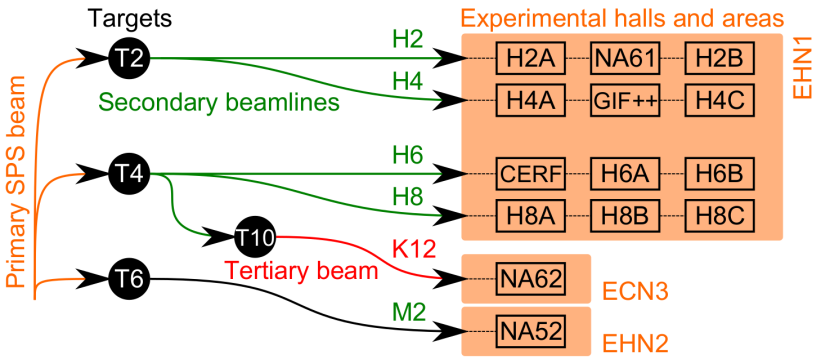

Figure 6.7: Beam generation and beam lines at the CERN North Area. [93]

6.2.2 Test Beam Infrastructure

Each test beam area is equipped with a EUDET-type beam telescope [94]. At CERN the telescopes "ACONITE" (in H6A) and "AIDA" (in H6B) and at DESY the "DURANTA" telescope in the area 22 were used. In Figure 6.8 an image of the telescope at CERN is presented. The telescopes are identical in construction and each of them consists of two telescope arms equipped with three MIMOSA26 monolithic active pixel silicon sensors [95]. A MIMOSA26 sensor features an active area of 21.2 mm × 10.6 mm divided into 1152 columns and 576 rows with a pixel size of 18.4 µm × 18.4 µm. The 50 µm thick sensor is shielded by 25 µm Kapton foil from environmental light and was chosen to minimize the material passed by the beam. The sensor is read out continuously with a rolling shutter requiring an integration time of 115.2 µs per frame.
A box in the center between the telescope arms contains the *Devices Under Test (DUTs)* and is mounted on an XY-table to adjust the position of the DUTs relative to the telescope and the beam. For test beam measurements the z-direction is in parallel to the beam axis while the x-direction is defined as the horizontal and y-as vertical direction. At H6A the box is cooled with a chiller while in H6B and at DESY dry ice is used for cooling. Nitrogen is flushed into the boxes to prevent condensation of water while cooling the setup. During the measurements the temperature is monitored with a Pt1000 temperature resistance mounted closely to an investigated module. For the chiller setup in H6A a temperature of −45 °C is set while for dry ice cooled setups a minimum temperature of about −50 °C can be achieved. As a result, the temperature at the sensors is around −35 °C corresponding to the minimal IBL CO_2 cooling system temperatures [96]. The box used for the dry ice cooled setups has a special design with two compartments to exchange the dry ice without opening the part of the DUTs. For more information on the

box design see [57].
The scattering of a particle while traversing the setup depends on its energy and the material budget passed. As a result, the track resolution deteriorates with lower beam energy, longer distances and more material. A maximum of two DUTs can be placed inside the box for test beam campaigns at DESY and an additional module behind the last telescope plane.
The high particle energy at CERN test beam campaigns results in almost no scattering and the maximum number of DUTs is only limited by the available space inside the box.

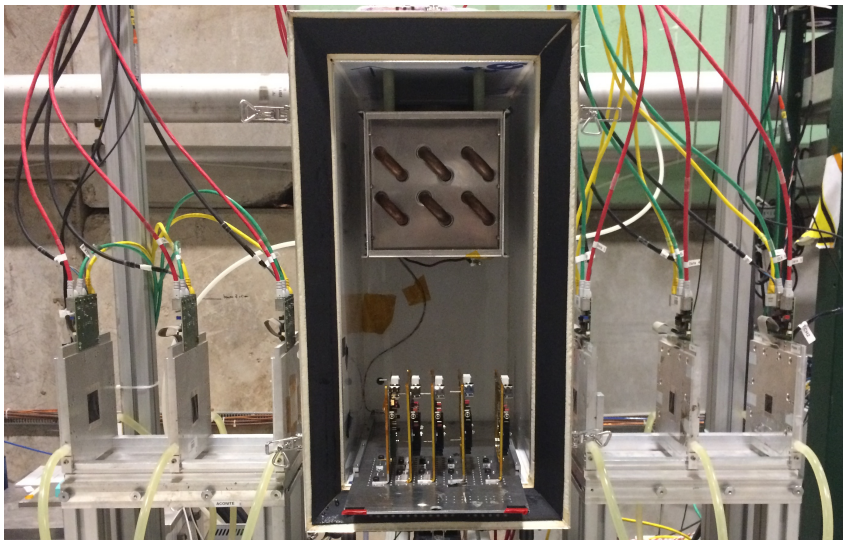

Figure 6.8: ACONITE beam telescope at CERN: Three MIMOSA26 telescope planes in front and behind the chiller cooled box. Five DUTs are mounted in the box and are investigated simultaneously. However, the cable connection for the modules is missing.

In front of and behind the telescope two scintillators are mounted and cover an area similar to the active area of the MIMOSA26 planes. If a particle passing is measured in coincidence by the scintillators, a signal is sent to the *EUDET Trigger Logic Unit (TLU)* [97] to start the readout chain. The TLU provides timing information of the passing particle as well as a trigger number. In addition, it triggers the connected *data acquisition (DAQ)* systems to read out the connected modules. From the telescope DAQ system a "busy" signal is transmitted to the TLU while the telescope planes are read out to prevent the TLU from submitting an additional trigger signal. The *EUDAQ* data acquisition framework [98, 99] merges the data streams from the different hardware components (telescope + DUTs) to one event-based data stream. This way, an *event* is defined as one trigger signal

from the TLU to start the readout. The full data is stored in so-called *runs* in the raw-file format. If the data file exceeds a configurable file size (typical file size is 250 MB to 1 GB) a new run is started automatically. During a test beam campaign, a variety of different modules are investigated and the DUTs are exchanged. The runs measured under the same conditions are summarized in a *batch*.

The DAQ PC is remotely controllable from the control room and data taking can be monitored with the *Online Monitor* provided by EUDAQ (more information in [98, 99]). With the Online Monitor the quality of the recorded data can be checked instantly and it allows for test beam measurements with reconstructible tracks.
For each plane used in the test beam measurement *hitmaps* are generated which are used to identify noisy pixels and review the module's position with respect to the beam. On the left in Figure 6.9 the 2D hitmap provided by the Online Monitor of an FE-I4 module is presented. A sharp increase in hits is visible starting at column 20 and between rows 110 to 280. These edges mark the region covered by the scintillators. Hits outside of the scintillator area are additionally recorded tracks which did not trigger the read out chain as they passed through the setup at the same time as another particle that did fulfill the trigger conditions.
The timing between the trigger signal and the measured hits is inspected with the *LVL1 distribution*. An example is shown on the right in Figure 6.9. In this plot the time difference between the measured hits and the trigger signal in bins of 25 ns is drawn. Hits generated by triggering particles are always measured at the same time difference resulting in a peak of the distribution. However, noise is produced permanently and is identified by a uniform distribution in the LVL1 histogram as shown in Figure 6.9.

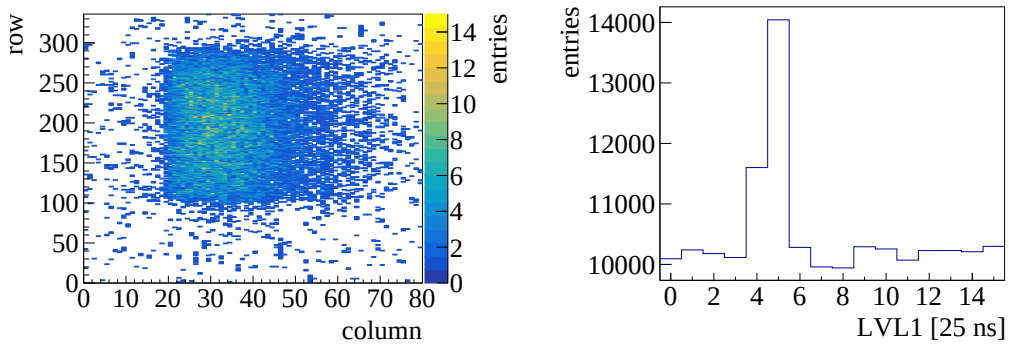

Figure 6.9: Exemplary plots of the Online Monitor. Left: Hitmap of an FE-I4 module. Right: LVL1 distribution of another, noisy FE-I4 module.

The *number of clusters per event* should be checked per plane at the beginning of the data taking of a test beam campaign since for too high numbers the particle tracks cannot be reconstructed. A *cluster* is defined as a collection of neighboring hits generated by the same particle. The number of clusters per event gives an estimation on the amount of particles passing through the module in one event (event multiplicity). If the number of particles is too high, the reconstruction software is not able to reconstruct the particles' trajectories from the high number of possible matching hits in the modules. In Figure 6.10 two images show the numbers of clusters per event for the first MIMOSA26 plane for two different test beam campaigns at CERN (left: May 2018, right: June 2016). In the left plot a Gaussian distributed number of clusters is visible with a mean value of 4.6 while in the right only a few entries with more than 20 clusters per event are visible. The majority of entries for the right histogram is registered in the overflow bin for more than 100 clusters per event. As a result the data measured at this test beam campaign cannot be reconstructed.

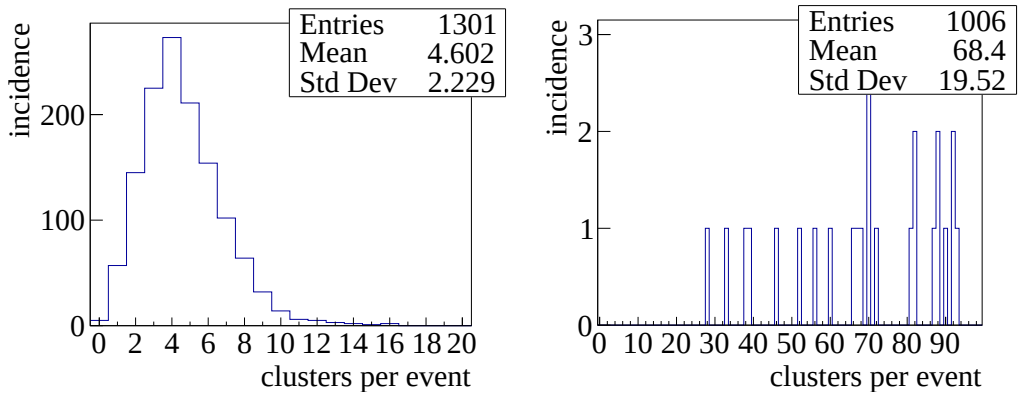

Figure 6.10: Number of clusters per event diagrams of the Online Monitor for the first MIMOSA26 plane measured in two CERN test beam campaigns. Left: A typical distribution of clusters per event (May 2018). Right: The event multiplicity for data of the June 2016 test beam campaign. Most entries are higher than the limits of the plot and the amount of clusters per event is too high to reconstruct the data.

To verify the correct timing of the data streams from the different systems the Online Monitor provides *correlation plots*. In Figure 6.11 exemplary correlation plots between the first MIMOSA26 plane and a DUT are shown for x- and y-direction (measured: CERN test beam campaign, May 2018). For correlation plots the hit position of one sensor is plotted against the hit position of another sensor. This is done for all hits measured in the same event. The position differences of hits on two different planes caused by the same particles are almost constant. Conse-

quently, a diagonal line in the images indicates that the hits of the two modules are correlated. Hits outside of this line are caused by multiple hits in one event. Vertical and horizontal lines in the correlation plots result from noisy pixels which are correlated to all hits of the other sensor. If the data stream is corrupted and the hits of the telescope and DUTs belong to different particles and events, no correlation line is visible. In a run the correlation between the different readout systems can be lost which is often caused by noisy modules probably due to buffer errors. More information can be found in [57]. However, only correlated data can be used for reconstruction. Thus, for repeatedly desynchronized data streams, additional masking of noisy pixels can increase the fraction of good data.

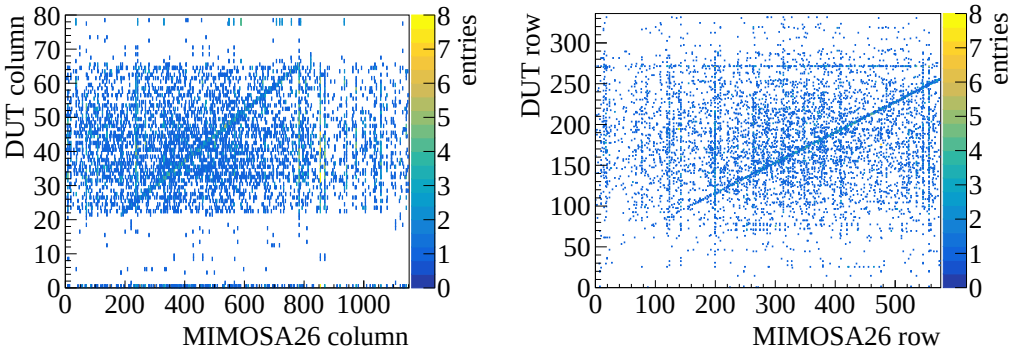

Figure 6.11: Correlation plots between the first MIMOSA26 plane and a DUT module. The correlation of the hits is identifiable by the diagonal line. Left: Correlation in x-direction (columns). Right: Correlation in y-direction (rows).

6.2.3 Reconstruction and Analysis Software

The data measured in test beam campaigns is afterwards reconstructed and analyzed. From the hit information of the telescope and DUT planes the particle tracks are reconstructed with the software *EUTelescope* [100, 101] and the reconstructed track positions are projected onto the DUTs. Afterwards, the analysis tool *TBmon2* [102] receives the projected track positions and the full hit information for all DUTs. From this information performance values of the investigated modules such as the hit detection and charge collection efficiency can be calculated. In the following sections the processing steps for both software tools are explained in more detail.

EUTelescope

For the reconstruction of the particle tracks the software EUTelescope uses the Modular Analysis and Reconstruction for Linear Collider (MARLIN) framework.

This framework is part of the International Collider Software package (ILC Soft) [103] and divides the reconstruction into several jobs in which different processors are executed. Each job handles a specific part in the reconstruction chain and reads in, modifies and stores data. The modularity of the jobs allows exchanging or skipping specific jobs or to iterate and execute the same job several times. The parameters for the different processors are organized in steering templates in the xml-data format.
The setup parameters like the number of modules and their location during the measurement and information about the used modules like pixel matrices and sensor thicknesses are stored in the GEAR-file (Geometry API for Reconstruction).
In Figure 6.12 a typical EUTelescope reconstruction chain is illustrated and the execution order of the different jobs is as follows:

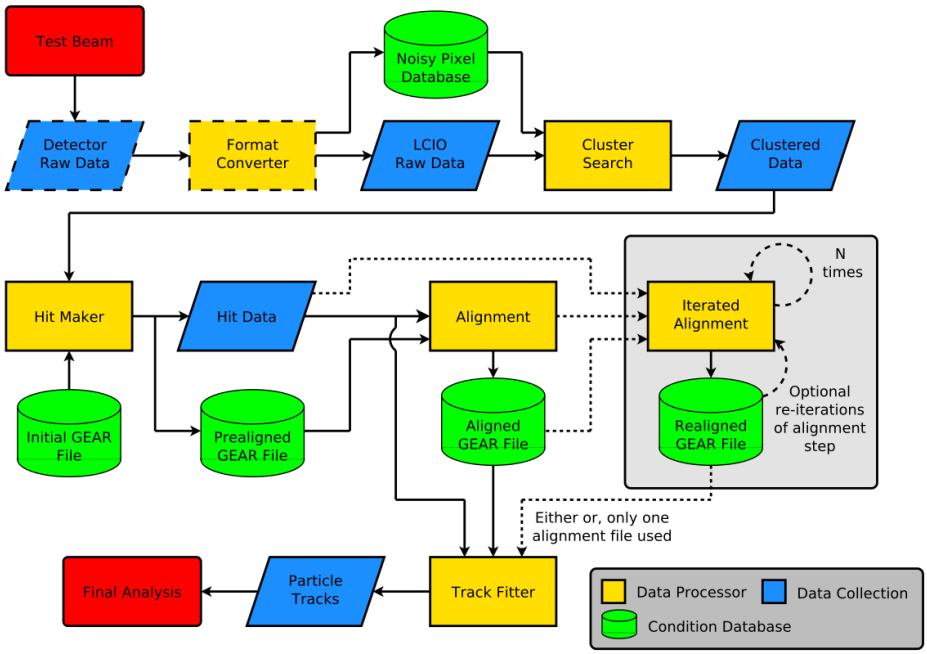

Figure 6.12: A typical EUTelescope test beam reconstruction chain.[93]

Converter: In the first step, the raw-data files are read-in and converted into the LCIO data format which is used by EUTelescope. While hit data of all pixels is converted their occupancy is checked to identify noisy pixels. If a pixel exceeds a firing frequency limit it is marked as noisy. The adjustment of the firing frequency can be checked with diagrams for each plane showing the number of masked pixels for different frequencies.

Clustering: In the following processor, hits from the DUTs and the telescope planes are grouped to clusters. A selection of different clustering algorithms can be used. For the data presented in this thesis the default "GeometricClustering" algorithm clusters the telescope and DUT hits. In contrast to the "SparseClustering" algorithm, the geometric position of the pixel is stored in addition to the pixel's indices, charge and time information. As a result, clusters for shifted pixel matrices (arranged like brick walls) are successfully clustered with the GeometricClustering. Furthermore, a limit on the maximum spatial extension of the clusters can be set which was not applied for this work. Afterwards, the information of pixels marked noisy in the converter is used to identify and remove noisy clusters from the cluster collection.

Hitmaker: The hitmaker converts each cluster center into a hit as the incident particle has a point like spatial extension. The cluster center can either be determined by the cluster shape or charge weighted with the ToT information from the cluster hits. In the presented reconstruction the charge weighted clustering is used. Afterwards the locations of the cluster centers (from now on hits) are transfered from a local coordinate system per sensor into an external, global coordinate system with the setup information provided in the GEAR-file.
Correlation plots similar to the ones provided by the Online Monitor of EUDAQ are created: The hit information in global coordinates in x- and y- direction of the first telescope plane is plotted against the hit information of another sensor. With these two dimensional diagrams the correct orientation of all modules with respect to the first MIMOSA26 plane is checked. If no correlation is visible the particular module has to be rotated in the GEAR-file and if the correlation line has a negative slope the module has to be mirrored.
In addition to these two dimensional diagrams the position difference in x- and y-direction between the hits in the first MIMOSA26 plane to the hits in another sensor are plotted. A histogram with Gaussian distributed values indicates a correct orientation. EUTelescope shifts the particular module by the difference with the most entries. This way a first alignment, so-called *pre-alignment*, of all modules in x- and y-direction with respect to the first telescope plane is performed. The new positions of the modules are stored in an updated GEAR-file.

Align: For the alignment of all modules the local hit information is transfered into the global coordinate system with the updated GEAR-file. With the hit information for each module, tracks are fitted and two different fitting algorithms were used to reconstruct the data presented in this thesis. For the data measured at the CERN test beam facility the deterministic annealing filter (DAF) fitter [104] is applied which is an extended Kalman fitter [105]: Hits on several planes are grouped together with a pattern recognition algorithm. Afterwards the algorithm starts with the hit position on a defined seed plane and searches within an extrapolated cone

on the next plane for matching hits. For tracks with overlapping hits only the most probable track is kept and a minimum number of planes with hits (usually 5 or 6) is required per track.
For the lower momentum particle beams at the DESY test beam facility another algorithm for track fitting, the general broken line (GBL) algorithm [106], is recommended for track reconstruction. The efficiencies of the investigated modules are unaffected but a better spatial resolution can be achieved. By considering kinks and offsets after passing the modules the GBL track fitting algorithm takes into account the scattering material and its thickness.
For both algorithms the calculated track collections are then passed on to the Millepede II software [107] to align the modules. With the distance between the hit position and the fitted track, so-called *residual*, the software performs a least square minimization of the whole system. Histograms containing the residuals are saved and the calculated new positions and rotations of all modules are stored in an updated GEAR-file.
This alignment procedure can be performed iteratively several times to achieve the best alignment and smallest residuals.

Fitter: For the final step in the track reconstruction the local hit information is transfered to the global coordinate system again with the latest GEAR-file. The tracks are fitted to the hits in the modules with the DAF or GBL algorithm used in the previous alignment procedure. In contrast to the previously described fitting in the alignment process the hit information from the DUTs is now disregarded to fit the final tracks (unbiased tracks). The final tracks have to satisfy quality requirements for acceptance like the $\frac{\chi^2}{\mathrm{ndf}}$, residual cuts and a minimum number of hits in the telescope planes (usually 5 or 6). The exact parameters are determined in the reconstruction of each test beam campaign. For the passed tracks the projected position on each DUT and the full hit information from the DUTs are stored in a ROOT-file for further analysis. In addition, the results of the final fitting process can be checked with residual plots.

In Figure 6.13 a comparison between the normalized residual plots for measurements performed at the CERN test beam facility, reconstructed with DAF (blue), and the DESY test beam facility, reconstructed with GBL (red), are presented. The width of the residual distribution depends on the pixel size and is wider for the x-direction (left) with a pixel size of 250 µm compared to the y-direction (right) with a pixel size of 50 µm. A better spatial resolution is achieved for the CERN test beam measurement as the residuals show a steeper increase at the edges of the distribution and a smaller spread around zero. This is a result of higher particle beam energy and therefore less scattering in CERN test beam measurements compared to the ones at DESY.
In addition, the residual plots for the most upstream telescope plane in Figure 6.14

demonstrate the better spatial resolution of the GBL algorithm for DESY test beam data compared to the reconstruction with the DAF algorithm.
However, for a numerical calculation of the spatial resolution only hits with cluster size one should be used while for the presented residuals the charge weighted cluster centers of all clusters are taken into account. For more information on the calculation and results of the spatial resolution of test beam measurements see [94].

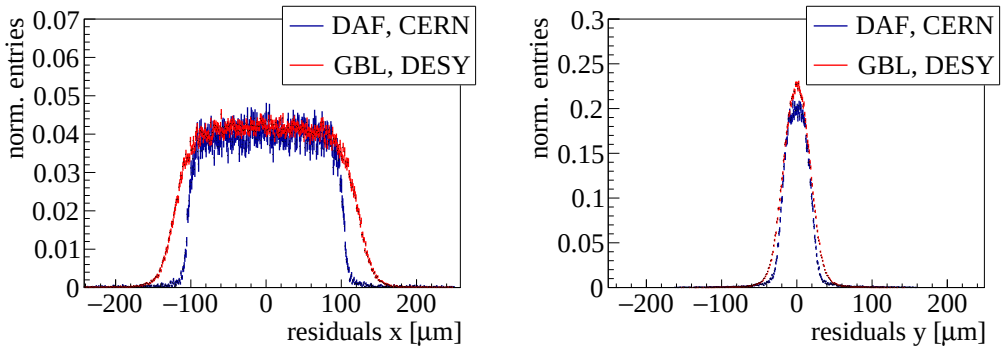

Figure 6.13: Normalized residual plots for the most upstream DUT inside the test beam box in x- (left) and y-direction (right): Measured at the CERN test beam campaign in August 2016, reconstructed with DAF (blue) and measured at the DESY test beam campaign December 2018, reconstructed with GBL (red).

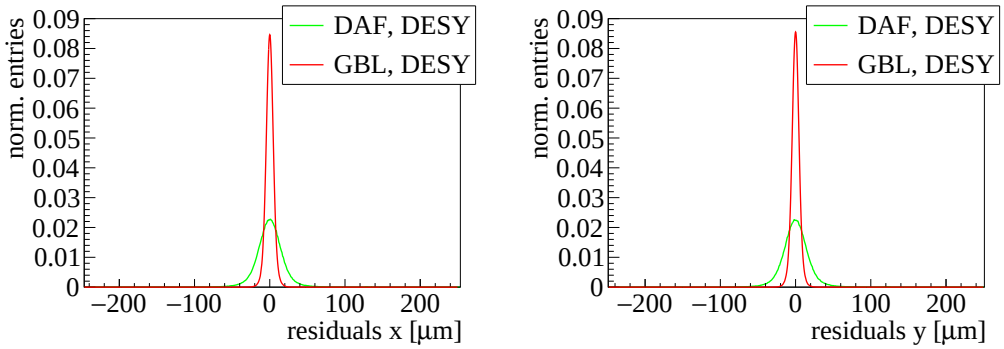

Figure 6.14: Normalized residual plots for the most upstream telescope plane in x- (left) and y-direction (right) measured at the DESY test beam campaign December 2018 for one specific run reconstructed with the DAF (green) and the GBL algorithm (red). The distributions in x- and y-direction for each algorithm have the same width as a MIMOSA26 sensor features symmetric pixel cells with a size of 18.4 µm × 18.4 µm.

TBmon2

The software tool TBmon2 performs analyses like hit and charge collection efficiency determination of the DUTs. The procedure is divided into preprocessors and the actual analysis.

Preprocessors

EuBuildTrack: In the first preprocessor the full hit information and the projected track positions are read in for all DUTs. Special adjustments were programmed in the course of this thesis to read in the test beam data reconstructed with the GBL track fitting algorithm as the storage of the data in the root-file is different to with DAF reconstructed data. Before these adjustments were made, test beam data were always reconstructed with the DAF fitter in the ATLAS ITk pixel group.
In addition, only tracks measured by a specific DUT (chosen with the parameter "matchDUT") are used for the further analysis. This so-called *reference sensor* is necessary as a timing device since the readout method of the telescope planes and the DUTs are different: The telescope planes are read out with a rolling shutter method which needs 115.2 µs for a single frame, while the FE-I4 modules are only sensitive for 400 ns. As a result, the telescope planes measure more particles per trigger and some reconstructed tracks are outside the detection window of the DUTs. To select the expected tracks for the investigated modules a non-irradiated sensor with high particle detection efficiency is used as reference device. In the analysis performed for this thesis not only the reference module but any DUT in the test beam setup were used as reference device.

HotPixelFinder: After reading in the data and selecting the tracks, the hit information of the DUTs is used to identify and mark dead and noisy pixels.

ClusterFinder: The hits for all DUTs are clustered with a clustering algorithm. In this step flags are set to specify if the cluster contains marked pixels or pixels at the edge of the sensor (*edge pixel*).
A new clustering algorithm was developed by the author to reduce the calculation time and is now used as default in the TBmon2 community. In the first step of the old clustering algorithm the list of hits is copied and the first hit of this copied list is the cluster seed. The hit is removed from the copied list. Afterwards, neighboring hits are searched: The cluster hit position is compared to the hit positions of all hits in the copied list. If a neighboring hit is found, the hit is added to the cluster and deleted from the copied list. When a hit is added to the cluster, the copied list has to be checked again for neighboring hits. If no neighbors for the cluster hits are found anymore, the next element from the copied list is the seed for the next cluster and removed from the copied list. The procedure to find neighboring

hits is repeated until the copied list is empty. This way, the size of the copied list is slowly reduced over time but repeated very often. Especially for large hit lists the analysis is very time consuming: About two hours for a run with 200 000 events and more than 1000 hits per event in the investigated module (very noisy module). This analysis time has been reduced to about two minutes with the new clustering algorithm: For the new clustering algorithm the first hit in the list of hits is the cluster seed. Afterwards, the program goes through the list of hits and compares the positions of the hits to the positions of all clustered hits. If the hit is a neighbor to a cluster hit, the hit is added to this cluster. If the hit additionally neighbors another cluster hit which is associated to a different cluster, the two clusters are merged together. If no neighbors are found the hit is used as a cluster seed for a new cluster. This way the list of hits is not copied and it is only passed through once. The number of clustered hits is slowly increasing and the hits are compared to an increasing number of clustered hits. However, merging of connected clusters saves time compared to searching for cluster hits one by one.

ClusterMatcher: In the following step the calculated clusters are matched to tracks by searching for clusters with a maximum distance of "matchX" and "matchY" between the cluster center and the track position. The cluster center is calculated using the charge (ToT) information from the clustered hits (charge weighted cluster center). For the analysis in this thesis the values of matchX = 600 µm and matchY = 150 µm were used for all DUTs.
In addition, the track and cluster information is ignored in the following calculations for clusters containing edge or noisy hits.

CheckAlign: From the positions of the track and the charge weighted cluster centers residual plots are created and the alignment between the modules and reconstructed tracks is monitored. In previous software versions only movements in x- and y-direction were possible. In the course of this thesis this functionality has been upgraded to also allow for rotational alignment. For each run analyzed with TBmon2 the alignment is calculated and applied independently. In Figure 6.15 the residuals in y-direction are plotted against the hit position in x-direction as provided from EUTelescope, without any alignment in TBmon2 (left) and after the improved alignment (right). For an optimal aligned module the residuals are independent of the hit position resulting in a fitted straight line with slope and y-intercept of zero.

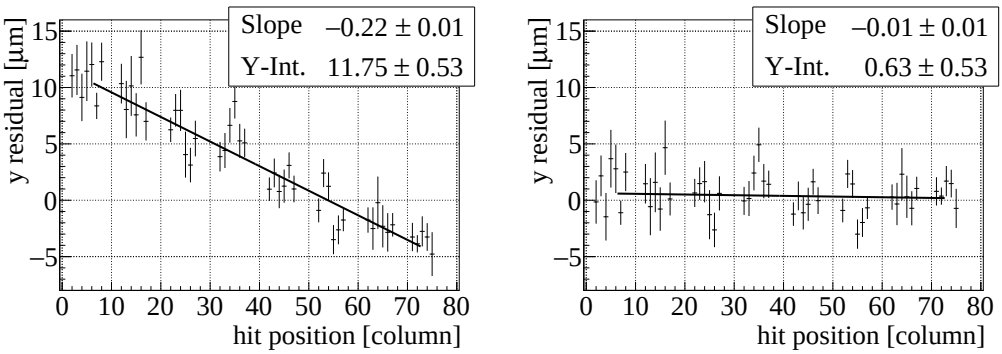

Figure 6.15: The residual in y-direction depending on the hit position. Left: Before the alignment. Right: After the improved alignment in TBmon2.

Analysis

With the optimally aligned modules the actual analysis of the DUTs is performed. Several predefined analysis tools are available which can be easily adjusted to the user's needs. Only good tracks and hits are used for the analysis: A *good track* is measured by at least one reference sensor and its position on the investigated module is not in a masked or edge region. For a *good hit* the good track is matched to a cluster on the DUT that contains no masked or edge pixels.

Efficiency: The number of hits measured by the module is binomially distributed and the efficiency ϵ of a module is defined as the fraction of the number of good hits measured by the module n_{hits} and the number of good tracks n_{tracks} [108]:

$$\epsilon = \frac{n_{\text{hits}}}{n_{\text{tracks}}}. \tag{6.3}$$

For the statistical error the standard deviation σ_ϵ of the efficiency is calculated with

$$\sigma_\epsilon = \sqrt{\frac{\epsilon \cdot (1-\epsilon)}{n_{\text{tracks}}}}. \tag{6.4}$$

With the efficiency analysis tool the efficiency per module is calculated and additionally displayed in two-dimensional diagrams. An exemplary efficiency map of the non-irradiated REINER module R2 is presented in Figure 6.16. For this image the module was tuned to a threshold value of 3200 e and a ToT response of 6 for a reference charge of 20 ke. It is biased with 90 V and the data of 15 runs measured under the same conditions are combined ($\sim$ 210 000 events per run). Only the four innermost columns of each group with different pixel designs are always used for the analysis to prevent an influence of the guard rings while all other pixel columns

are masked. Only data for the groups with pixel designs 05, V6, V4, V2, V3 and V1 are available since the beam spot was focused on the left side of the module. The efficiency of the illuminated area of module R2 is calculated to $(96.59 \pm 0.02)\,\%$.

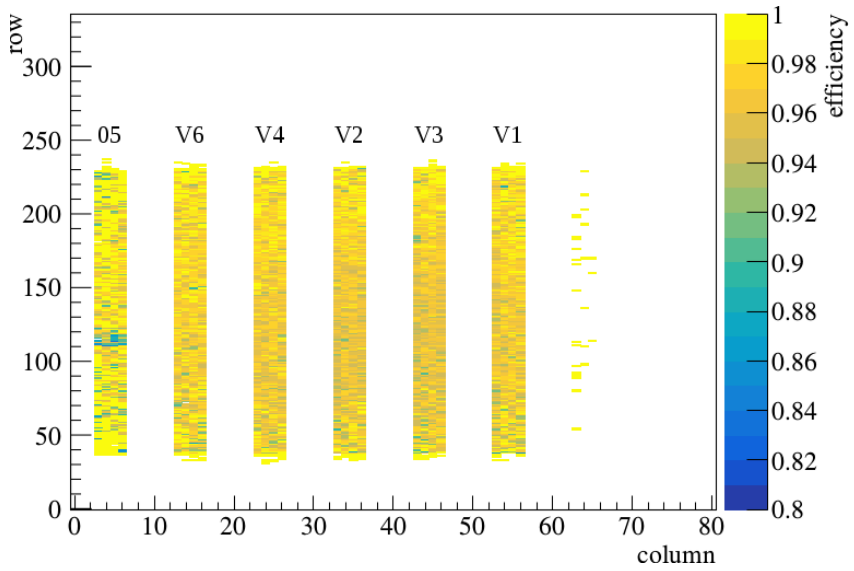

Figure 6.16: Efficiency map of the non-irradiated REINER module R2 investigated at the CERN test beam campaign August 2016. A total of 646 622 good tracks and 624 562 good hits were measured.

To investigate the performance of the groups with different pixel designs of the REINER sensor, special *geometries* are defined in the TBmon2 software. For these geometries, the efficiency analysis tool creates *in-pixel efficiency maps*: For all tracks passing through a pixel of a given geometry, the track position is projected into one virtual pixel. An example of an in-pixel efficiency map of the group with pixel design V2 of the non-irradiated module R2, biased with 90 V, is shown in the top of Figure 6.17 (Tuning: 3200 e, 6 ToT at 20 ke): For all good tracks passing through the four innermost columns (33 to 36) of the group V2 (columns 30 to 39) the efficiency is calculated and plotted against the folded track position. In this image a drop in efficiency is visible on the right side of the pixel design corresponding to the location of the bias dot (see bottom of Figure 6.17 for the layout of pixel design V2). This clear observation is possible for CERN test beam measurements due to a better spatial resolution compared to DESY test beam results. The efficiency drop is visible for all pixel designs and explained in more detail in [57, 109]. As this thesis focuses on the performance differences of the pixel designs which all feature the same bias dot and bias grid configuration, the region of the bias

dot is excluded from the region of interest. Only tracks with a projected position $< 200\,\mu m$ are considered for the analysis and are used for efficiency calculations in the following.

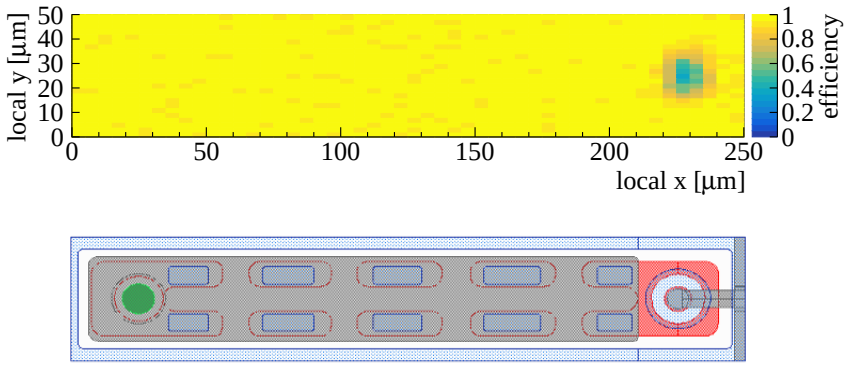

Figure 6.17: Top: In-pixel efficiency map of the group with pixel design V2 of the non-irradiated REINER module R2, biased with 90 V, investigated at the CERN test beam campaign August 2016. Bottom: Layout of the pixel design V2 for comparison. The color code of the pixel design is explained in Figure 5.4.

EfficiencyVsGeometry: The analysis tool EfficiencyVsGeometry was written in the course of this thesis to obtain the efficiencies for each implemented geometry. Two efficiencies per geometry are calculated: One over the full pixel length and the other excluding the bias dot region as explained above. The group with pixel design V2 presented in Figure 6.17 reaches an efficiency of $(97.21 \pm 0.05)\,\%$ with 117 998 tracks for the presented measurement (the area of the bias dot is excluded).
In Figure 6.18 the efficiencies per run for the group with pixel design V2 of module R2, biased with 90 V, are presented (Tuning: 3200 e, 6 ToT at 20 ke). The error bars for every run are calculated using the standard deviation of the binomial distribution of Equation 6.4. In addition, the mean efficiency for this geometry (97.21 %), indicated by a red line, is calculated by averaging the efficiencies per run weighted with the number of good tracks. To describe the efficiency deviations from run to run the Clopper-Pearson confidence interval [110] is calculated which was introduced for usage in TBmon2 in the PhD thesis of A. Gisen [79]: The ROOT-class "TEfficiency" [111] is applied with a confidence level of $\gamma = 95\,\%$. The upper and lower interval limits are calculated by the $\frac{1+\gamma}{2}$ and $\frac{1-\gamma}{2}$ quantile for every run. The fluctuation between the runs is considered by using the cumulative distribution function of the efficiency values. With this method, the error of the average efficiency for the cumulative runs are calculated and indicated as a blue band around the average efficiency in Figure 6.18. The efficiency for the group with pixel design V2 for the non-irradiated sensor R2, biased with 90 V, is $\left(97.21^{+0.51}_{-0.32}\right)\,\%$.

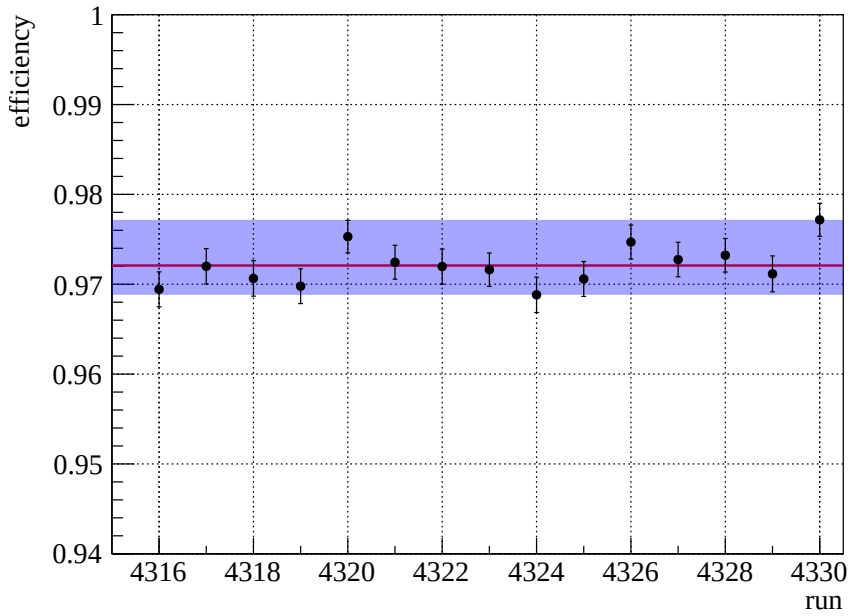

Figure 6.18: Efficiencies for the different runs calculated for the group with pixel design V2 of the non-irradiated REINER module R2, biased with 90 V, investigated at the CERN test beam campaign August 2016. The red line indicates the track weighted average efficiency, the blue band is the Clopper-Pearson confidence interval, the error bars per run are calculated with Formula 6.4.

6.2.4 Hit Detection Efficiency Results

Several modules have been investigated in different test beam campaigns at the DESY and CERN test beam facilities. Information on the non-irradiated modules, the campaigns and the performed measurements, like tuning parameters and bias voltage, are summarized in Table 6.1. Results of the measurements performed at the DESY test beam campaign in November 2013 (R2, non-irradiated) and the CERN test beam campaign in August 2016 (R1, irradiated and R2, non-irradiated), have already been presented in the thesis of R. Michallek [112] and in the author's master thesis [113]. Different calculation methods like the error calculation of the efficiency were used. Furthermore, the efficiency over the full pixel length including the region of the bias dot and bias grid was calculated. To compare the results with new measurements, the data is analyzed again using the previously described calculation methods and presented in this work.
The ITk acceptance criterion for non-irradiated modules is used to assess the efficiency performance of the different REINER pixel modules. It requires a hit detection efficiency of more than 98.5 % [85] for non-irradiated modules and is fulfilled for all REINER modules and measurements performed in DESY test beam campaigns. The pixel design variations on REINER pixel modules reach high particle detection efficiencies between $\left(98.76^{+1.24}_{-1.51}\right)$ % to $\left(99.87^{+0.07}_{-0.06}\right)$ % and perform as good as the standard pixel designs with efficiencies between $\left(99.26^{+0.74}_{-2.52}\right)$ % to $\left(99.92^{+0.08}_{-0.17}\right)$ %. For these measurements no variations in the efficiencies for the groups with different pixel designs are observed and the results seem independent from tuning settings and bias voltage. This is illustrated in Figure 6.19 showing the measurements of the module R6 for four different tunings and three different bias voltages.
More detailed information on the results of the other modules can be found in Appendix A, Figures A.1 to A.3 and Tables A.1 to A.4.
However, the efficiencies for modules measured in CERN test beam campaigns are always lower compared to results from DESY test beam measurements. As an example the test beam results for module R2 (biased with 150 V, tuned to 3200 e) are listed in Table 6.2: For the DESY measurements the ToT is tuned to a response of 8 at a reference charge of 16 ke while for the CERN measurement it is tuned to 6 ToT at 20 ke. The efficiency results with errors and the results of module R8 can be found in Appendix A. The observed lower efficiencies for CERN test beam campaigns are not yet understood.

Table 6.1: Summary of the measurements for the non-irradiated modules R2, R6 and R8 in different test beam campaigns, investigated with various tunings and bias voltages. The mean efficiency over all pixel designs and bias voltages is calculated for each tuning.

inv. module	test beam campaign	tuning threshold, ToT	bias voltage [V]	mean efficiency [%]
R2	DESY, Nov. 2013	3200 e, 8 ToT 16 ke	150	99.81
		1600 e, 8 ToT 16 ke	150	99.76
	CERN, Aug. 2016	3200 e, 6 ToT 20 ke	150, 120 90, 50	97.30
		1600 e, 6 ToT 20 ke	120, 90	93.65
R6	DESY, Dec. 2017	3200 e, 6 ToT 20 ke	150, 120, 100	99.10
		1600 e, 10 ToT 10 ke	150, 120, 100	99.25
		1000 e, 10 ToT 10 ke	150, 120, 100	99.29
		1000 e, 7 ToT 14 ke	120	99.15
R8	CERN, Oct. 2017	1600 e, 8 ToT 16 ke	120	96.02
	DESY, Dec. 2017	1600 e, 8 ToT 16 ke	70, 60	99.28
		1000 e, 10 ToT 10 ke	70, 60	99.31

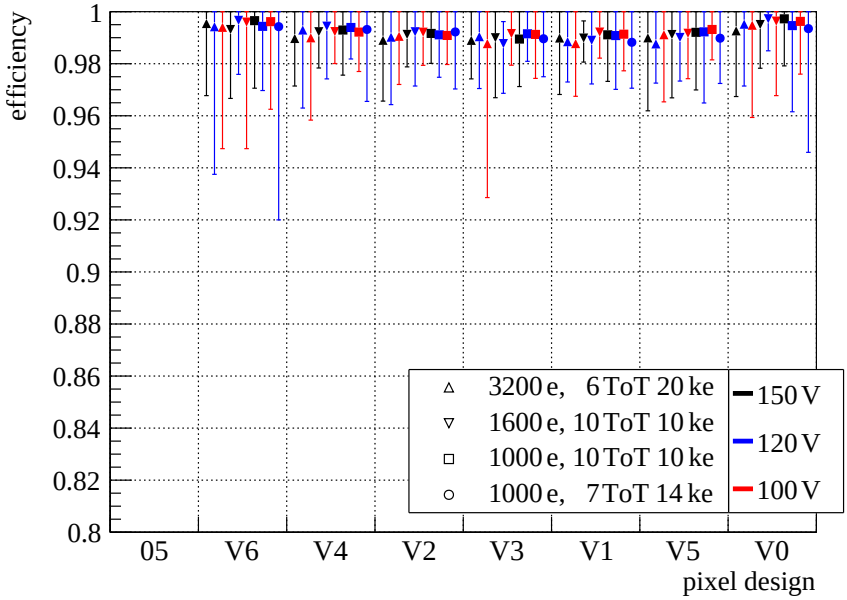

Figure 6.19: Efficiencies for the groups with different pixel designs of the non-irradiated REINER module R6 investigated at the DESY test beam campaign December 2017.

Table 6.2: Comparison of the efficiency results of the non-irradiated module R2 from the test beam campaigns in November 2013 at DESY and August 2016 at CERN. The module is biased with 150 V and tuned to a threshold value of 3200 e. The ToT is tuned to 8 at 16 ke for the DESY measurement and 6 ToT at 20 ke for the CERN measurement.

test	efficiencies of the groups with different pixel designs [%]						
beam	05	V6	V4	V2	V3	V1	V5
DESY	99.83	99.58	99.79	99.83	99.82	99.77	99.75
CERN	99.01	98.62	98.33	97.88	97.60	97.56	98.60

6.2.5 Charge Collection Efficiency Results

The different pixel designs of the REINER sensor are intended to increase the electric field resulting in a higher charge collection efficiency. To convert the ToT values into electron charge, calibration scans are necessary for each module and tuning setting. As there are many modules investigated and measurements performed, no calibration scans were done so that the following chapters focus on the ToT value analysis. For this analysis the ToT values for each group with a different pixel design are compared. Only clusters with one hit are considered for this analysis to ensure that the full deposited charge of the incident particle is detected by only one pixel. In addition, the majority of all clusters (about 86 %) has a cluster size of one. As an example the mean ToT value and the standard deviation are calculated for all hits in the group V4 with cluster size one for the module R2 biased with 150 V in Figure 6.20 (Tuning: 3200 e, 8 ToT at 16 ke). The ToT values above 13 are summarized in bin 14 (over flow bin).

In Figure 6.21 the mean ToT values (cluster size one) for the groups with different pixel designs of module R6 and the determined standard deviations of the ToT, indicated as error bars, are presented. The module is investigated in the December 2017 test beam campaign at DESY with four different tunings and three bias voltages. Visible differences in the measured charges for all pixel designs are caused by different tunings: For the two tunings 1600 e, 10 ToT at 10 ke and 1000 e, 10 ToT at 10 ke the generated charges per hit exceed a ToT value of 13. Consequently, most ToT entries are stored in the overflow bin. The slightly higher ToT values for pixel designs V6, V4 and V2 at these tunings compared to V5 and V0 are statistically not significant and might result from inaccuracies in the ToT tuning. Overall, the measured ToT is very consistent across the different pixel designs.

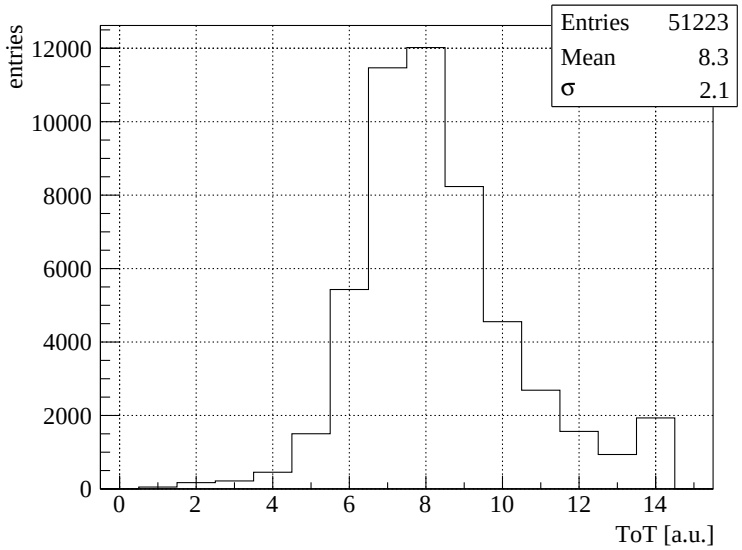

Figure 6.20: ToT values for all hits in the group with pixel design V4 of the non-irradiated REINER module R2, biased with 150 V and investigated at the DESY test beam campaign November 2013.

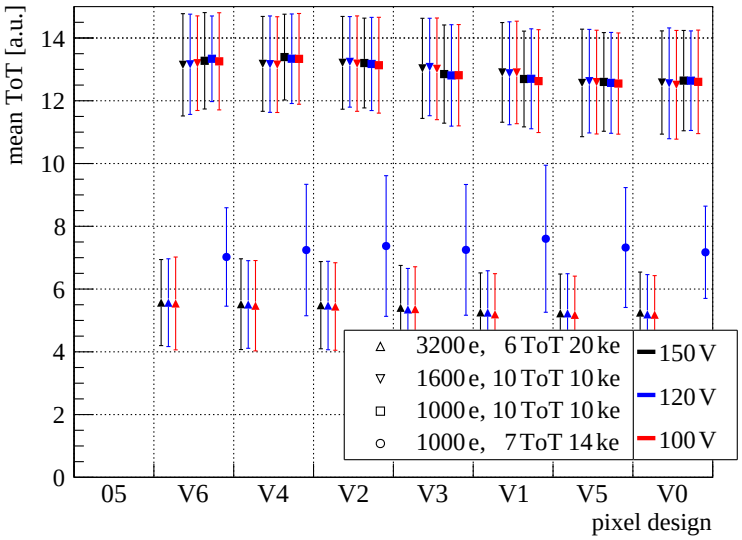

Figure 6.21: Mean ToT values for cluster size one of the groups with different pixel designs for the non-irradiated REINER module R6 investigated at the DESY test beam campaign December 2017.

These results of the module R6 are consistent with the DESY test beam results of the mean ToT values for the other modules R2 and R8 which can be found Appendix A. A discrepancy between the measured charges for CERN and DESY measurements is observable (Figure A.6): More charge is generated for the lower bias voltage measurement at DESY (70 V) compared to the higher bias voltage measurement (120 V) at CERN with the same tuning parameters. As described in the previous section, the reasons for the different performances of the same module in CERN and DESY test beam measurements are not yet understood.

6.3 Summary of the Results of non-irradiated REINER Pixel Modules

In the measurements of non-irradiated REINER pixel modules it was found that the best tuning parameters to identify differences in the charge generation between the different pixel designs are 3200 e, 6 ToT at 20 ke and 1000 e, 7 ToT at 14 ke for DESY test beam measurements. Here, the generated charge corresponds to a medium ToT value. The results of the charge collection efficiencies show no significant differences in the performances of the various pixel designs and no specific pixel design stands out in any module measurement.
The results of the hit detection efficiencies agree with the charge collection measurements: The different pixel designs of all modules reach a high particle detection efficiency ($> 98.5\,\%$) and no differences are measured in the performance among all pixel designs.
However, discrepancies between the pixel designs are observable in IV measurements as the groups with pixel designs V5 and V6 measure higher leakage currents in comparison.

To investigate the modules' radiation hardness they are irradiated in different irradiation facilities and re-tested. These irradiation facilities and the results of irradiated modules are described in the following chapter.

7 Investigation Methods and Results of irradiated REINER Pixel Modules

Modules inside the ATLAS detector are exposed to a high fluence of radiation. To ensure a good performance even after years of operation inside the detector, the modules need to have a high radiation hardness. Close to the interaction point, the modules are penetrated by a mixture of particles including pions, protons and neutrons which are the main contributors to radiation damage as discussed in Chapter 4. To simulate the damage of these particles, modules are artificially irradiated in *irradiation facilities* to the expected maximum lifetime fluence of the detector modules, including safety factors. The damage rate is calculated in 1 MeV neutron equivalent fluence by applying an individual hardness factor κ (see Eq. 4.1, Chapter 4.2) for each irradiation facility. The exact irradiation fluence of the modules is determined by spectroscopic analysis of special foils irradiated together with the modules. Afterwards the performance of the irradiated modules is checked in laboratory and test beam measurements.
The investigated modules for this thesis are irradiated with neutrons or protons in different irradiation facilities described in more detail in the following section. In addition, results of laboratory and test beam measurements are presented for these irradiated modules.

7.1 Irradiation Facilities

For neutron irradiation the modules are placed inside a reactor core. Due to space limitations and to reduce the amount of activated material, only the modules without a PCB are irradiated. The neutron irradiated modules investigated in this thesis are either irradiated at the TRIGA Mark II research reactor of the Ljubljana Neutron Irradiation Facility which is part of the Jožef Stefan Institute in Slovenia [114] or at the Annular Core Research Reactor (ACRR) of the Sandia National Laboratories in the United States [115].
The irradiation facility in Ljubljana provides a continuous neutron energy spectrum with an experimentally determined hardness factor of $\kappa_{\text{Ljubljana}} = 0.90 \pm 0.05$ [116]. For more information on the dose rates and energy spectra see [117]. The modules are prepared for irradiation in Ljubljana by wrapping them in clean room tissue,

sealing and storing them inside radiation tubes with a diameter of 2.2 cm. In Figure 7.1 pictures of the prepared modules and the aluminum irradiation tubes are presented.
Four different REINER pixel modules were irradiated to two different fluences in Ljubljana: The modules R7 and R9 to $1 \times 10^{15}\,\mathrm{n_{eq}/cm^2}$ (duration: 10 min 50 s) and the modules R3 and R5 to $5 \times 10^{15}\,\mathrm{n_{eq}/cm^2}$ (duration: 54 min 10 s). During irradiation the samples heated up to temperatures of about 40 °C. After the irradiation the modules were stored at room temperature for about two hours for spectroscopic measurements and have afterwards been cooled down to prevent annealing.

Figure 7.1: Images of the prepared modules for the irradiation at the TRIGA Mark II research reactor in Ljubljana: The modules are wrapped in clean room tissue and sealed before insertion into the aluminum irradiation tubes.

The module R1 was irradiated at the ACRR at Sandia to $5 \times 10^{15}\,\mathrm{n_{eq}/cm^2}$ (duration: about 155 min). During the neutron irradiation at the ACRR at Sandia absorption materials were placed around the modules to prevent influence of thermal neutrons. For more information on the neutron energy spectra at the ACRR see [118]. The module package reached temperatures of almost 100 °C and its temperature profile is illustrated in Figure 7.2. After irradiation the module was stored in the freezer, however no record of annealing times at room temperature for measurements like a spectroscopy are available.

For proton irradiation the modules can be irradiated while they are mounted on a PCB. The modules investigated in this thesis were irradiated with protons at the Birmingham Irradiation Facility of the University of Birmingham [119, 120] or the Proton Irradiation Facility (IRRAD) at CERN [121, 122].
The proton beam at the Birmingham Irradiation Facility is generated with an MC40 Cyclotron with a proton energy of 27 MeV. The beam spot of about 1 cm × 1 cm scans over the module to achieve a homogeneous irradiation over the full module size. The module is mounted inside a cooled box and a 350 µm thick aluminum plate is placed in front to shield the module from low energetic beam components. The

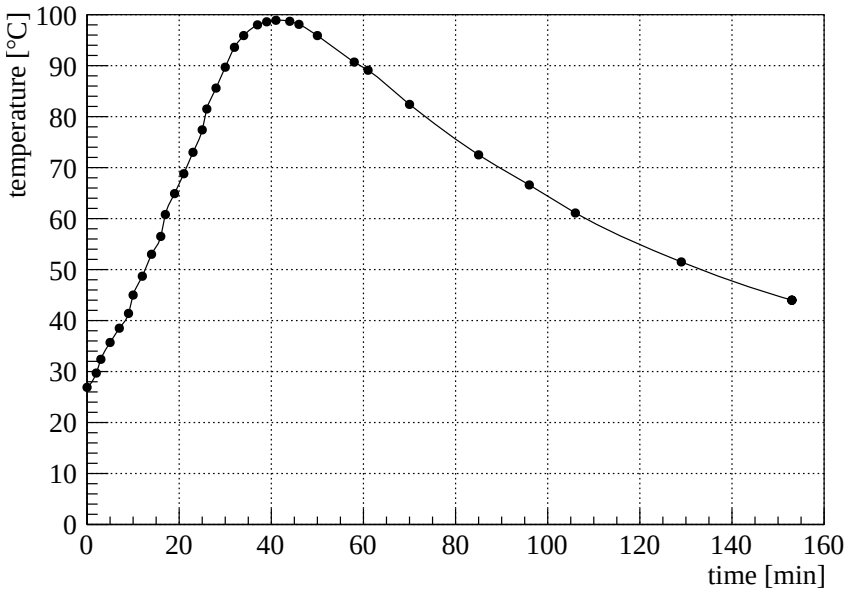

Figure 7.2: Temperature profile of the module package for neutron irradiation at the ACRR at Sandia provided by Sandia as an estimation for the R1 sensor temperatures.

aluminum plate reduces the proton energy to 24 MeV when reaching the module. The hardness factor is determined to $\kappa_{\text{Birmingham}} = 2.1 \pm 0.5$ [123]. Two REINER pixel modules were irradiated to $5 \times 10^{15}\,\text{n}_{\text{eq}}/\text{cm}^2$: R6 (duration: 3 h 15 min) and R12 (duration: 3 h 36 min). The irradiation to a lower fluence of $1 \times 10^{15}\,\text{n}_{\text{eq}}/\text{cm}^2$ for module R8 was finished after 42 min. During irradiation all modules were cooled down to −27 °C.
The particle beam for proton irradiation at the CERN Irradiation Facility has a much higher energy of 24 GeV. For the irradiation protons from the PS accelerator are extracted and guided to the modules. The beam spot size is adjustable to a maximum of 20 mm × 20 mm (FWHM) and no scanning was necessary to irradiate the full sensor surface. However, the irradiation is inhomogeneous and the highest irradiation fluences are reached in the center. The hardness factor for the 24 GeV protons is calculated to $\kappa_{\text{IRRAD}} = 0.62 \pm 0.04$ [123]. The REINER pixel module R2 was irradiated inhomogeneously to a mean fluence of $6 \times 10^{15}\,\text{n}_{\text{eq}}/\text{cm}^2$ and a peak fluence of $9 \times 10^{15}\,\text{n}_{\text{eq}}/\text{cm}^2$ in the center. The irradiation took 41 days and was performed at room temperature. Afterwards, the module was stored in a freezer to prevent annealing.

In Table 7.1 the different irradiations of the REINER pixel modules with the corresponding particle type and target fluences are summarized. The modules with an

even number in their name are proton irradiated while the ones with an odd number are irradiated with neutrons. The modules R4 and R10 are not irradiated since it was not possible to achieve an intact wire bond connection between the module and the PCB for module R4. The readout chip of module R10 was broken.

Table 7.1: Summary of the different irradiated REINER pixel modules: The location of the irradiation facility, particle type for irradiation, homogeneity of the irradiation and target fluence are indicated.

module name	location of irradiation facility	particle type	beam uniformity	target fluence [n_{eq}/cm^2]
R1	Sandia	n	uniform	5×10^{15}
R3	Ljubljana	n	uniform	5×10^{15}
R5	Ljubljana	n	uniform	5×10^{15}
R7	Ljubljana	n	uniform	1×10^{15}
R9	Ljubljana	n	uniform	1×10^{15}
R2	CERN	p	inhomogeneous	6×10^{15}
R6	Birmingham	p	uniform (scanned)	5×10^{15}
R12	Birmingham	p	uniform (scanned)	5×10^{15}
R8	Birmingham	p	uniform (scanned)	1×10^{15}

In the following sections the overall consistent results are presented for all modules and pixel designs while section 7.4 focuses on the results with exceptional performances of pixel designs V5 and V6. To indicate each section's focus the corresponding module names are highlighted in bold.

7.2 Laboratory Measurements

The modules are glued and wire-bonded to a PCB after neutron irradiation and stored at room temperature for one day for the glue to cure. The proton irradiation was performed while the modules were connected to a PCB. To measure the performance of irradiated modules they are investigated in cooled setups by using a chiller or dry ice. For measurements in the laboratory only IV and source scan measurements were performed for which the results are presented in the following section.

7.2.1 IV Measurements

For IV measurements the setup described in Chapter 6.1.2 is used. The chiller is set to $-45\,°C$, cooling the sensor to about $(-30 \pm 5)\,°C$. To achieve comparability of

different measurements and sensor temperatures, Pt1000 temperature resistors are taped close to the modules. The monitored module temperature is used to normalize the leakage current to a sensor temperature of −30 °C by applying equation 3.6. For all measurements of irradiated modules, the setup is flushed with pre-cooled dry air to prevent any water condensation.
An increase in leakage current is expected for higher irradiated modules when compared to lower irradiated ones. The IV measurement results presented in Figure 7.3 for the neutron (left) and proton (right) irradiated samples meet this expectation: The lowest leakage currents are measured for modules R7, R9 and R8 (1×10^{15} n_{eq}/cm^2). Furthermore, no difference between the results of neutron and proton irradiated samples is visible.
The early breakdown of the proton irradiated module R6 (5×10^{15} n_{eq}/cm^2) results from pixel design V4 as visible in the individual pixel design measurements in Appendix B, Figures B.1-B.5. As no other module shows this behavior for V4, it is, however, not treated representatively.

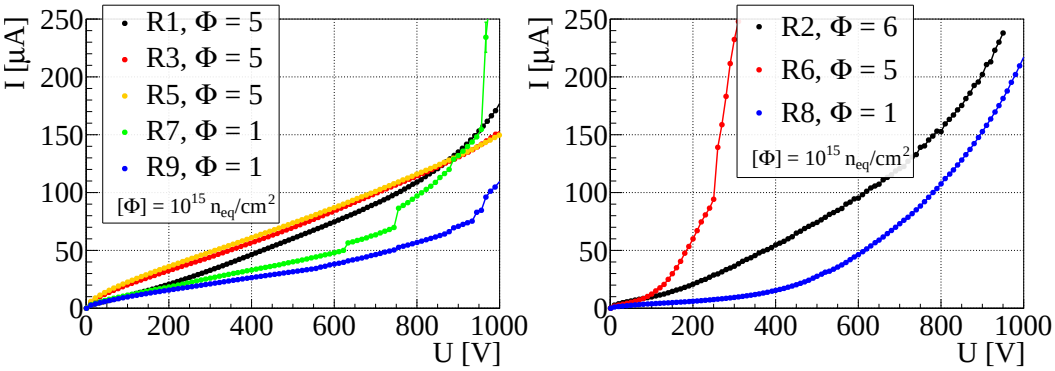

Figure 7.3: IV measurements of irradiated modules. Left: Neutron irradiated modules. Right: Proton irradiated modules. The measured leakage current is normalized to a sensor temperature of −30 °C.

7.2.2 Source Measurements

The irradiated module **R1** was studied in the master thesis of M. Grothe [86] with source measurements. For these measurements the setup described in Chapter 6.1.3 was used and the module was tuned to a threshold value of 3200 e and a ToT response of 6 for a reference charge of 20 ke. The groups with different pixel designs were biased individually and scans were performed at different bias voltages. The raw ToT data was taken by M. Grothe. Afterwards, the ToT values for cluster size one for every measurement were fitted with a Landau-Gauss convolution (see

Chapter 3.7) to determine the most probable ToT value (MPV[ToT]).
Since the different pixel designs on the REINER pixel sensor are intended to increase the electric field, it is expected to measure higher charge for the new designs compared to the standard design. Figure 7.4 presents the results of these source measurements for the neutron irradiated module R1 ($5 \times 10^{15}\,\mathrm{n_{eq}/cm^2}$, Sandia). All groups with new pixel designs (V1-V6) measure higher or similar charge compared to the standard designs 05/V0. Especially the group with pixel design V5 with narrowed implantation and enlarged p-spray area stands out at all bias voltages.
To check if the other irradiated modules show similar results they were investigated intensively in different test beam campaigns at the CERN and DESY test beam facilities.

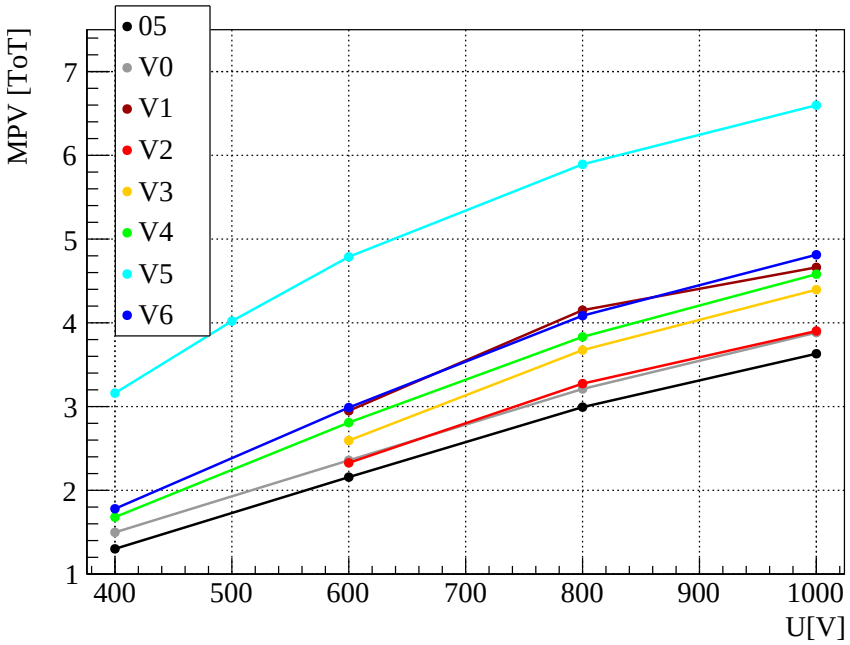

Figure 7.4: Most probable ToT values for cluster size one determined with source scan measurements for the different pixel design groups of the neutron irradiated module R1 ($5 \times 10^{15}\,\mathrm{n_{eq}/cm^2}$, Sandia). Raw ToT data taken from [86].

7.3 Test Beam Measurements

All irradiated modules have been measured in different test beam campaigns at the DESY and CERN test beam facilities. Table 7.2 summarizes the campaigns and the performed measurements, like tuning and bias voltages. As mentioned earlier, the results of the irradiated module R1, measured in the August 2016 campaign at CERN, have already been presented in the author's master thesis [113]. However, the data is analyzed again with the described calculation methods and presented in this work.

Table 7.2: Summary of the measurements for irradiated modules in different test beam campaigns. The irradiation fluence is indicated in $[\Phi] = 1 \times 10^{15}\,\mathrm{n_{eq}/cm^2}$ and the particle type with (n) for neutrons and (p) for protons.

inv. module	test beam campaign	tuning threshold, ToT	bias voltage [V]
R1, $\Phi = 5$ (n)	CERN, Aug.2016	3200 e, 6 ToT 20 ke	400, 600, 800, 1000
		1600 e, 6 ToT 20 ke	600, 1000
R2, $\Phi = 6$ (p)	CERN, Jul. 2017	3200 e, 6 ToT 20 ke	400, 600, 700, 800, 1000
		1600 e, 6 ToT 20 ke	600, 700, 800, 1000
		1600 e, 6 ToT 6 ke	400, 500, 600, 700, 800, 1000
R3, $\Phi = 5$ (n)	CERN, May 2018	3200 e, 6 ToT 20 ke	300, 400, 600, 800, 1000
		1600 e, 6 ToT 20 ke	300, 400, 600, 800
R5, $\Phi = 5$ (n)	CERN, May 2018	3200 e, 6 ToT 20 ke	300, 400, 600, 800, 1000
		2000 e, 6 ToT 20 ke	300, 400, 600, 800, 1000
R7, $\Phi = 1$ (n)	CERN, May 2018	3200 e, 6 ToT 20 ke	300, 400, 500, 600, 800
		1600 e, 6 ToT 20 ke	300, 400, 600
	CERN, Aug. 2018	1600 e, 6 ToT 20 ke	100, 150, 200, 300, 400
		1000 e, 10 ToT 10 ke	100, 150, 200, 250, 300, 400
R9, $\Phi = 1$ (n)	CERN, May 2018	3200 e, 6 ToT 20 ke	300, 400, 600, 800, 900
		1600 e, 6 ToT 20 ke	300, 400, 600, 800, 900
	CERN, Aug. 2018	1600 e, 6 ToT 20 ke	100, 150, 200, 300, 400
		1000 e, 10 ToT 10 ke	100, 150, 200, 250, 300, 400
R12, $\Phi = 5$ (p)	CERN, Oct. 2018	1600 e, 6 ToT 20 ke	400, 500, 600
		1000 e, 10 ToT 10 ke	400, 600
R6, $\Phi = 5$ (p)	DESY, Dec. 2018	1600 e, 6 ToT 20 ke	400
		1000 e, 10 ToT 10 ke	340
R8, $\Phi = 1$ (p)	DESY, Dec. 2018	1600 e, 6 ToT 20 ke	400, 600, 800, 1000
		1000 e, 10 ToT 10 ke	400, 600, 800, 1000

For test beam measurements with dry ice as described in Chapter 6.2.2 an alignment of the DUTs is necessary for every run while the ice sublimates. This weight loss results in a movement of the DUTs, which is compensated by the alignment of EUTelescope and TBmon2 software. In addition, the thermal coupling between dry ice and modules reduces over time so that the box warms up. To estimate the sensor temperatures inside the box, a Pt1000 temperature resistor mounted closely to the module as well as the module's leakage current is monitored. A significant change in temperature offsets the module tuning resulting in a changed module performance.
To illustrate the impact of changing temperature, the efficiencies of the group with pixel design V6 for module **R8** ($1 \times 10^{15}\,\mathrm{n_{eq}/cm^2}$, Birmingham) biased with 800 V are presented for 7 runs in Figure 7.5 (Tuning: 1600 e, 6 ToT at 20 ke). Each run took between 8 min to 11 min and the data was recorded over a time span of 1 h and 7 min. During the measurements the Pt1000 temperature rose from −42.7 °C to −35.2 °C and the leakage current of the module increased from about 106 µA to about 243 µA. For this increase in temperature of about 7.5 °C the efficiency drops significantly by about 7.4 %. A similar reduction in efficiency is also observable for the other pixel design groups.
Consequently, the presented data of module R8 biased with 800 V is neglected since the change in temperature and leakage current is higher than the usual increase between 0 °C to 3 °C and a clear correlation between change in efficiency and increase in temperature was observable. Small changes in efficiency between different runs are considered in the calculated errors and presented in error bars as described in Chapter 6.2.3.
For this reason the leakage currents and temperatures need to be monitored frequently to replace or refill the dry ice in time before the temperature reaches a high gradient. After every refill the quality of the tuning of the modules is checked and when necessary re-tuned to achieve comparable results.

Due to the large number of modules and measurements only the characteristic features of the modules are shown exemplary in the following section. Detailed results of all investigated modules for each tuning and measured bias voltage can be found in Appendix C. Most results come from combinations of sets of runs, where the beam spot is focused on one half of the module or the other, respectively. For the central pixel groups covered by both measurements the results with more tracks and thus higher statistics are used.
First the characteristics of the hit detection efficiency results for irradiated modules are discussed, followed by the charge collection efficiency results.

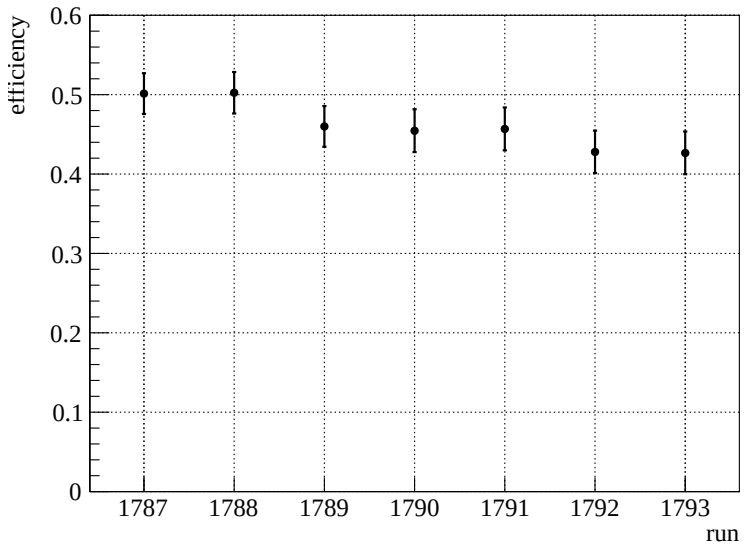

Figure 7.5: Efficiency per run of the group with pixel design V6 for the proton irradiated module R8 ($1 \times 10^{15}\,\mathrm{n_{eq}/cm^2}$, Birmingham). The temperature increased from $-42.7\,^{\circ}\mathrm{C}$ to $-35.2\,^{\circ}\mathrm{C}$ (measured closely to the modules) over 7 runs resulting in an increase in leakage current and drop in efficiency.

7.3.1 Hit Detection Efficiency Results

The first inspection of reconstructed and analyzed data in TBmon2 is done by checking the hit, track and efficiency maps of the full sensor for anomalies. For homogeneously irradiated modules the efficiencies between different pixel design groups might disagree, however, per pixel design group the performance is expected to be uniform. Striking features can be observed in the efficiency maps of all modules irradiated with protons in Birmingham. These modules, **R6** ($5 \times 10^{15}\,\mathrm{n_{eq}/cm^2}$), **R8** ($1 \times 10^{15}\,\mathrm{n_{eq}/cm^2}$) and **R12** ($5 \times 10^{15}\,\mathrm{n_{eq}/cm^2}$), were tested in test beam campaigns in October 2018 at CERN and December 2018 at DESY. In Figure 7.6 the efficiency map for module R12, biased with 400 V is presented (Tuning: 1600 e, 6 ToT at 20 ke.) A rectangular area in the central region of the module shows a higher efficiency which is also visible for modules R6 and R8 (Appendix C, Figures C.1 and C.2). The higher efficiencies in the central area have been verified to not be a result of tuning, particle beam or sensor feature. After consulting the Irradiation Facility Birmingham it became clear that a wrong shielding object not covering the full module was used during the irradiation of the three modules. Therefore, the regions with lower efficiencies were irradiated to a higher fluence by low energetic beam components and only the central area was irradiated to the target fluence. Consequently, no comparison between results of these modules' pixel design groups

to results of other modules is possible and they are not further analyzed in this work.

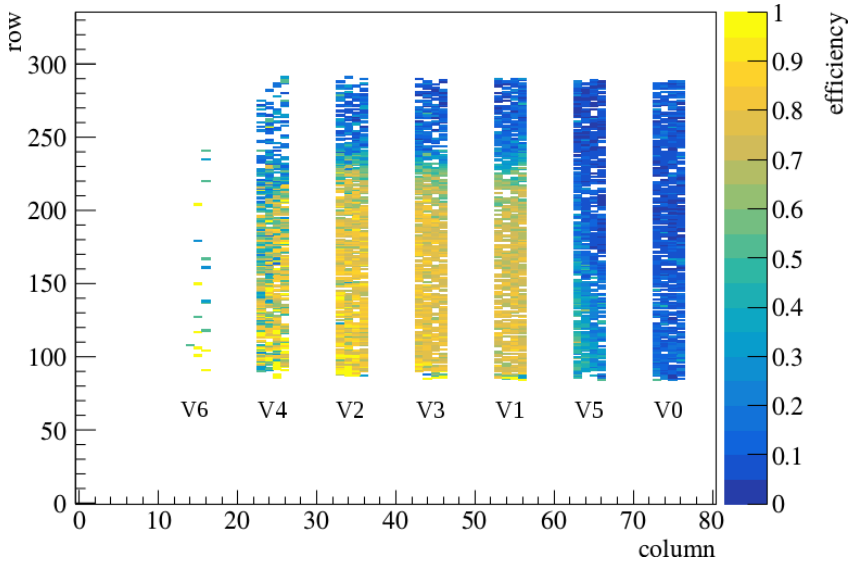

Figure 7.6: Efficiency map for the proton irradiated module R12 ($5 \times 10^{15}\,\mathrm{n_{eq}/cm^2}$, Birmingham) biased with 400 V.

For the remaining modules, high hit detection efficiencies are expected for all irradiated pixel design variations for fully depleted sensors. This assumption is validated with the results for the remaining modules: As an example, the hit detection efficiency results for the groups with different pixel designs of modules **R1**, **R2**, **R3** and **R7** at high bias voltages are presented in Figure 7.7. For modules **R5** and **R9** which are irradiated to the same target fluence at the same irradiation facility as modules R3 and R7, the results are left out since these modules show the same behavior as modules R3 and R7. For the presented results the modules are tuned to a threshold of 3200 e and a ToT response of 6 at a reference charge of 20 ke. Only module R2 is measured at a lower threshold of 1600 e so that a higher level of efficiency is expected for this module compared to the others. For the presented comparison, the irradiated modules R1, R3 and R2 are biased with 1000 V and module R7 with 600 V. Overall, high particle detection efficiencies are reached at these high bias voltages for all pixel design groups, independent of their tuning. As expected, higher irradiated modules show lower efficiency levels compared to lower irradiated modules. In this comparison, the highest particle detection efficiency is reached by pixel design V0 of module R7 ($1 \times 10^{15}\,\mathrm{n_{eq}/cm^2}$) of $\left(99.7^{+0.2}_{-0.4}\right)$ % and the lowest by design V6 of module R3 ($5 \times 10^{15}\,\mathrm{n_{eq}/cm^2}$) of $\left(91.8^{+0.4}_{-1.0}\right)$ %.
As a reference the ITk criterion requires a hit detection efficiency at 600 V to be

more than 97 % for 150 µm thick modules after irradiation[85]. Such high particle detection efficiencies after irradiation are reached by almost all pixel designs of the investigated REINER pixel modules with a thickness of 200 µm but at bias voltages higher than 600 V.

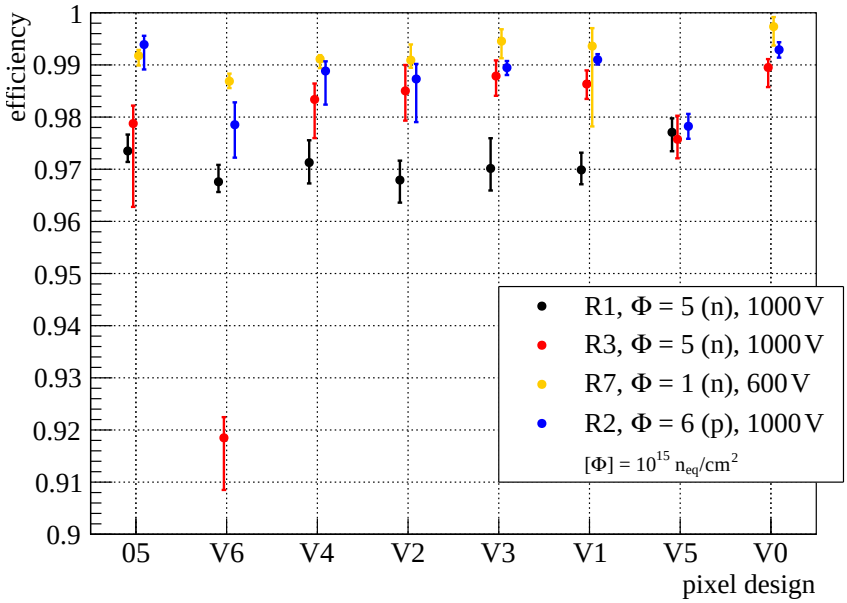

Figure 7.7: Efficiencies of the different pixel design groups at higher bias voltages of the irradiated modules R1, R3, R7 and R2.

At these high bias voltages only small variations in the performance of the groups with different pixel designs are observable: For module R1 the pixel design V5 reaches slightly higher particle detection efficiencies, while for modules R2, R3, R5, R7 and R9 the efficiencies of pixel designs V5 and V6 are lower compared to all other designs. These differences in efficiency are even more pronounced at lower bias voltages and will be discussed in more detail in section 7.4.2.

7.3.2 Charge Collection Efficiency Results

For **all irradiated modules** investigated in this thesis, the mean ToT increases with bias voltage for all pixel design groups and no plateau or saturation value is reached. As an example, the mean ToT values for the different pixel designs of the proton irradiated module R2 (6×10^{15} n_{eq}/cm^2, CERN) measured at four different bias voltages in the test beam campaign at CERN in July 2017 are presented in

Figure 7.8 (Tuning: 1600 e, 6 ToT at 20 ke).
As described in Chapter 6.2.3 the mean ToT value is calculated from all hits with cluster size one and its deviation is indicated as error bars. The standard deviation of the ToT values increases for irradiated samples since the distribution of ToT values is broader and more entries are stored in the overflow bin 14. Consequently, the deviation from the mean value, is larger compared to non-irradiated ToT results. As a result, differences in the mean ToT values between different designs are often not significant.

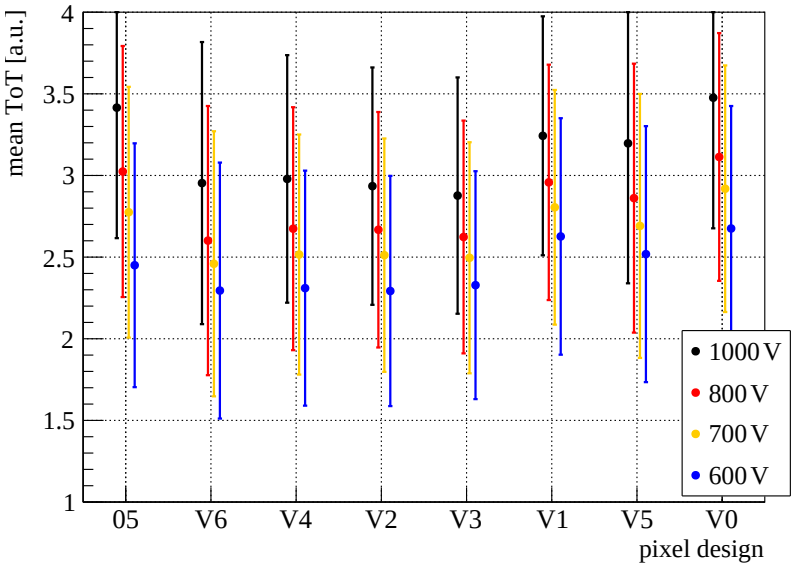

Figure 7.8: Mean ToT values for cluster size one for the different pixel design groups for the proton irradiated module R2 (6×10^{15} n_{eq}/cm^2, CERN) measured at different bias voltages.

The different pixel designs are intended to increase the electric field and thus measure higher charge after irradiation. Consequently, differences in the charge collection efficiency after irradiation are expected.
For the proton irradiated module **R2** (6×10^{15} n_{eq}/cm^2, CERN), the standard designs measure slightly more charge compared to all other designs as visible in Figure 7.8. At higher bias voltages these differences are more noticeable: At 1000 V the highest mean ToT value of 3.4 ± 0.8 is determined for the standard pixel design while the lowest value of 2.9 ± 0.7 is measured for design V3.
It must be taken into account that module R2 is irradiated inhomogeneously and the outermost pixel designs 05 and V0 are irradiated to a lower fluence compared to all other designs. Therefore, a direct comparison of the performance between the different pixel designs might be misleading. It is not clear if the higher charge

generated for the standard pixel designs in comparison to all other designs is an effect of the lower irradiation fluence of these designs. Furthermore, the higher charge for the standard design might be an effect caused by the particles used for irradiation since the neutron irradiated modules show different results: The charge collection efficiency results for neutron irradiated modules show a special behavior for pixel designs V5 and V6 and are presented in more detail in section 7.4.3.

7.4 Remarkable Results of Pixel Designs V5 and V6

The groups with pixel designs V5 and V6 of any irradiated module show different results compared to all other designs, especially after neutron irradiation. For this reason, the different results between the standard design 05 and designs V5 and V6 are discussed in the following section in more detail.

7.4.1 Individual IV Measurements

In the IV measurements of the individual pixel design groups, some neutron irradiated samples show a special behavior for pixel design group V5. As exemplary presented in Figure 7.9 for module **R1** ($5 \times 10^{15}\,\mathrm{n_{eq}/cm^2}$, Sandia), pixel design V5 measures higher leakage currents compared to all other designs at a given bias voltage. A similar behavior is observable for the lower neutron irradiated samples **R7** and **R9**, both irradiated to $1 \times 10^{15}\,\mathrm{n_{eq}/cm^2}$ at Ljubljana, which can be found in Appendix B, Figures B.4 and B.5. Against the assumption that this effect is related only to the particle type used for irradiation (neutrons), higher leakage currents for design V5 are not visible for the two highly neutron irradiated modules R3 and R5, both irradiated in Ljubljana to $5 \times 10^{15}\,\mathrm{n_{eq}/cm^2}$, and all proton irradiated samples (see Appendix B, Figures B.2 to B.3 and Figures B.6 to B.8).
This could be a first indication of a change in electric field of pixel design V5 with increasing neutron irradiation fluence for Ljubljana irradiated samples. In addition, the different results between samples that are highly neutron irradiated at Sandia and in Ljubljana might result from different irradiation conditions.

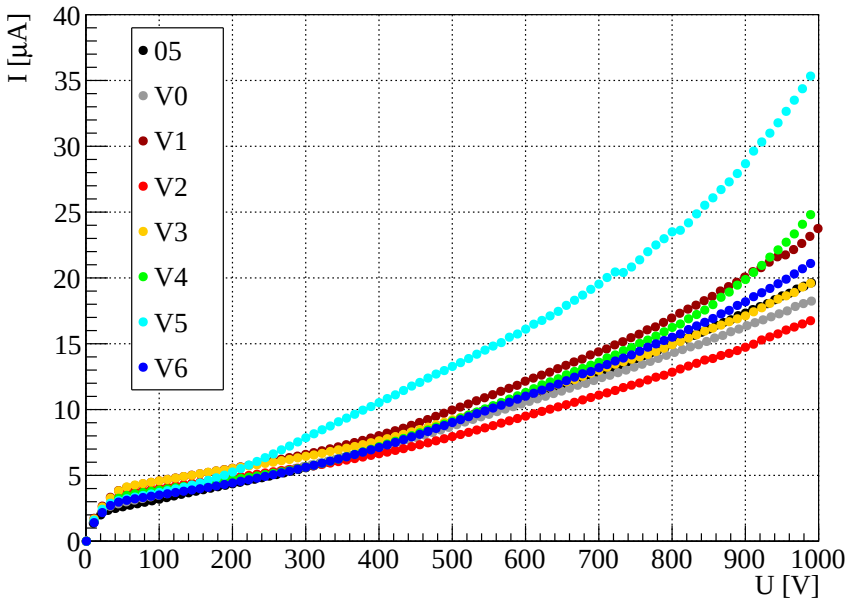

Figure 7.9: IV measurement of the individual pixel design groups of the neutron irradiated module R1 ($5 \times 10^{15}\,\mathrm{n_{eq}/cm^2}$, Sandia). The leakage current is normalized to a sensor temperature of $-30\,^{\circ}\mathrm{C}$.

7.4.2 Hit Detection Efficiency Results

The maximum bias voltage to investigate the hit detection efficiency is limited by noise which increases with bias voltage due to charge multiplication effects. The maximum bias voltage for the lower neutron irradiated modules **R7** and **R9** (both $1 \times 10^{15}\,\mathrm{n_{eq}/cm^2}$, Ljubljana) for pixel design V5 is reached at 200 V. For higher bias voltages, pixel design V5 often shows no results for these modules as the majority of pixels became noisy and the complete group had to be masked. This is consistent with the IV curves of these modules showing a steep increase in leakage current for design V5 starting at 280 V (see Appendix B, Figures B.4 and B.5). At the highest measured bias voltage of 200 V pixel design V5 of module R7 reaches an efficiency of about $\left(97.3^{+0.5}_{-1.5}\right)$ % (Tuning: 1600 e, 6 ToT 20 ke).
These results might indicate higher electric fields and charge multiplication effects for pixel design V5 after low neutron irradiations to $1 \times 10^{15}\,\mathrm{n_{eq}/cm^2}$ in Ljubljana.

At low bias voltages, the electric field inside the sensor influences the shape and expansion of the depletion zone which does not cover the sensor's full thickness. Consequently, for pixel designs with enlarged electric fields, higher hit detection efficiencies for not fully depleted sensors are expected.

At first, the results for the proton irradiated module R2 and all at Ljubljana neutron irradiated modules are presented. Afterwards, the results for module R1, neutron irradiated at Sandia, are discussed which are contrary to the ones of the other modules.
At low bias voltages and independent of the module tuning, the two groups with narrowed pixel designs V5 and V6 always measure lower efficiencies compared to all other designs for the proton irradiated module **R2** ($6 \times 10^{15}\,\mathrm{n_{eq}/cm^2}$, CERN) and all Ljubljana neutron irradiated modules, **R3** ($5 \times 10^{15}\,\mathrm{n_{eq}/cm^2}$), **R5** ($5 \times 10^{15}\,\mathrm{n_{eq}/cm^2}$), **R7** ($1 \times 10^{15}\,\mathrm{n_{eq}/cm^2}$) and **R9** ($1 \times 10^{15}\,\mathrm{n_{eq}/cm^2}$). For these modules exemplary results at lower bias voltages for the different pixel design groups are presented in Figure 7.10. Each module's results are shown for the lowest investigated threshold at the lowest measured bias voltage: The tuning parameters and bias voltages are summarized in Table 7.3. Due to the different tunings and bias voltages, the performance of the different pixel design groups can only be compared per module. The numerical efficiency values for these results for pixel designs 05, V0, V5 and V6 are summarized in Table 7.4.

Table 7.3: Tuning parameters and bias voltages per module for investigations at lower bias voltages for which the results are presented in Figure 7.10 and Table 7.4. The particle fluence for irradiation is indicated in $[\Phi] = 1 \times 10^{15}\,\mathrm{n_{eq}/cm^2}$ and the particle type with (n) for neutrons and (p) for protons.

module	tuning threshold, ToT	bias voltage [V]
R3, $\Phi = 5$ (n)	1600 e, 6 ToT 20 ke	300 V
R5, $\Phi = 5$ (n)	2000 e, 6 ToT 20 ke	400 V
R7, $\Phi = 1$ (n)	1000 e, 10 ToT 10 ke	100 V
R9, $\Phi = 1$ (n)	1000 e, 10 ToT 10 ke	100 V
R2, $\Phi = 6$ (p)	1600 e, 6 ToT 20 ke	600 V

The standard pixel designs 05 and V0 reach highest hit detection efficiencies for all these modules. In addition, the results in Table 7.4 show similar values for both standard design groups 05 and V0 per module as expected. Both pixel designs with narrowed implantations V5 and V6 perform worst in all these modules: The largest difference between design V5 and the standard design 05 of about 13.1 % points is determined for module R2. For pixel design V6 and the standard design 05, the largest difference in efficiency of about 27.5 % points is observed for module R3.

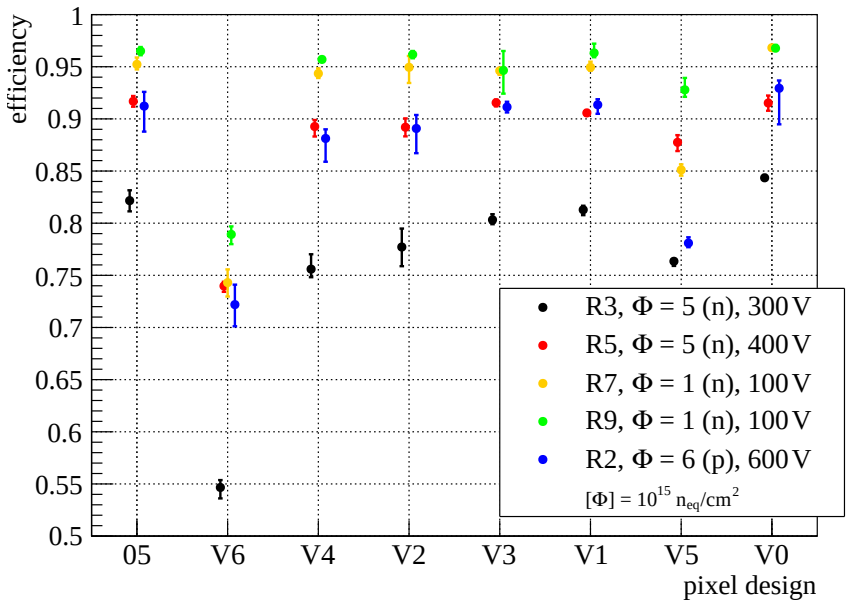

Figure 7.10: Efficiencies of the different pixel design groups at lower bias voltages of the irradiated modules R3, R5, R7, R9 and R2. The modules are tuned to different threshold values and ToT responses which can be found in table 7.3.

Table 7.4: Efficiencies of the standard pixel designs 05 and V0, together with the results for designs V5 and V6 for the neutron irradiated modules R3, R5, R7, R9 and the proton irradiated module R2 at lower bias voltages. See Table 7.3 for the corresponding tuning parameters.

module	bias voltage [V]	efficiency [%] 05	V0	V6	V5
R3, $\Phi = 5$ (n)	300	$82.2^{+1.0}_{-1.0}$	$84.3^{+0.3}_{-0.2}$	$54.7^{+0.7}_{-1.1}$	$76.3^{+0.2}_{-0.4}$
R5, $\Phi = 5$ (n)	400	$91.7^{+0.5}_{-0.5}$	$91.5^{+0.7}_{-0.7}$	$74.0^{+0.4}_{-0.6}$	$87.8^{+0.7}_{-0.8}$
R7, $\Phi = 1$ (n)	100	$95.2^{+0.7}_{-0.5}$	$96.8^{+0.2}_{-0.1}$	$74.3^{+1.3}_{-1.3}$	$85.1^{+0.5}_{-0.6}$
R9, $\Phi = 1$ (n)	100	$96.5^{+0.4}_{-0.4}$	$96.8^{+0.3}_{-0.2}$	$78.9^{+0.8}_{-0.9}$	$92.8^{+1.1}_{-0.7}$
R2, $\Phi = 6$ (p)	600	$91.2^{+1.4}_{-2.4}$	$92.9^{+0.7}_{-3.5}$	$72.2^{+1.9}_{-2.1}$	$78.1^{+0.6}_{-0.4}$

It seems like the depletion zones of pixel designs with narrowed implantations are smaller compared to the standard design after irradiation with neutrons and protons so that the efficiency is reduced. The lateral expansion of the depletion zone for the different pixel designs can be investigated in more detail with in-pixel efficiency maps for not fully depleted sensors. It is expected that the standard pixel design shows a uniform efficiency over the pixel area due to its pixel layout. For the other, new designs, regions with higher efficiencies located at electric field strength maxima might be visible.
In Figure 7.11 the in-pixel efficiency maps for all pixel designs of module **R3** are presented for a bias voltage of 300 V (Tuning: 1600 e, 6 ToT at 20 ke). The in-pixel efficiency maps for modules **R5** and **R2** show large similarities to the presented one of module R3 and can be found in Appendix C, Figures C.10 and C.11.
Except for the pixel designs with narrowed implantations, all in-pixel efficiency maps of the different pixel designs show large similarities to the one of the standard design: A high detection efficiency of about 90 % is measured for most of the pixel area with a significant decrease to about 66 % at the edges. This reduced efficiency at the edges might be related to charge sharing effects: The generated charge by a traversing particle is induced in two neighboring pixels. If the distributed charge is below the threshold value, no hit is detected and an inefficiency is determined for track positions close to pixel edges. In pixel designs V5 and V6 the central region with high efficiency of about 89 % (V5) and 84 % (V6) is narrowed. At the edges, the efficiency drops faster to about 53 % for design V5 and to about 14 % for design V6. To illustrate the efficiency performance in the central regions for these pixel designs, vertical profiles of the in-pixel efficiency maps at local x = 125 µm are presented on the left in Figure 7.13. The profile positions are indicated as dashed lines in the in-pixel efficiency maps in Figure 7.11.
Consequently, the lower efficiency values for both pixel designs with narrowed implantations can be traced to significant inefficiencies at the pixel edges for the highly irradiated modules R3 ($5 \times 10^{15}\,\mathrm{n_{eq}/cm^2}$, Ljubljana), R5 ($5 \times 10^{15}\,\mathrm{n_{eq}/cm^2}$, Ljubljana) and R2 ($6 \times 10^{15}\,\mathrm{n_{eq}/cm^2}$, CERN).

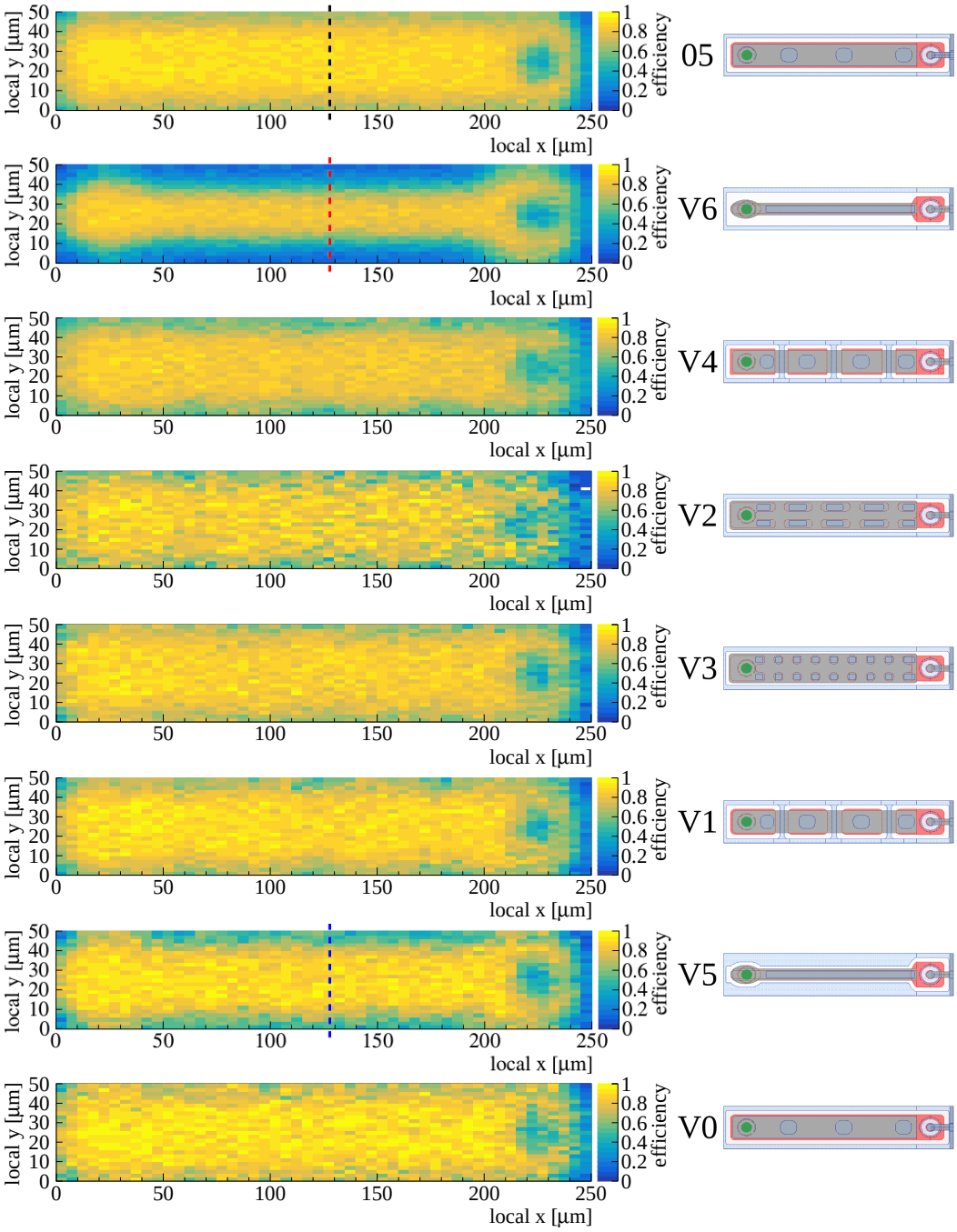

Figure 7.11: In-pixel efficiency maps of the neutron irradiated module R3 (5×10^{15} n_{eq}/cm^2, Ljubljana), biased with 300 V. On the right schematic layouts illustrate the corresponding pixel designs. The order from top to bottom corresponds to the order on the module: 05, V6, V4, V2, V3, V1, V5, V0. Vertical dashed lines for pixel designs 05, V6 and V5 illustrate the profile positions used in Figure 7.13 (left).

In contrast to the previously presented results, the in-pixel efficiency maps of pixel design V5 for the lower neutron irradiated modules **R7** and **R9** (1×10^{15} n_{eq}/cm^2, Ljubljana) show a more homogeneously distributed efficiency but lower absolute efficiency values compared to their standard designs. In addition, the efficiency drop at the edges for all pixel designs is smaller for these lower irradiated modules compared to the higher irradiated ones.
Figure 7.12 shows the in-pixel efficiency maps for pixel designs 05, V6 and V5 of module R7 while the corresponding profiles at local x = 125 µm are illustrated on the right side in Figure 7.13. For these results, module R7 is biased with 100 V and tuned to the lowest measured threshold of 1000 e, 10 ToT at 20 ke. The in-pixel efficiency maps for all different pixel design groups of modules R7 and R9 can be found in Appendix C, Figures C.12 and C.13.
These results show that a higher radiation fluence reduces the efficiency for all pixel designs especially at the edges towards neighboring pixels. For the pixel designs with narrowed implantations, V5 and V6, this reduction in efficiency at the edges is more pronounced compared to the standard design.

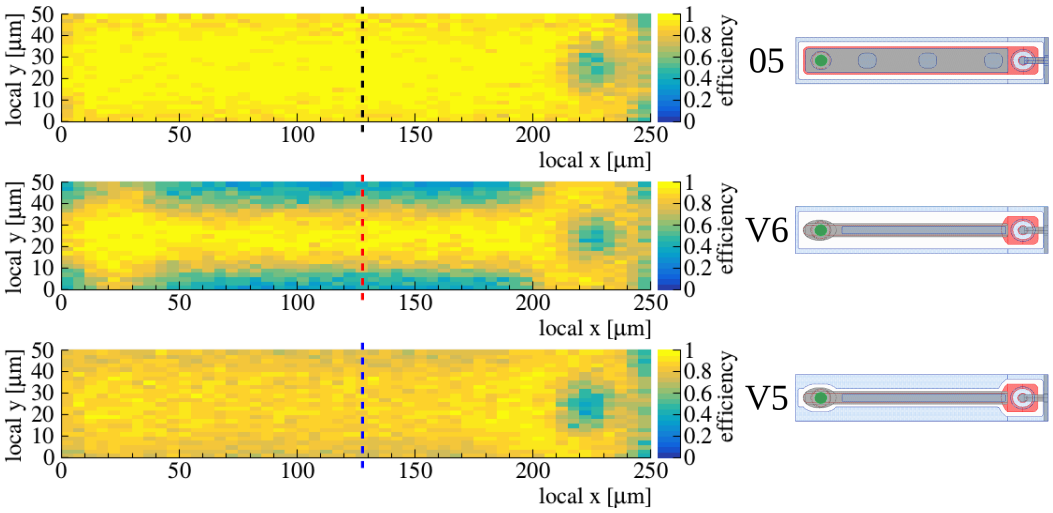

Figure 7.12: In-pixel efficiency maps of the neutron irradiated module R7 (1×10^{15} n_{eq}/cm^2, Ljubljana) at a bias voltage of 100 V. The order from top to bottom is 05, V6 and V5. Vertical dashed lines illustrate the profile positions used in Figure 7.13 (right).

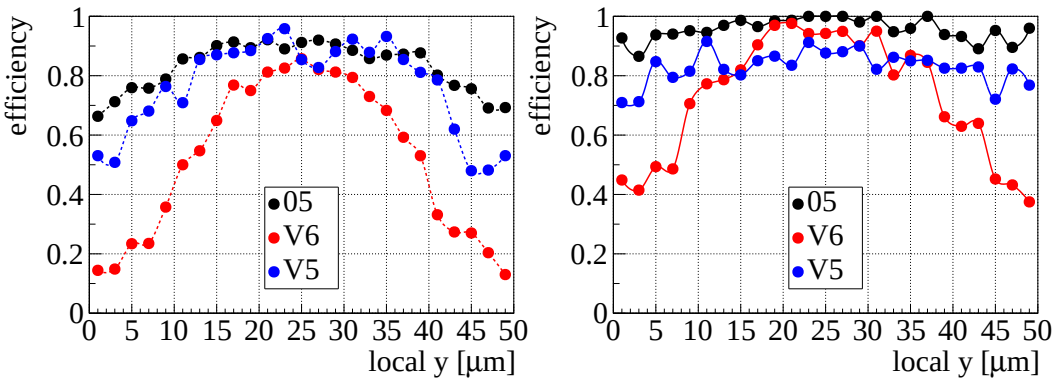

(a) R3 **(b)** R7

Figure 7.13: Profiles of the in-pixel efficiency maps at local x = 125 µm of the pixel design groups 05, V6 and V5 for the neutron irradiated module R3 ($5 \times 10^{15}\,\mathrm{n_{eq}/cm^2}$) at 300 V on the left and for the neutron irradiated module R7 ($1 \times 10^{15}\,\mathrm{n_{eq}/cm^2}$) at 100 V on the right side.

The presented results of modules R3, R5, R7, R9 and R2 showed highest hit detection efficiencies for the standard designs whereas pixel designs V5 and V6 showed lowest. In contrast, pixel design V5 of the at Sandia neutron irradiated module **R1** ($5 \times 10^{15}\,\mathrm{n_{eq}/cm^2}$) reaches highest efficiencies for this module at all bias voltages: As an example, Figure 7.14 presents these contrary results of module R1 together with the results of module R3. Both modules are neutron irradiated to a fluence of $5 \times 10^{15}\,\mathrm{n_{eq}/cm^2}$ and biased with 400 V. For these measurements module R1 is tuned to a higher threshold of 3200 e while for module R3 a lower threshold tuning of 1600 e, 6 ToT at 20 ke is used. Consequently, higher levels of efficiency for the pixel designs on module R3 are expected because of the lower threshold value. However, the highest efficiency in this comparison is reached by pixel design V5 of module R1 with $\left(97.2^{+0.3}_{-0.2}\right)$ %. For the standard design of module R1 such high hit detection efficiencies are only reached at much a higher bias voltage. The second highest efficiency on module R1 is reached by design V6 with $\left(75.7^{+0.9}_{-1.2}\right)$ % while the standard design 05 performs worst with $\left(62.9^{+0.7}_{-0.8}\right)$ %. No data is available for the standard design V0 of this module as it was not covered by the test beam spot. These higher detection efficiencies of pixel designs V5 and V6 on module R1 result from higher efficiencies at the corners and edges of the n^+-implantations as illustrated in the in-pixel efficiency maps of all designs at 400 V in Figure 7.15 (Tuning: 3200 e, 6 ToT at 20 ke). All in-pixel efficiency maps of modified pixel designs show such areas with higher efficiency values. Only for pixel design V5 a high and uniform detection efficiency over the full pixel size of about 97 % without decreases at the pixel edges is visible. The lower efficiencies of the standard design 05 is a conse-

quence of lower efficiencies of about 45 % in the pixel center. Towards neighboring pixels the efficiency for the standard design increases to about 71 %. The profiles at a local x = 125 µm of the in-pixel efficiency maps for these designs in Figure 7.16 clarify the described differences in hit detection efficiency for the central pixel area. For pixel regions with higher efficiencies the depletion zone seems to be broader already at lower bias voltages. This might result from higher electric fields from the p-n junctions at the corners and edges of the n^+-implantations after high neutron irradiation at Sandia.

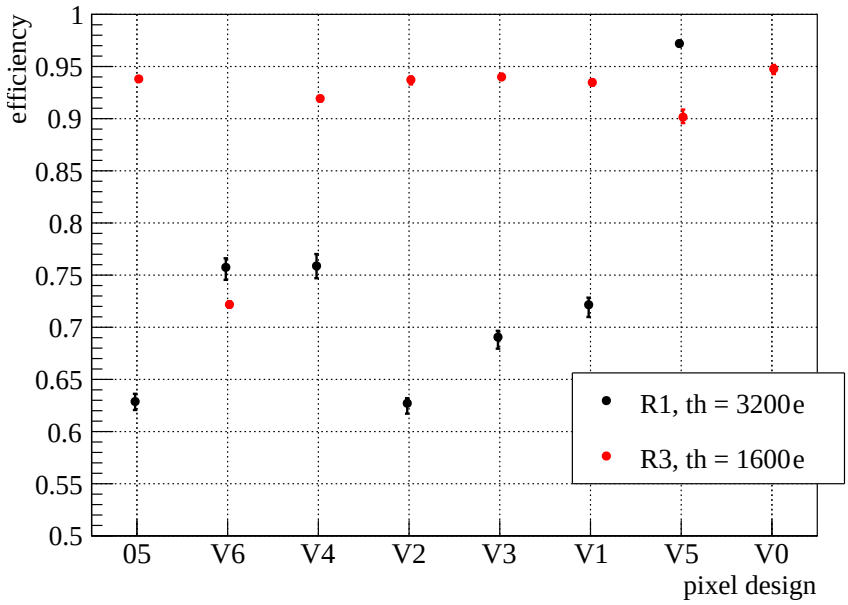

Figure 7.14: Efficiencies of the different pixel design groups at 400 V of the neutron irradiated modules R1 ($5 \times 10^{15}\,n_{eq}/cm^2$, Sandia) and R3 ($5 \times 10^{15}\,n_{eq}/cm^2$, Ljubljana).

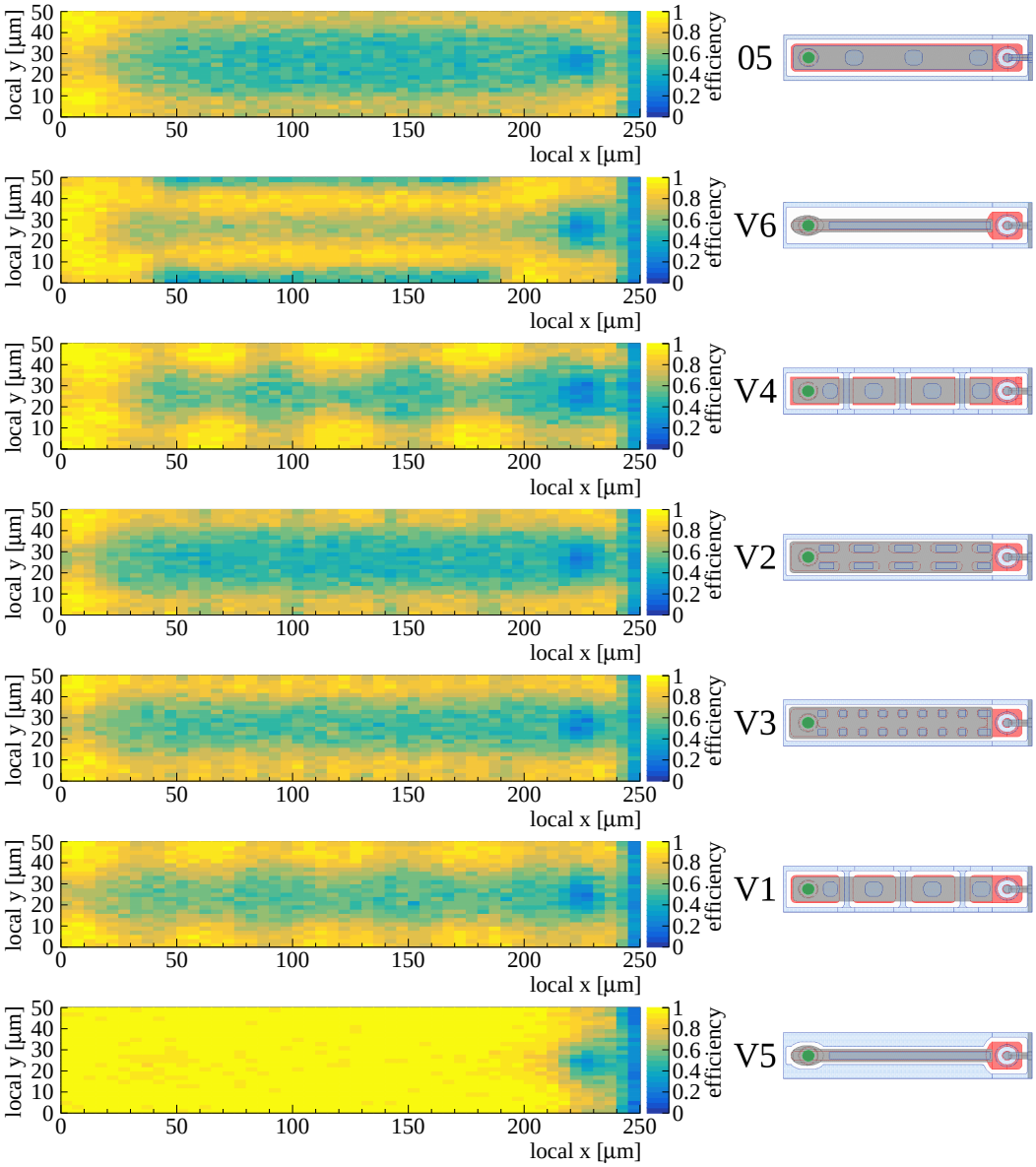

Figure 7.15: In-pixel efficiency maps of the neutron irradiated module R1 ($5 \times 10^{15}\,\mathrm{n_{eq}/cm^2}$, Sandia), biased with 400 V. The order from top to bottom corresponds to the order on the module: 05, V6, V4, V2, V3, V1, V5.

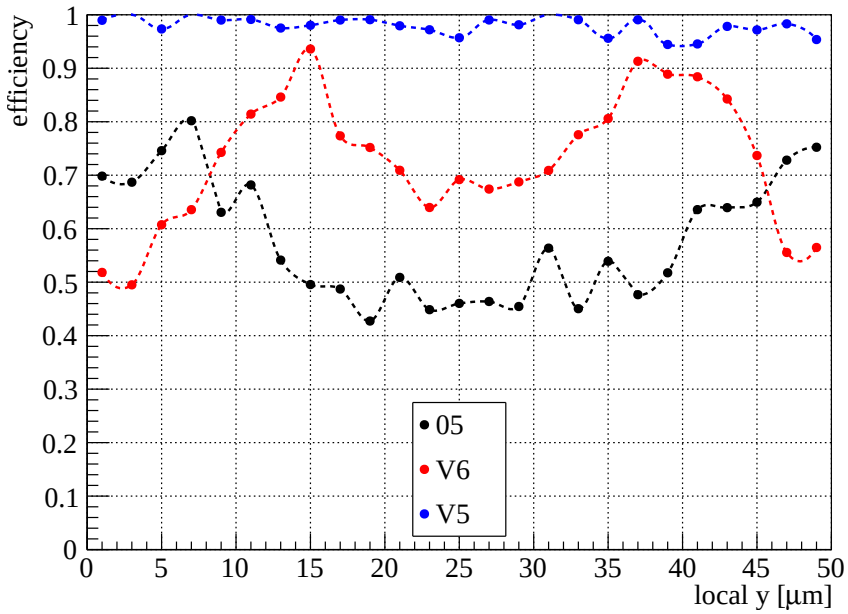

Figure 7.16: Profiles of the in-pixel efficiency maps at local x = 125 µm of the pixel design groups 05, V6 and V5 for the neutron irradiated module R1 (5×10^{15} n_{eq}/cm^2, Sandia), biased with 400 V.

To check if these higher electric fields also promote charge multiplication at the edges of the n^+-implant of designs V5 and V6, the charge collection results are presented in the following section.

7.4.3 Charge Collection Efficiency Results

For the proton irradiated module **R2**, only slightly more charge is measured for the standard designs compared to the other ones as already presented in Figure 7.8. However, large differences in the in-pixel ToT maps between the standard designs and the designs with narrowed implantations, V5 and V6, are observable: The collected charge is highest in those regions of the pixel which show higher hit detection efficiencies. This is visible in Figure 7.17 presenting the in-pixel ToT results of the proton irradiated module R2 at 1000 V for the standard design 05, design V6 and V5 (Tuning: 1600 e, 6 ToT at 20 ke). The highest ToT values of about 3.6 for the standard design and design V5, and of about 3.4 for design V6 are measured in the central region. Towards the edges the generated charge is reduced to about 3.2 for the standard design, to about 2.4 for design V5 and to about 2.1 for design V6. This reduction in generated charge is clearly observable

in the profile images of the in-pixel ToT maps at local x = 125 µm for these designs in Figure 7.18.
The reduced charge at the edges of the pixel designs might be a result of charge sharing between neighboring pixels. This charge sharing effect seems to be more pronounced for pixel designs V5 and V6.
The in-pixel ToT results of module R2 for all pixel designs can be found in Appendix C, Figure C.16.

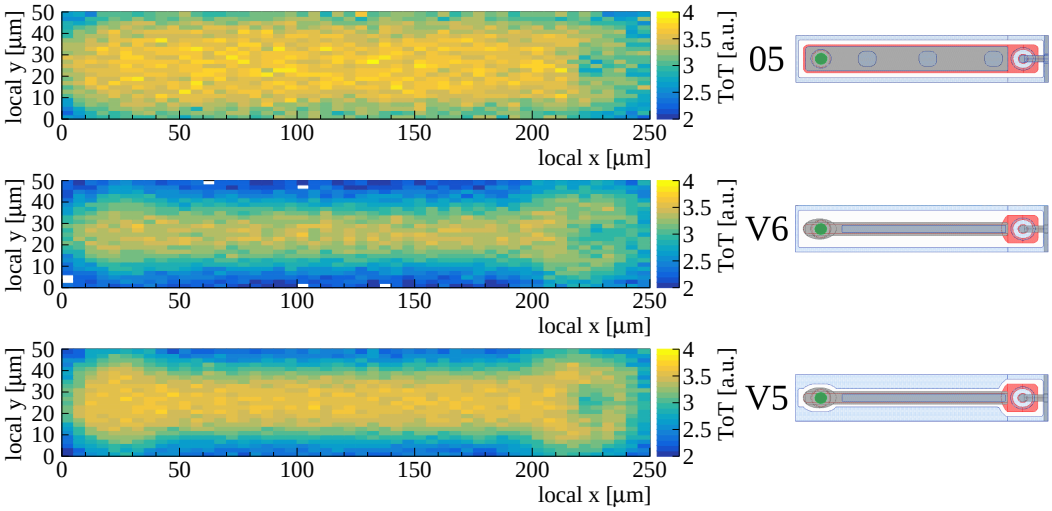

Figure 7.17: In-pixel ToT maps for cluster size one of groups with pixel design 05, V6 and V5 of the proton irradiated module R2 ($6 \times 10^{15}\,n_{eq}/cm^2$, CERN), biased with 1000 V. On the right schematic layouts illustrate the corresponding pixel designs.

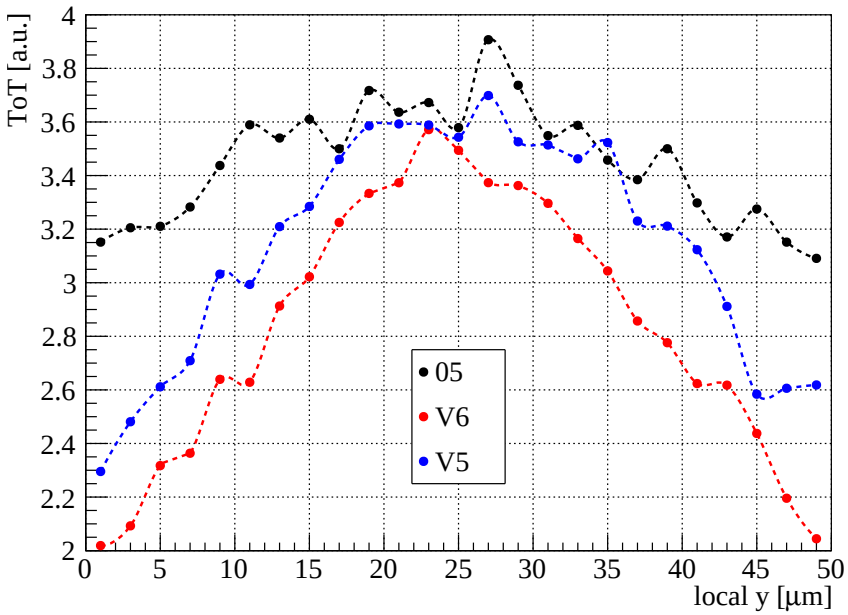

Figure 7.18: Profiles of the in-pixel ToT maps (cluster size one) at local x = 125 µm of the pixel design groups 05, V6 and V5 for the proton irradiated module R2 (6×10^{15} n_{eq}/cm^2, CERN), biased with 1000 V.

For all highly neutron irradiated modules, **R1**, **R3**, **R5**, pixel design V5 collects most charge for all bias voltages and tunings. As an example, the mean ToT values for cluster size one for the different pixel designs of module R1 measured at four different bias voltages are presented in Figure 7.19 (Tuning: 3200 e, 6 ToT at 20 ke). The largest differences in mean ToT are visible at the highest bias voltage of 1000 V: Pixel design V5 reaches a maximum ToT value of 6.9 ± 2.5 while the standard design 05 measures the lowest one of 4.5 ± 2.0.

For the lower neutron irradiated modules **R7** and **R9** (1×10^{15} n_{eq}/cm^2, Ljubljana), a dependency between the bias voltage and the generated charge of pixel design V5 compared to all other designs is visible: For bias voltages of 200 V and below this design with narrowed implantation generates charges similar to those of all other designs. For higher bias voltages it measures the highest ToT values. This observation is illustrated in Figure 7.20 presenting the mean ToT values for cluster size one of the different pixel designs of module R9 for a higher bias voltage of 400 V at a higher threshold value of 3200 e, 6 ToT at 20 ke and a lower bias voltage of 200 V and lower threshold value of 1600 e, 6 ToT at 20 ke.

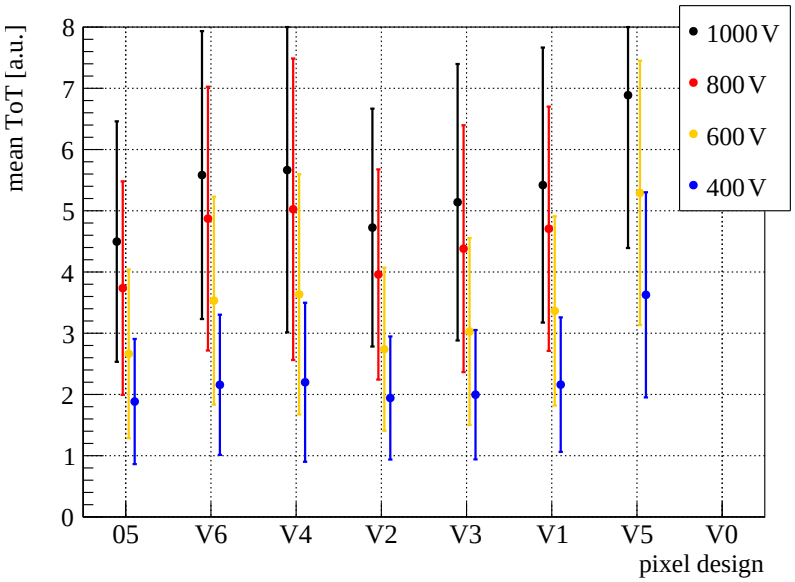

Figure 7.19: Mean ToT values for cluster size one for the different pixel design groups of the neutron irradiated module R1 ($5 \times 10^{15}\,\mathrm{n_{eq}/cm^2}$, Sandia) at four different bias voltages.

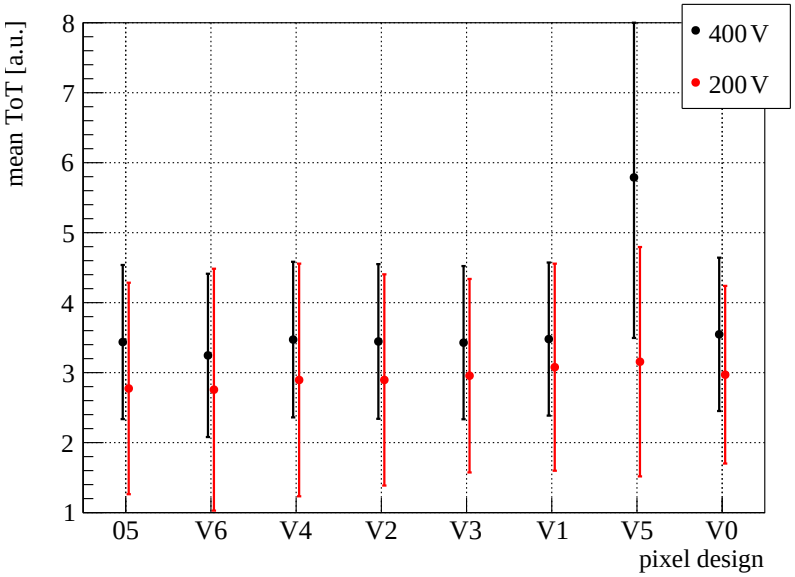

Figure 7.20: Mean ToT values for cluster size one for the different pixel design groups for the neutron irradiated module R9 ($1 \times 10^{15}\,\mathrm{n_{eq}/cm^2}$, Ljubljana) measured at two different bias voltages and tunings.

The measured higher charges for pixel design V5 for all neutron irradiated modules seem to result from charge multiplication effects at the corners and edges of the n^+-implantations. Higher charges are visible in Figure 7.21 showing the in-pixel ToT results for the two highly neutron irradiated modules R1 (left) and R3 (right). For this illustration, both modules are biased with 1000 V and tuned to threshold value of 3200 e, 6 ToT at a reference charge of 20 ke.
In module **R3**, the in-pixel ToT maps of designs V1 to V4 look similar to the one of the standard pixel design with a nearly homogeneously distributed ToT value of about 3.2 over the full pixel area and a small decrease to about 3.0 towards neighboring pixels. Only for the two designs with narrowed implantations on module R3 variations are visible: Design V6 measures a steeper decrease in generated charge towards neighboring pixels to about 2.5 while for design V5 higher ToT values are determined in the central region of about 4.6 to 5.1 with lower charges towards the edges of about 3.5.
For the comparison with the results of module **R1** in Figure 7.21, a different color scale for the ToT values of these two modules is necessary since for module R1 maximum mean ToT values of about 10.8 are measured while for module R3 the maximum value is about 5.4. Overall, the in-pixel ToT results of these two modules look slightly different: For module R1, higher ToT values for almost all pixel designs are observable at the corners and edges of the different pixel designs. Especially for pixel design V5, two areas with higher charges of about 7.4 to 8.5 extend along over almost the complete pixel long edge. Only in the pixel's center a small strip with lower ToT values of about 5.2 is visible.
The profiles at local x = 125 µm of designs 05, V6 and V5 for these two modules in Figure 7.22 allow for a better performance comparison in the central region.
The left-right asymmetry in these profile plots might result from small shifts (1 µm to 2 µm) of the different pixel layers during production so that the implant, metal or p-spray regions are not perfectly aligned. Only minimal asymmetries are visible in other, previously presented results which are probably caused by even smaller layer displacements.
Surprisingly, these two modules show different regions with higher charge collection efficiencies although they are measured at the same tuning and bias voltage. In addition, these two modules are both neutron irradiated to a high fluence of $5 \times 10^{15}\,n_{eq}/cm^2$. Consequently, different conditions during the irradiation at Sandia for module R1 and at Ljubljana for module R3 might have influenced the shape and strength of the electric fields so that the charge multiplication effects are more pronounced for module R1.

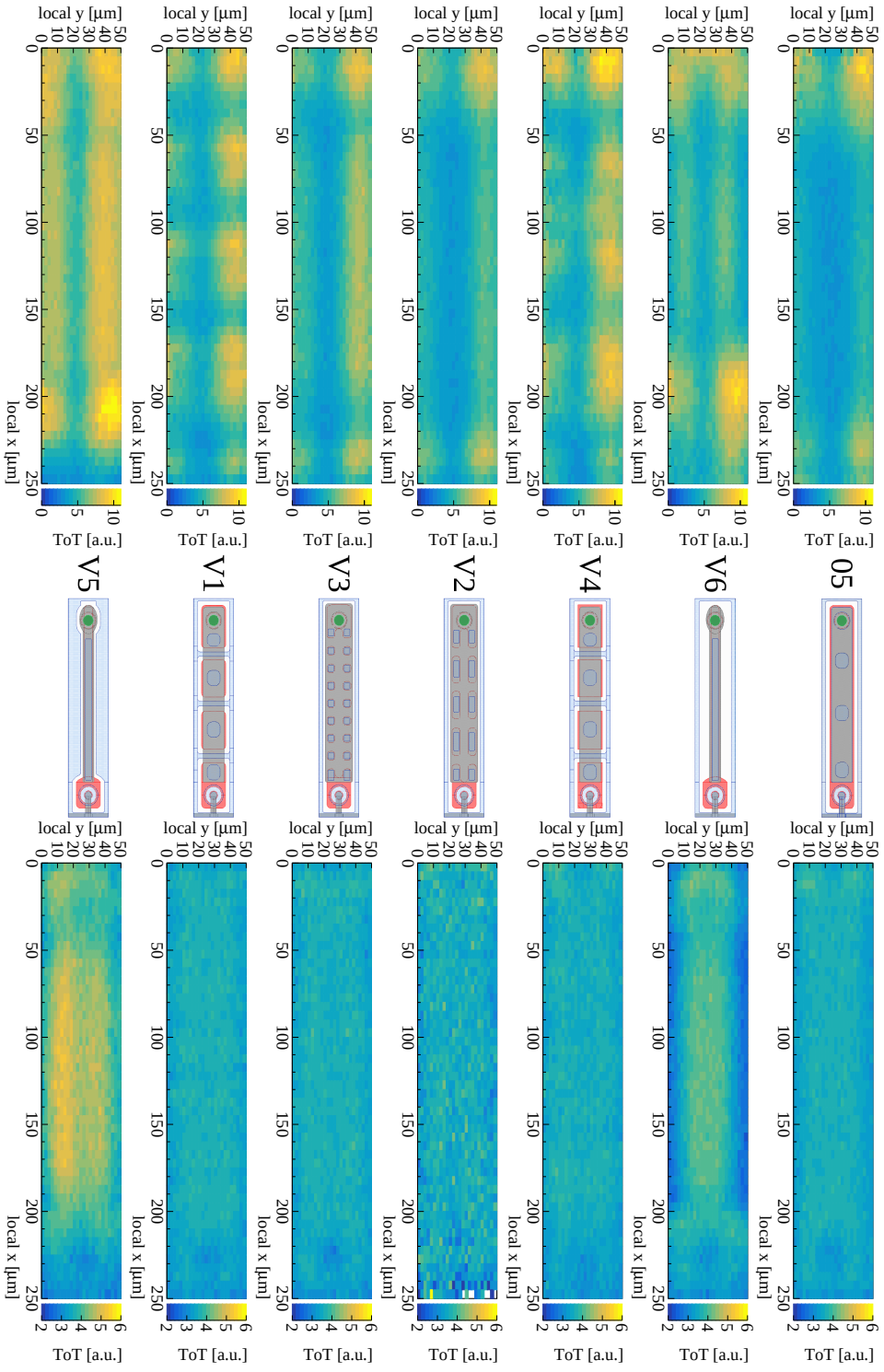

Figure 7.21: In-pixel ToT maps for cluster size one at 1000 V of the two neutron irradiated modules R1 (5×10^{15} n_{eq}/cm^2, Sandia) on the left and for module R3 (5×10^{15} n_{eq}/cm^2, Ljubljan) on the right. The order from top to bottom corresponds to the order on the module: 05, V6, V4, V2, V3, V1, V5.

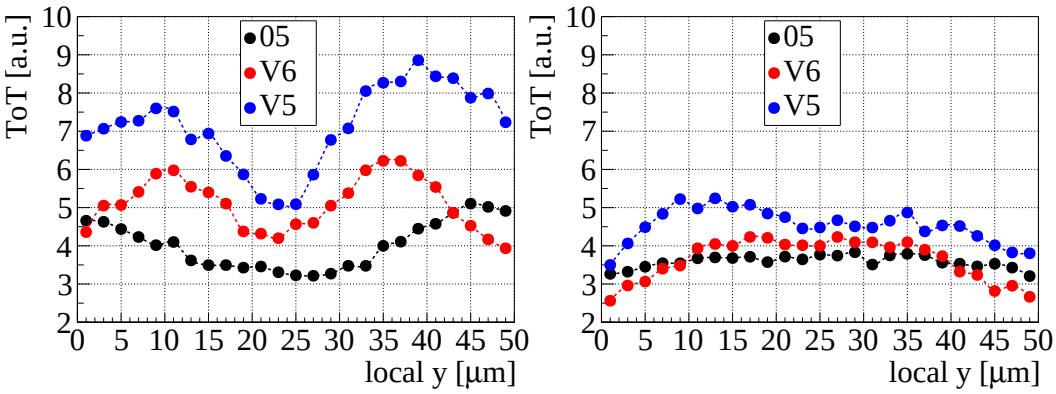

(a) R1 **(b)** R3

Figure 7.22: Profiles of the in-pixel ToT maps (cluster size one) at local x = 125 µm at 400 V of the pixel design groups 05, V6 and V5 for the two highly neutron irradiated modules R1 (5×10^{15} n_{eq}/cm^2, Sandia) on the left side and module R3 (5×10^{15} n_{eq}/cm^2, Ljubljan) on the right side.

The lower neutron irradiated modules **R7** and **R9** (1×10^{15} n_{eq}/cm^2, Ljubljana) show a significant higher charge in the central pixel with ToT values about 5.0 at high bias voltages for pixel design V5 while the standard design measures about 3.5. In addition, the charge increases towards neighboring pixels for design V5 to about 8.8 while for the standard design a reduction to about 3.3 is visible. For this reason a different color-scale range in the z-axis is necessary in the illustration of the in-pixel charge collection efficiency maps for design V5 of module R9 in Figure 7.23. The profile at local x = 125 µm is presented in Figure 7.24 to clarify the described differences in generated charge in the central area. For these results, module R9 is biased with 400 V and tuned to a threshold value of 3200 e, 6 ToT at a reference charge of 20 ke.

The in-pixel ToT results for the pixel designs V1-V4 of module R9 show large similarities to the presented standard design and can be found in Appendix C, Figure C.23.

Since no differences in the collected charge were observable for non-irradiated samples, the shape and strength of the electric field for pixel design V5 are influenced after low neutron irradiations in a way, that significantly higher charges are reached for this design compared to the standard design. Further neutron irradiation to high fluences diminishes these positives effects, however, higher charge compared to the standard design is still observable for design V5 for highly neutron irradiated samples.

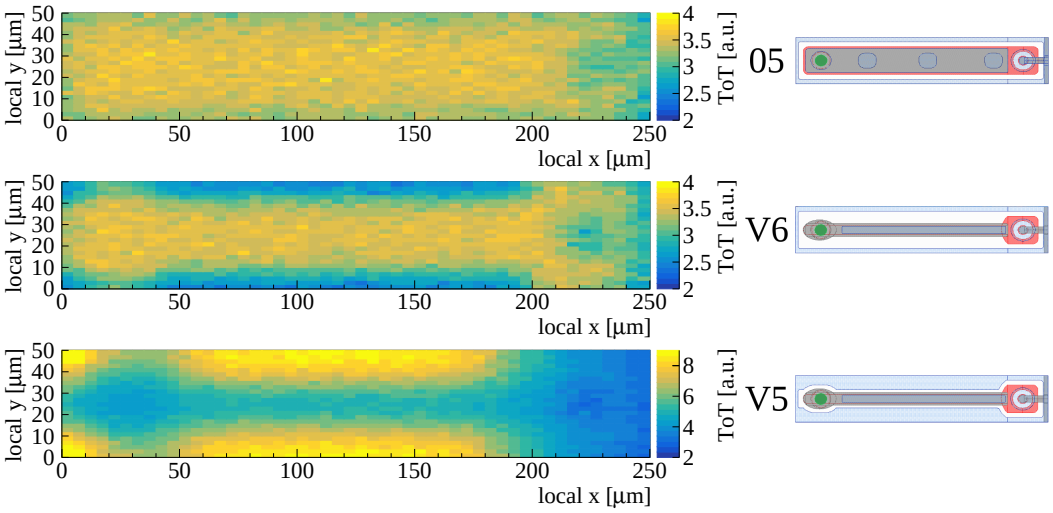

Figure 7.23: In-pixel ToT maps for cluster size one of the neutron irradiated module R9 ($1 \times 10^{15}\,\mathrm{n_{eq}/cm^2}$, Ljubljana) at 400 V. From top to bottom the in-pixel maps of groups with pixel designs 05, V6 and V5 on the left side and schematic layouts of the corresponding pixel designs on the right side are presented.

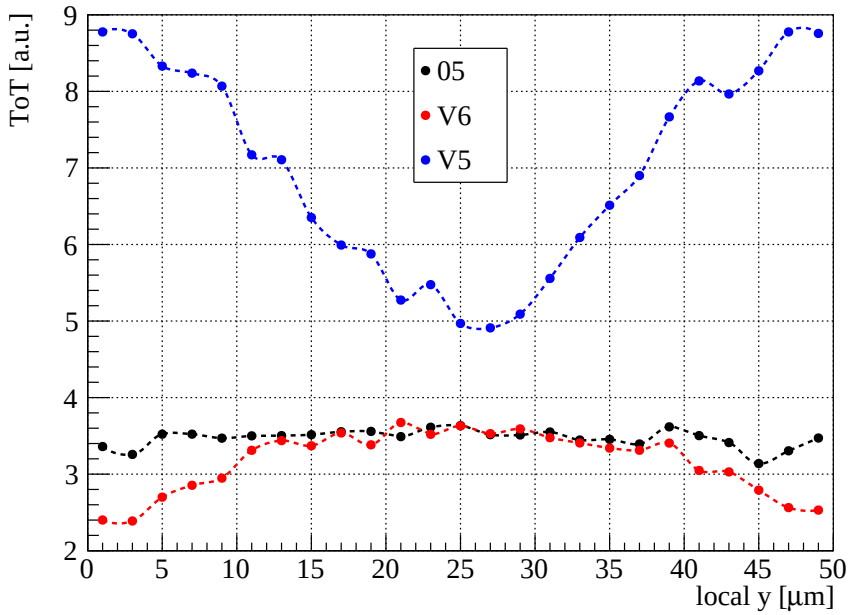

Figure 7.24: Profiles of the in-pixel ToT maps (cluster size one) at local x = 125 µm at 400 V of the pixel design groups 05, V6 and V5 for the neutron irradiated module R9 ($1 \times 10^{15}\,\mathrm{n_{eq}/cm^2}$, Ljubljana).

Over all neutron irradiated modules, the highest ToT values are measured for design V5. However, it is observed, that different parts of the pixels show the highest charge collection efficiency, depending on the actual sample: For module R1, increases in generated charge are visible for almost all pixel designs at the corners and edges of the n^+-implantations, while for module R3 designs V1 to V4 show nearly homogeneously distributed ToT values over the complete pixel area. For design V5 the results are consistent and both modules measured higher ToT values at similar positions in the pixel. For the lower neutron irradiated module R9 the in-pixel ToT maps showed similarities to the results of module R3. For design V5 of module R9 at high bias voltages the maximum ToT values are reached at the corners of the implantation and no decrease towards neighboring pixels is visible.

7.5 Summary and Discussion of the Results of irradiated REINER Pixel Modules

In total nine REINER pixel modules were irradiated at four different irradiation facilities to investigate the radiation hardness of the individual pixel designs. The proton irradiation of modules R6, R8 and R12 at Birmingham was unsuccessful so that only the central region was irradiated to the target fluence. Due to their inhomogeneous irradiation these modules are not analyzed further in this work.

The hit detection efficiency results for the remaining modules showed high particle detection efficiencies above 97 % for fully depleted sensors for all groups with different pixel designs. For the application in high energy physics experiments, a high particle detection efficiency even at lower bias voltages would be beneficial as the power dissipation is reduced and less heat must be compensated by the cooling system.
At lower bias voltages, variations in the performance of the different pixel designs were observed and the results for the various modules are contradictory: Only in module R1 pixel design V5 reaches highest hit detection efficiency while it performs second worst after V6 for the other modules. The lower particle detection efficiencies of pixel design V5 for modules R2 and R3 are caused by inefficiencies towards the edges of neighboring pixels which is not the case for design V5 on module R1 where a high particle detection efficiency is measured over the full pixel area.
In summary, the hit detection efficiency results of the proton irradiated module R2 match with the Ljubljana neutron irradiated modules R3, R5, R7 and R9. Only module R1, neutron irradiated at Sandia, shows a different hit detection performance. This module R1 might have been irradiated under different conditions which will be examined further with annealing studies in the following chapter.

The charge collection efficiency results from laboratory and test beam measurements showed that more charge is measured at higher bias voltages for all investigated modules.
For the inhomogeneously proton irradiated module R2 the standard designs irradiated to a lower particle fluence generate most charge. In contrast, for all neutron irradiated modules pixel design V5 measures the highest ToT values. Other studies found differences in collected charge after proton and neutron irradiations of not fully depleted sensors for n^+-in-p strip detectors as described in [124]. Consequently, it is not clear if the particle type used for irradiation influences the charge multiplication effect of pixel design V5 or if the discrepancies result from the inhomogeneous particle fluences.
Since increased ToT values for neutron irradiated modules are measured only for pixel design V5 and not for pixel design V6, this effect might be related to the enlarged p-spray profile rather than the reduced width pixel implant.
Furthermore, for the lower neutron irradiated modules ($1 \times 10^{15}\,n_{eq}/cm^2$) a dependency between the applied bias voltage and the performance of pixel design V5 is observed: For lower bias voltages design V5 measures charges similar to the other designs while for higher bias voltages it generates significantly more charge than these. It seems like an increase in bias voltage enlarges the electric field significantly for this design after low dose neutron irradiations. For higher neutron irradiated modules ($5 \times 10^{15}\,n_{eq}/cm^2$) pixel design V5 always measures the highest ToT values independent of bias voltages and irradiation facilities. A comparison of the in-pixel ToT maps of modules R9 ($1 \times 10^{15}\,n_{eq}/cm^2$) and R3 ($5 \times 10^{15}\,n_{eq}/cm^2$) shows that with increasing radiation fluence the generated charge decreases especially at the corners towards neighboring pixels for all pixel designs.

The irradiation fluences of $5 \times 10^{15}\,n_{eq}/cm^2$ and $1 \times 10^{15}\,n_{eq}/cm^2$ are higher than the type inversion fluence of $2 \times 10^{13}\,n_{eq}/cm^2$ for IBL sensors [125]. Consequently, the n-type bulks of the investigated modules are inverted and the electric fields inside the bulks have changed. *TCAD (Technology Computer Aided Design) simulations* were performed in other studies on the strength of the electric field with the sensor depth for IBL sensors as presented in Figure 7.25: For non-irradiated sensors, the electric field grows from the backside towards the pixel side with increasing bias voltage. Furthermore, the electric field strength is almost linear to the sensor depth for a fully depleted sensor (black). After type inversion and bias voltages below the depletion voltage, a minimum in electric field strength is reached in the center of the sensor bulk (green). With increasing bias voltages, the depletion regions develop from both sides of the sensor surfaces.

Differences in the efficiency performance of the different pixel designs for irradiated REINER pixel modules occur mainly at lower bias voltages (not fully depleted bulk) so that the characteristic of the electric field minimum in the center is apparently

influenced by the pixel designs. So far, no TCAD simulations to evaluate the electric field of irradiated REINER pixel modules have been performed.

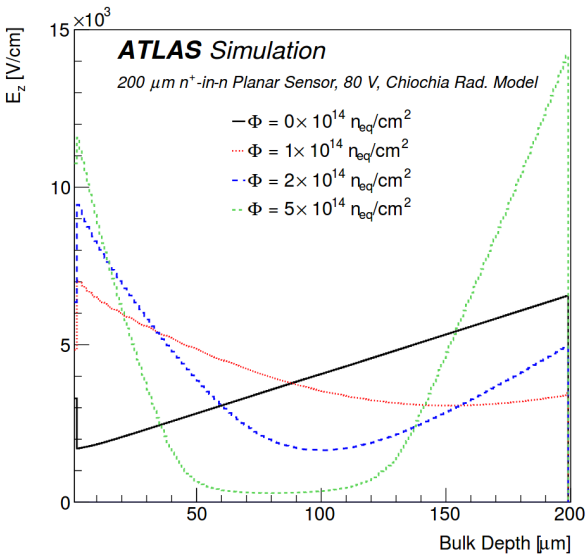

Figure 7.25: Simulated electric field magnitude along the bulk depth, averaged over the pixel long and short side for an ATLAS IBL sensor biased with 80 V for various fluences. The pixel side is defined at a bulk depth of 0 µm and the back side of the sensor at 200 µm. [125]

To investigate the differing hit detection efficiency results of module R1 and its different in-pixel ToT results compared to all other modules, a comparison with module R3 might help to understand the underlying effects: Both modules are irradiated with neutrons to the same target fluence of $5 \times 10^{15}\,\mathrm{n_{eq}/cm^2}$. Only the irradiation facilities differ with module R1 being irradiated at Sandia and R3 being irradiated in Ljubljana.
One difference in the neutron irradiations is the energy spectrum. At Sandia absorber material was used to prevent thermal neutrons from reaching the sample while in Ljubljana a continuous neutron energy spectrum was used.
Another effect to be considered is annealing of module R1 during the Sandia irradiation at temperatures of up to 100 °C. In Ljubljana the maximum temperature of module R3 was about 40 °C.
To check if the observed higher detection efficiencies of pixel design V5 is an annealing effect, module R3 was annealed in several steps and investigated in laboratory and test beam measurements. The annealing procedure and the results are described in the following chapter.

8 Annealing of Radiation Damages in REINER Pixel Modules

The conflicting hit detection efficiency results at lower bias voltages for the pixel design V5 described in the previous chapter might result from annealing effects during irradiation. At Sandia, the module R1 reached temperatures of about 100 °C during irradiation while the maximum temperature for module R3 was 40 °C in Ljubljana. To compare the annealing effects, module R3 was annealed in various steps and the performance was tested in laboratory and test beam measurements after each annealing step. In addition, module R9 was annealed in shorter time steps to observe the change in efficiency over time and to check if the increase in efficiency is also visible for lower irradiations.

8.1 Annealing Procedure

The irradiation of module R1 at Sandia took about 150 min with a peak temperature of 100 °C. As described in Chapter 4.3, the annealing process is temperature dependent and accelerated at higher temperatures. Therefore, the annealing profile of module R1 corresponds to long annealing times at room temperature, the long term annealing. To achieve a similar annealing state, module R3 was annealed for about 3 h at 80 °C in the first annealing step. Six additional annealing steps of 2 h each were performed afterwards. For the lower irradiated module R9 ($1 \times 10^{15}\,\mathrm{n_{eq}/cm^2}$, Ljubljana), shorter annealing times of about 5 min at 80 °C were used to investigate changes in performance in early stages of annealing.
The annealing procedure in the laboratory faces the challenge of a slowly and asymptotically reached target annealing temperature. Consequently, the module is exposed at temperatures between room and target annealing temperature for longer times. To accelerate the process of reaching the target temperature, a climate chamber is preheated to 80 °C. Afterwards, the module is inserted into the chamber and left for the desired annealing time while its temperature is monitored continuously. The module is then extracted and cooled down at room temperature. On the left side of Figure 8.1 the temperature profile for the first annealing step of 3 h at 80 °C for module R3 is visible. In total, the sensor was exposed to temperatures above 70 °C for about 183 min.

Overall, module R3 was annealed in four steps for 9 h (3 h + 2 h + 2 h + 2 h) at 80 °C and module R9 in three steps for 15 min (5 min + 5 min + 5 min) at the same temperature. On the right in Figure 8.1 the temperature profile for the first annealing step of module R9 for 5 min at 80 °C is presented. Due to the short annealing time, this profile is dominated by increasing and decreasing temperature flanks while the module temperature was above 65 °C for 5 min.
The temperature profiles for the other annealing steps for both modules can be found in Appendix D, Figures D.1 to D.5. After every annealing step IV measurements and test beam measurements were performed.

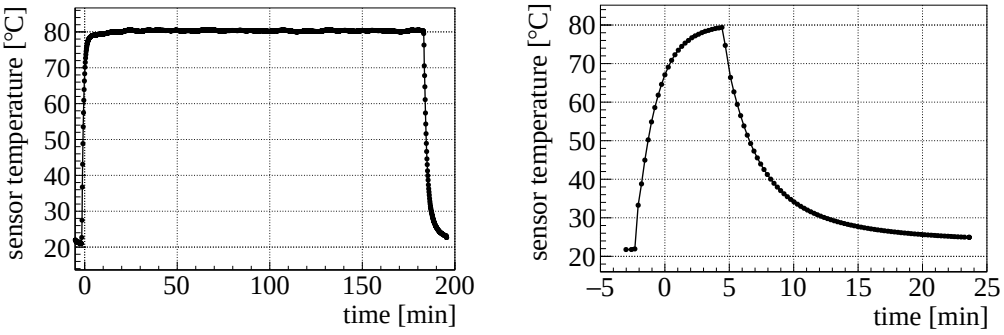

Figure 8.1: Annealing temperature profiles for the first annealing steps of the neutron irradiated module R3 ($5 \times 10^{15}\,n_{eq}/cm^2$) on the left and of module R9 ($1 \times 10^{15}\,n_{eq}/cm^2$) on the right side. The sensor temperature was above 70 °C for about 183 min for module R3 and above 65 °C for about 5 min for module R9.

8.2 IV Measurements

For IV measurements, the setup and procedure as described in Chapter 6.1.2 are used. In Figure 8.2 the IV measurements for the full sensor R3 normalized to a sensor temperature of −30 °C are shown after each annealing step: A zoom for the lower voltages is presented on the left while the full bias voltage range is plotted on the right. The expected decrease in leakage current over annealing time is visible for lower bias voltages of up to 200 V as described in Chapter 4.3.
However, at higher bias voltage the leakage current increases quicker after each annealing step. This unexpected increase is dominated by pixel design V5 as shown in Figure 8.3. In this figure, the individual IV curves of the standard design 05 on the left and of design V5 on the right side are presented for module R3 after each annealing step. The IV measurements for the annealing steps for all pixel designs can be found individually in Appendix D, Figures D.6 to D.9.

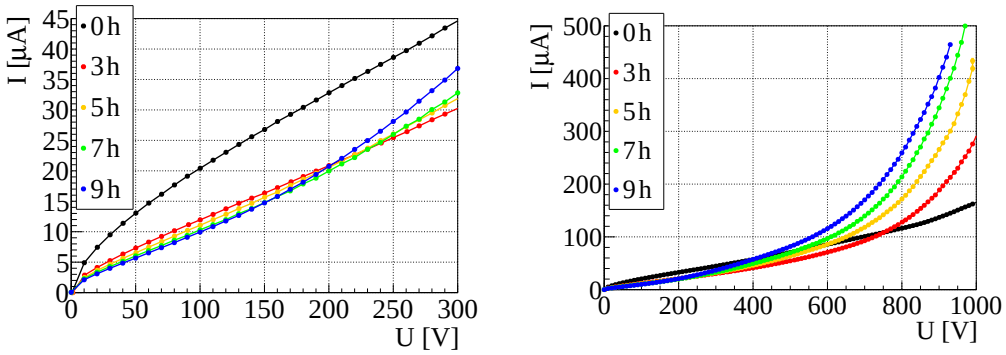

Figure 8.2: Results of the IV measurements after each annealing step at 80 °C for the complete sensor R3 normalized to a sensor temperature of −30 °C: A zoom for small bias voltages on the left and the full bias voltage range on the right side.

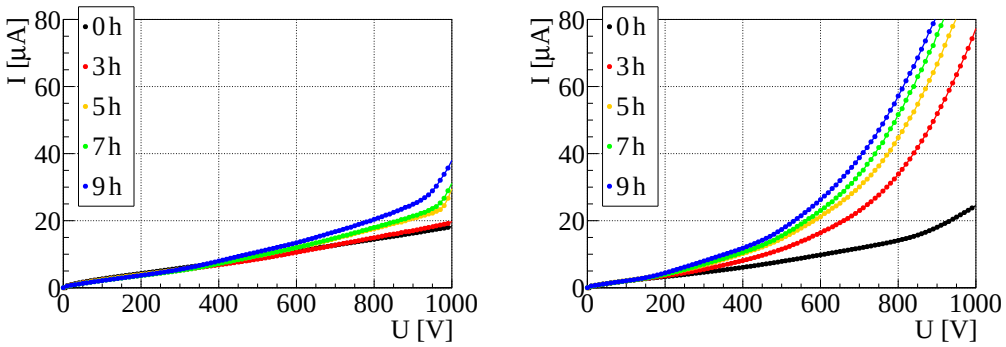

Figure 8.3: Results of the IV measurements after each annealing step at 80 °C for the standard design 05 (left) and design V5 (right) of module R3 normalized to a sensor temperature of −30 °C.

The IV measurements after each annealing step for the complete module R9, normalized to a sensor temperature of −30 °C, are presented in Figure 8.4. The leakage current only shows small changes with annealing for the first two annealing steps. A significantly lower leakage current is measured after the third annealing step (blue) which most likely is a result of a bad connection, biasing only design V6. This dramatic change is not visible in the IV curves of the individual pixel designs, summarized in Appendix D, Figures D.10 to D.13. For this reason, the results of the complete sensor measurement after the third annealing step of 15 min at 80 °C are neglected.
Overall, compared to module R3 the same trend of the change in the IV curves with annealing is visible but less pronounced: Up to a bias voltage of 500 V the highest leakage current is measured for the non-annealed case. At higher bias voltages of about 600 V the maximum leakage current is generated after the longest annealing time of 10 min for the complete module R9.

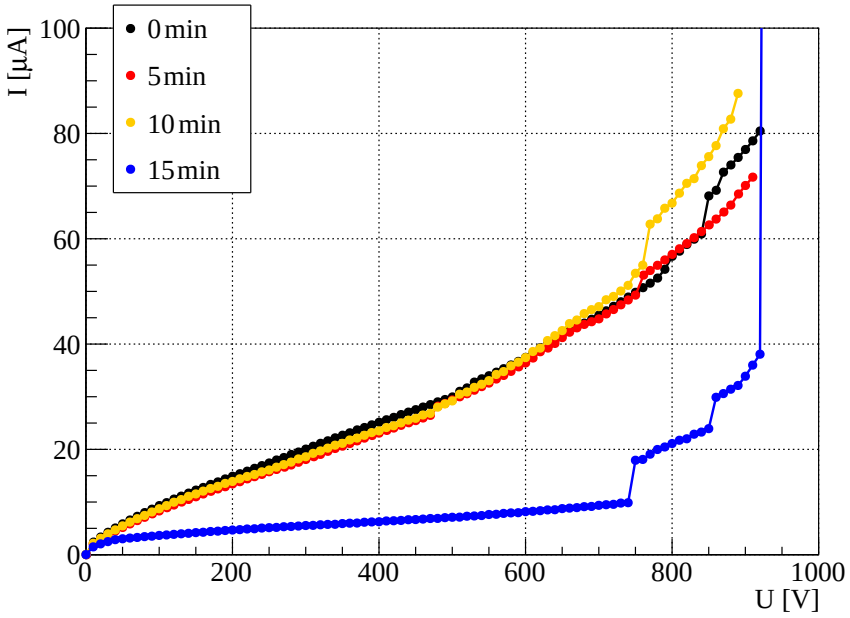

Figure 8.4: Results of the IV measurements after each annealing step at 80 °C for the full sensor R9, normalized to a sensor temperature of −30 °C. In the measurement after 15 min at 80 °C probably only design V6 was biased instead of the complete sensor.

Surprisingly, the leakage current increases with annealing at high bias voltages for both sensors which is in conflict with the theory described Chapter 4.3. This phenomenon might be a result of the annealing process leading to an increase in

space charge concentration. This results in higher electric field strength and charge multiplication as well as higher measurable leakage currents. These changes seem to affect all pixel designs, however, the largest differences are observable for pixel design V5 on module R3. The hypothesis of increased space charge concentration can be tested with charge collection measurements that would develop in the same way.

8.3 Test Beam Measurements

After each annealing step of the two neutron irradiated modules R3 ($5 \times 10^{15}\,\mathrm{n_{eq}/cm^2}$) and R9 ($1 \times 10^{15}\,\mathrm{n_{eq}/cm^2}$) test beam measurements were performed at the DESY test beam facility. For these measurements, the modules were investigated at different bias voltages and tuned to two different tunings. In the following section, only the characteristics for each annealed module are discussed. The detailed results of both modules for each annealing step, tuning and bias voltage can be found in Appendix E.
At high bias voltages all pixel designs still reach particle detection efficiencies above 97 % after annealing for both modules. At lower bias voltages, changes in the performance of the different pixel designs for the annealed modules are more pronounced which is similar to the results after irradiation without annealing. At first, the hit detection and charge collection efficiency results after annealing of the higher neutron irradiated module R3 are presented, followed by the results for the lower neutron irradiated module R9.

8.3.1 Results of the higher Neutron irradiated Module

At a lower bias voltage of 300 V the hit detection efficiency results of module R3 show an increase in efficiency for pixel design V5 with annealing time: Figure 8.5 presents the hit detection efficiencies for the different pixel designs at a bias voltage of 300 V for each annealing step (Tuning: 1600 e, 6 ToT at 20 ke). After the first annealing step, the efficiency is significantly reduced for all pixel designs except for design V5 while for this long annealing time a reduction in efficiency would be expected as a reverse annealing effect (see Chapter 4.3). Between the non-annealed case and the first annealing step of 3 h at 80 °C the hit detection efficiency of the standard design 05 is reduced by about 13.2 % while for pixel design V5 the efficiency increases by about 14.5 %. With additional annealing the hit detection efficiency of the standard design remains about same at (70.7 ± 1.2) % while for pixel designs V1, V4, V5 and V6 the efficiency increases with further annealing. Only in designs V2 and V3 a drop in efficiency between the 7 h and 9 h annealing

steps are observed. Overall, the highest particle detection efficiency at 300 V is reached after 9 h of annealing at 80 °C for pixel design V5 with $(98.2^{+0.2}_{-0.8})$ %. In contrast, for the standard design a minimum bias voltage of 600 V is necessary to achieve this high particle detection efficiency after 9 h of annealing. This would mean a reduction in operation voltage after irradiation and annealing of a complete sensor with design V5 by 50 % compared to a standard sensor.

Consequently, the high particle detection efficiency for pixel design V5 of the Sandia neutron irradiated module R1 ($5 \times 10^{15}\,n_{eq}/cm^2$) at low bias voltages can be explained with annealing during the irradiation. With long annealing times for the Ljubljana neutron irradiated module R3 ($5 \times 10^{15}\,n_{eq}/cm^2$) an improvement in efficiency for pixel design V5 is measured at low bias voltages.

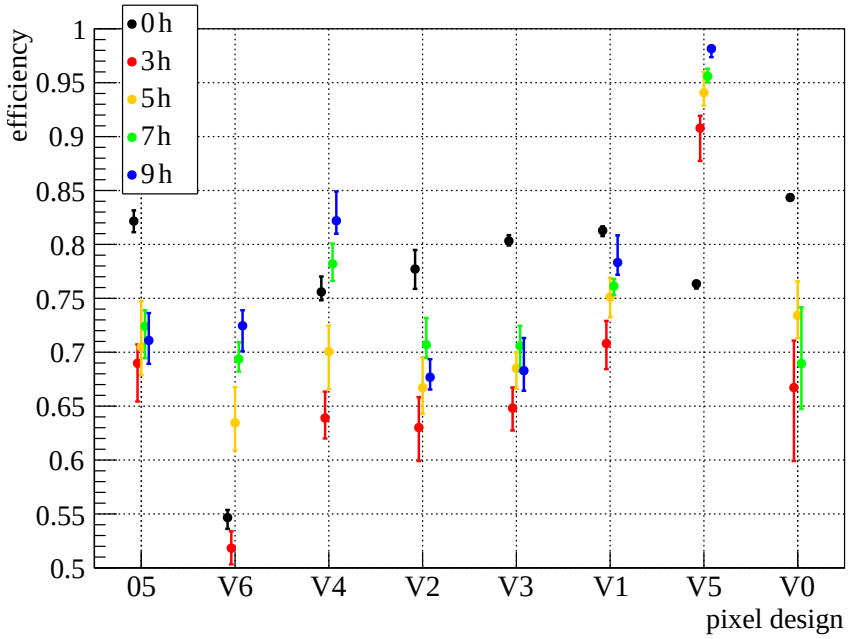

Figure 8.5: Hit detection efficiencies for the groups with different pixel designs of module R3 ($5 \times 10^{15}\,n_{eq}/cm^2$, Ljubljana), biased with 300 V measured at different annealing steps.

To identify which pixel areas become more efficient through long term annealing, a visualization with in-pixel efficiency maps of pixel design V5 would be useful. As previously described in Chapter 6.2.3 the spatial resolution of DESY test beam measurements is worse compared to CERN measurements which results in inconclusive in-pixel efficiency maps. As an example, the in-pixel efficiency map of the standard pixel design of module R3 after 9 h annealing biased with 300 V is presented in the top of Figure 8.6 (Tuning: 1600 e, 6 ToT at 20 ke). White spots in the

map indicate a lack of statistics. Compared to the in-pixel efficiency map based on CERN measurements (bottom of Figure 8.6), the lower spatial resolution of the DESY measurements results in an indistinct inefficient region around the bias dot and bias grid. Overall, no conclusion about the in-pixel hit detection performance can be drawn from such in-pixel efficiency maps. The in-pixel maps for all pixel designs of module R3 after 9 h of annealing can be found in Appendix E, Figure E.4.
For the same reason, no in-pixel ToT maps based on DESY test beam data are analyzed in the following charge collection efficiency study.

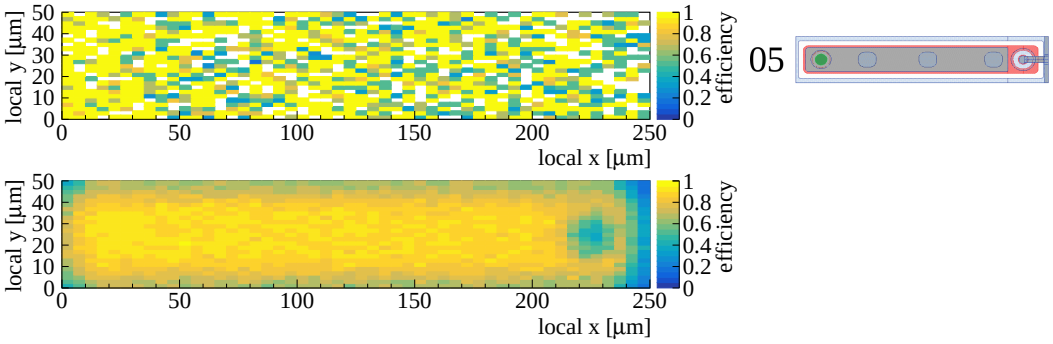

Figure 8.6: In-pixel efficiency maps for the standard pixel design 05 of the neutron irradiated module R3 (5×10^{15} n_{eq}/cm^2, Ljubljana) biased with 300 V. Top: After annealing for 9 h at 80 °C. Bottom: Without annealing.

To investigate the annealing effect on the charge collection efficiency, the mean ToT values for cluster size one for module R3 are analyzed. Similar to the previously presented ToT results of non-annealed modules in Chapter 7.3.2, more charge is generated at higher bias voltages for all designs, tunings, and annealing times. Furthermore, variances in the mean ToT values are more pronounced at higher bias voltages for all pixel designs.
Figure 8.7 shows the mean ToT values for cluster size one for the different pixel designs of module R3 biased with 600 V for each annealing step (Tuning: 1600 e, 6 ToT at 20 ke). Similar to the results of irradiated modules in Chapter 7.3.2, larger error bars in the following ToT results are caused by entries with ToT values higher than 13 so that the deviation from the mean ToT value is enlarged. With every annealing step from 0 h until 7 h of annealing at 80 °C more charge is generated for all pixel designs. In addition, the gradient of these changes varies significantly with the pixel design: The largest increase of measured charge with annealing time is noticeable for pixel design V5 from a mean ToT value of 3.5 ± 1.4 (0 h) to 10.4 ± 3.1 (7 h) and for pixel design V4 from 3.1 ± 1.2 (0 h) to 8.8 ± 3.5 (7 h). Contrarily, the lowest increase in measured charge is determined for the standard pixel design 05

from a mean ToT value of 3.1 ± 0.9 (0 h) to 6.1 ± 2.5 (7 h).
The results after the last annealing step of 9 h show a decrease of mean ToT values for all pixel designs. A similar drop in generated charge from the 7 h to 9 h annealing step is also visible for the other tuning with a threshold value of 1000 electrons. Consequently, a bad tuning of the module can be excluded as an original cause for the charge reduction but the decreased ToT values might result from test beam conditions like a lower temperature. Additional annealing and further investigations of the module in test beam measurements would clarify if this drop in generated charge after 9 h of annealing is an irregularity or prevails.

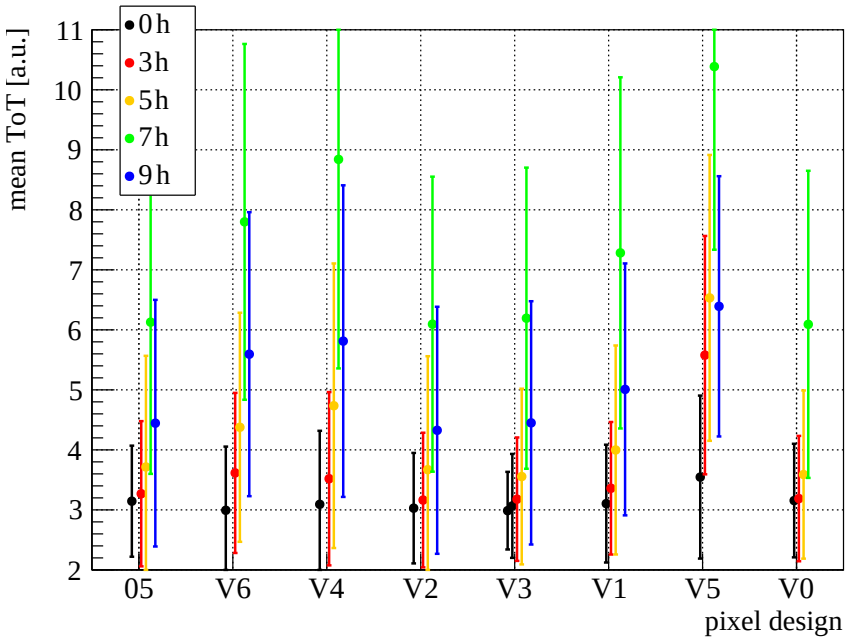

Figure 8.7: Mean ToT values for clusters with size one for the groups with different pixel designs of module R3 (5×10^{15} n_{eq}/cm^2, Ljubljana) biased with 600 V at different annealing steps.

To clarify if the observed improvements of design V5 are a reverse annealing effect after long annealing times and if it is influenced by the irradiation fluence, the lower irradiated module R9 (1×10^{15} n_{eq}/cm^2) was annealed in several shorter steps and investigated in test beam measurements.

8.3.2 Results of the lower Neutron irradiated Module

Module R9 was annealed to a total of 15 min at 80 °C with each annealing step lasting about 5 min. Test beam measurements were performed for annealing times

from 0 min to 10 min. The following section will give an overview of the test beam results. Detailed results for all annealing steps, tunings and bias voltages can be found in Appendix E. Pixel design V5 became noisy for some measurements of the 1000 electron threshold tuning and had to be masked so that no data points are available for these measurements.
At lower bias voltages performance differences in the hit detection efficiencies of the different pixel designs with annealing occur as exemplarily presented in Figure 8.8 for 100 V (Tuning: 1600 e, 6 ToT at 20 ke). For the non-annealed case (0 min) the module was only investigated on the left side with designs 05, V6, V4 and V2. The hit detection efficiencies increase for all these designs with the first annealing step which can be explained with the beneficial annealing effect for short annealing times as described in Chapter 4.3. After the additional annealing to 10 min at 80 °C an expected drop in efficiency is visible for all pixel designs caused by reverse annealing.
In conclusion, all pixel designs of module R9 show similar changes for these two annealing steps. In contrast to the higher irradiated module R3, no massive increase in detection efficiency for pixel design V5 is visible for these shorter annealing times.

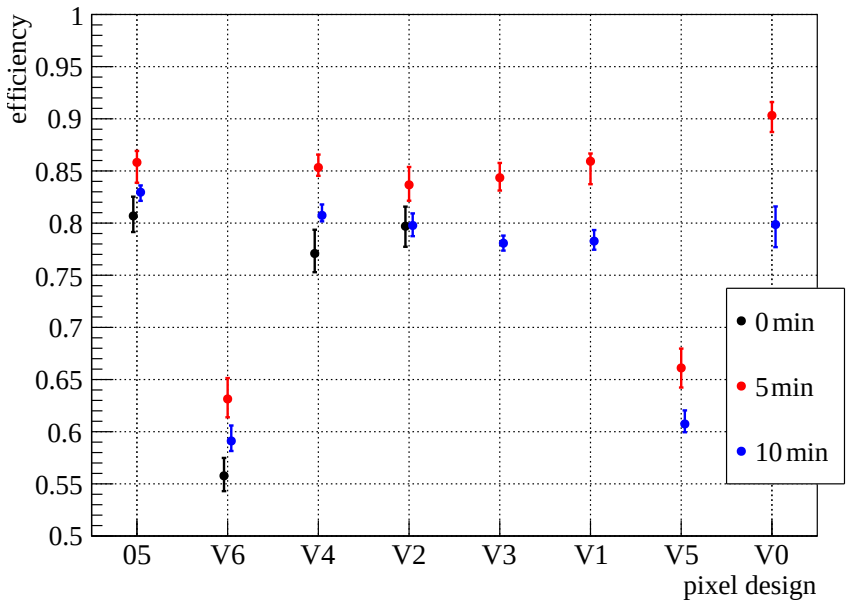

Figure 8.8: Hit detection efficiencies for the groups with different pixel designs of module R9 ($1 \times 10^{15}\,n_{eq}/cm^2$, Ljubljana) biased with 100 V at different annealing steps.

The change in charge collection efficiency of module R9 with annealing is presented in Figure 8.9. As an example the mean ToT values for cluster size one of the different pixel designs biased with 200 V after every annealing step are shown (Tuning:1600 e, 6 ToT at 20 ke). After the first annealing step of 5 min slightly higher ToT values are measured for all pixel designs. The largest improvements are determined for the standard design 05 from 2.8 ± 1.5 (0 min) to 3.8 ± 3.3 (5 min) and for design V5 from a mean ToT value of 3.2 ± 1.6 (0 min) to 3.7 ± 3.0 (5 min). After the additional annealing to 10 min at 80 °C slightly less charge is generated for all pixel design except for design V0. However, the described changes with annealing are very small and the uncertainty indicated as large error bars is high.
Overall, the same behavior of generated charge and particle detection efficiency for all pixel designs of the lower irradiated module R9 after short annealing steps are observed: An initial improvement caused by beneficial annealing is followed by a reverse annealing degradation.

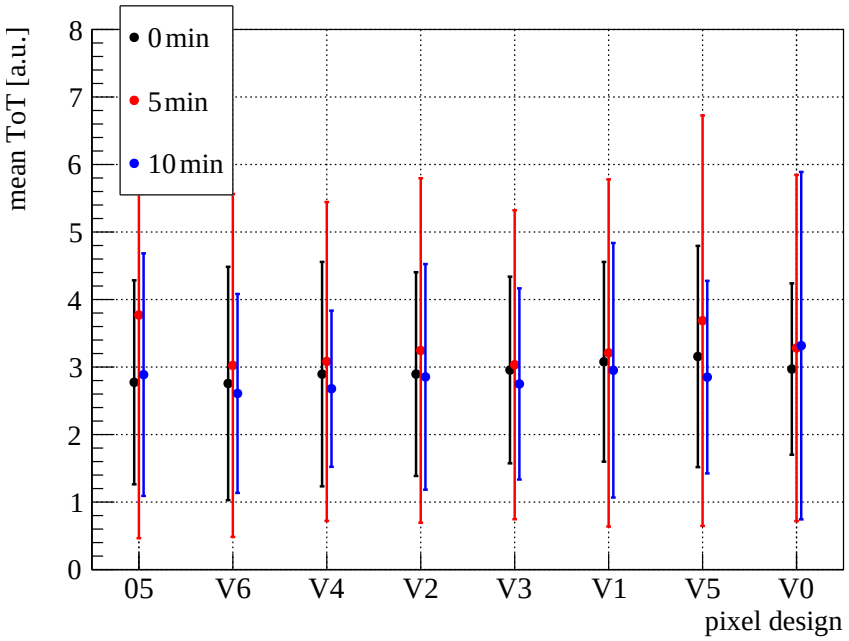

Figure 8.9: Mean ToT values for cluster size one for the groups with different pixel designs of module R9 (1×10^{15} n_{eq}/cm^2, Ljubljana) biased with 200 V at different annealing steps.

Future research could continue the annealing of module R9 with annealing times of 3 h to 9 h. These findings could then further explain if the higher detection and charge collection efficiencies of pixel design V5 for module R3 are a matter of annealing duration or irradiation fluence.
Due to the long shut down at CERN the test beam measurements of annealed modules were carried out at the DESY test beam facility. As test beam capabilities at CERN and DESY are very time consuming and limited in time, a laboratory measurement setup to investigate charge multiplication would be beneficial. This was developed as part of this thesis and is described in the following section.

8.4 New Laboratory Charge Collection Measurement Setup

In the course of this thesis the laboratory setup used for TCT measurements was modified to investigate the charge multiplication of REINER pixel modules. In the TCT a laser generates free charge carriers in the silicon bulk to investigate the resulting sensor signal (see Chapter 3.8). The setup was re-assembled and characterized during the master thesis of F. Barth [126] which is illustrated on the left in Figure 8.10. The pulsed laser signal (500 Hz) with a selectable wavelength of 672 nm, 908 nm or 1057 nm is focused with an optical fiber, focal lens and beam splitter onto an investigated sample. The laser intensity is adjusted with a potentiometer between 0 to 14. A camera is positioned above the setup to monitor the position of the beam spot on the module. In addition, these optical instruments are mounted on a PI-Stage for height adjustments (z-direction) so that the beam is perfectly focused on the sample. For a focused beam, the minimal beam spot size of (9.6 ± 1.4) µm (FWHM) is determined for the here used 908 nm laser [126]. For this wavelength electron-hole pairs are generated down to a sensor depth of about 39.1 µm [53].
The investigated module is positioned inside an insulating box on a holder which features four adjustment screws for horizontal alignment of the module. For the investigation of irradiated modules the box is filled with dry ice and flushed with dry air. The module temperature is continuously monitored with Pt1000 temperature resistors. Furthermore, the box is attached to the PI-Stage to adjust the module position in x- and y-direction. The remote control of this PI-Stage was integrated into the software STcontrol in the course of this thesis. This way, an irradiated module is scanned automatically in steps of about 8 µm while at each position a source scan measurement with adjustable number of trigger signals is started. The trigger signal for the MMC3 read out system is provided externally by the laser pulse generator. The measured charge of the module is read out via the MMC3 and STcontrol. The analysis of all scans is performed with the fei4Analyzer.

To measure a signal, free charge carriers must be generated inside the sensor bulk of the REINER pixel modules. However, the sensor's n-side is attached to the readout chip and the p-side is almost completely covered with a metal and a passivation layer above. Only the HV pads are not covered with passivation. For this reason, the metal layer of the unused HV pad was removed by etching it with a sodium hydroxide solution (20 %). On the right in Figure 8.10 the etching process of the HV pads is illustrated: The HV metal layers for the designs V0 and V5 are already removed so that they appear purple. Furthermore, a drop of sodium hydroxide solution is placed on the pad of design V1 to remove the metal. The chemical reaction lasts for about 5 min and is afterwards rinsed with purified water.
The IV curves of a test sensor before and after etching were studied in the master thesis of S. Di Pede [81]: Only small changes are observable indicating that the etching process does not damage the sensors. Consequently, the metal of all unused HV pads of the groups with different pixel designs of the irradiated module R3 were removed. Each pad provides an area of 1000 µm × 1000 µm (4 × 20 pixels) for the investigation of laser induced charge collection measurements. The electrons generated by the laser illumination of the sensor p-side drift through the majority of the bulk and induce the signal on the readout electrode.

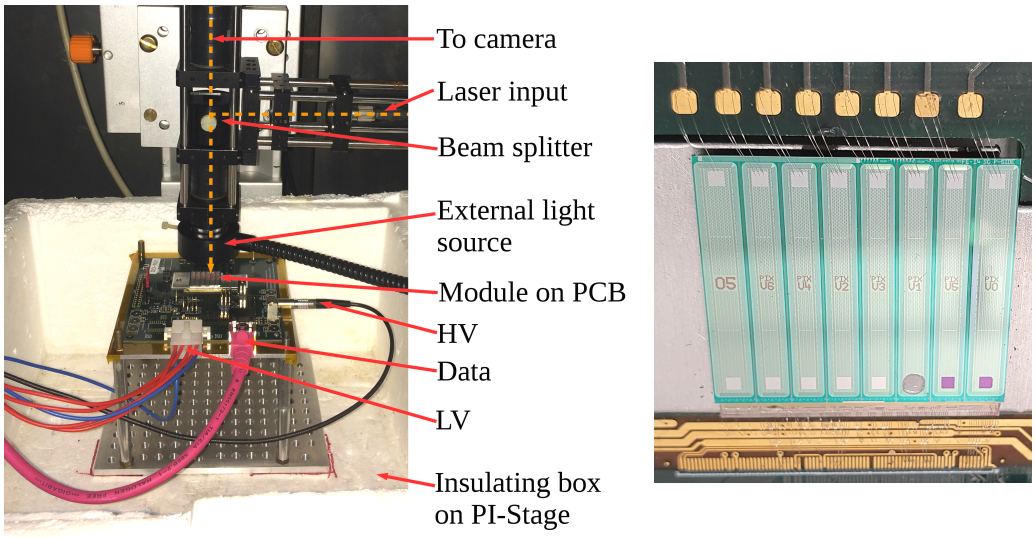

Figure 8.10: Laboratory setup to measure the laser induced charge collection efficiency (left) and the preparation of module R3 with NaOH (right). From left to right the HV pads of the first five structures are untreated, of V1 it is etched with sodium hydroxide and of the last two structures the metal has been removed.

After tuning module R3 (annealed for 9 h at 80 °C), the laser spot is focused on the central area of a specific pixel and the mean ToT values are determined at different laser intensities of the 908 nm laser. The results of the central areas of pixel designs V0 and V5 biased with 400 V are plotted in Figure 8.11 (Tuning: 1600 e, 10 ToT at 10 ke): The mean ToT values and the standard deviation are determined at different laser intensities while for the measurement of V0 per laser intensity 5000 trigger signals and for pixel design V5 1000 trigger signals were recorded. All measured hits have a cluster size of one as the small beam spot is focused on the center of each pixel. For each pixel design only one run with four different laser intensity settings was performed, so that for future measurements the reproducibility of these results needs to be demonstrated.
Both pixel designs show a rise in measured charge with higher laser intensities. Overall, pixel design V5 measures more charge even at lower intensities compared to the standard design V0. These results are consistent with test beam charge collection results.
A laser intensity with medium ToT values for pixel design V5 is reached at a potentiometer setting of about 8.65. However, at this low laser intensity no charge will be measured for the standard design V0. Here a optimum laser intensity with medium Tot values would be about 8.83 while at this intensity all ToT results of design V5 are already stored in the overflow bin. Consequently, there is no common laser intensity to investigate both designs and it must be adjusted per measurement.

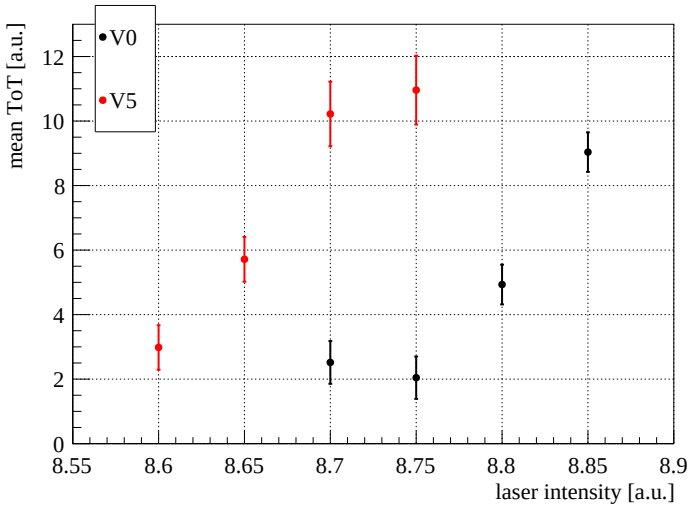

Figure 8.11: Mean ToT values for the laser induced charge collection measurement of module R3 (annealed for 9 h at 80 °C) for the central area of the pixel designs V0 and V5 at different laser intensities.

In Figure 8.12 the mean ToT values for a scan over a specific pixel with design V5 of module R3 ($5 \times 10^{15}\,n_{eq}/cm^2$, annealed for 9 h) biased with 400 V are presented as a function of the laser spot position (Tuning: 1600 e, 10 ToT at 10 ke). For these measurements an area of 370 µm × 100 µm is scanned with the 908 nm laser in 8 µm steps along the local x of the pixels and 2 µm steps along the local y side with a laser intensity of 8.65. If neighboring pixels measure a signal as well, only the ToT information of the investigated pixel is used for the image (no clustering is performed).
For the presented results no alignment is performed and ToT values are measured between 60 µm to 340 µm local x and 0 µm to 80 µm local y. The pixel area is visible with a small tilt since the module was not mounted in parallel to the PI-Stage axes. For future measurements the results should be corrected for these torsions by an alignment in the analysis software.
The highest ToT values between 7.1 to 8.7 are determined at the corners of the pixel. A vertical dashed line at local x = 200 µm in the in-pixel map of Figure 8.12 clarifies the position used for the profile image in Figure 8.13. With this profile image a better comparison in the central region is possible, which shows higher ToT values at the edges of the n^+-implantation of about 4.3 ± 0.2. Towards neighboring pixels and at the center the ToT drops to about 2.5.
The test beam results of the annealed irradiated module R3 proved that the higher efficiencies for pixel design V5 on the irradiated module R1 were an annealing effect. Consequently, it is expected that the pixel regions of design V5 of the annealed module R3 with higher charges are the same as the ones observed on module R1. Overall, similarities between this laser induced ToT map of module R3 and the ToT in-pixel map for design V5 from CERN test beam measurements of module R1 in Figure 7.15 are observable.
Consequently, this new laboratory setup allows for investigations of the regions with higher charge collection efficiency with sub-pixel resolution.

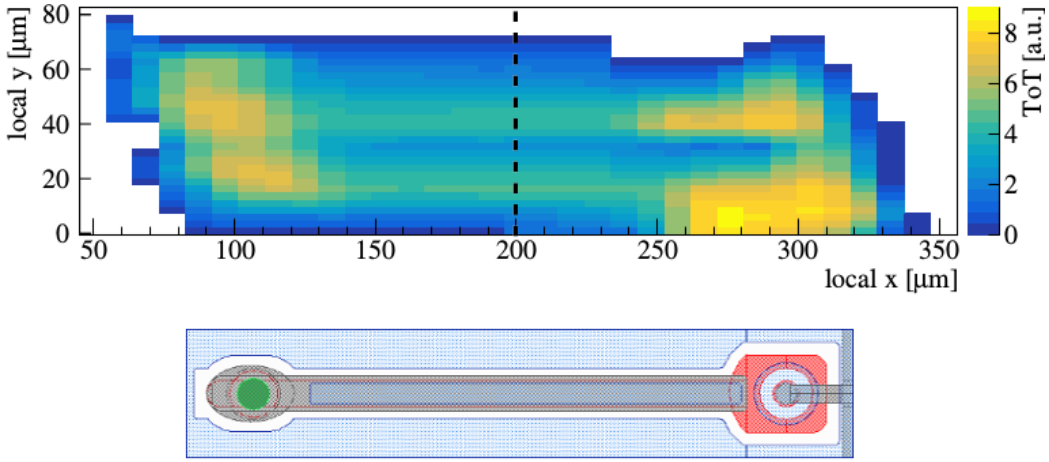

Figure 8.12: Scan of the mean ToT values for the laser induced charge collection measurement without clustering of a specific pixel with design V5 of module R3 (annealed for 9 h at 80 °C), biased with 400 V. At the bottom a schematic layout of the corresponding pixel design is presented.

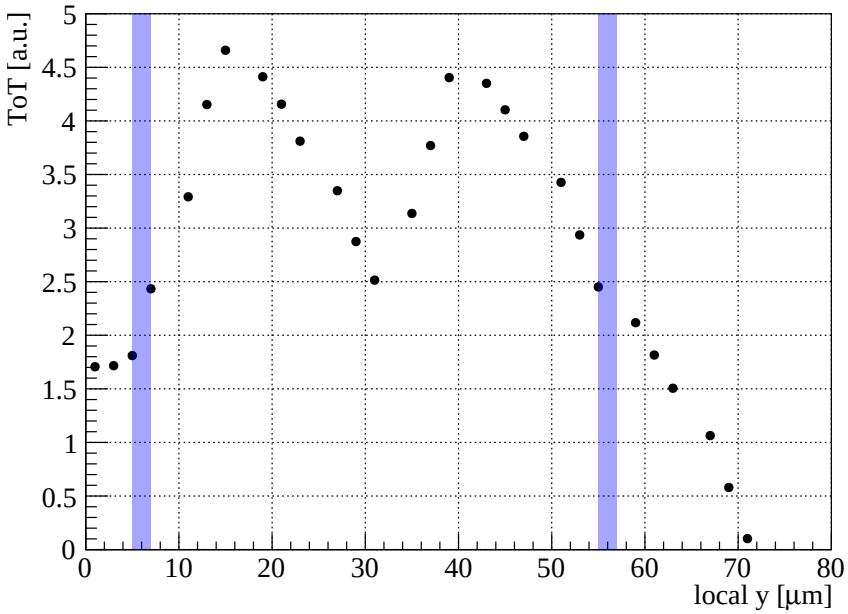

Figure 8.13: Profile of the in-pixel charge collection map at local x = 200 µm of design V5 for the neutron irradiated module R3 (5×10^{15} n_{eq}/cm^2, annealed 9 h at 80 °C), biased with 400 V. The pixel width is indicated with blue bands with a distance of (25 ± 1) µm from the central minimum.

8.5 Summary of the Results of annealed REINER Pixel Modules

To test the hypothesis that the higher particle detection efficiency of pixel design V5 of module R1 is caused by annealing during the irradiation at Sandia, the modules R3 and R9 were annealed in several steps and investigated in laboratory and test beam measurements. In total, module R3 is long term annealed in four steps for 9 h (3 h + 2 h + 2 h + 2 h) and module R9 in three steps for 15 min (5 min + 5 min + 5 min) at 80 °C.
For module R3, the expected decrease in leakage current with annealing time is only visible below 200 V. At higher bias voltages the IV curves start to shift: The voltage, at which an exponential increase of the leakage current starts, decreases with annealing time. Similar but less pronounced results are observable in the IV curves of the lower irradiated module R9.
The test beam results of module R3 showed that pixel design V5 became more and more efficient with annealing time while the efficiency of the standard design became less efficient with the first annealing step and stayed constant afterwards. The charge collection efficiency increased until the 7 h annealing step for all pixel designs, however, with V5 showing the largest increase. With the last annealing step to 9 h at 80 °C the collected charge is reduced for all designs.
Module R9 shows similar results for the hit detection and charge collection efficiency: The first annealing step in the range of beneficial annealing improves the module performance. After the beneficial annealing, reverse annealing reduces the performance of all pixel designs at 10 min at 80 °C.
No in-pixel maps can be computed from test beam results after annealing due to a lack of statistics and limited spatial resolution. Therefore, a laboratory setup for laser induced charge collection measurements of irradiated modules was modified in the course of this thesis. The measured laser induced charges vary with the different pixel designs and no common laser intensity could be found. Consequently, the laser intensity needs to be characterized in the future and converted to number of photons to compare results between different pixel designs. In addition, an offline alignment for rotational corrections between module and PI-Stage needs to be implemented. A first proof of concept of this modified setup with with a single in-pixel charge collection measurement run for pixel design V5 of module R3 was presented and showed promising results. Further investigations must demonstrate the reproducibility of the results and laser intensity. Afterwards, the irradiated modules R5 ($5 \times 10^{15}\,\mathrm{n_{eq}/cm^2}$) and R7($1 \times 10^{15}\,\mathrm{n_{eq}/cm^2}$) can be annealed successively and forthcoming measurements can investigate the change in generated charge in laboratory measurements with this modified setup.

Other studies on highly neutron irradiated n^+-in-p strip detectors observed similar behaviors of leakage currents and charge collections with annealing as reported in [72] and [127]: At low bias voltages the leakage current decreases but at higher bias voltages it increases with longer annealing times caused by charge multiplications which were also observed in these studies. With edge-TCT measurements it was concluded that it derives from an increase in electric field close to the p-n junction at the implant edges [128], [129]. Furthermore, for proton irradiated n^+-in-p micro strip detectors studies report an increase in collected charge after long annealing times as well [71].
Consequently, the desired electrical field strength maxima of the REINER pixel structure V5 cause the observed charged multiplication effect and improve the performance of this pixel design after irradiation and annealing.

9 Conclusion and Outlook

Based on the IBL ATLAS pixel design, the REINER pixel modules were designed to create electric field strength maxima for charge multiplication inside a sensor. Especially after irradiation, this would result in higher charge collection and hit detection efficiencies already at lower bias voltages. The special composition of REINER pixel sensors with six design shapes together with the IBL standard design on one sensor allows for direct performance comparisons between the different pixel designs.

For the investigation of non-irradiated REINER pixel modules the test beam results showed no discrepancies in the charge collection and hit detection efficiency of the different pixel designs and the modified ones performed as good as the standard designs. Discrepancies were only observable in the IV curves where the two groups with narrowed implantations (V5 and V6) always showed higher leakage currents compared to all other groups.
To investigate the radiation hardness and check for the intended charge multiplication effect, in total nine REINER pixel modules were irradiated with protons and neutrons in four irradiation facilities to different fluences. All successful irradiated modules showed increasing charge collection efficiencies with increasing bias voltages. For the inhomogeneously proton irradiated module, the most charge is generated by the standard designs while for all neutron irradiated samples pixel design V5 measures most charge. For now, it is unclear if this difference is caused by the different type of irradiation particle (protons and neutrons) or by the lower irradiation fluence of the standard designs for the proton irradiated module. Investigations of homogeneously proton irradiated modules could clarify this ambiguity in the future.
The hit detection efficiency of irradiated REINER pixel modules reached high, consistent values for all different pixel design groups at high bias voltages. Performance differences were more pronounced at lower bias voltages: On the one hand, all modules which were neutron irradiated at Ljubljana and one module which was irradiated with protons at CERN measured highest particle detection efficiencies for the standard design and lowest for the two designs with narrowed implantations (V5 and V6). The poor performances of these two designs result from inefficiencies towards neighboring pixels due to charge sharing effects. On the other hand, the module irradiated with neutrons at Sandia measured highest particle detection

efficiencies for the pixel group with design V5 while no inefficiencies towards neighboring pixels were observable.
These clear discrepancies in hit detection efficiency of pixel design V5 for two modules, neutron irradiated to the same fluence ($5 \times 10^{15}\,\mathrm{n_{eq}/cm^2}$) could be traced back to the conditions during irradiation: An annealing effect during the irradiation at Sandia led to an improvement of design V5. To recreate the annealing status, two Ljubljana irradiated modules were annealed in several steps at 80 °C and their performance was tested after each step. The higher irradiated module showed an increase in hit detection and charge collection efficiency of pixel design group V5 with long annealing times. However, this effect was not visible for the lower irradiated module with shorter annealing times. Consequently, further long term annealing times of the lower irradiated module and short annealing times for a highly irradiated module need to be studied to clarify if the increase in efficiency of pixel design V5 is only observable after long annealing times and whether it depends on the irradiation fluence.
A TCT laboratory setup modified in the course of this thesis identified the corners and edges of the n^+-implantation to be responsible for the observed charge multiplication. A first proof of concept for the setup was provided with the results of laser induced charge collection measurements for pixel design V5 on a highly irradiated and long term annealed module.
The observed effect of higher efficiencies for design V5 seems to be a combination of a small implantation and enlarged p-spray profile since such higher efficiency values with annealing are not observed for pixel designs V1 to V4 with segmented implantations. For pixel design V6 with narrowed implantation and regular p-spray profile, an increase in detection efficiency and charge collection with annealing is visible but not as extreme as for pixel design V5.
In conclusion, pixel design V5 showed the intended charge multiplication effect and increased hit detection efficiencies at lower bias voltages after irradiation and annealing of neutron irradiated modules. Other studies of annealed n^+-in-p strip detectors also measured an increased electric field and higher collected charges at the p-n junction similar to the results presented here.

Based on pixel design V5 five new pixel designs (V7, V7M, V7D, V8 and V8D) were developed in the PhD thesis of A. Gisen [79] and produced in n^+-in-n sensor technology on the so-called REINER Mk II sensor.
The future ITk sensors will be produced in n^+-in-p technology and the REINER pixel sensor and the new REINER Mk II sensor were adapted in the master thesis of S. Dungs [130] and produced in this technology. These modules were measured in a test beam campaign at DESY and more information on the modules and results can be found in Appendix F. Future studies will investigate the performance of these new modules after irradiation and annealing.

Bibliography

[1] O. S. Brüning et al. *LHC Design Report*. 2004. DOI: 10.5170/CERN-2004-003-V-1.

[2] *Our people*. URL: https://home.cern/about/who-we-are/our-people (visited on Jan. 10, 2020).

[3] *CERN experiments observe particle consistent with long-sought Higgs boson*. 2012. URL: https://home.cern/news/press-release/cern/cern-experiments-observe-particle-consistent-long-sought-higgs-boson (visited on Jan. 10, 2020).

[4] R. Scrivens et al. Overview of the status and developments on primary ion sources at CERN (2020). URL: https://cds.cern.ch/record/1382102.

[5] ATLAS Collaboration. The ATLAS Experiment at the CERN Large Hadron Collider. *JINST* 3 (2008). DOI: 10.1088/1748-0221/3/08/S08003.

[6] CMS Collaboration. The CMS Experiment at the CERN LHC. *JINST* 3 (2008). DOI: 10.1088/1748-0221/3/08/S08004.

[7] ALICE Collaboration. The ALICE experiment at the CERN LHC. *JINST* 3 (2008). DOI: 10.1088/1748-0221/3/08/S08002.

[8] LHCb Collaboration. The LHCb Detector at the LHC. *JINST* 3 (2008). DOI: 10.1088/1748-0221/3/08/S08005.

[9] E. Mobs. The CERN accelerator complex - 2019. Complexe des accélérateurs du CERN - 2019 (2019). URL: https://cds.cern.ch/record/2684277.

[10] W. Herr and B. Muratori. Concept of luminosity (2006). DOI: 10.5170/CERN-2006-002.361.

[11] M. Lamont. The First Years of LHC Operation for Luminosity Production (2013). URL: https://cds.cern.ch/record/2010134.

[12] G. Aad et al. Observation of a new particle in the search for the Standard Model Higgs boson with the ATLAS detector at the LHC. *Physics Letters B* 716 (2012). DOI: 10.1016/j.physletb.2012.08.020.

[13] S. Chatrchyan et al. Observation of a new boson at a mass of 125 GeV with the CMS experiment at the LHC. *Physics Letters B* 716 (2012). DOI: 10.1016/j.physletb.2012.08.021.

[14] ATLAS Collaboration. *ATLAS public results*. 2018. URL: https://twiki.cern.ch/twiki/bin/view/AtlasPublic/LuminosityPublicResultsRun2 (visited on Jan. 7, 2020).

[15] J. Wenninger. *LHC Report: The final days of Run 2*. 2018. URL: https://home.cern/news/news/accelerators/lhc-report-final-days-run-2 (visited on Jan. 10, 2020).

[16] J. Pequenao. Computer generated image of the whole ATLAS detector (2008). URL: https://cds.cern.ch/record/1095924.

[17] ATLAS Collaboration. *ATLAS magnet system: Technical Design Report*. 1997. URL: http://cds.cern.ch/record/338080.

[18] ATLAS Collaboration. *ATLAS muon spectrometer: Technical Design Report*. 1997. URL: https://cds.cern.ch/record/331068.

[19] ATLAS Collaboration. *ATLAS calorimeter performance: Technical Design Report*. 1996. URL: http://cds.cern.ch/record/331059.

[20] ATLAS Collaboration. *ATLAS tile calorimeter: Technical Design Report*. 1996. URL: http://cds.cern.ch/record/331062.

[21] ATLAS Collaboration. *ATLAS liquid-argon calorimeter: Technical Design Report*. 1996. URL: http://cds.cern.ch/record/331061.

[22] ATLAS Collaboration. *ATLAS inner detector: Technical Design Report*. 1997. URL: http://cds.cern.ch/record/331063.

[23] ATLAS Collaboration. The ATLAS Inner Detector commissioning and calibration. *Eur. Phys. J. C* 70 (2010). DOI: 10.1140/epjc/s10052-010-1366-7.

[24] ATLAS Collaboration. *Track Reconstruction Performance of the ATLAS Inner Detector at $\sqrt{s} = 13$ TeV*. Tech. rep. 2015. URL: http://cds.cern.ch/record/2037683.

[25] The ATLAS TRT collaboration. The ATLAS TRT Barrel Detector. *JINST* 3 (2008). DOI: 10.1088/1748-0221/3/02/p02014.

[26] The ATLAS TRT collaboration. The ATLAS TRT end-cap detectors. *JINST* 3 (2008). DOI: 10.1088/1748-0221/3/10/p10003.

[27] A. Vogel. *ATLAS Transition Radiation Tracker (TRT): Straw Tube Gaseous Detectors at High Rates*. Tech. rep. 2013. URL: http://cds.cern.ch/record/1537991.

[28] A. Abdesselam et al. The barrel modules of the ATLAS semiconductor tracker. *Nucl. Instr. Meth. A* 568 (2006). DOI: 10.1016/j.nima.2006.08.036.

[29] A. Abdesselam et al. The ATLAS semiconductor tracker end-cap module. *Nucl. Instr. Meth. A* 575 (2007). DOI: 10.1016/j.nima.2007.02.019.

[30] ATLAS Collaboration. *ATLAS pixel detector: Technical Design Report*. 1998. URL: https://cds.cern.ch/record/381263.

[31] A. G. Clark and G. Mornacchi. *ATLAS B-Layer Task Force: Final Report*. Tech. rep. 2008. URL: https://edms.cern.ch/document/1027820/1 (visited on Jan. 14, 2020).

[32] ATLAS Collaboration. *ATLAS Insertable B-Layer Technical Design Report*. Tech. rep. 2010. URL: https://cds.cern.ch/record/1291633.

[33] C. Da Via et al. 3D silicon sensors: Design, large area production and quality assurance for the ATLAS IBL pixel detector upgrade. *Nucl. Instr. Meth. A* 694 (2012). DOI: 10.1016/j.nima.2012.07.058.

[34] ATLAS Collaboration. *The FE-I4 Pixel Readout Integrated Circuit*. Tech. rep. 2010. URL: https://cds.cern.ch/record/1231359.

[35] M. Backhaus. The upgraded Pixel Detector of the ATLAS Experiment for Run 2 at the Large Hadron Collider. *Nucl. Instr. Meth. A* 831 (2016). DOI: 10.1016/j.nima.2016.05.018.

[36] G. Apollinari et al. *High-Luminosity Large Hadron Collider (HL-LHC): Technical Design Report V. 0.1*. 2017. DOI: 10.23731/CYRM-2017-004.

[37] ATLAS Collaboration. *Expected performance of the ATLAS detector at the High-Luminosity LHC*. Tech. rep. 2019. URL: http://cds.cern.ch/record/2655304.

[38] ATLAS Collaboration. ATLAS searches for double Higgs production (2018). URL: https://atlas-public.web.cern.ch/updates/physics-briefing/atlas-searches-double-higgs-production (visited on Jan. 14, 2020).

[39] *LHC/ HL-LHC Plan (last update January 2020)*. 2020. URL: https://hilumilhc.web.cern.ch/content/hl-lhc-project (visited on Jan. 14, 2020).

[40] ATLAS Collaboration. *Technical Design Report for the ATLAS Inner Tracker Pixel Detector*. Tech. rep. 2017. URL: https://cds.cern.ch/record/2285585.

[41] ATLAS Collaboration. *Technical Design Report for the ATLAS Inner Tracker Strip Detector*. Tech. rep. 2017. URL: https://cds.cern.ch/record/2257755.

[42] ATLAS Collaboration. *Expected Tracking Performance of the ATLAS Inner Tracker at the HL-LHC*. Tech. rep. 2019. URL: http://cds.cern.ch/record/2669540.

[43] *IceCube, South Pole Neutrino Obseratory.* URL: https://icecube.wisc.edu/ (visited on Mar. 23, 2020).

[44] H. Kolanoski and N. Wermes. *Teilchendetektoren, Grundlagen und Anwendung.* Springer Spektrum, 2016. DOI: 10.1007/978-3-662-45350-6.

[45] W. R. Leo. *Techniques for Nuclear and Particle Physics Experiments, A How-to Approach.* Springer, 1994. DOI: 10.1007/978-3-642-57920-2.

[46] G. Lutz. *Semiconductor Radiation Detectors, Device Physics.* Springer, 2007. DOI: 10.1007/978-3-540-71679-2.

[47] S. Sze. *Semiconductor Devices, Physics and Technology.* John Wiley & Sons, 1985.

[48] J. Stachel. *Detectors in Nuclear and Particle Physics.* 2018. URL: https://www.physi.uni-heidelberg.de/~fschney/detektoren/detector-2018-4.pdf (visited on Apr. 15, 2020).

[49] F. Wizemann. "Temperature Scaling of Leakage Current in Irradiated Silicon Sensors". PhD Thesis. TU Dortmund, 2019.

[50] H. Pernegger and M. Friedl. *Convoluted Landau and Gaussian Fitting Function.* 2015. URL: https://root.cern.ch/doc/v614/langaus_8C_source.html (visited on Feb. 14, 2020).

[51] M. Berger et al. *Stopping-Power and Range Tables for Electrons, Protons, and Helium Ions.* URL: https://www.nist.gov/pml/stopping-power-range-tables-electrons-protons-and-helium-ions (visited on Mar. 25, 2020).

[52] Z. He. Review of the Shockley–Ramo theorem and its application in semiconductor gamma-ray detectors. *Nucl. Instr. Meth. A* 463 (2001). DOI: 10.1016/S0168-9002(01)00223-6.

[53] O. Krasel. "Charge Collection in Irradiated Silicon-Detectors. A Study of the Operation Conditions of Silicon Sensors in the ATLAS Pixel Detector". PhD Thesis. TU Dortmund, 2004.

[54] G. Lindström. Radiation damage in silicon detectors. *Nucl. Instr. Meth. A* 512 (2002). DOI: 10.1016/S0168-9002(03)01874-6.

[55] M. Moll. "Radiation damage in silicon particle detectors: Microscopic defects and macroscopic properties". PhD Thesis. Hamburg Univ., 1999.

[56] J. Wüstenfeld. "Characterisation of Ionisation-Induced Surface Effects for the Optimisation of Silicon-Detectors for Particle Physics Applications". PhD Thesis. Dortmund Univ., 2001.

[57] G. Troska. "Development and operation of a testbeam setup for qualification studies of ATLAS Pixel Sensors". PhD Thesis. TU Dortmund, 2012.

[58] M. Huhtinen. Simulation of non-ionising energy loss and defect formation in silicon. *Nucl. Instr. Meth. A* 491 (2002). DOI: 10.1016/S0168-9002(02)01227-5.

[59] G. Lindström et al. Radiation hard silicon detectors—developments by the RD48 (ROSE) collaboration. *Nucl. Instr. Meth. A* 466 (2001). DOI: 10.1016/S0168-9002(01)00560-5.

[60] FE-I4 Collaboration. The FE-I4B Integrated Circuit Guide. Version 2.3 (2012). URL: https://indico.cern.ch/event/261840/contributions/1594374/attachments/462649/641213/FE-I4B_V2.3.pdf.

[61] G. Kramberger. "Signal development in irradiated silicon detectors". PhD Thesis. Ljubljana Univ., 2001.

[62] N. Wermes. Pixel detectors ... where do we stand? *Nucl. Instr. Meth. A* 924 (2019). DOI: 10.1016/j.nima.2018.07.003.

[63] F. Hüggig. "Der ATLAS Pixelsensor, Der state-of-the-art Pixelsensor für teilchenphysikalische Anwendungen mit extrem hohen Strahlungsfeldern". PhD Thesis. Dortmund Univ., 2001.

[64] T. Wittig. "Slim Edge Studies, Design and Quality Control of Planar ATLAS IBL Pixel Sensors". PhD Thesis. TU Dortmund, 2013.

[65] C. da Viá, G. F. Betta, and S. Parker. *Radiation Sensors with 3D Electrodes*. CRC Press, 2019.

[66] E. Currás et al. First study of small-cell 3D Silicon Pixel Detectors for the High Luminosity LHC (2018). URL: https://cds.cern.ch/record/2622152.

[67] G. Aad et al. ATLAS pixel detector electronics and sensors. *JINST* 3 (2008). DOI: 10.1088/1748-0221/3/07/P07007.

[68] B. Abbott et al. Production and integration of the ATLAS Insertable B-Layer. *JINST* 13 (2018). DOI: 10.1088/1748-0221/13/05/t05008.

[69] RD53 Collaboration. *The RD53A Integrated Circuit*. Tech. rep. CERN, 2017. URL: http://cds.cern.ch/record/2287593.

[70] K. Dette. "Commissioning of the ATLAS Insertable B-Layer and first operation experience". PhD Thesis. TU Dortmund, 2017.

[71] G. Casse et al. Enhanced efficiency of segmented silicon detectors of different thicknesses after proton irradiations up to $1\times10^{16}\,\mathrm{n_{eq}cm^2}$. *Nucl. Instr. Meth. A* 624 (2010). DOI: 10.1016/j.nima.2010.02.134.

[72] I. Mandić et al. Annealing effects in $\mathrm{n^+}$–p strip detectors irradiated with high neutron fluences. *Nucl. Instr. Meth. A* 629 (2011). DOI: 10.1016/j.nima.2010.11.057.

[73] S. Altenheiner et al. Planar slim-edge pixel sensors for the ATLAS upgrades. *JINST* 7 (2012). DOI: 10.1088/1748-0221/7/02/C02051.

[74] *RCE Data Acquisition Framework Development Portal*. URL: https://rceproject.web.cern.ch/ (visited on Mar. 30, 2020).

[75] *USBpix - USB based readout system for ATLAS FE-I3 and FE-I4*. URL: http://icwiki.physik.uni-bonn.de/twiki/bin/view/Systems/UsbPix (visited on Mar. 30, 2020).

[76] M. Backhaus et al. Development of a versatile and modular test system for ATLAS hybrid pixel detectors. *Nucl. Instr. Meth. A* 650 (2011). DOI: 10.1016/j.nima.2010.12.087.

[77] *STcontrol User Guide*. URL: http://icwiki.physik.uni-bonn.de/twiki/bin/view/Systems/STcontrolI4 (visited on Mar. 31, 2020).

[78] J.-C. Beyer. "Optimisation of Pixel Modules for the ATLAS Inner Tracker at the High-Luminosity LHC". PhD Thesis. LMU Munich, 2019.

[79] A. Gisen. "Quad module prototypes and design improvement studies of planar n^+-in-n silicon pixel sensors for the ATLAS Inner Tracker upgrade". PhD Thesis. TU Dortmund, 2018.

[80] *E4control, A Python Based Software for Device Controlling and Data Taking*. URL: https://github.com/sdungs/E4control (visited on May 18, 2020).

[81] S. Di Pede. "Guard rings investigation of silicon sensors with modified pixel implant shapes in the context of the ATLAS experiment". Master Thesis. TU Dortmund, 2020.

[82] F. Wizemann. "Building and Testing of a Setup for Capacitance Measurements of ATLAS-Pixel-Sensors Under the Influence of High-Voltage". Master Thesis. TU Dortmund, 2015.

[83] J. Helmig. "Investigation of Modified Pixel Implantations for Planar n^+-in-n Silicon Sensors". Master Thesis. TU Dortmund, 2015.

[84] A.-K. Raytarowski. "Comparison of Leakage Current Characteristics of the Pixel Designs of Irradiated and non-Irradiated REINER Pixel Sensors". Master Thesis. TU Dortmund, 2018.

[85] A. Macchiolo. Technical Specification and Acceptance Criteria for the Planar Pixel Sensors for the ITkproject (2017). URL: https://cds.cern.ch/record/2255076.

[86] M. Grothe. "Laboratory Studies of Planar n^+-in-n Silicon Pixel Sensors with Modified Pixel Implantations for the ATLAS Experiment". Master Thesis. TU Dortmund, 2017.

[87] S. Müller. "Aufbau und Untersuchung an einer ATLAS-Pixel Teststrahl Anordnung". Bachelor Thesis. TU Dortmund, 2010.

[88] *Nuclear Data Services*. URL: https://www-nds.iaea.org/ (visited on Apr. 21, 2020).

[89] S. Terzo. *fei4Analyzer*. URL: https://github.com/terzo/fei4Analyzer (visited on Apr. 21, 2020).

[90] R. Diener et al. The DESY II test beam facility. *Nucl. Instr. Meth. A* 922 (2019). DOI: 10.1016/j.nima.2018.11.133.

[91] *Schematic Layout of a Test Beam at DESY*. URL: https://particle-physics.desy.de/test_beams_at_desy/beam_generation/index_ger.html (visited on Apr. 22, 2020).

[92] *SBA, Secondary Beam Areas of the PS, SPS machines: NTOF, AD, East Area, North Area, AWAKE*. URL: http://sba.web.cern.ch/sba/ (visited on May 7, 2020).

[93] T. Bisanz. "Test beam studies of pixel detector prototypes for the ATLAS-Experiment at the High Luminosity Large Hadron Collider". PhD Thesis. Göttingen Univ., 2018.

[94] H. Jansen et al. Performance of the EUDET-type beam telescopes. *EPJ Techn. Instr.* 3 (2016). DOI: 10.1140/epjti/s40485-016-0033-2.

[95] C. Hu-Guo et al. First reticule size MAPS with digital output and integrated zero suppression for the EUDET-JRA1 beam telescope. *Nucl. Instr. Meth. A* 623 (2010). DOI: 10.1016/j.nima.2010.03.043.

[96] B. Verlaat et al. The ATLAS IBL CO_2 cooling system. *JINST* 12 (2017). DOI: 10.1088/1748-0221/12/02/c02064.

[97] D. Cussans. Description of the JRA1 Trigger Logic Unit (TLU), v0.2c (2009). URL: https://www.eudet.org/e26/e28/e42441/e57298/EUDET-MEMO-2009-04.pdf.

[98] P. Ahlburg et al. EUDAQ — A Data Acquisition Software Framework for Common Beam Telescopes. *JINST* 15 (2020). DOI: 10.1088/1748-0221/15/01/p01038.

[99] EUDAQ Development Team. EUDAQ User Manual. EUDAQ version v1.7 (2016). URL: http://eudaq.github.io/manual/EUDAQUserManual_v1.pdf (visited on May 6, 2020).

[100] *EUTelescope, a generic beam telescope data analysis framework*. URL: https://eutelescope.github.io/ (visited on May 6, 2020).

[101] T. Bisanz, A. Morton, and I. Rubinskiy. EUTelescope 1.0: Reconstruction Software for the AIDA Testbeam Telescope (2015). URL: http://cds.cern.ch/record/2000969.

[102] *TBMon2, The ATLAS Pixel testbeam analysis framework*. URL: https://gitlab.cern.ch/tbmon2 (visited on May 6, 2020).

[103] *ILC Soft*. URL: https://ilcsoft.desy.de/portal/ (visited on July 9, 2020).

[104] S. Fleischmann. "Track Reconstruction in the ATLAS Experiment: The Deterministic Annealing Filter". PhD Thesis. Wuppertal Univ., 2006.

[105] R. E. Kalman. A New Approach to Linear Filtering and Prediction Problems. *J. Basic Eng.* 82 (1960). DOI: 10.1115/1.3662552.

[106] C. Kleinwort. General broken lines as advanced track fitting method. *Nucl. Instr. Meth. A* 673 (2012). DOI: 10.1016/j.nima.2012.01.024.

[107] V. Blobel. Software alignment for tracking detectors. *Nucl. Instr. Meth. A* 566 (2006). DOI: 10.1016/j.nima.2006.05.157.

[108] G. Cowan. Error analysis for efficiency (2008). URL: https://www.pp.rhul.ac.uk/~cowan/stat/notes/efferr.pdf.

[109] A. Rummler. "Investigation of radiation damage in n^+-in-n planar pixel sensors for future ATLAS pixel detector upgrades". PhD Thesis. TU Dortmund, 2014.

[110] C. J. Clopper and E. S. Pearson. The use of confidence or fiducial limits illustrated in the case of the binomial. *Biometrika* 26 (1934). DOI: 10.1093/biomet/26.4.404.

[111] *TEfficiency Class Reference, Class to handle efficiency histograms*. URL: https://root.cern.ch/doc/master/classTEfficiency.html (visited on May 14, 2020).

[112] R. Michallek. "Test Beam Studies of unirradiated Planar n^+-in-n Silicon Pixel Sensors with Modified Pixel Implantations for the ATLAS Experiment". Master Thesis. TU Dortmund, 2017.

[113] M. Weers. "Test Beam Studies of Planar n^+-in-n Silicon Pixel Sensors with Modified Pixel Implantations for the ATLAS Experiment". Master Thesis. TU Dortmund, 2017.

[114] *Reactor Centre, Jožef Stefan Institute*. URL: http://www.rcp.ijs.si/en/index.html (visited on June 3, 2020).

[115] *Annular Core Research Reactor facility, Sandia National Laboratories*. URL: https://www.sandia.gov/research/facilities/annular_core_research_reactor.html (visited on June 3, 2020).

[116] M. Moll, E. Fretwurst, and G. Lindström. Leakage current of hadron irradiated silicon detectors – material dependence. *Nucl. Instr. Meth. A* 426 (1999). DOI: 10.1016/S0168-9002(98)01475-2.

[117] K. Ambrožič, G. Žerovnik, and L. Snoj. Computational analysis of the dose rates at JSI TRIGA reactor irradiation facilities. *Applied Radiation and Isotopes* 130 (2017). DOI: https://doi.org/10.1016/j.apradiso.2017.09.022.

[118] E. J. Parma et al. Radiation Characterization Summary: ACRR Polyethylene-Lead-Graphite (PLG) Bucket Located in the Central Cavity on the 32-Inch Pedestal at the Core Centerline (ACRR-PLG-CC-32-cl). (2015). DOI: 10.2172/1195437.

[119] P. Dervan et al. The Birmingham Irradiation Facility. *Nucl. Instr. Meth. A* 730 (2013). DOI: 10.1016/j.nima.2013.05.156.

[120] P. Dervan et al. Upgrade to the Birmingham Irradiation Facility. *Nucl. Instr. Meth. A* 796 (2015). DOI: 10.1016/j.nima.2015.02.005.

[121] *PS-IRRAD Proton Facility*. URL: https://ps-irrad.web.cern.ch/ (visited on June 4, 2020).

[122] B. Gkotse et al. IRRAD: The New 24 GeV/c Proton Irradiation Facility at CERN. AIDA-2020-CONF-2016-006 (2015). URL: https://cds.cern.ch/record/2237333.

[123] P. Allport et al. Experimental determination of proton hardness factors at several irradiation facilities. *JINST* 14 (2019). DOI: 10.1088/1748-0221/14/12/p12004.

[124] K. Hara et al. Charge collection and field profile studies of heavily irradiated strip sensors for the ATLAS inner tracker upgrade. *Nucl. Instr. Meth. A* 831 (2016). DOI: https://doi.org/10.1016/j.nima.2016.04.035.

[125] ATLAS Collaboration. Modelling radiation damage to pixel sensors in the ATLAS detector. *JINST* 14 (2019). DOI: 10.1088/1748-0221/14/06/p06012.

[126] F. Barth. "Studies of the charge collection of silicon diodes and sensors with modified ATLAS Pixel implantations using Transient Current Technique". Master Thesis. TU Dortmund, 2020.

[127] G. Kramberger. Reasons for high charge collection efficiency of silicon detectors at HL-LHC fluences. *Nucl. Instr. Meth. A* 924 (2019). DOI: https://doi.org/10.1016/j.nima.2018.08.034.

[128] M. Milovanović et al. Effects of accelerated long term annealing in highly irradiated n^+-p strip detector examined by Edge-TCT. *JINST* 7 (2012). DOI: 10.1088/1748-0221/7/06/p06007.

[129] G. Kramberger et al. Investigation of Irradiated Silicon Detectors by Edge-TCT. *IEEE Transactions on Nuclear Science* 57 (2010). DOI: 10.1109/TNS.2010.2051957.

[130] S. Dungs. "Design und Charakterisierung von planaren n^+-in-p Pixelsensoren für das ATLAS Experiment". Master Thesis. TU Dortmund, 2017.

Danksagung

Als erstes möchte ich mich bei Herrn Prof. Dr. Kröninger und Herrn Prof. Dr. Dr. Rhode bedanken, dass Sie meine Arbeit begutachten und bewerten. Ich bin dankbar, dass Herr Prof. Dr. Kröninger es mir ermöglicht hat, das Forschungsthema meiner Masterarbeit am Lehrstuhl E4 fortzusetzen. Ich hatte eine tolle Zeit an Ihrem Lehrstuhl mit einer unterstützenden, produktiven Arbeitsatmosphäre und netten Arbeitskollegen. Danke Jens, für dein offenes Ohr für Fragen und Diskussionen und die gute Betreuung.
Furthermore, I would like to thank the test beam coordinators, Andre, Jörn and Marco for supporting my measurements in numerous test beam campaigns at CERN and DESY. Even if my REINER pixel modules were not prioritized in ATLAS ITk test beam campaigns, you made it possible to study them intensively.
Bei den zahlreichen Dienstreisen zu Testbeam-Einrichtungen hatte ich große Unterstützung durch viele Kolleginnen und Kollegen, die einen enormen Beitrag zu dieser Arbeit geleistet haben: Ohne eure Hilfe wären die Daten nicht aufgenommen worden, deren Ergebnisse hier präsentiert wurden! Danke, Alex, Andreas, Anna-Katharina, Felix, Jonas, Marius G., Marius H., Mike, Valerie, Sascha und Raphael. Besonderer Dank gilt Andreas und Valerie mit denen ich zum Teil mehr Zeit auf Dienstreisen verbracht habe als mit meinem Mann in meiner Freizeit. Auch Mikes Einsatz soll hier besonders hervorgehoben werden, der an Wochenenden und nach Feierabend noch kurzfristig Module für mich reparierte, wenn ich sie dringend brauchte. Vielen Dank auch an Markus, der mit vielen Papieren dafür gesorgt hat, dass ich bestrahlte Module von und nach Dortmund transportieren konnte.
Ich möchte mich bei Felix, Jens, Paul und Volker bedanken für konstruktive Kommentare und Kritik an dieser Arbeit, auch wenn mich das Kapitel 7 manchmal fast verzweifeln ließ. Meine Familie, Freunde und die “Kaffeeläuschen” haben mich wieder aufgebaut und mich zum Weitermachen motiviert. Ich bin dankbar dafür, dass ihr das immer wieder tut.
Als letztes möchte ich mich bei meiner Familie bedanken: Ihr seid immer für mich da, ich kann auf euch zählen und ihr unterstützt mich in allem, was ich tue: Danke! Danke Volker, du weißt, was du für mich bedeutest.

A Measurements of Non-Irradiated Modules

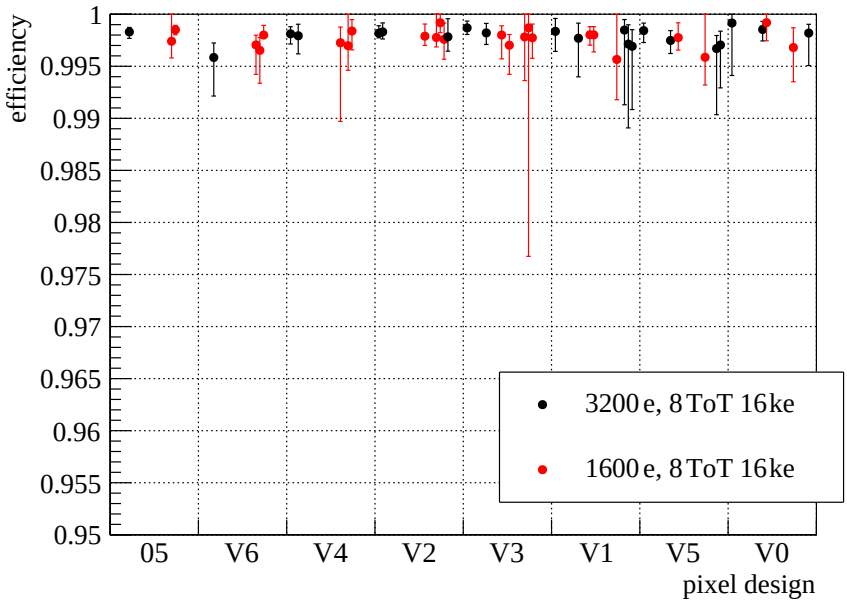

Figure A.1: Efficiencies for the groups with different pixel designs of the non-irradiated REINER module R2 investigated at the DESY test beam campaign November 2013 and biased with 150 V.

Table A.1: Efficiencies of the non-irradiated module R2 biased with 150 V measured at the test beam campaign November 2013 at DESY. For the runs 282 to 424 and 583 to 667 the module is tuned to a threshold value of 3200 e and a ToT response of 8 for a reference charge of 16 ke while for the runs 425 to 582 it is tuned to a lower threshold value of 1600 e.

	efficiencies of the groups with different pixel designs [%]							
runs	05	V6	V4	V2	V3	V1	V5	V0
282-288			$99.81^{+0.07}_{-0.10}$	$99.82^{+0.07}_{-0.05}$	$99.87^{+0.07}_{-0.06}$	$99.84^{+0.12}_{-0.19}$	$99.84^{+0.07}_{-0.11}$	$99.92^{+0.08}_{-0.50}$
292-309				$99.83^{+0.09}_{-0.07}$				
310-322			$99.79^{+0.11}_{-0.17}$					
324-334		$99.58^{+0.14}_{-0.37}$						
340-354	$99.83^{+0.04}_{-0.06}$							
356-370					$99.82^{+0.09}_{-0.11}$			
371-391						$99.77^{+0.15}_{-0.37}$		
392-405							$99.75^{+0.09}_{-0.13}$	
406-424								$99.85^{+0.08}_{-0.11}$
425-436					$99.80^{+0.09}_{-0.23}$	$99.80^{+0.08}_{-0.10}$	$99.78^{+0.14}_{-0.12}$	$99.92^{+0.08}_{-0.17}$
477-492						$99.80^{+0.08}_{-0.16}$		
494-509					$99.7^{+0.10}_{-0.28}$			
510-541				$99.79^{+0.12}_{-0.09}$				
542-557			$99.73^{+0.15}_{-0.76}$					
562-576		$99.71^{+0.09}_{-0.28}$						
577-582	$99.74^{+0.26}_{-0.16}$	$99.65^{+0.12}_{-0.32}$	$99.70^{+0.30}_{-0.24}$	$99.78^{+0.22}_{-0.09}$	$99.78^{+0.22}_{-0.42}$			
583-592	$99.85^{+0.04}_{-0.05}$	$99.80^{+0.09}_{-0.03}$	$99.84^{+0.11}_{-0.18}$	$99.92^{+0.08}_{-0.10}$	$99.87^{+0.13}_{-2.20}$	$99.57^{+0.43}_{-0.39}$	$99.59^{+0.41}_{-0.27}$	$99.68^{+0.19}_{-0.33}$
593-624				$99.76^{+0.16}_{-0.19}$	$99.77^{+0.13}_{-0.20}$			
625-639				$99.78^{+0.17}_{-0.14}$		$99.85^{+0.10}_{-0.72}$		
640-656						$99.71^{+0.19}_{-0.81}$	$99.67^{+0.13}_{-0.64}$	
657-667						$99.69^{+0.16}_{-0.61}$	$99.70^{+0.13}_{-0.41}$	$99.82^{+0.08}_{-0.31}$

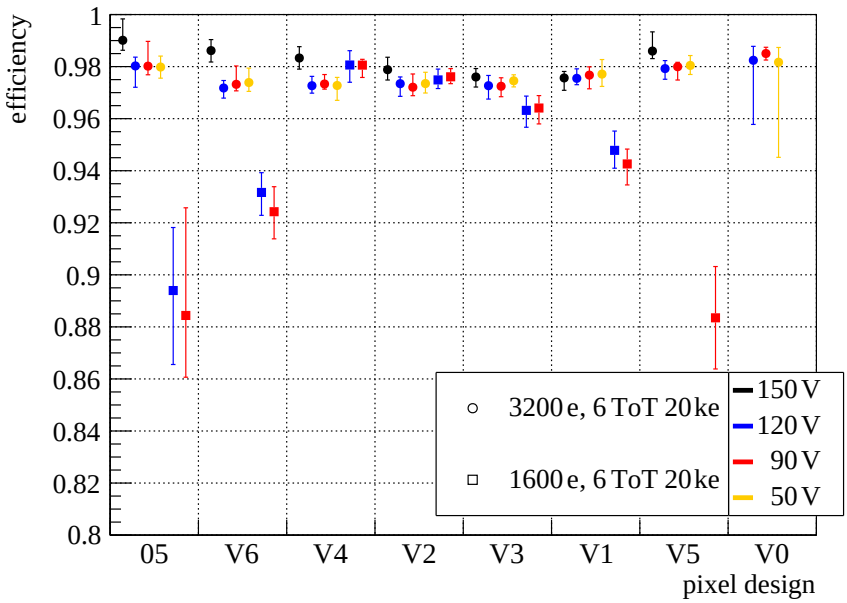

Figure A.2: Efficiencies for the groups with different pixel designs of the non-irradiated REINER module R2 investigated at the CERN test beam campaign August 2016 at four different bias voltages and two tuning settings.

Table A.2: Efficiencies of the non-irradiated module R2 measured at the test beam campaign August 2016 at CERN. The module is measured with the beam focusing the left, middle and right part of the module. Only for the last two measurements in this table the module is centered in the beam and tuned to a threshold value of 1600 e and a ToT response of 6 for a reference charge of 20 ke. For all other measurements the threshold value is set to 3200 e.

bias voltage [V]	efficiencies of the groups with different pixel designs [%]							
	05	V6	V4	V2	V3	V1	V5	V0
150	$99.01^{+0.82}_{-0.38}$	$98.62^{+0.42}_{-0.44}$	$98.33^{+0.44}_{-0.43}$	$97.88^{+0.48}_{-0.40}$	$97.60^{+0.32}_{-0.39}$	$97.56^{+0.25}_{-0.48}$	$98.60^{+0.74}_{-0.29}$	
120	$98.03^{+0.34}_{-0.82}$	$97.18^{+0.29}_{-0.39}$	$97.27^{+0.36}_{-0.29}$	$97.34^{+0.26}_{-0.49}$	$97.27^{+0.39}_{-0.51}$	$97.55^{+0.37}_{-0.24}$	$97.92^{+0.31}_{-0.41}$	$98.24^{+0.53}_{-2.50}$
90	$98.02^{+0.95}_{-0.33}$	$97.32^{+0.70}_{-0.25}$	$97.33^{+0.36}_{-0.20}$	$97.21^{+0.51}_{-0.33}$	$97.24^{+0.33}_{-0.40}$	$97.67^{+0.32}_{-0.53}$	$98.00^{+0.17}_{-0.51}$	$98.50^{+0.24}_{-0.25}$
50	$97.98^{+0.42}_{-0.43}$	$97.39^{+0.55}_{-0.34}$	$97.27^{+0.31}_{-0.57}$	$97.35^{+0.43}_{-0.36}$	$97.46^{+0.23}_{-0.24}$	$97.71^{+0.56}_{-0.47}$	$98.05^{+0.38}_{-0.35}$	$98.17^{+0.57}_{-3.70}$
120	$89.4^{+2.4}_{-2.8}$	$93.17^{+0.76}_{-0.88}$	$98.06^{+0.55}_{-0.66}$	$97.49^{+0.42}_{-0.33}$	$96.32^{+0.55}_{-0.65}$	$94.78^{+0.74}_{-0.69}$		
90	$88.4^{+4.1}_{-2.4}$	$92.42^{+0.96}_{-1.00}$	$98.06^{+0.22}_{-0.47}$	$97.61^{+0.31}_{-0.26}$	$96.41^{+0.48}_{-0.61}$	$94.26^{+0.57}_{-0.81}$	$88.4^{+2.0}_{-2.0}$	

Table A.3: Efficiencies of the non-irradiated module R6 measured at the test beam campaign December 2017 at DESY. The module is tuned to 3200 e, 6 ToT at 20 ke (tuning no. 1), 1600 e, 10 ToT at 10 ke (tuning no. 2), 1000 e, 10 ToT at 10 ke (tuning no. 3) and 1000 e, 7 ToT at 14 ke (tuning no. 4).

tuning	bias	efficiencies of the groups with different pixel designs [%]							
no.	voltage [V]	05	V6	V4	V2	V3	V1	V5	V0
	150		$99.54^{+0.46}_{-2.77}$	$98.97^{+1.03}_{-1.83}$	$98.90^{+1.10}_{-2.34}$	$98.90^{+1.10}_{-1.48}$	$98.99^{+1.01}_{-2.17}$	$98.99^{+1.01}_{-2.80}$	$99.26^{+0.74}_{-2.52}$
1	120		$99.42^{+0.58}_{-5.67}$	$99.29^{+0.71}_{-3}$	$99.02^{+0.98}_{-2.59}$	$99.04^{+0.96}_{-1.99}$	$98.85^{+1.15}_{-1.55}$	$98.76^{+1.24}_{-1.51}$	$99.52^{+0.48}_{-2.37}$
	100		$99.40^{+0.60}_{-4.66}$	$98.99^{+1.01}_{-3.16}$	$99.05^{+0.95}_{-1.85}$	$98.77^{+1.23}_{-5.91}$	$98.77^{+1.23}_{-2.03}$	$99.11^{+0.89}_{-2.58}$	$99.48^{+0.52}_{-3.54}$
	150		$99.31^{+0.69}_{-2.65}$	$99.23^{+0.77}_{-1.39}$	$99.13^{+0.87}_{-1.25}$	$99.00^{+1.00}_{-2.31}$	$98.99^{+0.66}_{-0.92}$	$99.12^{+0.88}_{-2.43}$	$99.51^{+0.49}_{-1.68}$
2	120		$99.67^{+0.33}_{-2.08}$	$99.44^{+0.56}_{-2.03}$	$99.23^{+0.77}_{-2.09}$	$98.77^{+0.84}_{-1.91}$	$98.90^{+1.10}_{-1.68}$	$99.01^{+0.99}_{-1.68}$	$99.73^{+0.27}_{-1.23}$
	100		$99.60^{+0.40}_{-4.86}$	$99.23^{+0.77}_{-1.23}$	$99.21^{+0.79}_{-1.27}$	$99.16^{+0.84}_{-1.22}$	$99.22^{+0.78}_{-1.00}$	$99.17^{+0.83}_{-1.75}$	$99.64^{+0.36}_{-2.86}$
	150		$99.65^{+0.35}_{-2.60}$	$99.29^{+0.71}_{-1.73}$	$99.16^{+0.84}_{-1.15}$	$98.95^{+1.05}_{-1.82}$	$99.11^{+0.89}_{-1.79}$	$99.21^{+0.79}_{-2.21}$	$99.72^{+0.28}_{-1.81}$
3	120		$99.44^{+0.57}_{-2.47}$	$99.39^{+0.61}_{-1.21}$	$99.11^{+0.89}_{-1.63}$	$99.15^{+0.85}_{-1.06}$	$99.08^{+0.92}_{-2.07}$	$99.22^{+0.78}_{-2.73}$	$99.46^{+0.54}_{-3.31}$
	100		$99.62^{+0.38}_{-3.37}$	$99.22^{+0.79}_{-1.51}$	$99.09^{+0.91}_{-1.12}$	$99.13^{+0.87}_{-1.69}$	$99.13^{+0.87}_{-1.41}$	$99.32^{+0.68}_{-1.17}$	$99.63^{+0.37}_{-2.03}$
4	120		$99.42^{+0.58}_{-7.42}$	$99.32^{+0.68}_{-2.76}$	$99.22^{+0.78}_{-2.19}$	$98.96^{+1.04}_{-1.46}$	$98.82^{+1.18}_{-1.76}$	$98.98^{+1.02}_{-1.74}$	$99.35^{+0.65}_{-4.75}$

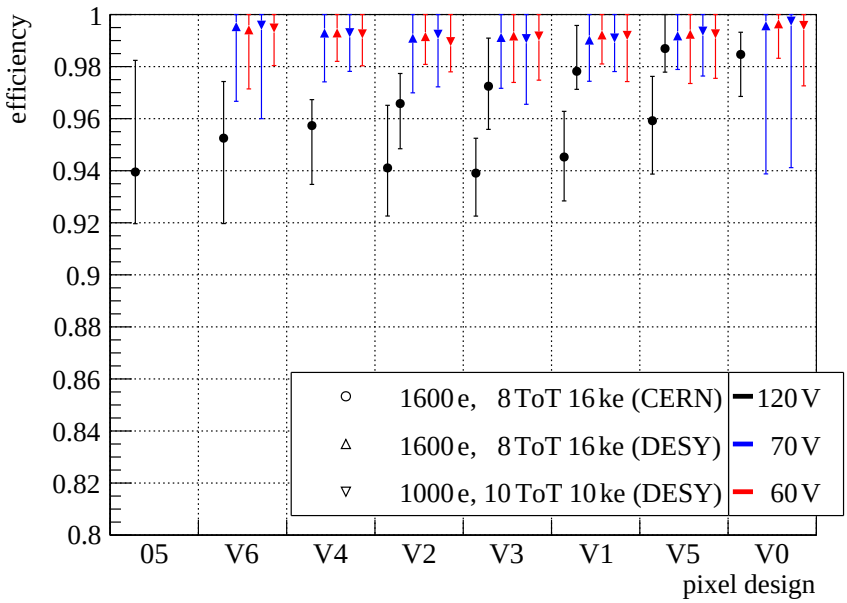

Figure A.3: Efficiencies for the groups with different pixel designs of the non-irradiated REINER module R8 investigated at the CERN test beam campaign October 2017 (dots) and at DESY in December 2017 (triangles). The module is measured at three different bias voltages and two tuning settings.

Table A.4: Efficiencies of the non-irradiated module R8 measured at the test beam campaign October 2017 at CERN tuned to 1600 e, 8 ToT at 16 ke (first two measurements in the table) and at the DESY December 2017 test beam campaign. For the measurements at the DESY test beam facility the module is tuned to 1600 e, 8 ToT at 16 ke (measurements above the dashed line) and 1000 e, 10 ToT at 10 ke (measurements below the dashed line).

bias	efficiencies of the groups with different pixel designs [%]							
vol. [V]	05	V6	V4	V2	V3	V1	V5	V0
120				$94.07^{+2.44}_{-1.81}$	$93.87^{+1.31}_{-1.61}$	$94.51^{+1.77}_{-1.57}$	$95.89^{+1.41}_{-2.02}$	$98.46^{+0.86}_{-1.61}$
120	$93.95^{+4.29}_{-1.99}$	$95.25^{+2.18}_{-3.28}$	$95.73^{+0.997}_{-2.26}$	$96.58^{+1.15}_{-1.74}$	$97.25^{+1.85}_{-1.66}$	$97.82^{+1.76}_{-0.69}$	$98.69^{+1.31}_{-0.91}$	
70		$99.54^{+0.46}_{-2.87}$	$99.29^{+0.71}_{-1.88}$	$99.09^{+0.91}_{-2.1}$	$99.12^{+0.88}_{-1.95}$	$99.02^{+0.98}_{-1.58}$	$99.18^{+0.82}_{-1.29}$	$99.57^{+0.43}_{-5.69}$
60		$99.41^{+0.59}_{-2.27}$	$99.30^{+0.71}_{-1.09}$	$99.15^{+0.85}_{-1.07}$	$99.18^{+0.82}_{-1.79}$	$99.22^{+0.78}_{-1.12}$	$99.24^{+0.76}_{-1.89}$	$99.64^{+0.36}_{-1.32}$
70		$99.59^{+0.41}_{-3.59}$	$99.30^{+0.70}_{-1.49}$	$99.24^{+0.76}_{-2.02}$	$99.07^{+0.93}_{-2.52}$	$99.10^{+0.902}_{-1.29}$	$99.36^{+0.64}_{-1.73}$	$99.75^{+0.25}_{-5.63}$
60		$99.48^{+0.52}_{-1.44}$	$99.26^{+0.74}_{-1.23}$	$98.96^{+1.04}_{-1.16}$	$99.17^{+0.83}_{-1.70}$	$99.20^{+0.80}_{-1.77}$	$99.26^{+0.74}_{-1.71}$	$99.58^{+0.42}_{-2.32}$

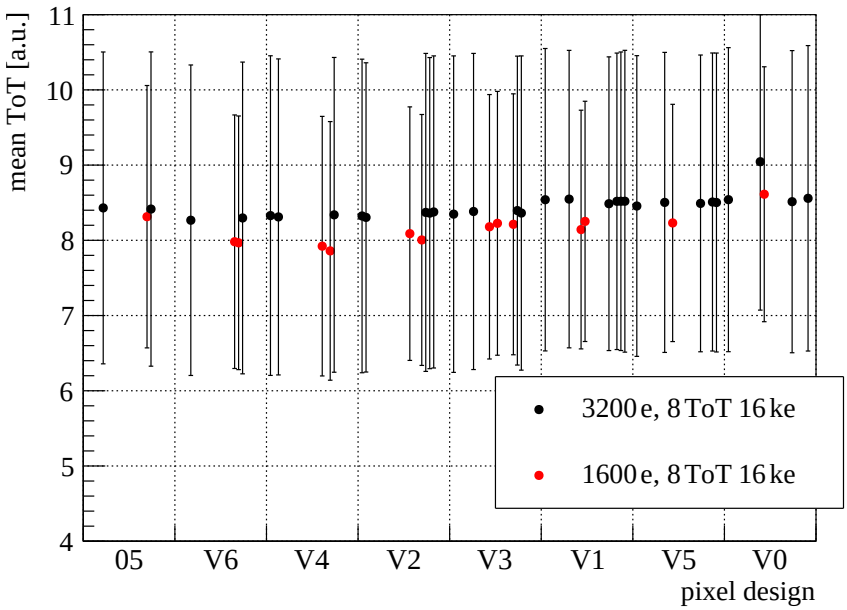

Figure A.4: Mean ToT values for cluster size one of the groups with different pixel designs of the non-irradiated REINER module R2 investigated at the DESY test beam campaign November 2013. The module is biased with 150 V and investigated at two different tuning settings.

Table A.5: Mean ToT values for cluster size one of the non-irradiated module R2 biased with 150 V measured at the test beam campaign November 2013 at DESY. For the runs 282 to 424 and 583 to 667 the module is tuned to a threshold value of 3200 e and a ToT response of 8 for a reference charge of 16 ke while for the runs 425 to 582 it is tuned to a lower threshold value of 1600 e.

	mean ToT [a.u.]							
runs	05	V6	V4	V2	V3	V1	V5	V0
282-288			8.33 ± 2.12	8.32 ± 2.08	8.35 ± 2.10	8.54 ± 2.01	8.46 ± 2.00	8.54 ± 2.02
292-309				8.30 ± 2.06				
310-322			8.31 ± 2.10					
324-334		8.27 ± 2.06						
340-354	8.43 ± 2.07							
356-370					8.38 ± 2.10			
371-391						8.55 ± 1.98		
392-405							8.50 ± 1.99	
406-424								9.04 ± 1.97
425-436					8.18 ± 1.76	8.14 ± 1.59	8.23 ± 1.58	8.61 ± 1.69
477-492						8.25 ± 1.60		
494-509					8.23 ± 1.75			
510-541				8.09 ± 1.69				
542-557			7.92 ± 1.73					
562-576		7.98 ± 1.69						
577-582	8.31 ± 1.74	8.00 ± 1.69	7.86 ± 1.72	8.00 ± 1.67	8.21 ± 1.73			
583-592	8.42 ± 2.09	8.30 ± 2.10	8.34 ± 2.09	8.37 ± 2.11	8.40 ± 2.05	8.49 ± 1.95	8.49 ± 1.97	8.51 ± 2.01
593-624				8.36 ± 2.07	8.36 ± 2.09			
625-639				8.38 ± 2.07		8.52 ± 1.97		
640-656						8.52 ± 1.98	8.51 ± 1.98	
657-667						8.52 ± 2.01	8.50 ± 1.99	8.56 ± 2.03

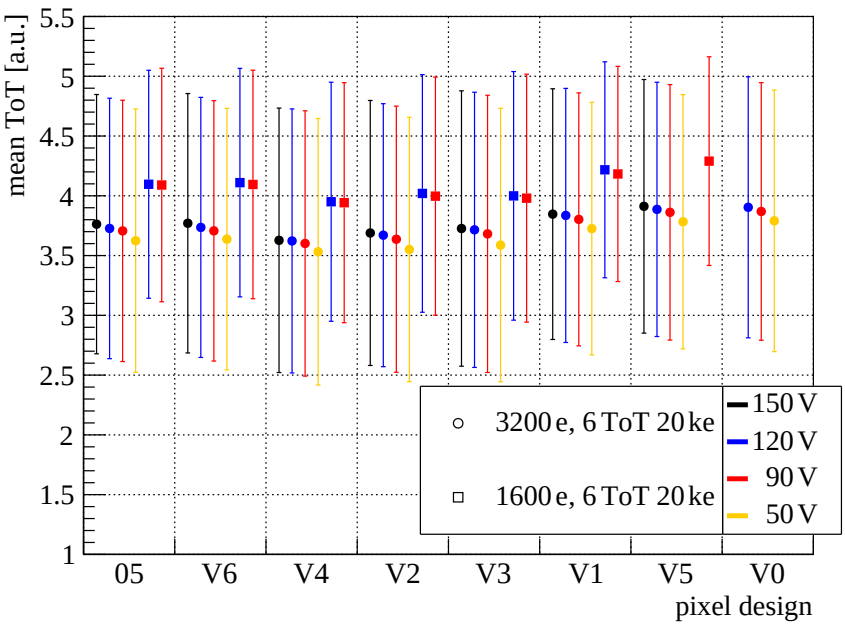

Figure A.5: Mean ToT values for cluster size one of the groups with different pixel designs of the non-irradiated REINER module R2 investigated at the CERN test beam campaign August 2016. The module is measured at four different bias voltages and two tuning settings.

Table A.6: Mean ToT values for cluster size one of the non-irradiated module R2 measured at the test beam campaign August 2016 at CERN. The module is measured with the beam focusing the left, middle and right part of the module. Only for the last two measurements in this table the module is centered in the beam and tuned to a threshold value of 1600 e and a ToT response of 6 for a reference charge of 20 ke. For all other measurements the threshold value is set to 3200 e.

bias vol. [V]	mean ToT [a.u.]							
	05	V6	V4	V2	V3	V1	V5	V0
150	3.76 ± 1.08	3.77 ± 1.08	3.63 ± 1.11	3.69 ± 1.11	3.73 ± 1.15	3.85 ± 1.05	3.91 ± 1.06	
	3.73 ± 1.09	3.74 ± 1.09	3.62 ± 1.10					
120				3.67 ± 1.10	3.72 ± 1.15			
						3.84 ± 1.06	3.89 ± 1.06	3.90 ± 1.09
	3.71 ± 1.09	3.71 ± 1.09	3.60 ± 1.11					
90				3.64 ± 1.11	3.68 ± 1.16			
						3.80 ± 1.06	3.86 ± 1.07	3.87 ± 1.08
	3.62 ± 1.10	3.64 ± 1.09	3.53 ± 1.11					
50				3.55 ± 1.11	3.59 ± 1.14			
						3.73 ± 1.06	3.78 ± 1.06	3.79 ± 1.09
120	4.10 ± 0.95	4.11 ± 0.96	3.95 ± 1.00	4.02 ± 0.99	4.00 ± 1.04	4.22 ± 0.90		
90	4.09 ± 0.98	4.09 ± 0.96	3.94 ± 1.00	4.00 ± 1.00	3.98 ± 1.04	4.18 ± 0.90	4.29 ± 0.87	

Table A.7: Mean ToT values for cluster size one of the non-irradiated module R6 measured at the test beam campaign December 2017 at DESY. The module is tuned to 3200 e, 6 ToT at 20 ke (tuning no. 1), 1600 e, 10 ToT at 10 ke (tuning no. 2), 1000 e, 10 ToT at 10 ke (tuning no. 3) and 1000 e, 7 ToT at 14 ke (tuning no. 4).

tuning	bias	mean ToT [a.u.]							
no.	vol. [V]	05	V6	V4	V2	V3	V1	V5	V0
	150		5.57 ± 1.37	5.52 ± 1.45	5.49 ± 1.39	5.40 ± 1.35	5.26 ± 1.26	5.23 ± 1.25	5.25 ± 1.29
1	120		5.57 ± 1.40	5.51 ± 1.40	5.48 ± 1.41	5.35 ± 1.31	5.25 ± 1.33	5.23 ± 1.26	5.19 ± 1.27
	100		5.54 ± 1.48	5.47 ± 1.44	5.44 ± 1.39	5.36 ± 1.35	5.20 ± 1.30	5.18 ± 1.23	5.18 ± 1.25
	150		13.15 ± 1.63	13.18 ± 1.51	13.21 ± 1.48	13.03 ± 1.60	12.90 ± 1.59	12.57 ± 1.71	12.58 ± 1.65
2	120		13.16 ± 1.60	13.17 ± 1.54	13.24 ± 1.44	13.08 ± 1.55	12.88 ± 1.64	12.62 ± 1.65	12.56 ± 1.77
	100		13.20 ± 1.51	13.15 ± 1.53	13.18 ± 1.52	13.02 ± 1.62	12.90 ± 1.63	12.59 ± 1.65	12.51 ± 1.73
	150		13.27 ± 1.54	13.39 ± 1.37	13.20 ± 1.43	12.85 ± 1.56	12.69 ± 1.53	12.60 ± 1.57	12.64 ± 1.60
3	120		13.34 ± 1.36	13.34 ± 1.43	13.17 ± 1.48	12.81 ± 1.62	12.70 ± 1.59	12.57 ± 1.61	12.64 ± 1.59
	100		13.26 ± 1.55	13.34 ± 1.45	13.13 ± 1.53	12.81 ± 1.61	12.63 ± 1.64	12.55 ± 1.61	12.60 ± 1.65
4	120		7.02 ± 1.57	7.24 ± 2.09	7.37 ± 2.24	7.25 ± 2.08	7.60 ± 2.34	7.32 ± 1.91	7.17 ± 1.47

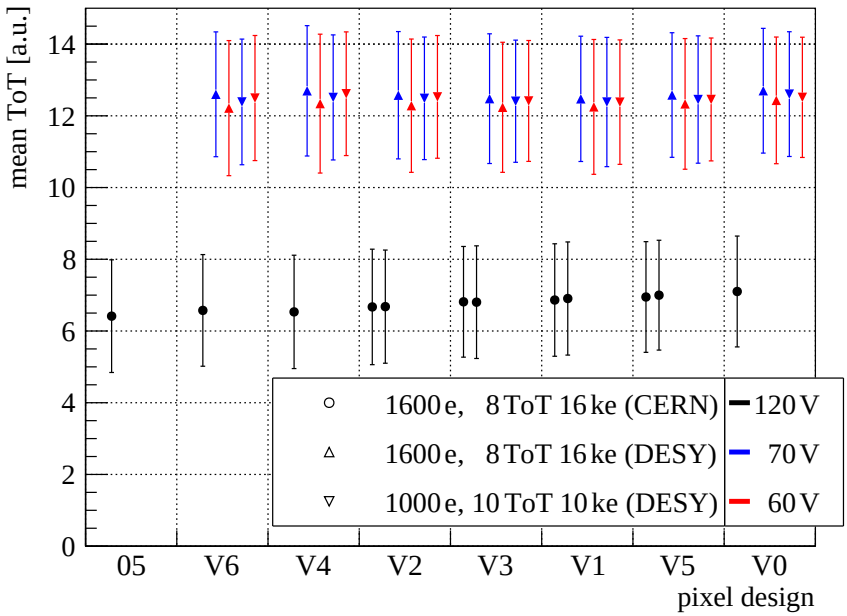

Figure A.6: Mean ToT values for cluster size one of the groups with different pixel designs of the non-irradiated REINER module R8 investigated at the CERN test beam campaign October 2017 (dots) and at DESY in December 2017 (triangles). The module is measured with different bias voltages and tuning settings.

Table A.8: Mean ToT values for cluster size one of the non-irradiated module R8 measured at the test beam campaign October 2017 at CERN tuned to 1600 e, 8 ToT at 16 ke (first two measurements in the table) and at the DESY December 2017 test beam campaign. For the measurements at the DESY test beam facility the module is tuned to 1600 e, 8 ToT at 16 ke (measurements above the dashed line) and 1000 e, 10 ToT at 10 ke (measurements below the dashed line).

bias	mean ToT [a.u.]							
vol. [V]	05	V6	V4	V2	V3	V1	V5	V0
120				6.67 ± 1.61	6.81 ± 1.54	6.86 ± 1.57	6.95 ± 1.54	7.10 ± 1.55
120	6.41 ± 1.57	6.57 ± 1.56	6.53 ± 1.58	6.68 ± 1.58	6.80 ± 1.57	6.91 ± 1.58	67.00 ± 1.53	
70		12.60 ± 1.74	12.70 ± 1.82	12.57 ± 1.78	12.48 ± 1.81	12.47 ± 1.75	12.58 ± 1.74	12.70 ± 1.74
60		12.21 ± 1.88	12.34 ± 1.94	12.28 ± 1.86	12.24 ± 1.81	12.25 ± 1.88	12.33 ± 1.82	12.43 ± 1.77
70		12.39 ± 1.75	12.51 ± 1.74	12.49 ± 1.71	12.41 ± 1.70	12.38 ± 1.80	12.45 ± 1.78	12.61 ± 1.74
60		12.50 ± 1.74	12.62 ± 1.72	12.53 ± 1.71	12.41 ± 1.69	12.38 ± 1.73	12.46 ± 1.71	12.51 ± 1.68

B IV-Measurements of Irradiated Modules

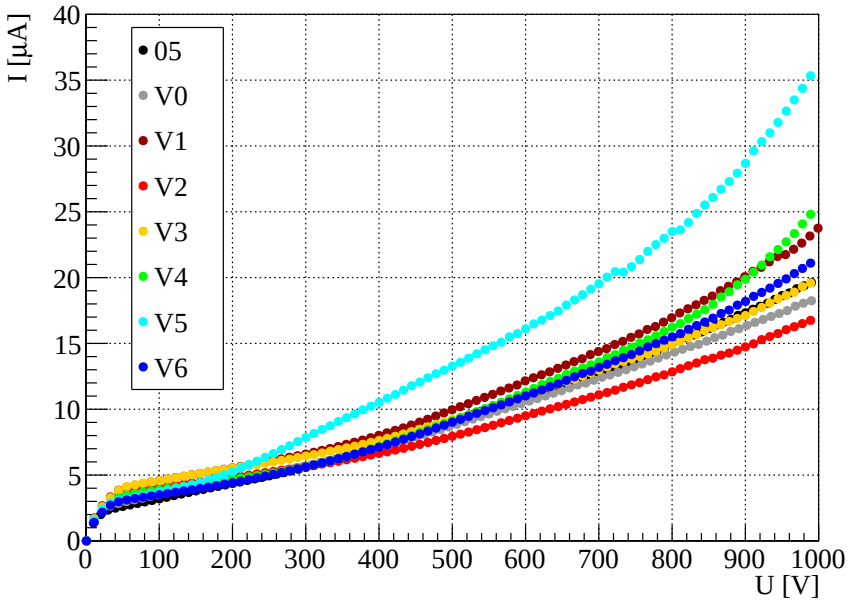

Figure B.1: IV measurement of the individual pixel design groups of module R1, irradiated with neutrons at Sandia to $5 \times 10^{15}\,\mathrm{n_{eq}/cm^2}$. The leakage current is normalized to a sensor temperature of $-30\,^{\circ}\mathrm{C}$.

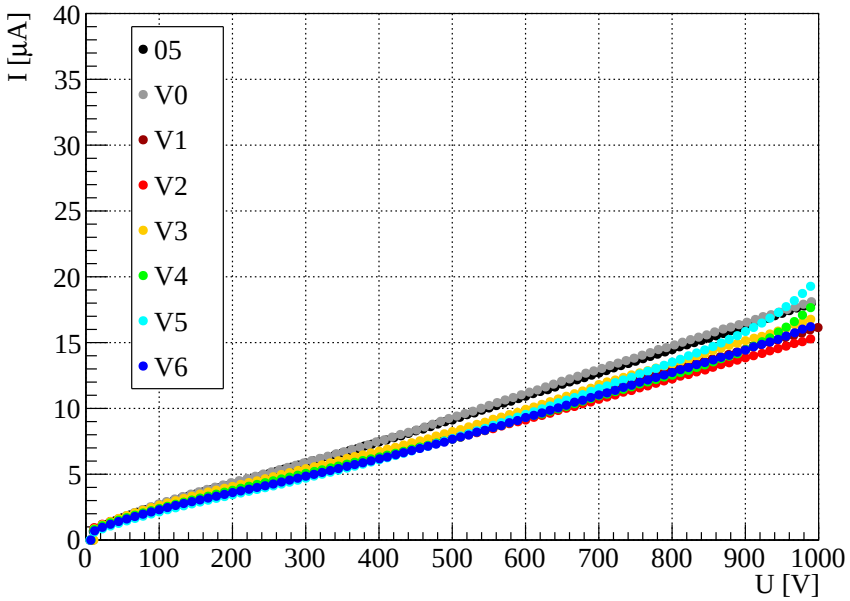

Figure B.2: IV measurement of the individual pixel design groups of module R3, irradiated with neutrons in Ljubljana to $5 \times 10^{15}\,\mathrm{n_{eq}/cm^2}$. The leakage current is normalized to a sensor temperature of $-30\,^{\circ}\mathrm{C}$.

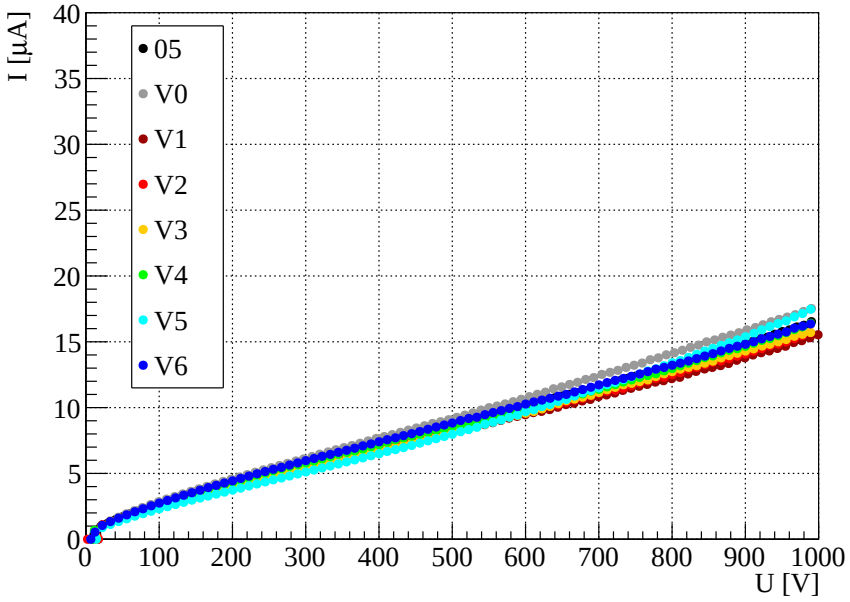

Figure B.3: IV measurement of the individual pixel design groups of module R5, irradiated with neutrons in Ljubljana to $5 \times 10^{15}\,\mathrm{n_{eq}/cm^2}$. The leakage current is normalized to a sensor temperature of $-30\,^{\circ}\mathrm{C}$.

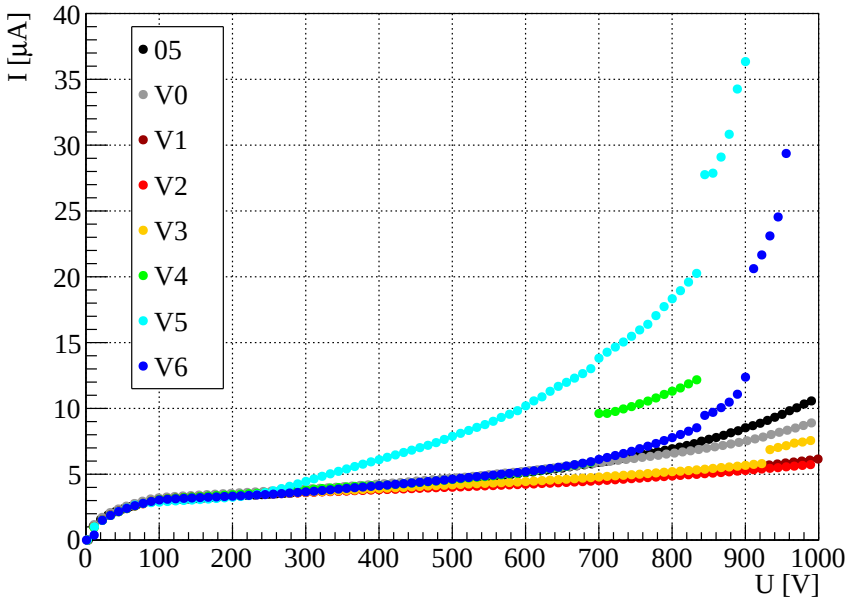

Figure B.4: IV measurement of the individual pixel design groups of module R7, irradiated with neutrons in Ljubljana to $1 \times 10^{15}\,\mathrm{n_{eq}/cm^2}$. The leakage current is normalized to a sensor temperature of $-30\,^{\circ}\mathrm{C}$.

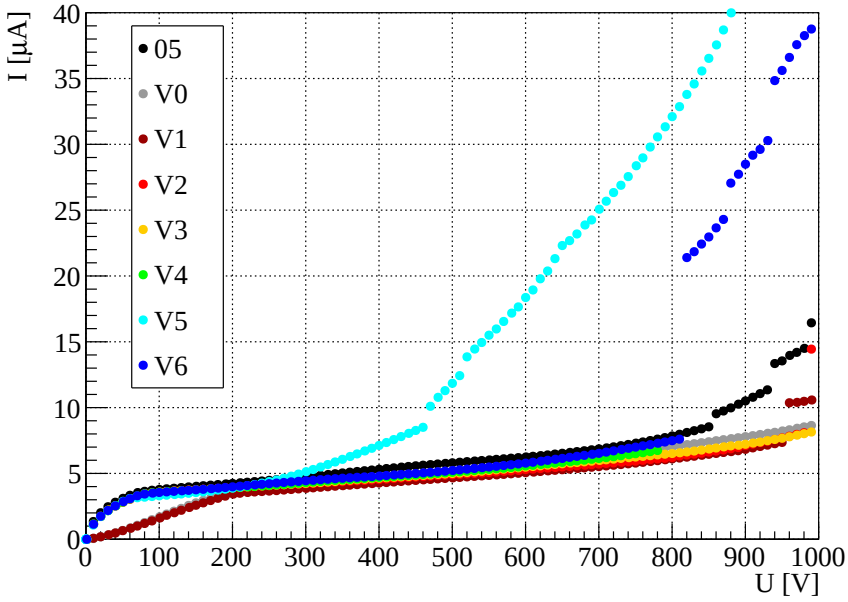

Figure B.5: IV measurement of the individual pixel design groups of module R9, irradiated with neutrons in Ljubljana to $1 \times 10^{15}\,\mathrm{n_{eq}/cm^2}$. The leakage current is normalized to a sensor temperature of $-30\,^{\circ}\mathrm{C}$.

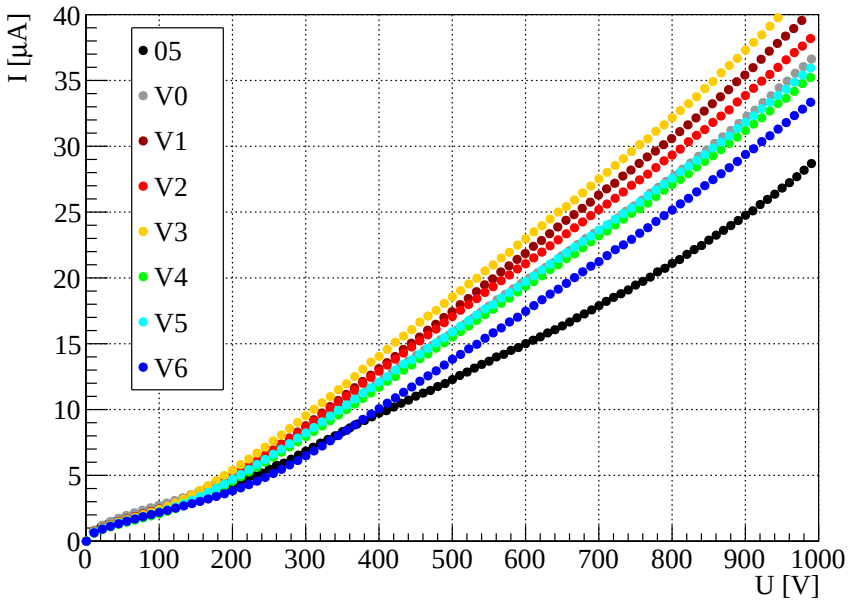

Figure B.6: IV measurement of the individual pixel design groups of module R2, irradiated inhomogeneously with protons at CERN to a mean fluence of $6 \times 10^{15}\,\mathrm{n_{eq}/cm^2}$. The leakage current is normalized to a sensor temperature of $-30\,^{\circ}\mathrm{C}$.

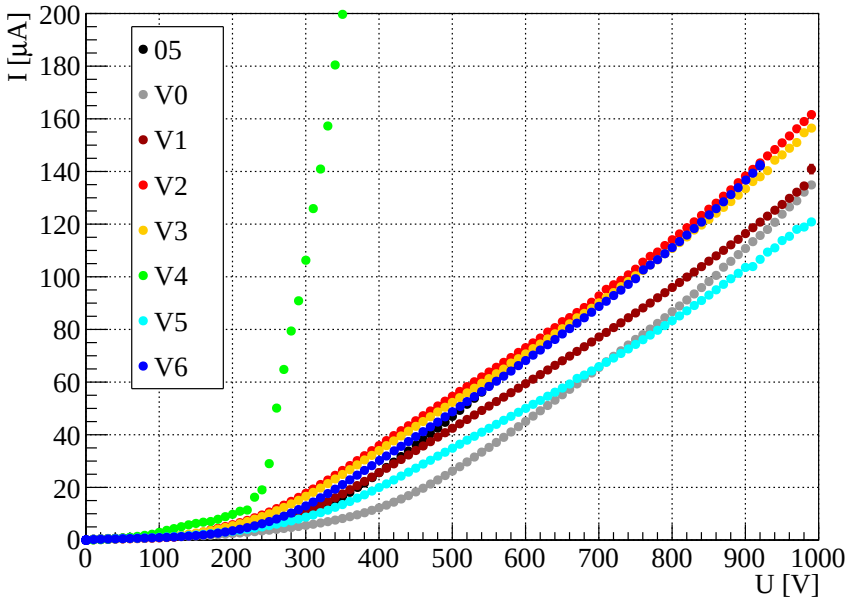

Figure B.7: IV measurement of the individual pixel design groups of module R6, irradiated homogeneously with protons in Birmingham to $5 \times 10^{15}\,\mathrm{n_{eq}/cm^2}$. The leakage current is normalized to a sensor temperature of $-30\,^{\circ}\mathrm{C}$.

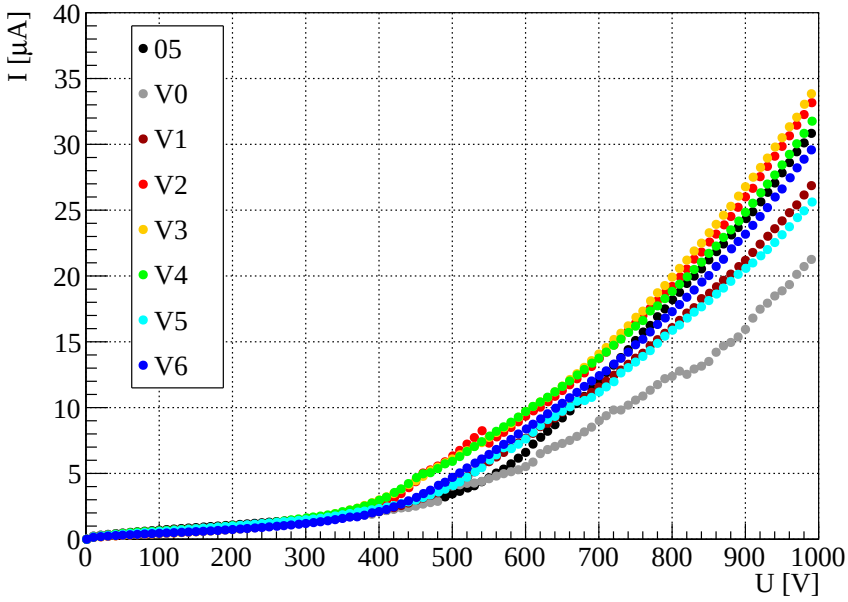

Figure B.8: IV measurement of the individual pixel design groups of module R8, irradiated homogeneously with protons in Birmingham to $1 \times 10^{15}\,\mathrm{n_{eq}/cm^2}$. The leakage current is normalized to a sensor temperature of $-30\,^{\circ}\mathrm{C}$.

C Test Beam Measurements of Irradiated Modules

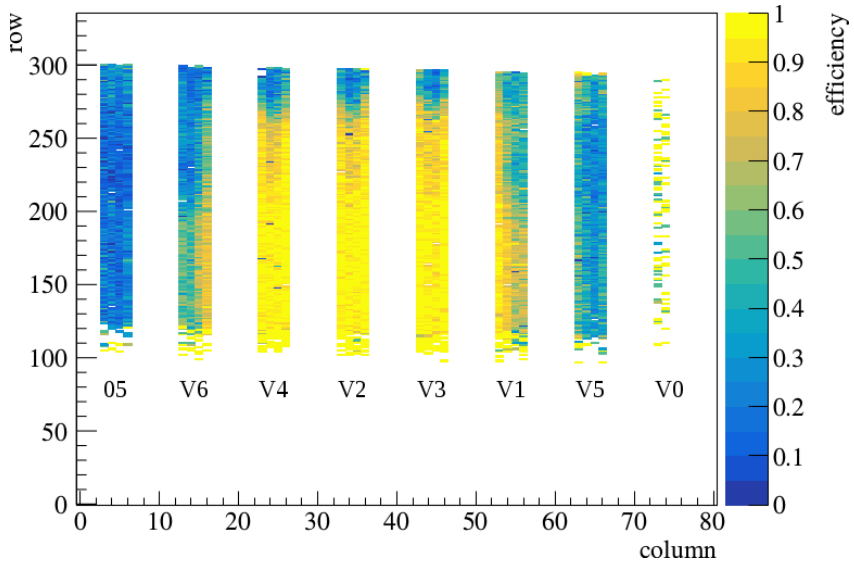

Figure C.1: Efficiency map for the proton irradiated module R8 ($1 \times 10^{15}\,\mathrm{n_{eq}/cm^2}$, Birmingham) measured at the DESY test beam facility in December 2018. The module is tuned to 1600 e, 6 ToT at 20 ke and biased with 800 V.

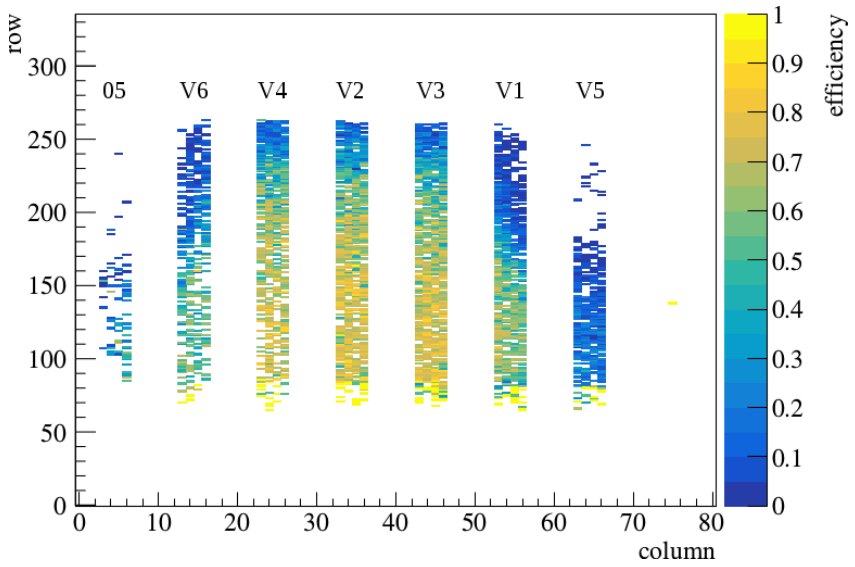

Figure C.2: Efficiency map for the proton irradiated module R6 ($5 \times 10^{15}\,\mathrm{n_{eq}/cm^2}$, Birmingham) measured at the DESY test beam facility in December 2018. The module is tuned to 1600 e, 6 ToT at 20 ke and biased with 400 V.

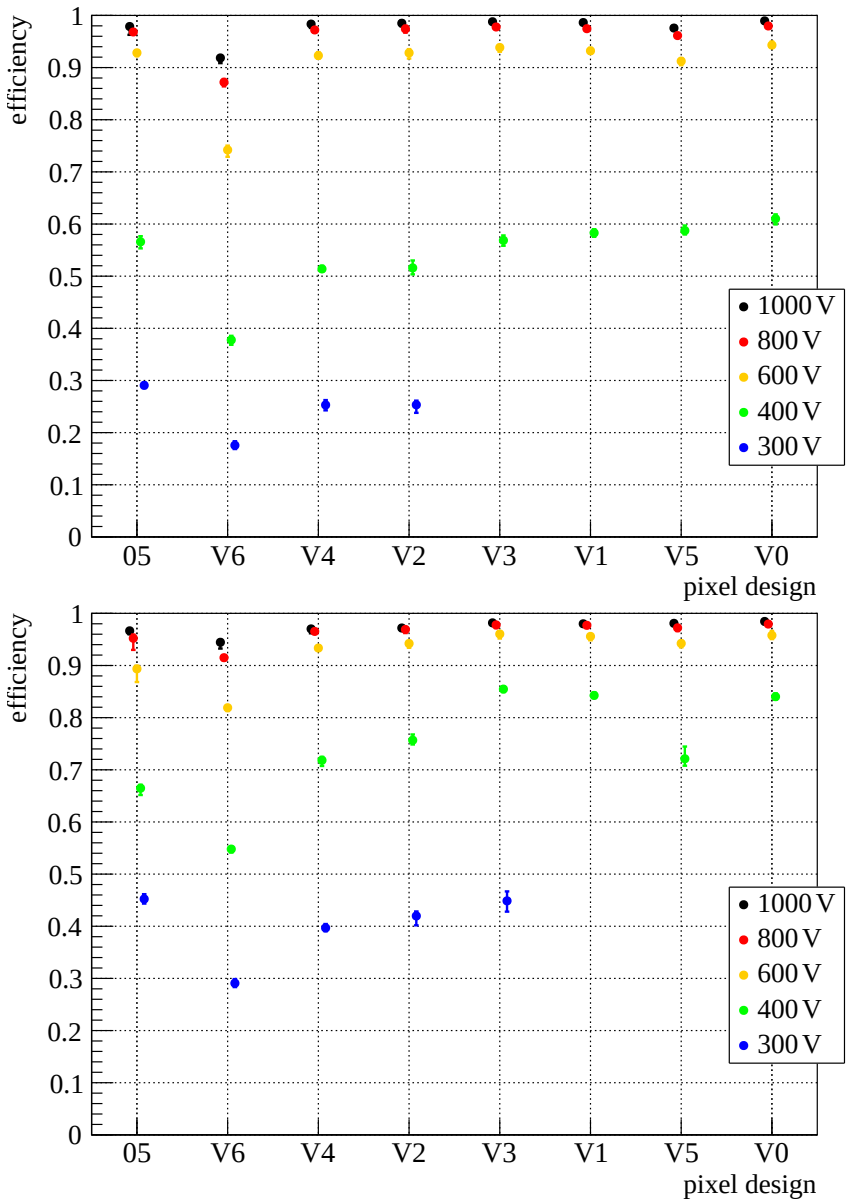

Figure C.3: Efficiencies of the different pixel design groups for the neutron irradiated modules R3 (top) and R5 (bottom), both irradiated to $5 \times 10^{15}\,\mathrm{n_{eq}/cm^2}$ in Ljubljana, measured at the CERN test beam facility in May 2018. The modules are tuned to 3200 e, 6 ToT at 20 ke and measured at different bias voltages.

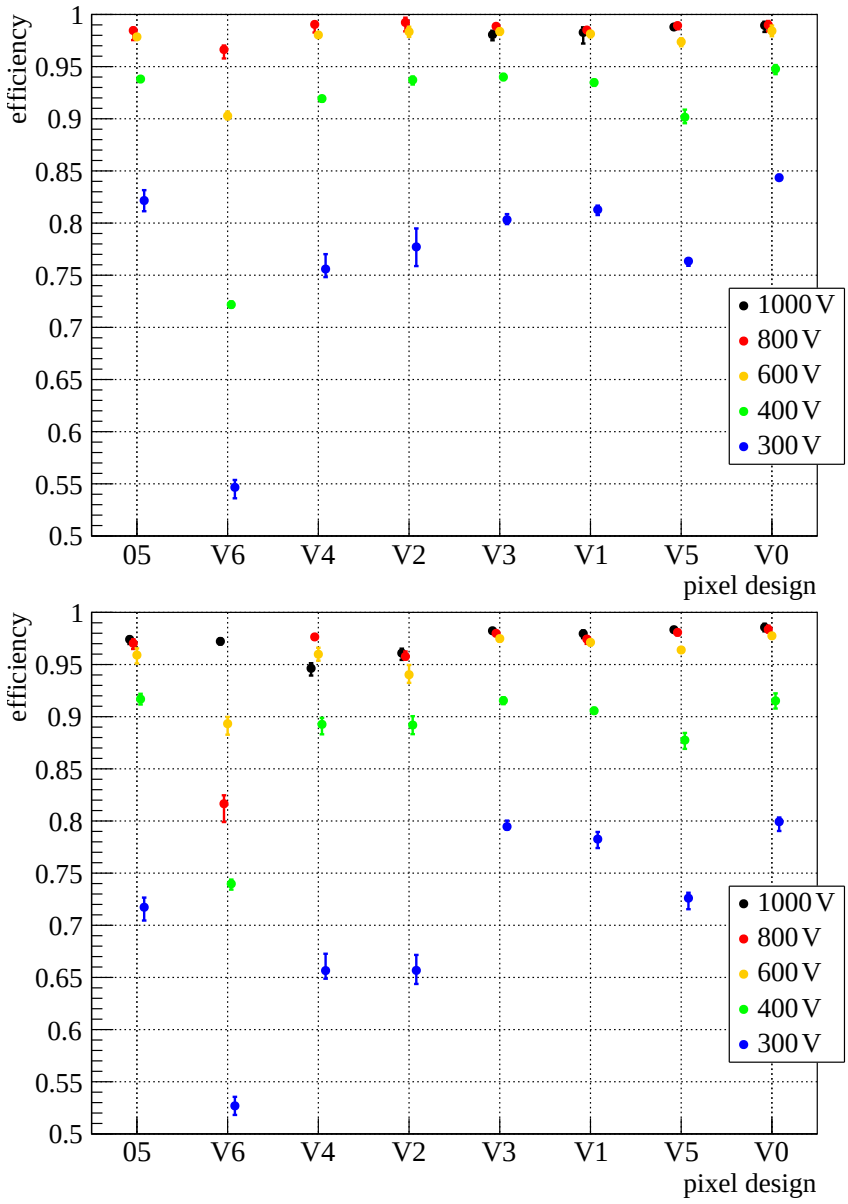

Figure C.4: Efficiencies of the different pixel design groups for the neutron irradiated modules R3 (top) and R5 (bottom), both irradiated to $5 \times 10^{15}\,\mathrm{n_{eq}/cm^2}$ in Ljubljana, measured at the CERN test beam facility in May 2018 at different bias voltages. The module R3 is tuned to 1600 e, 6 ToT at 20 ke and the module R5 to 2000 e, 6 ToT at 20 ke.

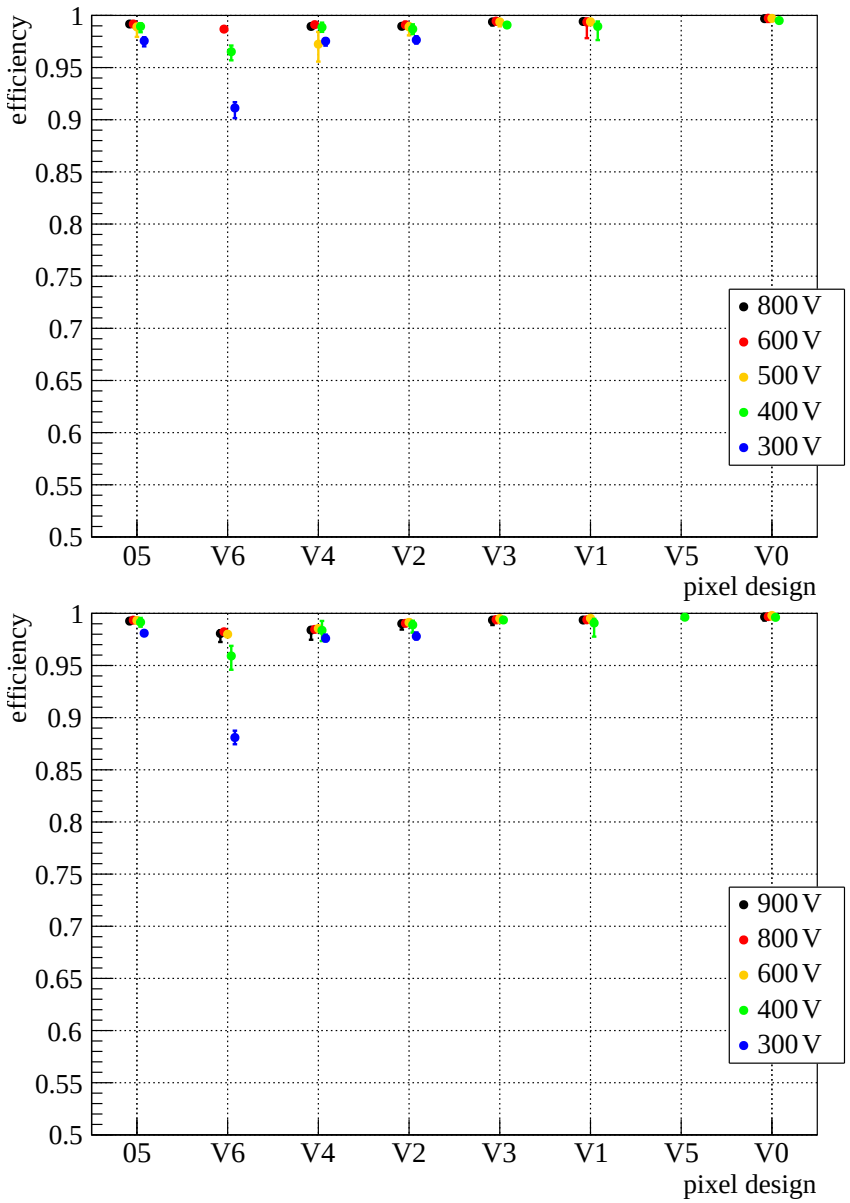

Figure C.5: Efficiencies of the different pixel design groups for the neutron irradiated modules R7 (top) and R9 (bottom), both irradiated to $1 \times 10^{15}\,\mathrm{n_{eq}/cm^2}$ in Ljubljana, measured at the CERN test beam facility in May 2018. The modules are tuned to 3200 e, 6 ToT at 20 ke and measured at different bias voltages.

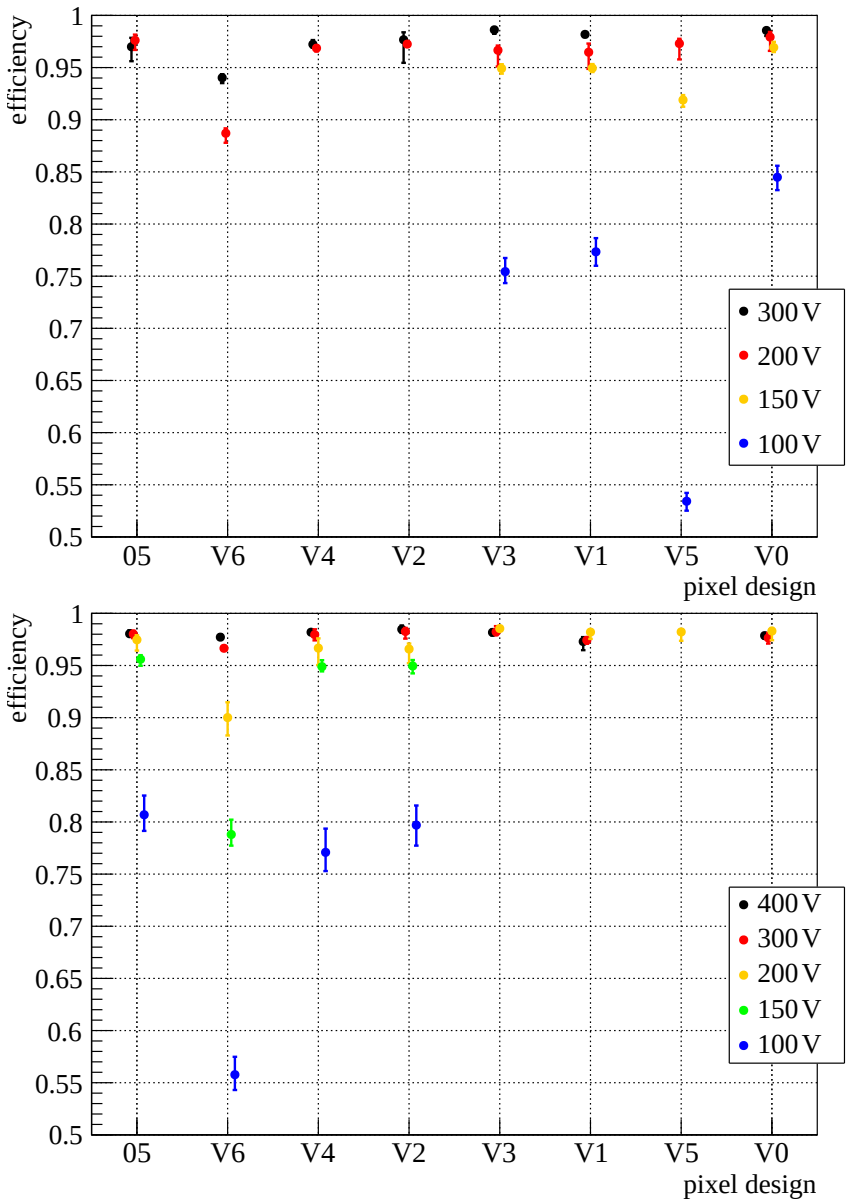

Figure C.6: Efficiencies of the different pixel design groups for the neutron irradiated modules R7 (top) and R9 (bottom), both irradiated to $1 \times 10^{15}\,\mathrm{n_{eq}/cm^2}$ in Ljubljana, measured at the CERN test beam facility in August 2018. The modules are tuned to 1600 e, 6 ToT at 20 ke and measured at different bias voltages.

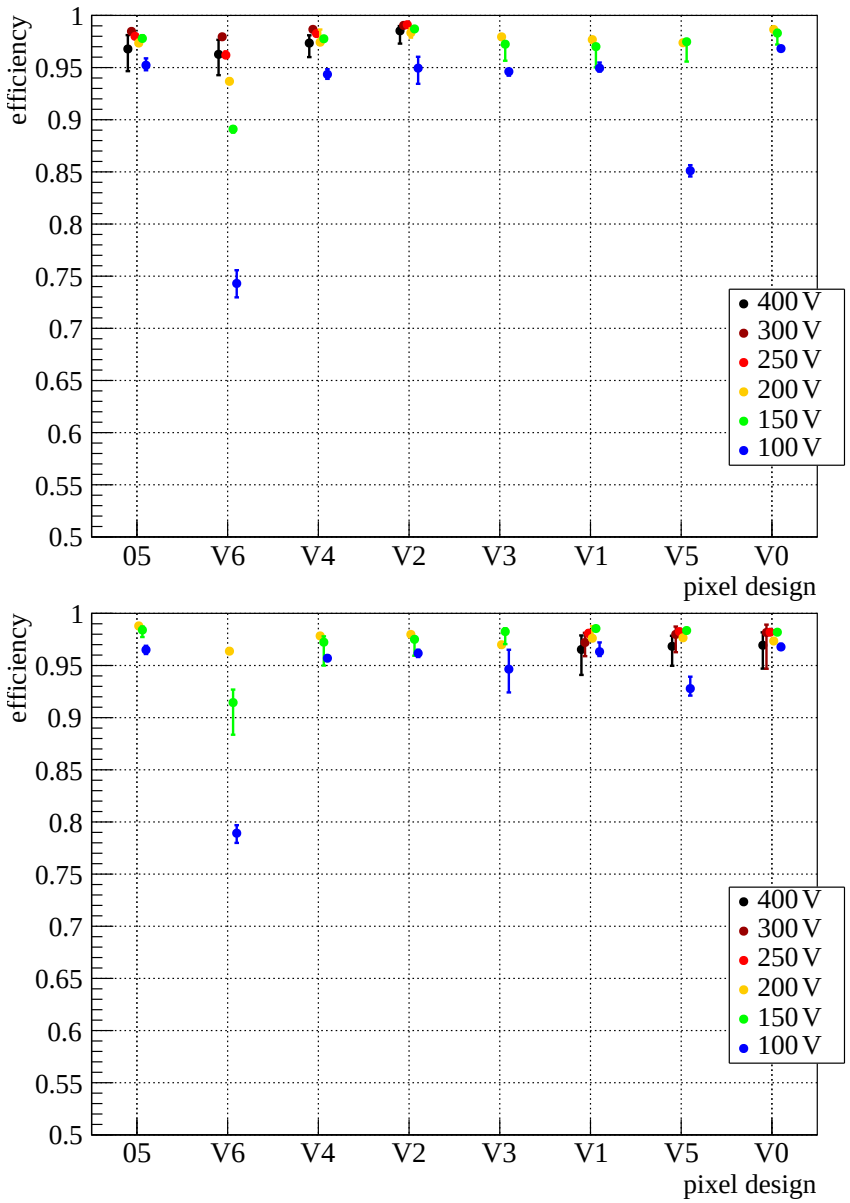

Figure C.7: Efficiencies of the different pixel design groups for the neutron irradiated modules R7 (top) and R9 (bottom), both irradiated to $1 \times 10^{15}\,\mathrm{n_{eq}/cm^2}$ in Ljubljana, measured at the CERN test beam facility in August 2018. The modules are tuned to 1000 e, 10 ToT at 10 ke and measured at different bias voltages.

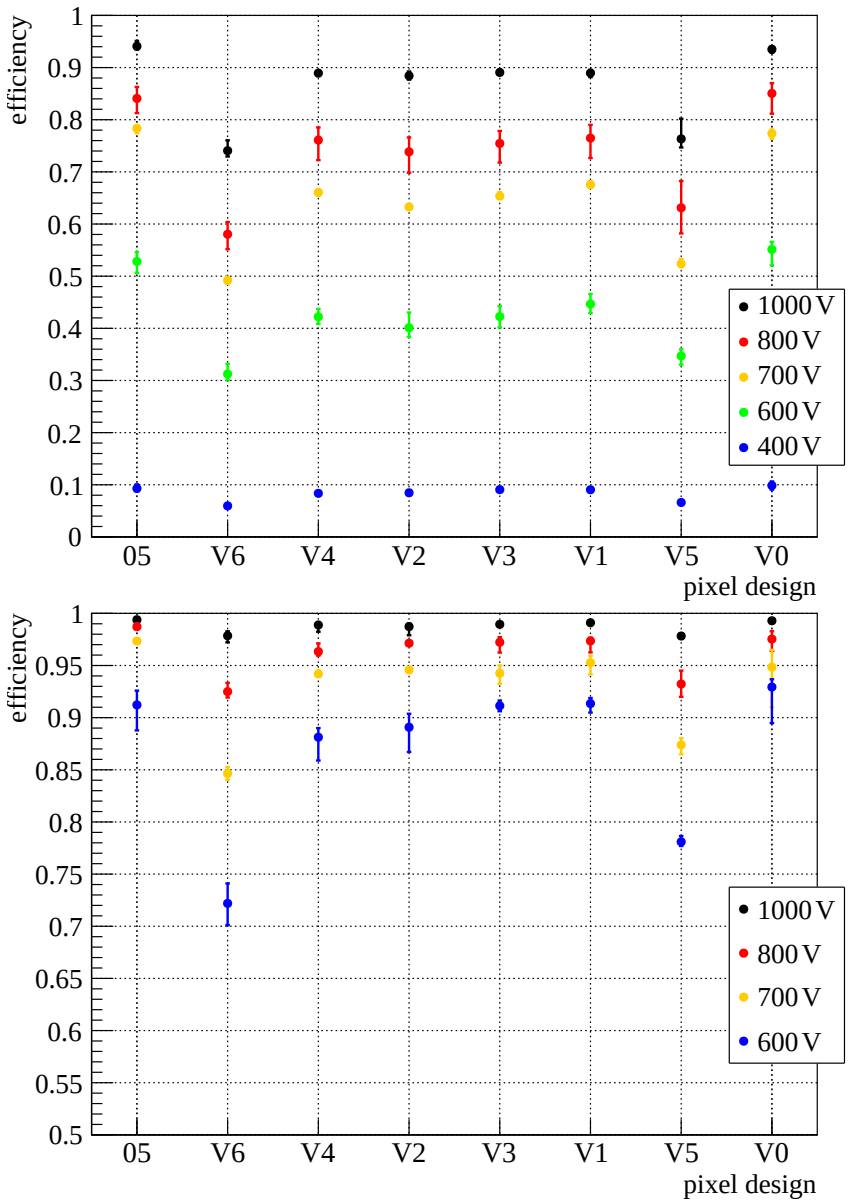

Figure C.8: Efficiencies of the different pixel design groups for the proton irradiated module R2 ($6 \times 10^{15}\,\mathrm{n_{eq}/cm^2}$, CERN) measured at the CERN test beam facility in July 2017. The module is measured at different bias voltages and tuned to 3200 e, 6 ToT at 20 ke (top) and to 1600 e, 6 ToT at 20 ke (bottom).

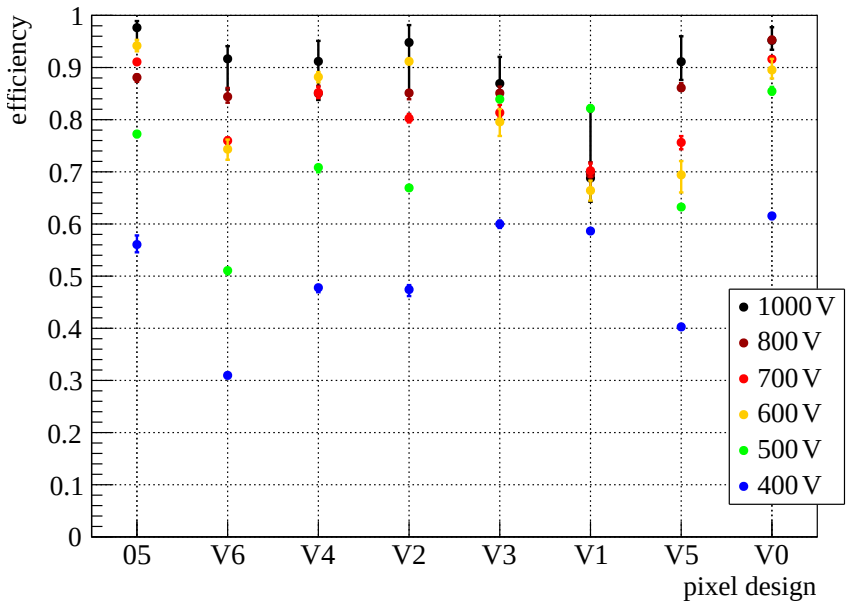

Figure C.9: Efficiencies of the different pixel design groups for the proton irradiated module R2 ($6 \times 10^{15}\,\mathrm{n_{eq}/cm^2}$, CERN) measured at the CERN test beam facility in July 2017. The module is tuned to 1600 e, 6 ToT at 6 ke and measured at six different bias voltages.

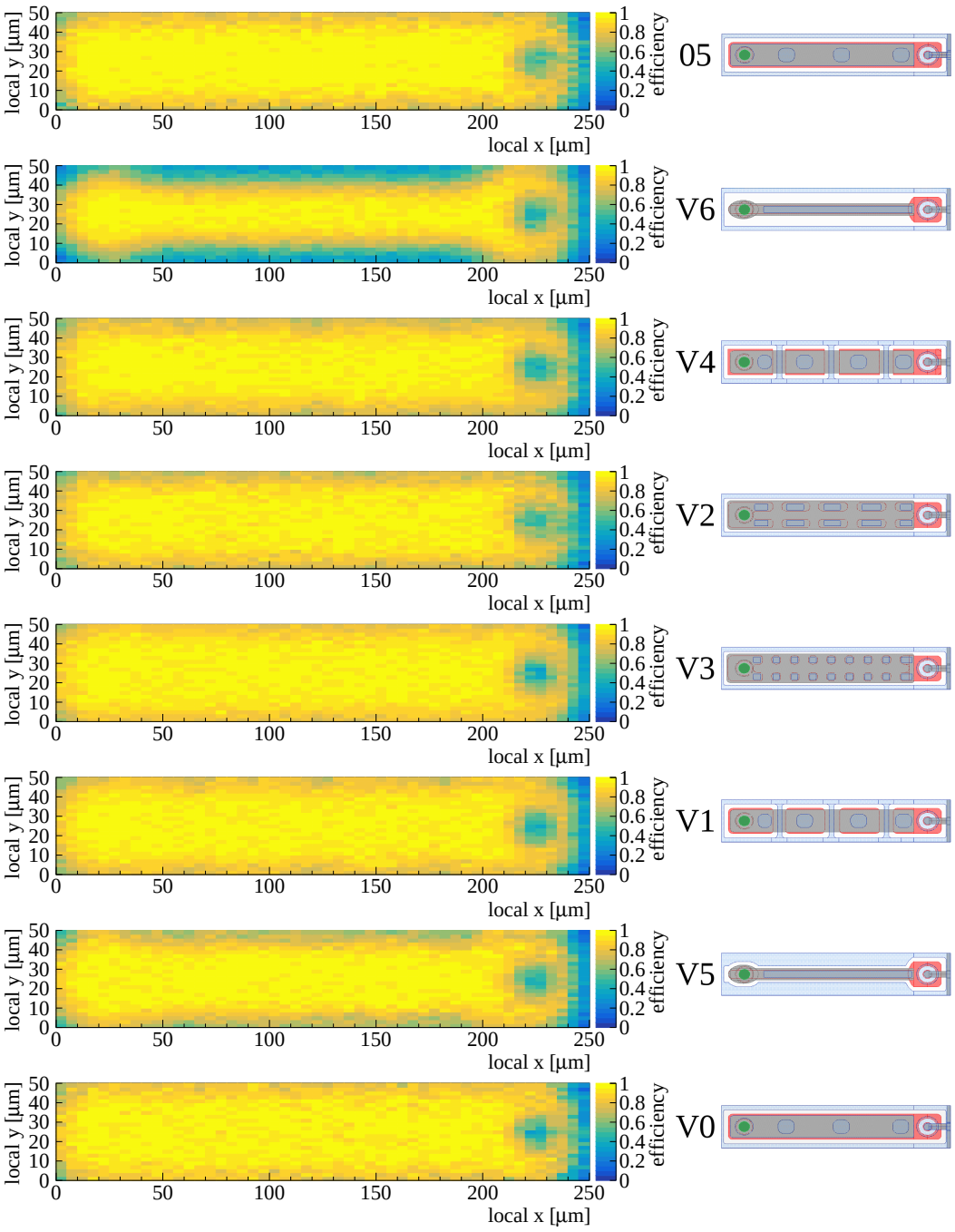

Figure C.10: In-pixel efficiency maps of the neutron irradiated module R5 ($5 \times 10^{15}\,\mathrm{n_{eq}/cm^2}$, Ljubljana), biased with 400 V and tuned to 2000 e, 6 ToT at 20 ke. The order from top to bottom corresponds to the order on the module: 05, V6, V4, V2, V3, V1, V5, V0.

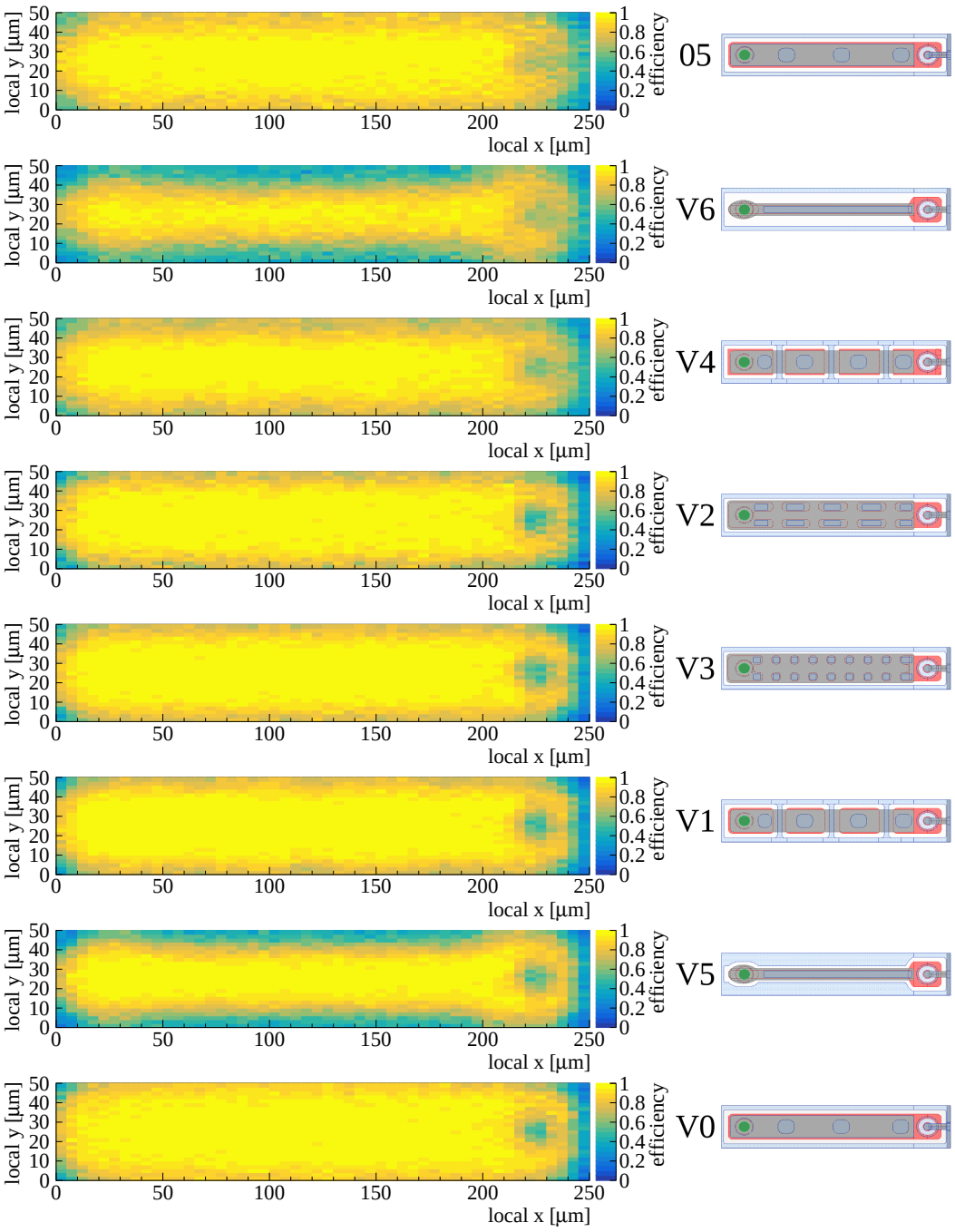

Figure C.11: In-pixel efficiency maps of the proton irradiated module R2 (6×10^{15} n_{eq}/cm^2, CERN), biased with 600 V and tuned to 1600 e, 6 ToT at 20 ke. The order from top to bottom corresponds to the order on the module: 05, V6, V4, V2, V3, V1, V5, V0.

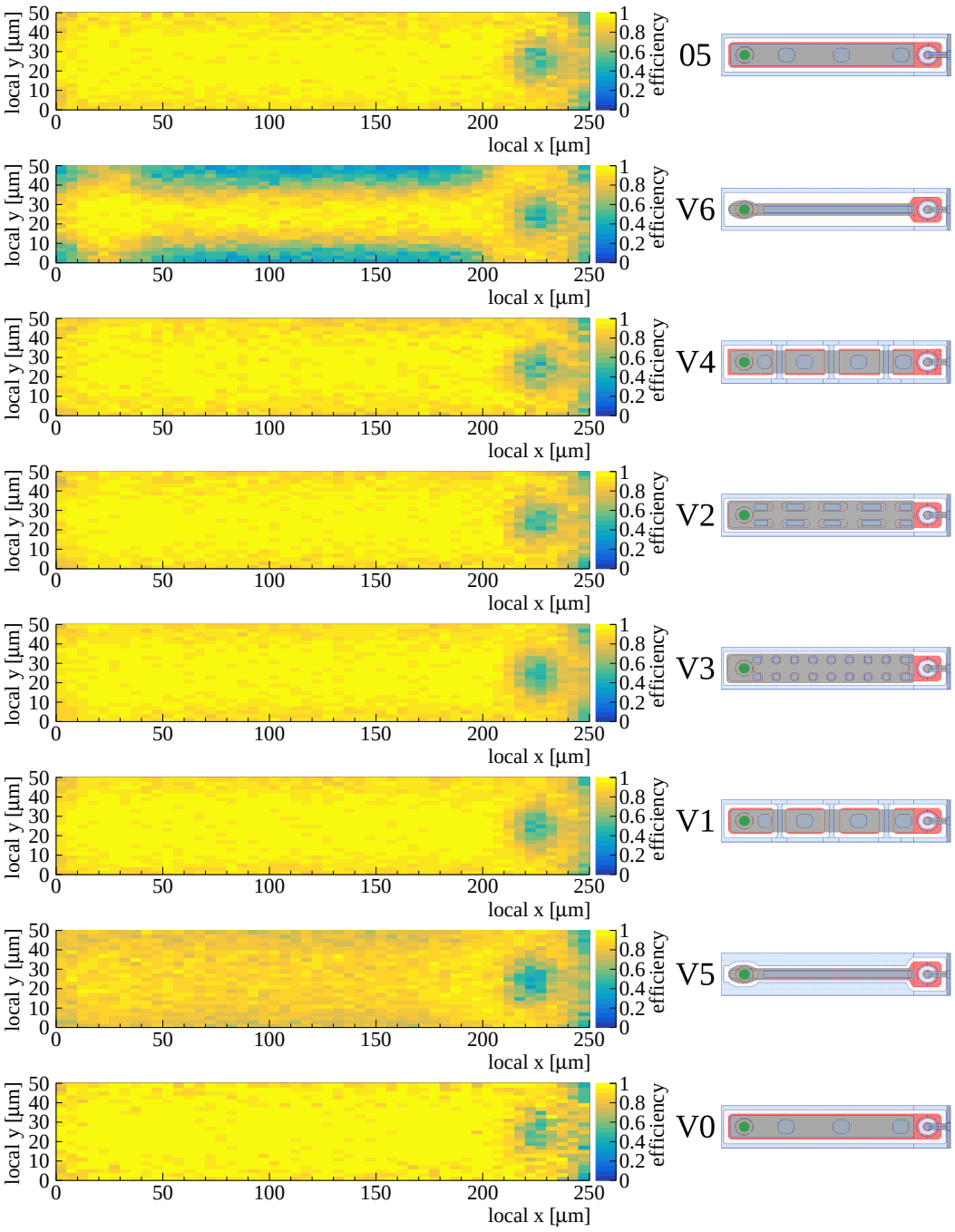

Figure C.12: In-pixel efficiency maps of the neutron irradiated module R7 ($1 \times 10^{15}\,\mathrm{n_{eq}/cm^2}$, Ljubljana), biased with 100 V and tuned to 1000 e, 10 ToT at 100 ke. The order from top to bottom corresponds to the order on the module: 05, V6, V4, V2, V3, V1, V5, V0.

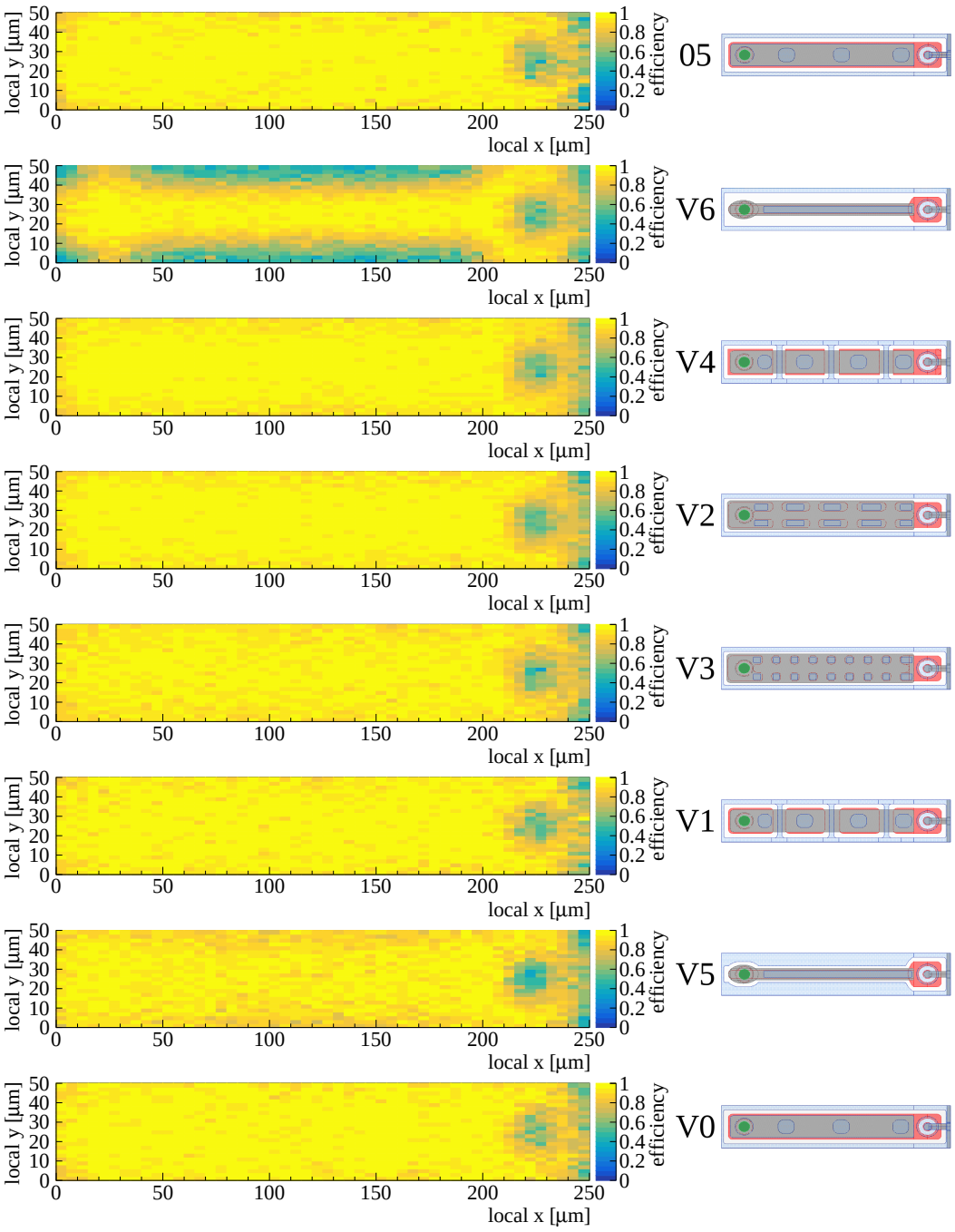

Figure C.13: In-pixel efficiency maps of the neutron irradiated module R9 (1×10^{15} n_{eq}/cm^2, Ljubljana), biased with 100 V and tuned to 1000 e, 10 ToT at 100 ke. The order from top to bottom corresponds to the order on the module: 05, V6, V4, V2, V3, V1, V5, V0.

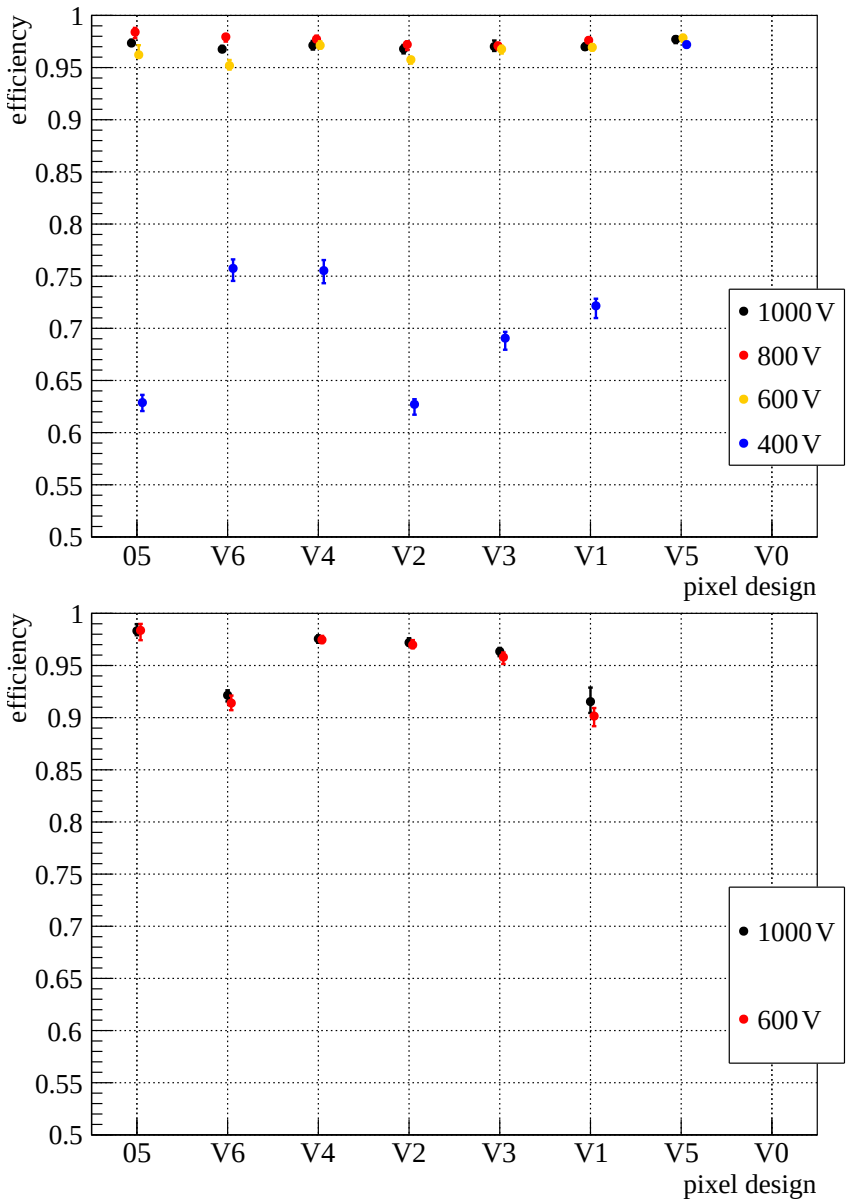

Figure C.14: Efficiencies of the different pixel design groups for the neutron irradiated module R1 ($5 \times 10^{15}\,\mathrm{n_{eq}/cm^2}$, Sandia) measured at the CERN test beam facility in August 2016. The module is measured at different bias voltages and tuned to 3200 e, 6 ToT at 20 ke (top) and to 1600 e, 6 ToT at 20 ke (bottom).

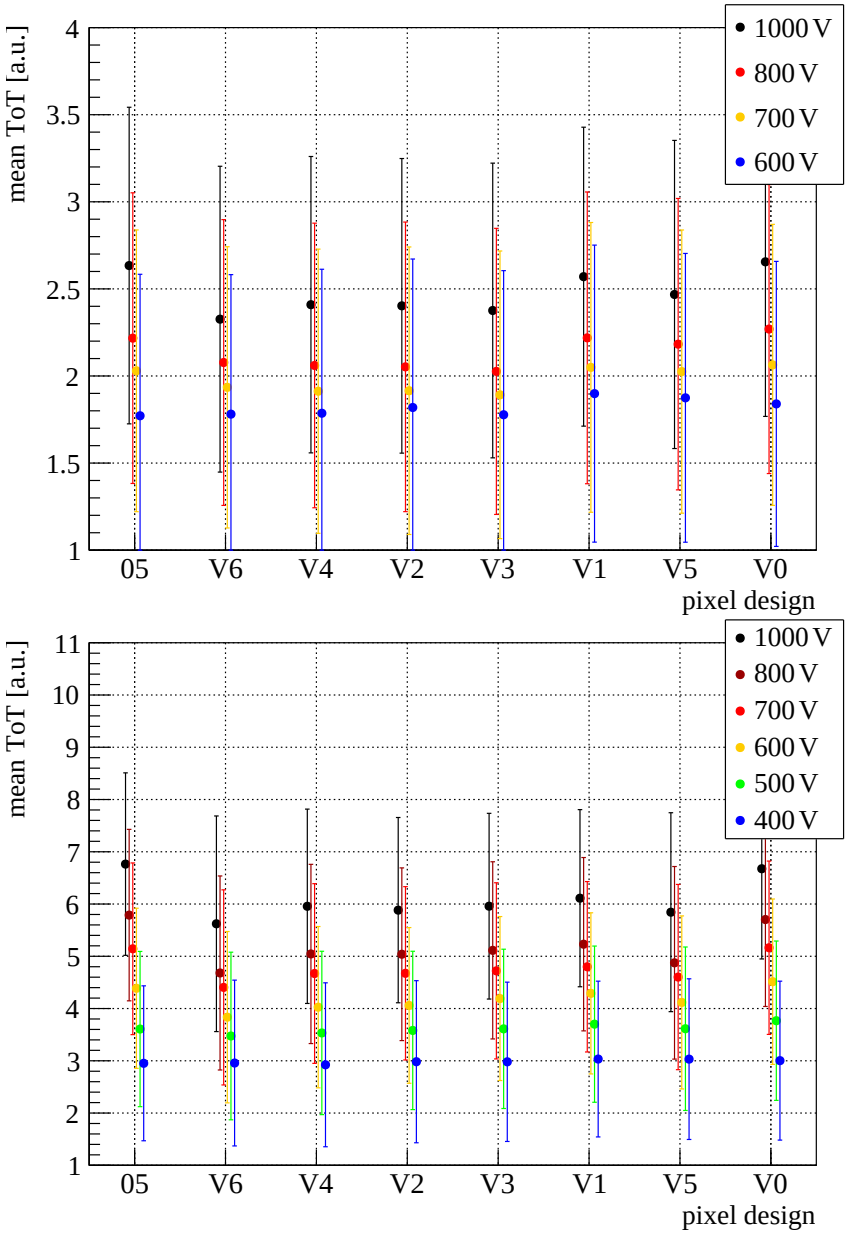

Figure C.15: Mean ToT values for cluster size one for all groups with different pixel designs for the proton irradiated module R2 ($6 \times 10^{15}\,\mathrm{n_{eq}/cm^2}$, CERN) measured at the CERN test beam facility in July 2017 at different bias voltages. Top: The module is tuned to 3200 e, 6 ToT at 20 ke and the results of the last voltage step of 400 V are excluded from this analysis as the hit detection efficiency of about 10 % results in only a few hits per measurement point. Bottom: The module is tuned to 1600 e, 6 ToT at 6 ke.

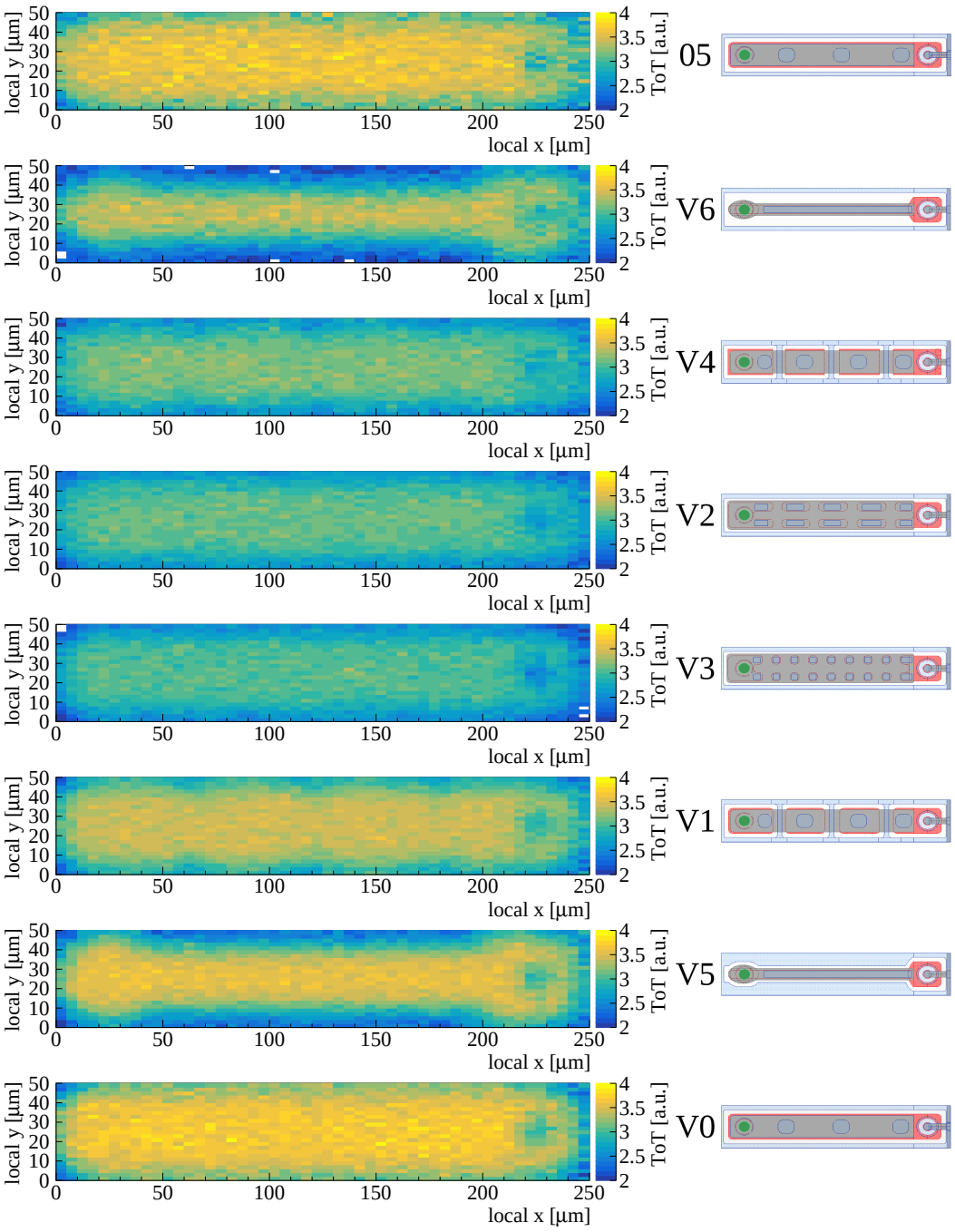

Figure C.16: In-pixel ToT maps with cluster size one of the proton irradiated module R2 (6×10^{15} n_{eq}/cm^2, CERN), biased with 1000 V and tuned to 1600 e, 6 ToT at 20 ke. The order from top to bottom corresponds to the order on the module: 05, V6, V4, V2, V3, V1, V5, V0.

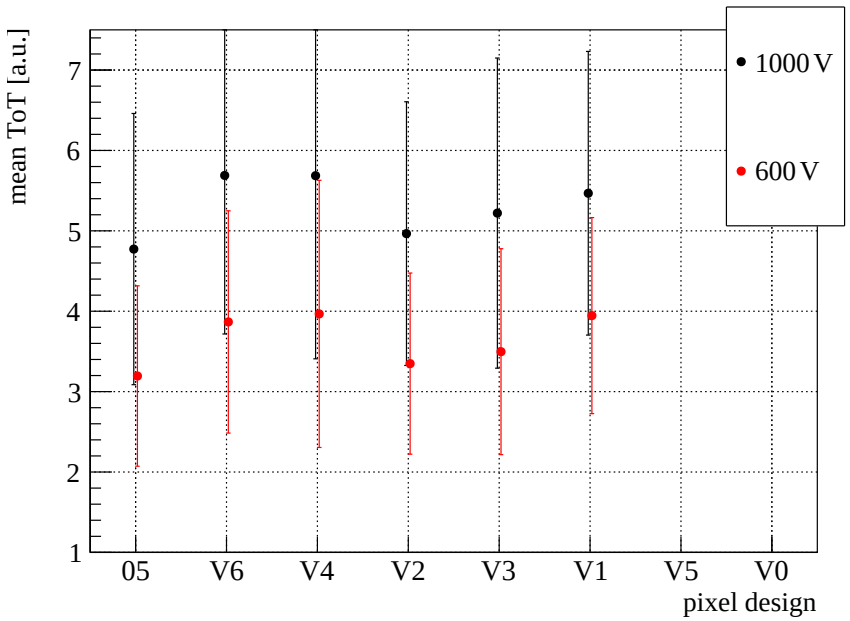

Figure C.17: Mean ToT values for cluster size one for all groups with different pixel designs for the neutron irradiated module R1 ($5 \times 10^{15}\,\mathrm{n_{eq}/cm^2}$, Sandia) measured at the CERN test beam facility in August 2016. The module is tuned to 1600 e, 6 ToT at 20 ke and measured at two different bias voltages.

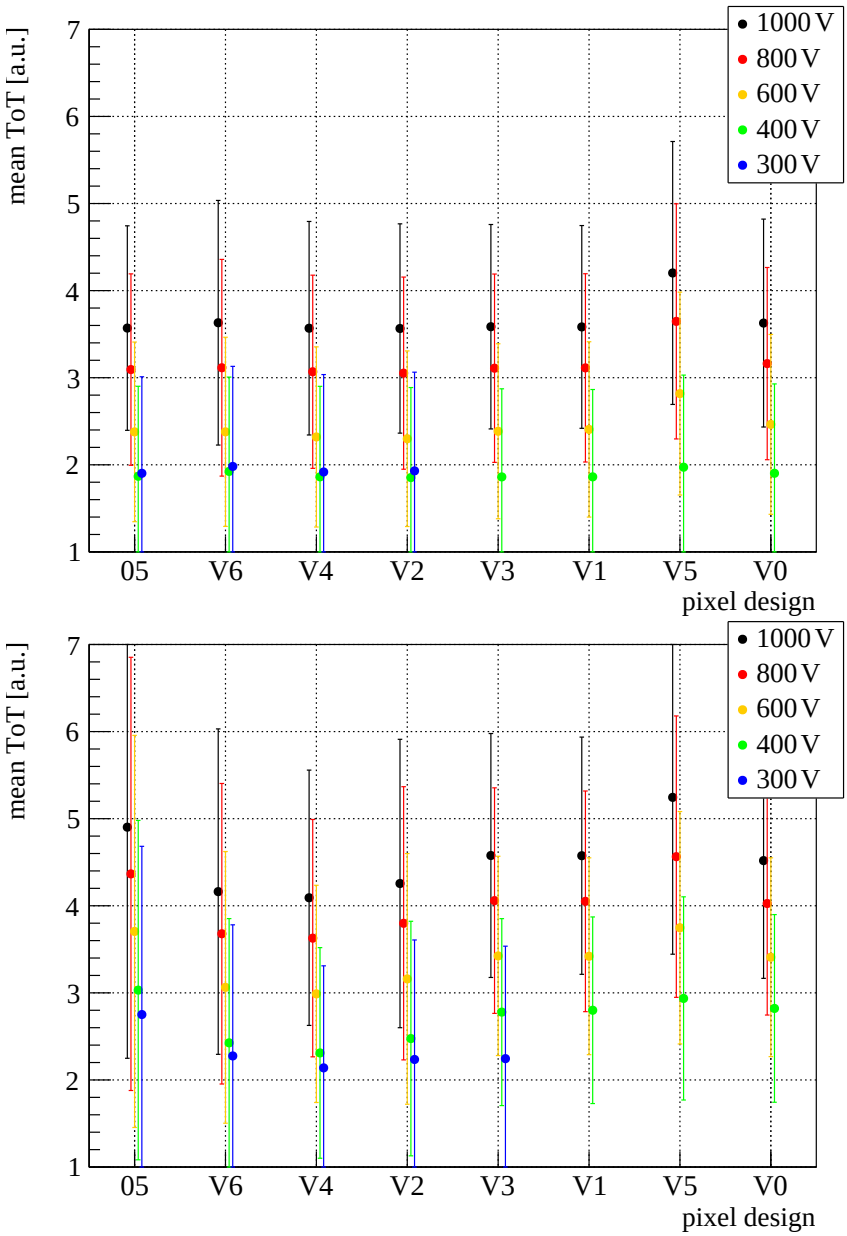

Figure C.18: Mean ToT values for cluster size one for all groups with different pixel designs for the neutron irradiated modules R3 (top) and R5 (bottom), both irradiated to $5 \times 10^{15}\,\mathrm{n_{eq}/cm^2}$ in Ljubljana, measured at the CERN test beam facility in May 2018. The modules are tuned to 3200 e, 6 ToT at 20 ke and measured at different bias voltages.

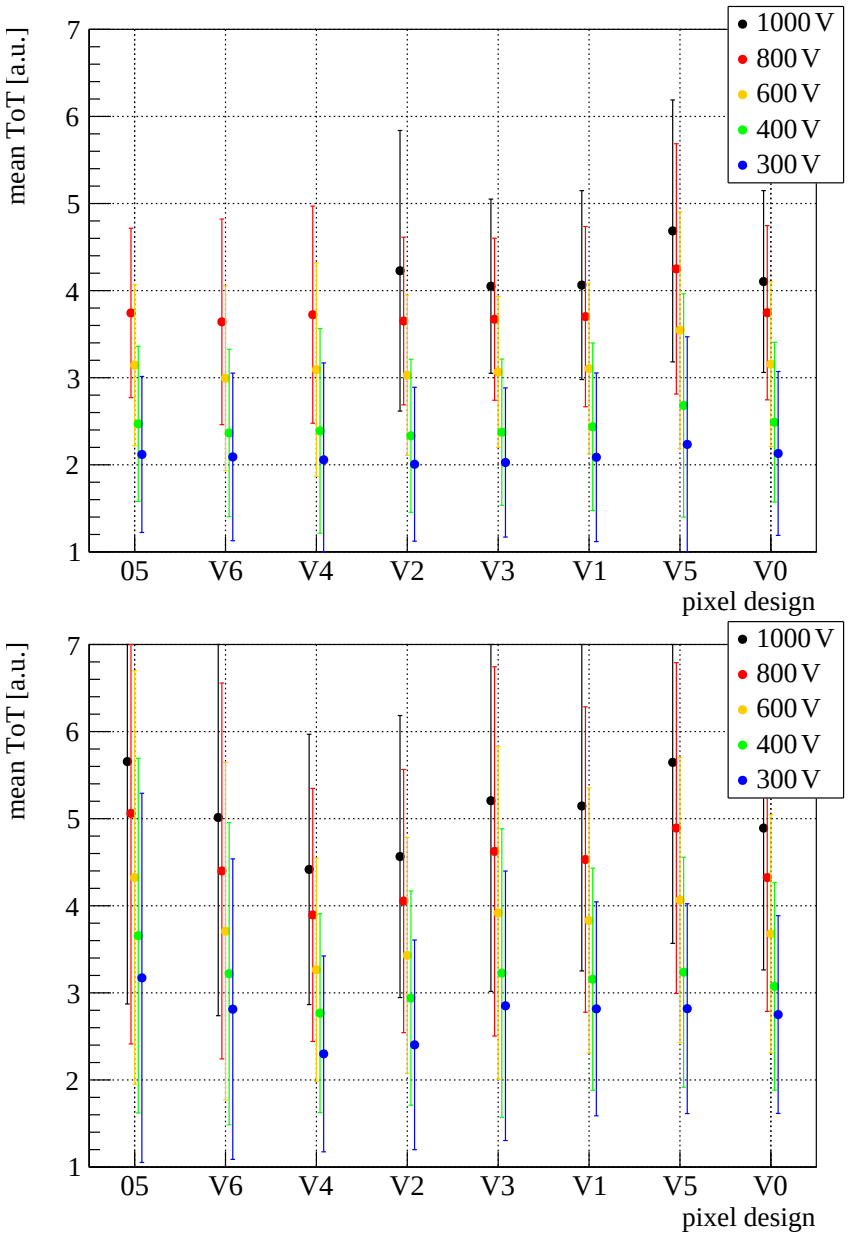

Figure C.19: Mean ToT values for cluster size one for all groups with different pixel designs for the neutron irradiated modules R3 (top) and R5 (bottom), both irradiated to $5 \times 10^{15}\,\mathrm{n_{eq}/cm^2}$ in Ljubljana, measured at the CERN test beam facility in May 2018 at different bias voltages. The module R3 is tuned to 1600 e, 6 ToT at 20 ke and the module R5 to 2000 e, 6 ToT at 20 ke.

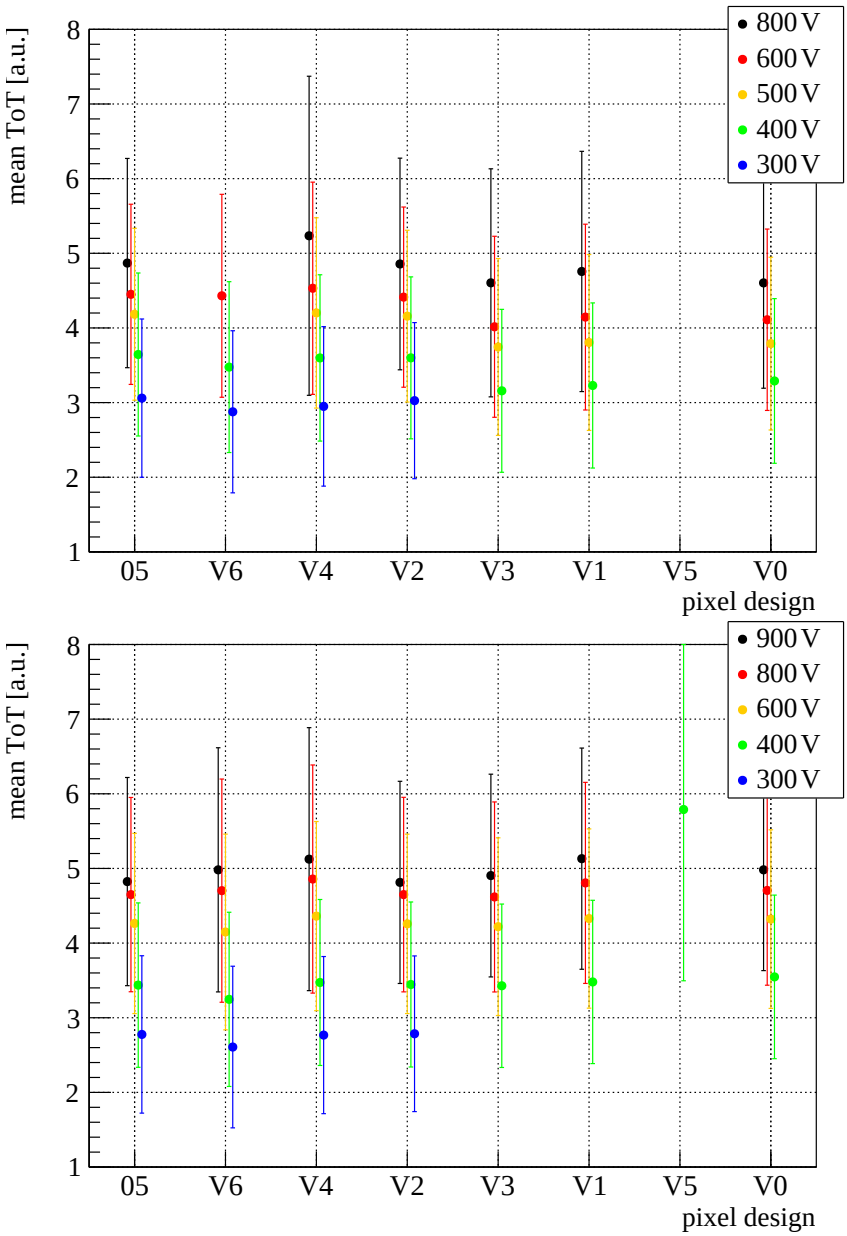

Figure C.20: Mean ToT values for cluster size one for all groups with different pixel designs for the neutron irradiated modules R7 (top) and R9 (bottom), both irradiated to $1 \times 10^{15}\,\mathrm{n_{eq}/cm^2}$ in Ljubljana, measured at the CERN test beam facility in May 2018. The modules are tuned to 3200 e, 6 ToT at 20 ke and measured at different bias voltages.

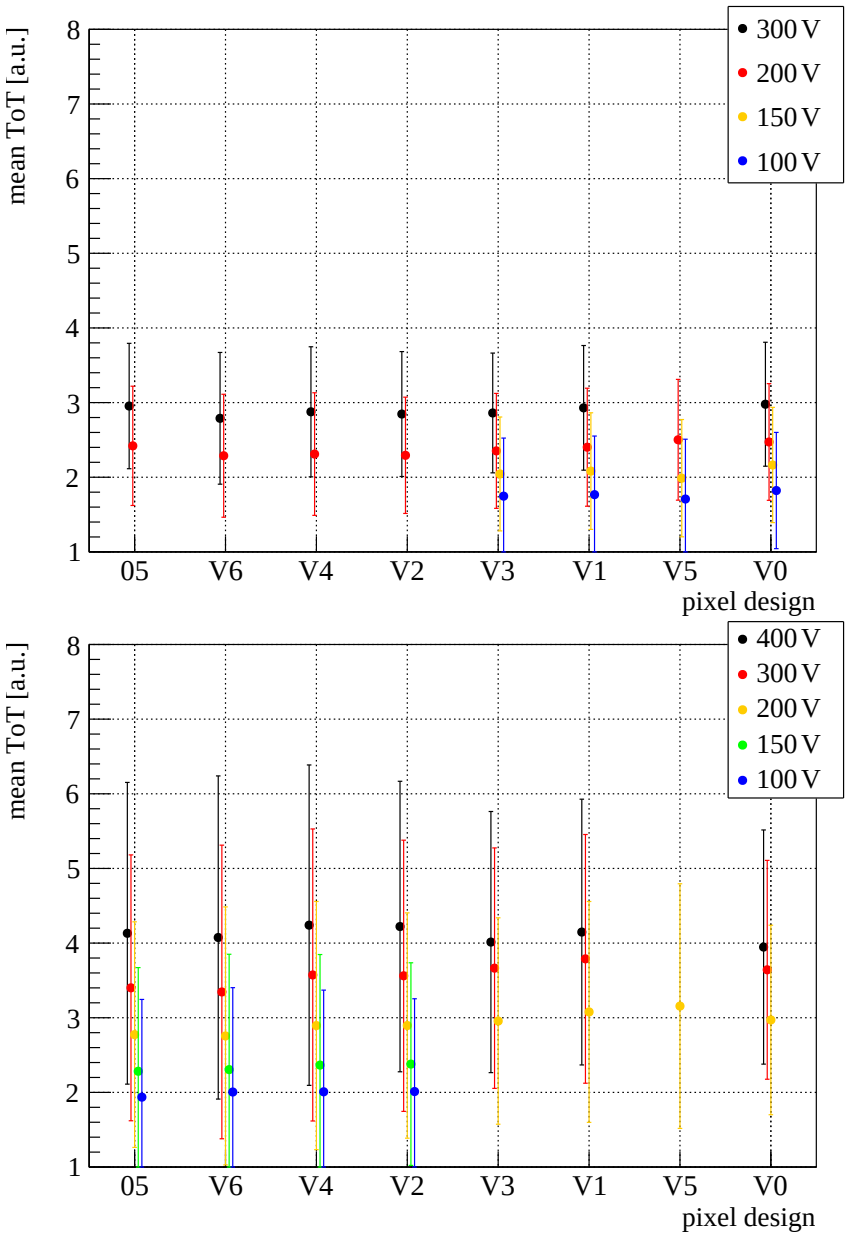

Figure C.21: Mean ToT values for cluster size one for all groups with different pixel designs for the neutron irradiated modules R7 (top) and R9 (bottom), both irradiated to $1 \times 10^{15}\,\mathrm{n_{eq}/cm^2}$ in Ljubljana, measured at the CERN test beam facility in August 2018. The modules are tuned to 1600 e, 6 ToT at 20 ke and measured at different bias voltages.

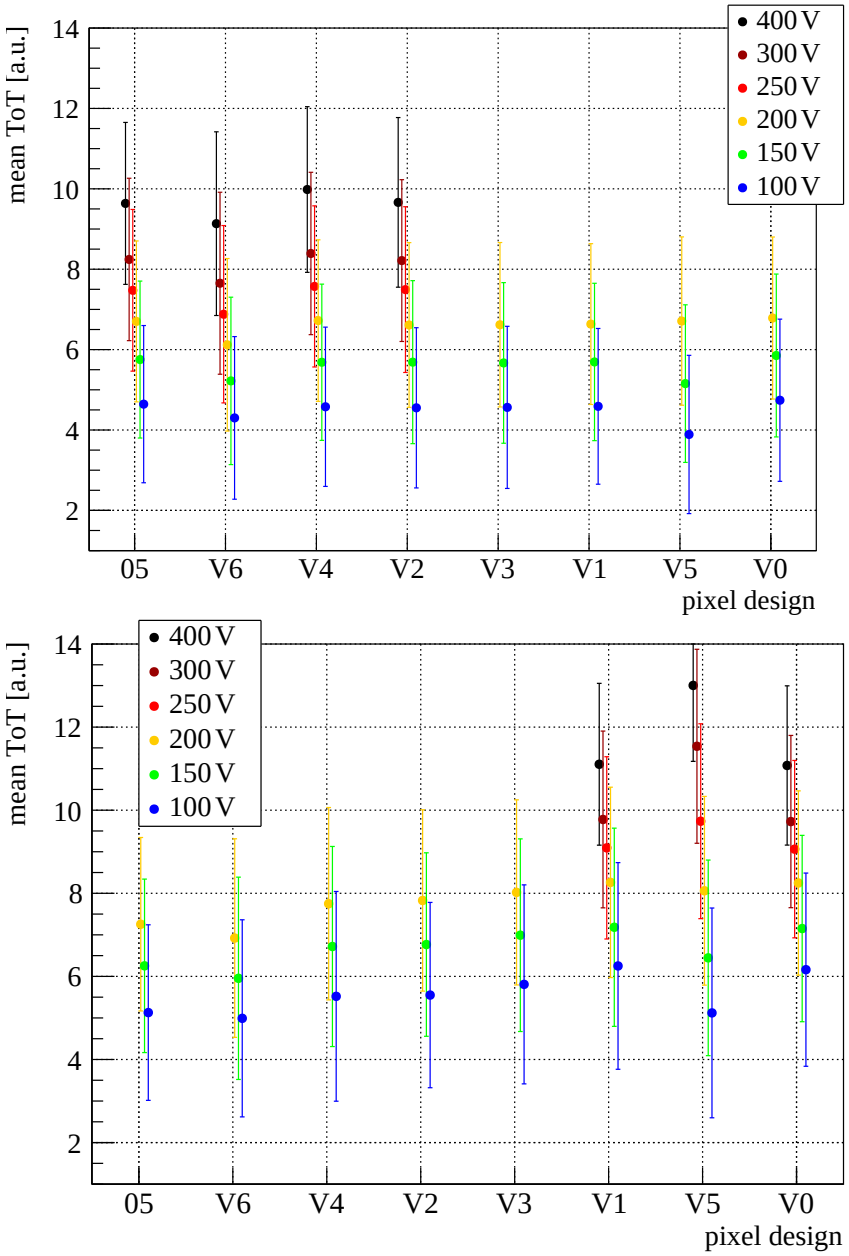

Figure C.22: Mean ToT values for cluster size one for all groups with different pixel designs for the neutron irradiated modules R7 (top) and R9 (bottom), both irradiated to $1 \times 10^{15}\,\mathrm{n_{eq}/cm^2}$ in Ljubljana, measured at the CERN test beam facility in August 2018. The modules are tuned to 1000 e, 10 ToT at 10 ke and measured at different bias voltages.

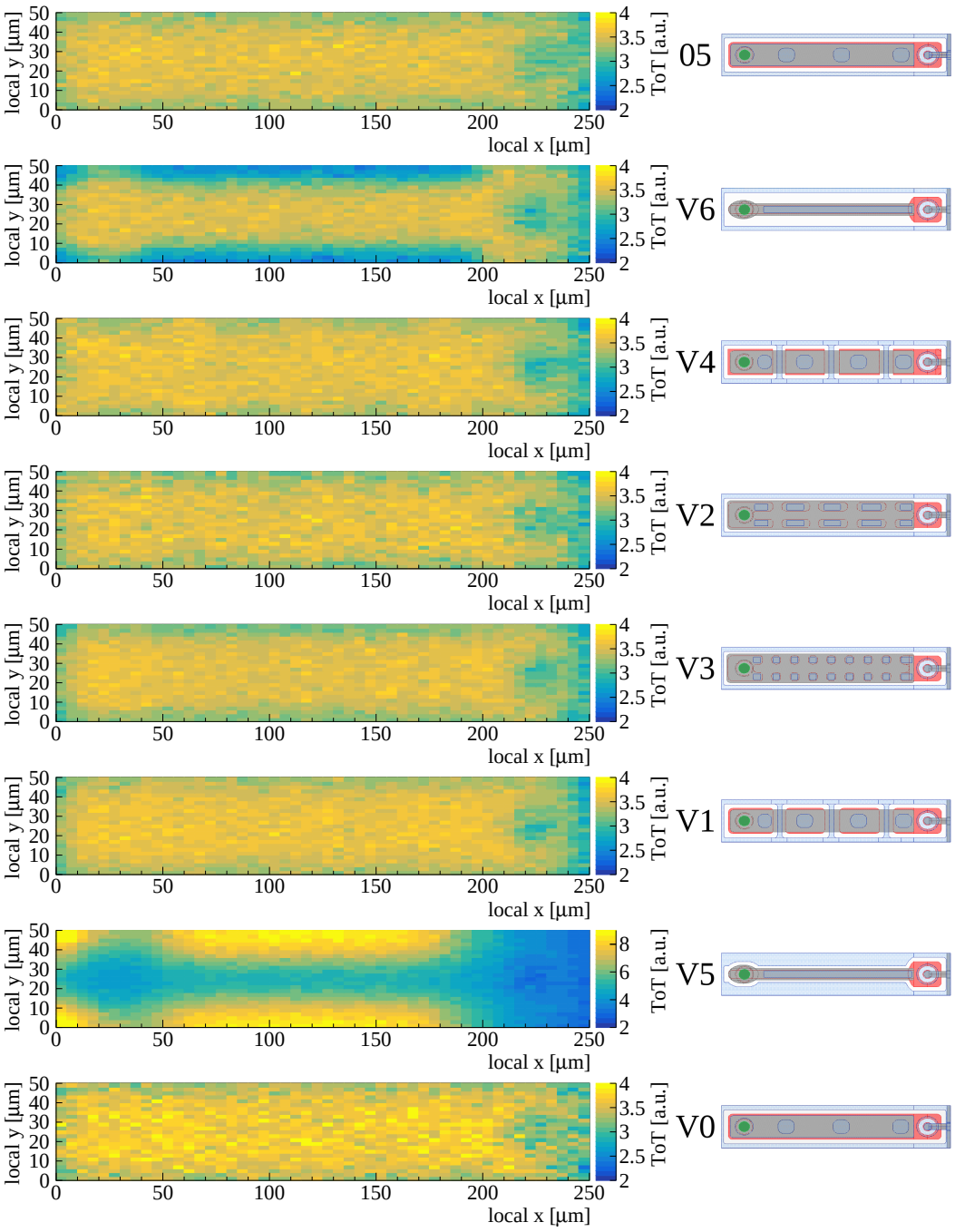

Figure C.23: In-pixel ToT maps for cluster size one of the neutron irradiated module R9 ($1 \times 10^{15}\,\mathrm{n_{eq}/cm^2}$, Ljubljana), biased with 400 V and tuned to 3200 e, 6 ToT at 20 ke. The order from top to bottom corresponds to the order on the module: 05, V6, V4, V2, V3, V1, V5, V0. Due to the high charges measured for the pixel design V5 a different scale is necessary compared to all other designs.

D Laboratory Measurements of Irradiated and Annealed Modules

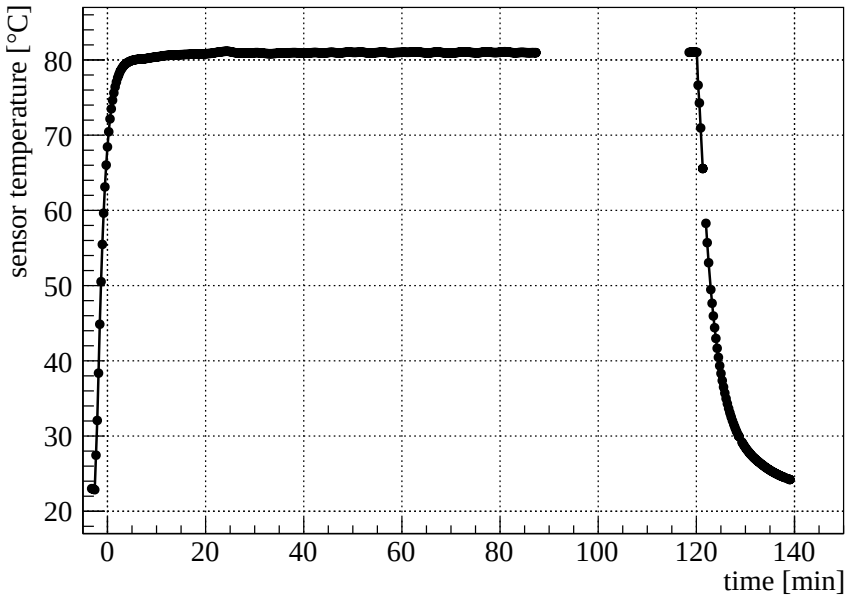

Figure D.1: Annealing temperature profile for the second annealing step (3 h+2 h) of the neutron irradiated module R3 ($5 \times 10^{15}\,\mathrm{n_{eq}/cm^2}$). The sensor temperature is about 120 min above 70 °C. The temperature monitoring was interrupted from minute 80 to 118 while the temperature of the module stayed about 80 °C.

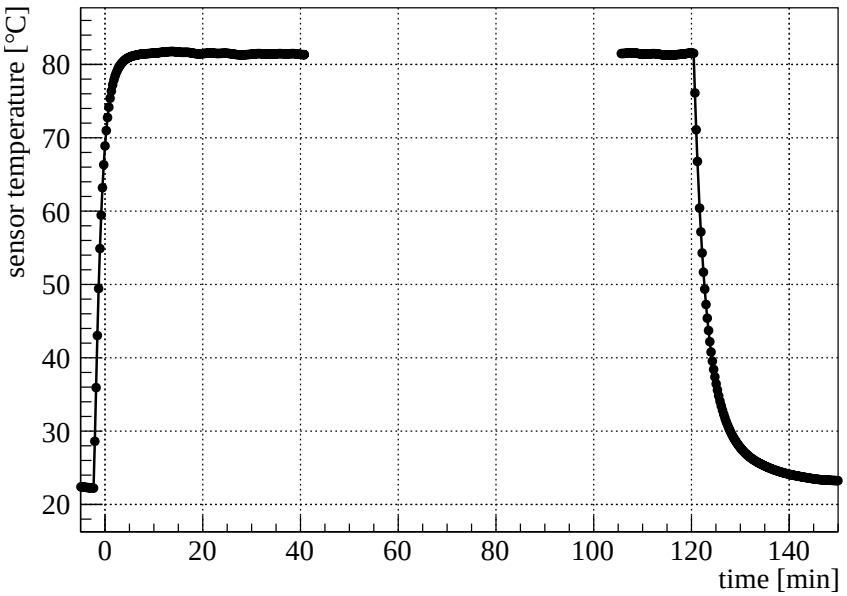

Figure D.2: Annealing temperature profile for the third annealing step (3 h+2 h+2 h) of the neutron irradiated module R3 ($5 \times 10^{15}\,\mathrm{n_{eq}/cm^2}$). The sensor temperature is about 121 min above 70 °C. The temperature monitoring was interrupted from minute 42 to 106 while the temperature of the module stayed about 80 °C.

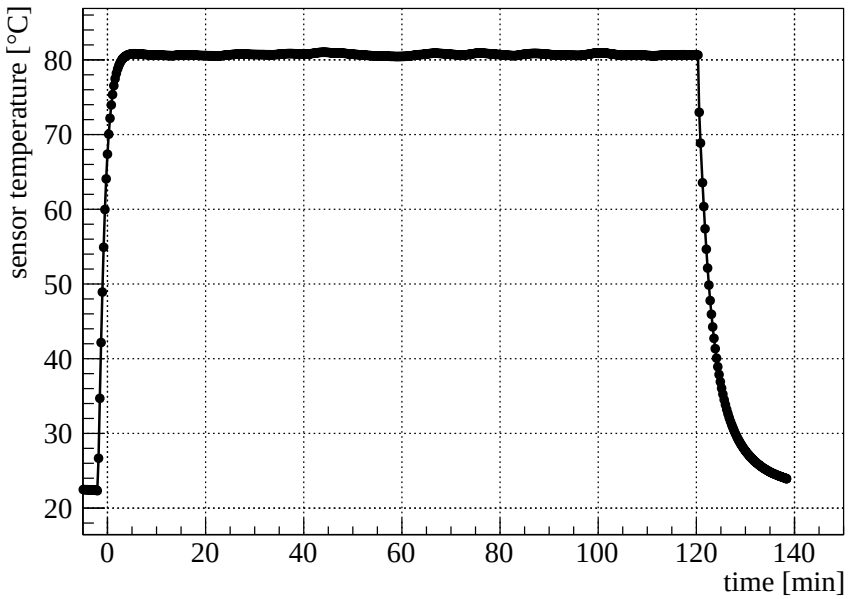

Figure D.3: Annealing temperature profile for the fourth annealing step (3 h+2 h+2 h+2 h) of the neutron irradiated module R3 (5×10^{15} n_{eq}/cm^2). The sensor temperature is about 121 min above 70 °C.

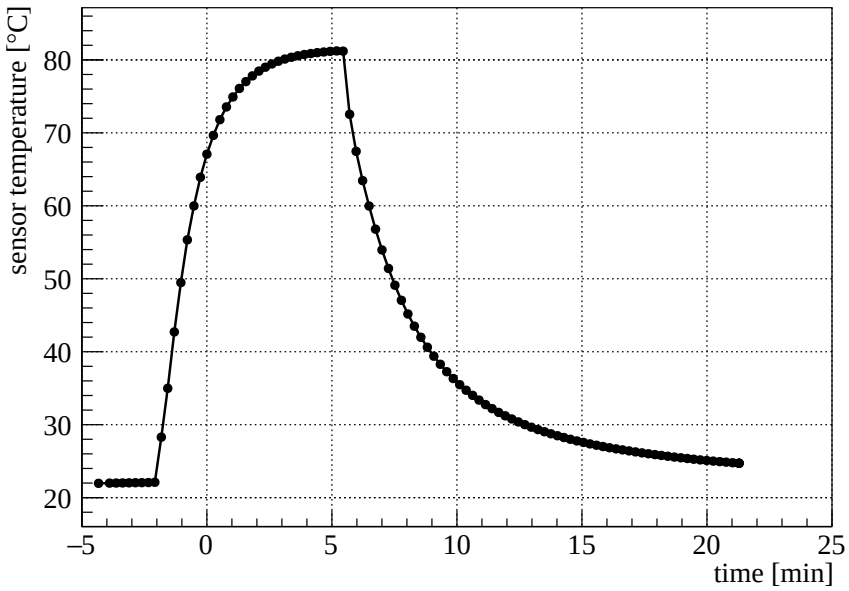

Figure D.4: Annealing temperature profile for the second annealing step (5 min+5 min) of the neutron irradiated module R9 (1×10^{15} n_{eq}/cm^2). The sensor temperature is about 6 min above 65 °C.

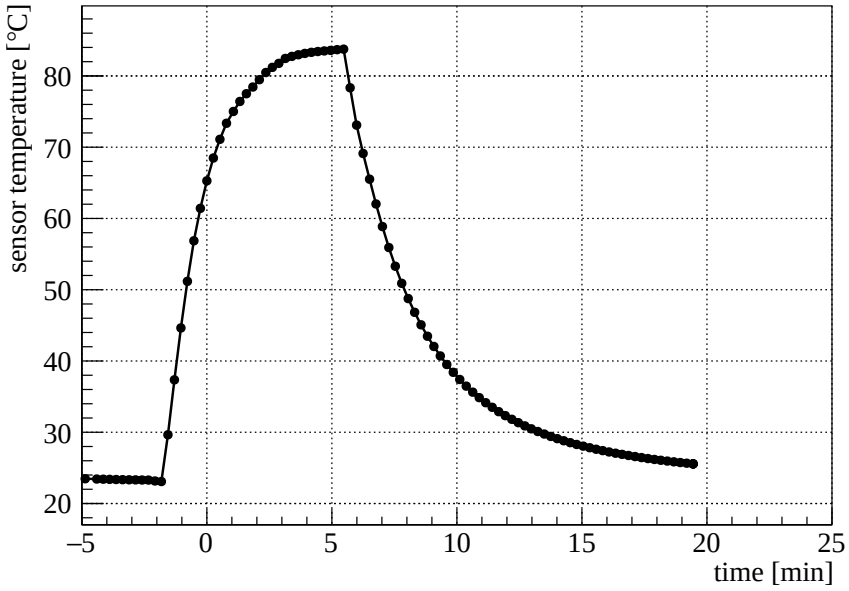

Figure D.5: Annealing temperature profile for the third annealing step (5 min+5 min+5 min) of the neutron irradiated module R9 (1×10^{15} n_{eq}/cm^2). The sensor temperature is about 6.5 min above 65 °C.

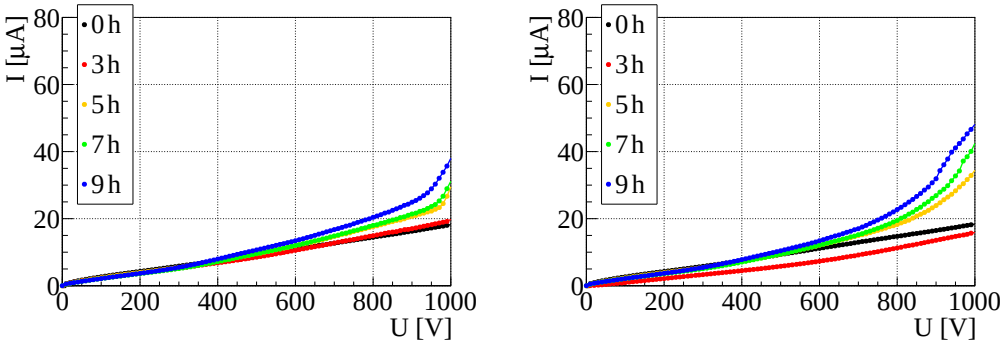

Figure D.6: Results of the IV measurements after each annealing step at 80 °C for the pixel designs 05 (left) and V0 (right) of the sensor R3 normalized to a sensor temperature of −30 °C.

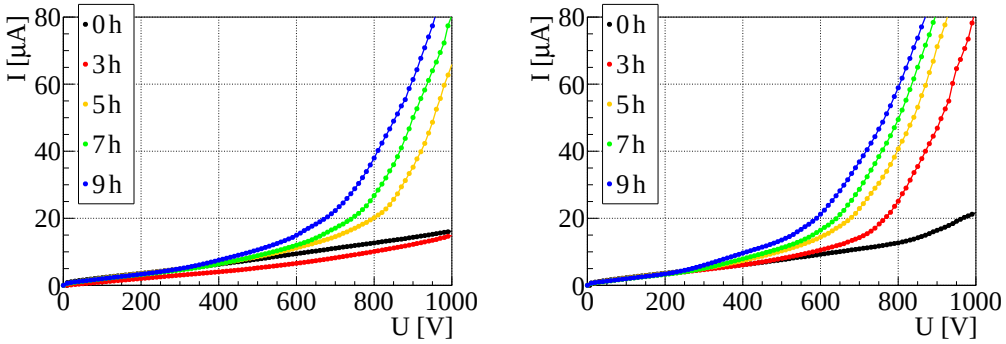

Figure D.7: Results of the IV measurements after each annealing step at 80 °C for the pixel designs V1 (left) and V4 (right) of the sensor R3 normalized to a sensor temperature of −30 °C.

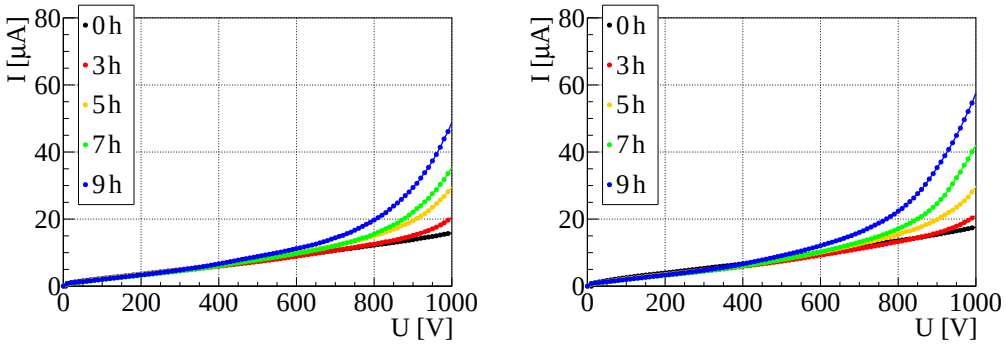

Figure D.8: Results of the IV measurements after each annealing step at 80 °C for the pixel designs V2 (left) and V3 (right) of the sensor R3 normalized to a sensor temperature of −30 °C.

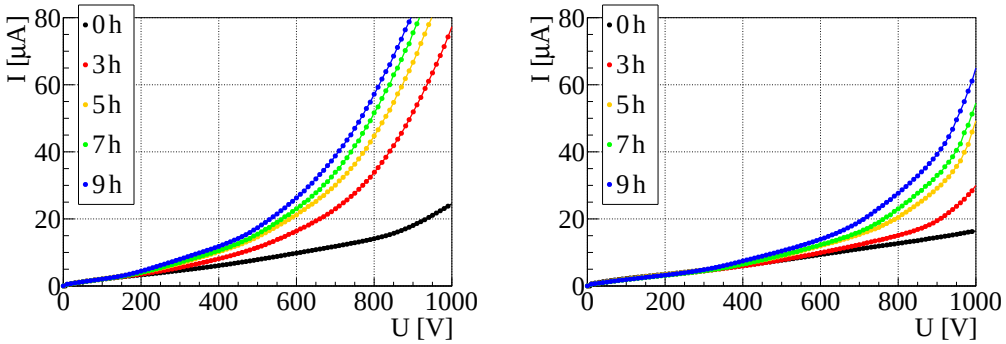

Figure D.9: Results of the IV measurements after each annealing step at 80 °C for the pixel designs V5 (left) and V6 (right) of the sensor R3 normalized to a sensor temperature of −30 °C.

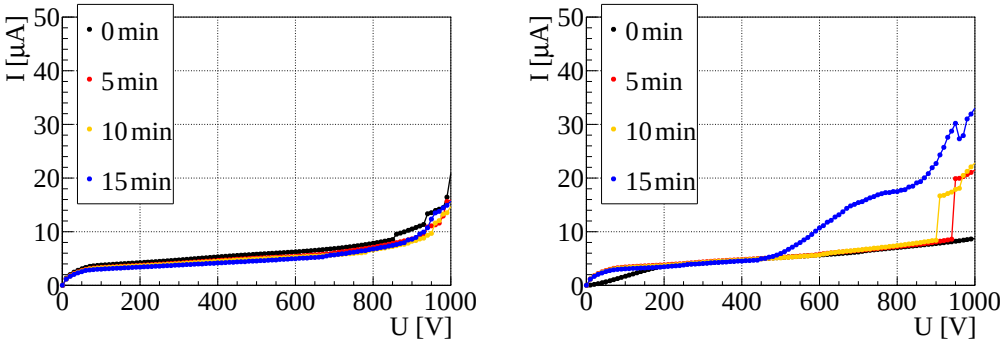

Figure D.10: Results of the IV measurements after each annealing step at 80 °C for the pixel designs 05 (left) and V0 (right) of the sensor R9 normalized to a sensor temperature of −30 °C.

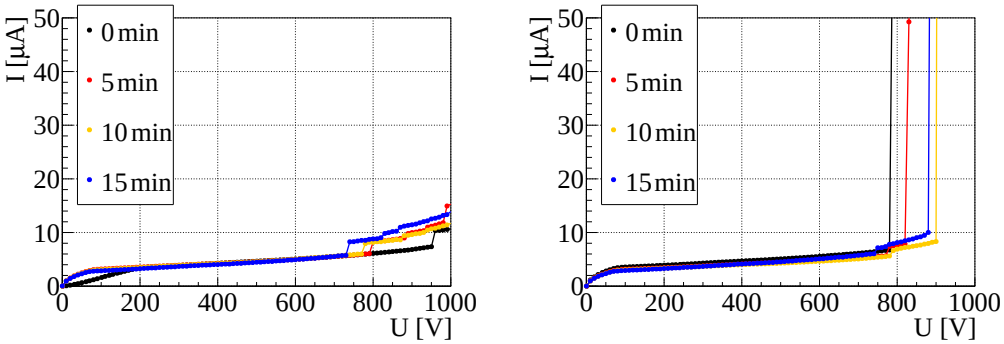

Figure D.11: Results of the IV measurements after each annealing step at 80 °C for the pixel designs V1 (left) and V4 (right) of the sensor R9 normalized to a sensor temperature of −30 °C.

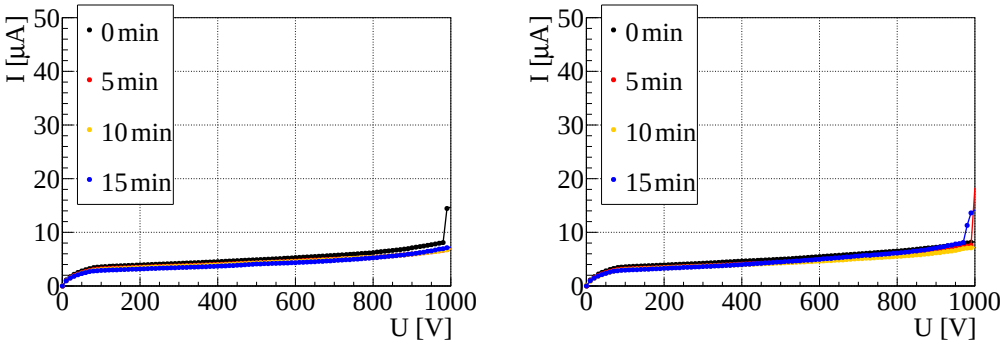

Figure D.12: Results of the IV measurements after each annealing step at 80 °C for the pixel designs V2 (left) and V3 (right) of the sensor R9 normalized to a sensor temperature of −30 °C.

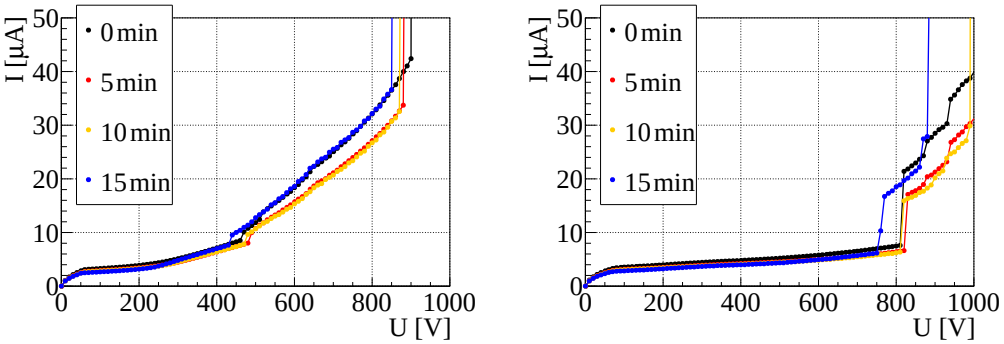

Figure D.13: Results of the IV measurements after each annealing step at 80 °C for the pixel designs V5 (left) and V6 (right) of the sensor R9 normalized to a sensor temperature of −30 °C.

E Test Beam Measurements of Irradiated and Annealed Modules

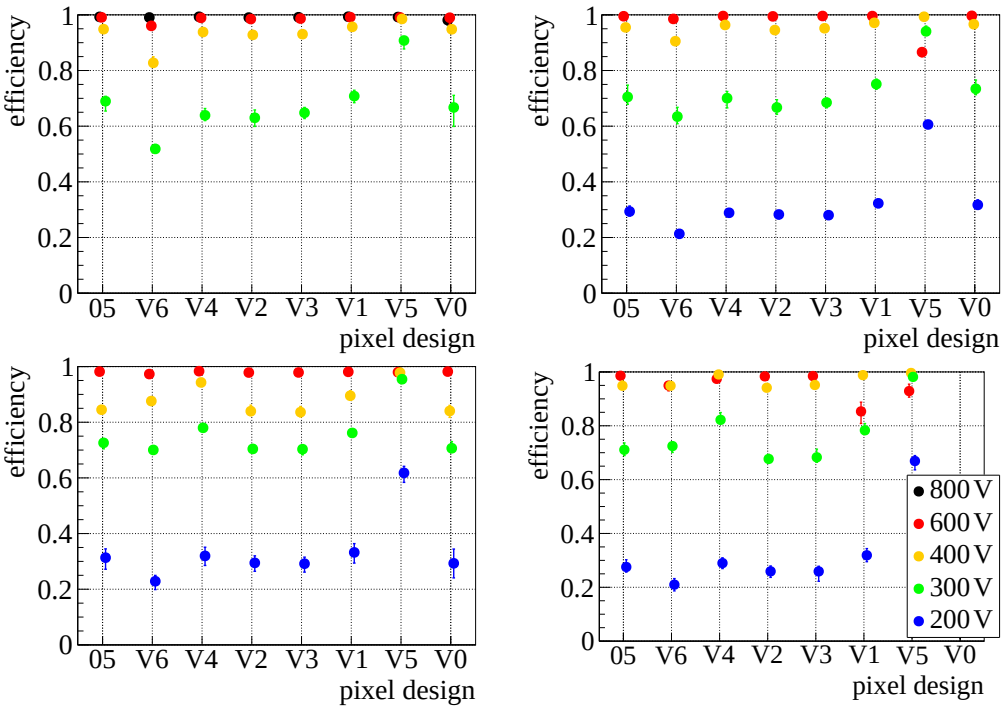

Figure E.1: Hit detection efficiencies for the groups with different pixel designs of the module R3 at different bias voltages for the tuning of 1600 e 6 ToT at 20 ke. The module is annealed at 80 °C for 3 h (top left), 5 h (top right), 7 h (bottom left) and 9 h (bottom right).

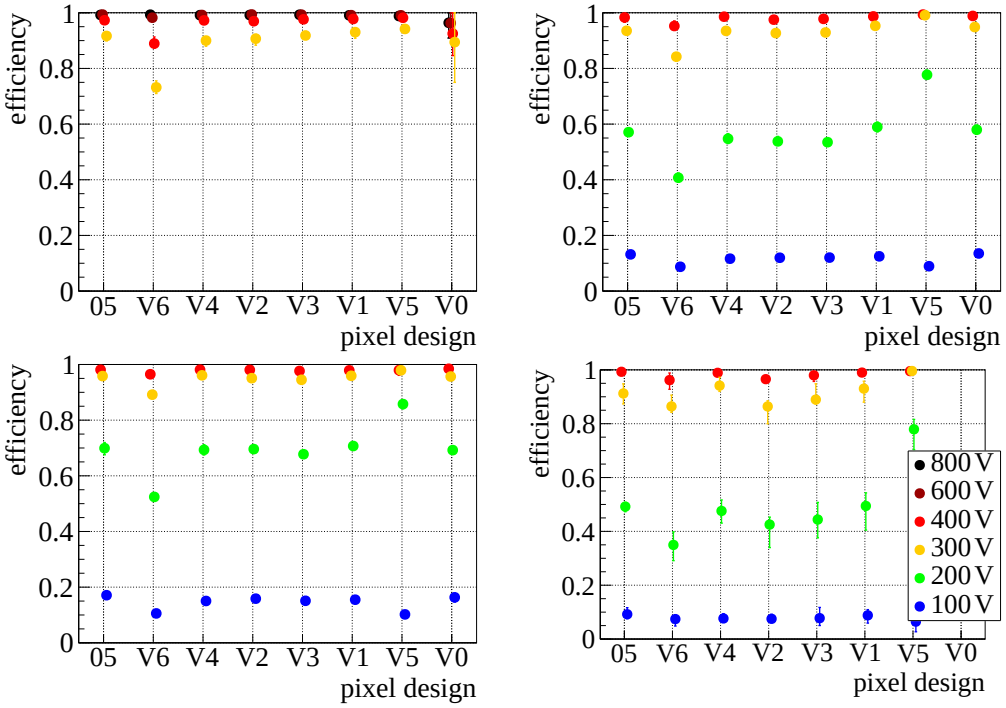

Figure E.2: Hit detection efficiencies for the groups with different pixel designs of the module R3 at different bias voltages for the tuning of 1000 e 10 ToT at 10 ke. The module is annealed at 80 °C for 3 h (top left), 5 h (top right), 7 h (bottom left) and 9 h (bottom right).

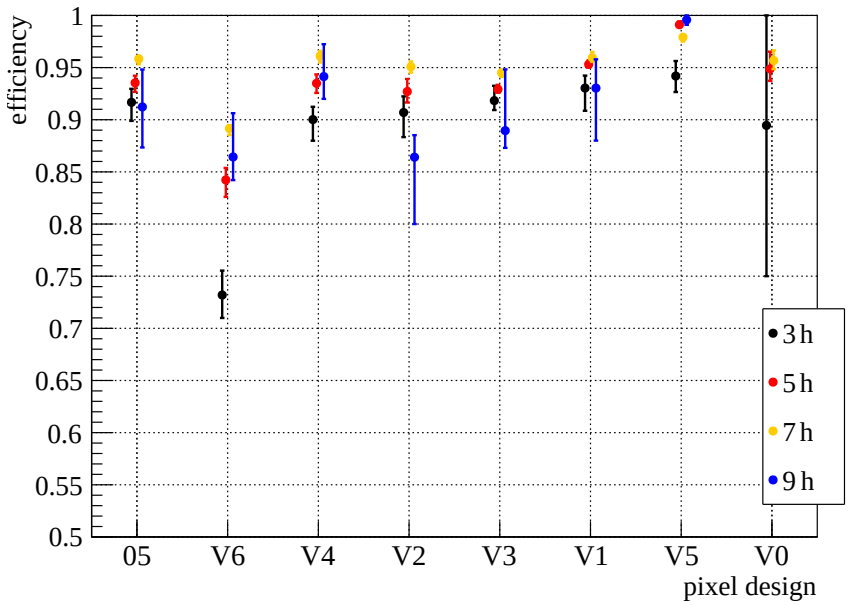

Figure E.3: Hit detection efficiencies for the groups with different pixel designs of the module R3 ($5 \times 10^{15}\,\mathrm{n_{eq}/cm^2}$) at different annealing steps measured at the DESY test beam facility (May 2018, December 2018, March 2019, May 2019 and July 2019). The module is biased with 300 V and tuned to 1000 e and a ToT response of 10 for a reference charge of 10 ke.

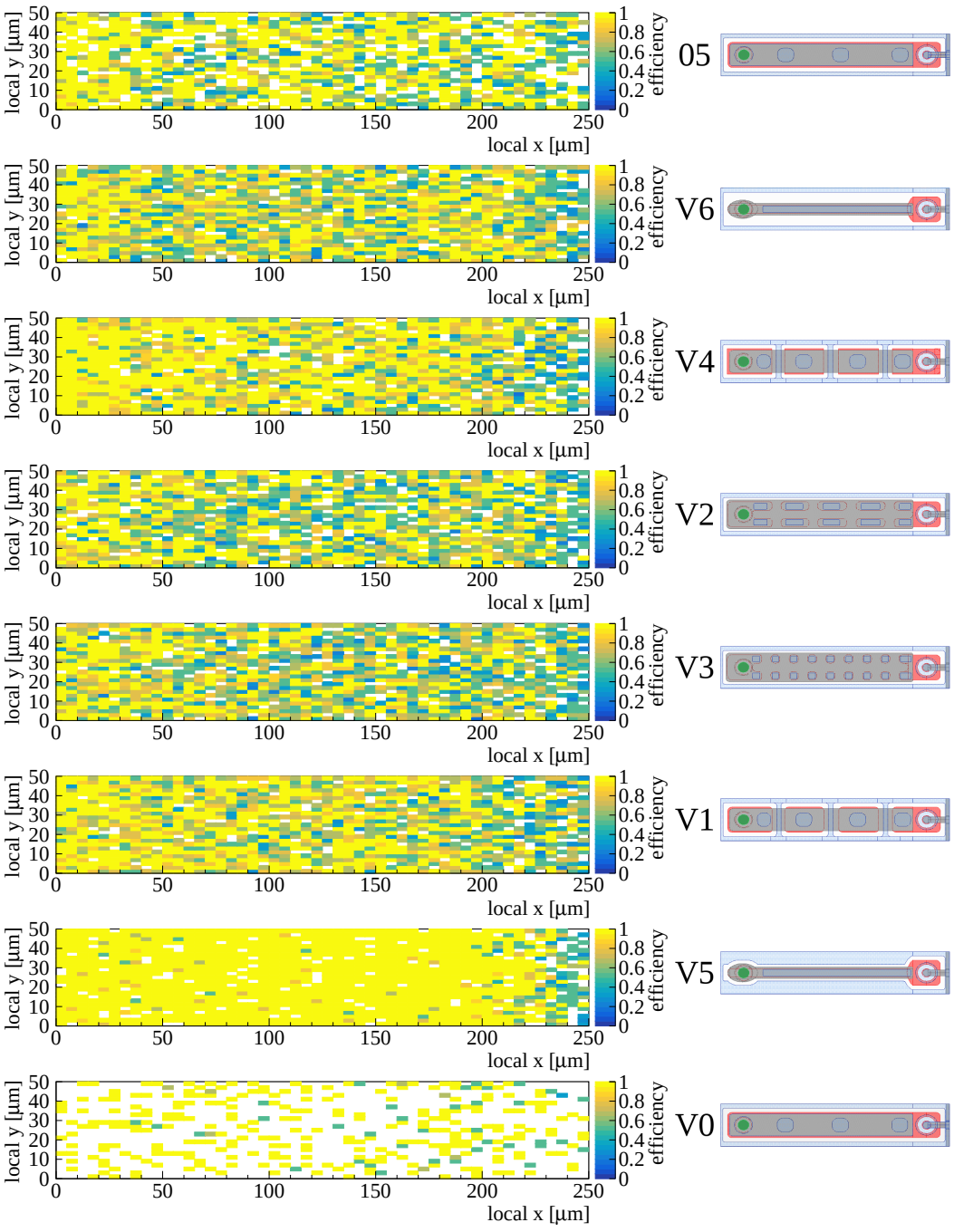

Figure E.4: In-pixel efficiency maps of the neutron irradiated module R3 ($5 \times 10^{15}\,\mathrm{n_{eq}/cm^2}$), annealed for 9 h at 80 °C, biased with 300 V and tuned to 1600 e, 6 ToT at 20 ke. The order from top to bottom corresponds to the order on the module: 05, V6, V4, V2, V3, V1, V5, V0.

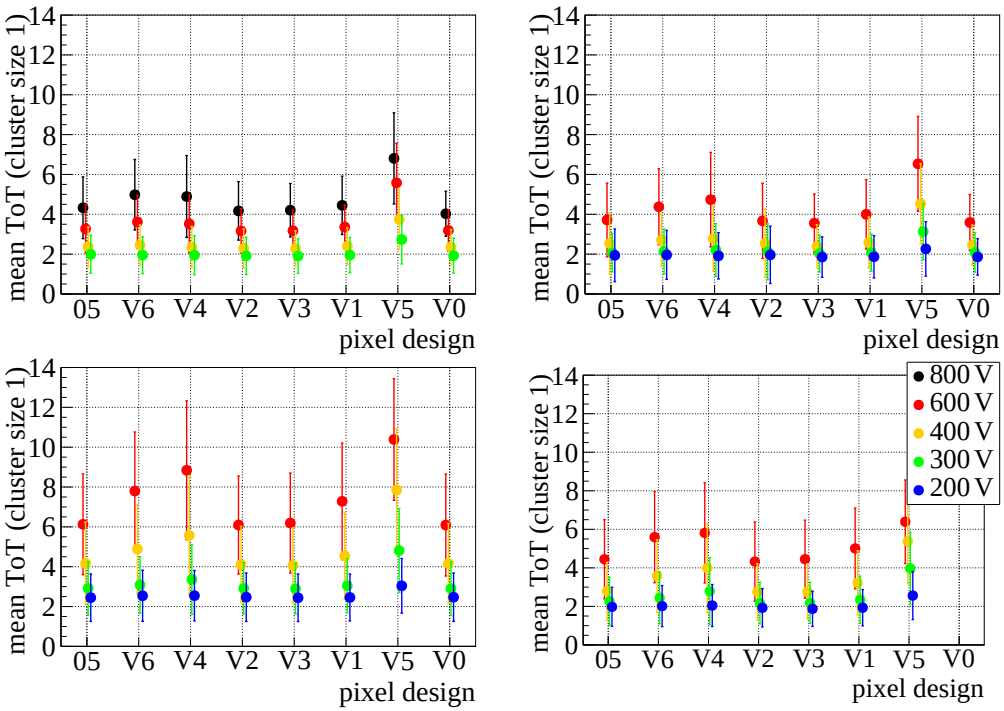

Figure E.5: Mean ToT values for clusters with size one for the groups with different pixel designs of the module R3 at different bias voltages for the tuning of 1600 e 6 ToT at 20 ke. The module is annealed at 80 °C for 3 h (top left), 5 h (top right), 7 h (bottom left) and 9 h (bottom right).

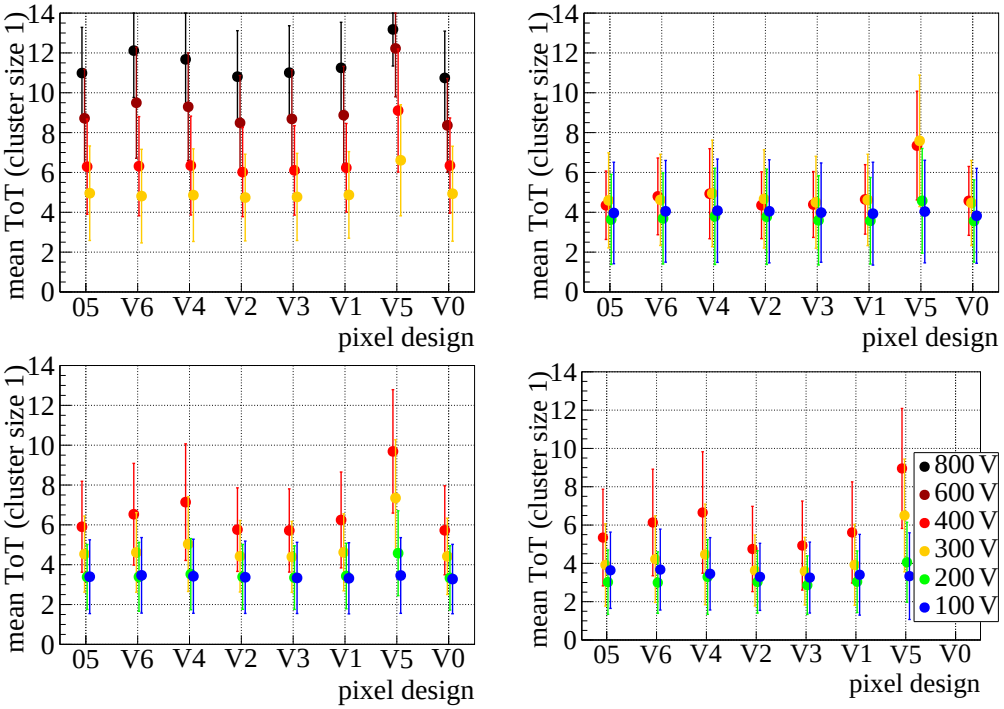

Figure E.6: Mean ToT values for clusters with size one for the groups with different pixel designs of the module R3 at different bias voltages for the tuning of 1000 e 10 ToT at 10 ke. The module is annealed at 80 °C for 3 h (top left), 5 h (top right), 7 h (bottom left) and 9 h (bottom right).

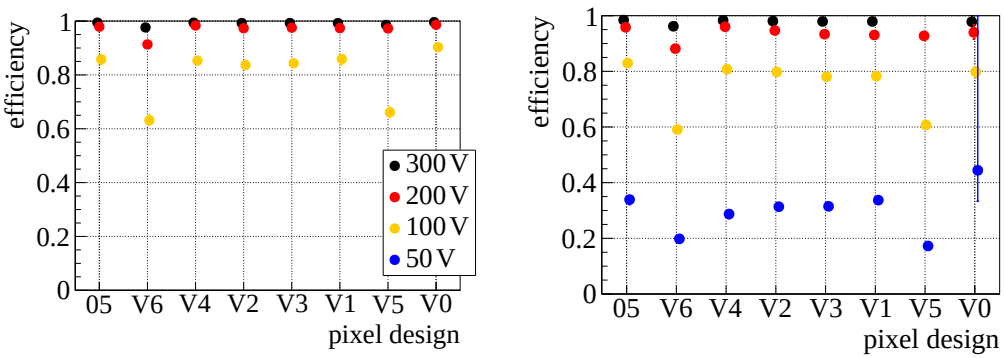

Figure E.7: Hit detection efficiencies for the groups with different pixel designs of the module R9 at different bias voltages for the tuning of 1600 e 6 ToT at 20 ke. The module is annealed at 80 °C for 5 min (left) and 10 min (right).

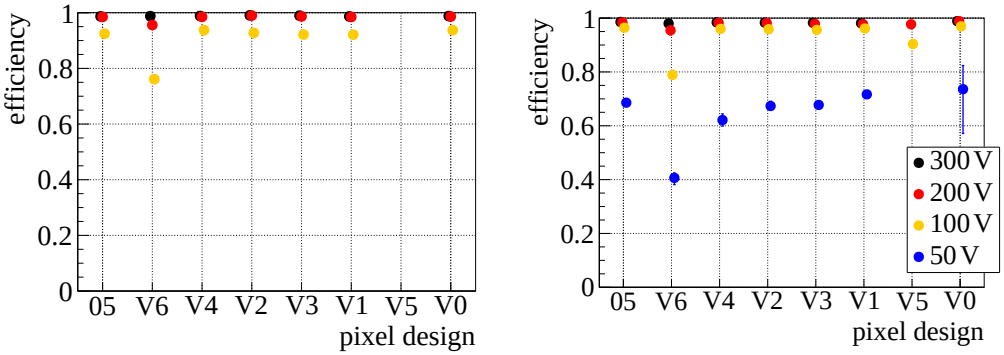

Figure E.8: Hit detection efficiencies for the groups with different pixel designs of the module R9 at different bias voltages for the tuning of 1000 e 10 ToT at 10 ke. The module is annealed at 80 °C for 5 min (left) and 10 min (right).

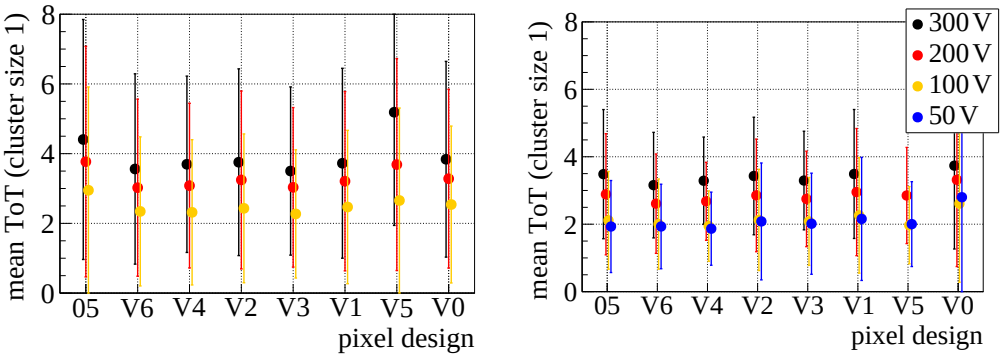

Figure E.9: Mean ToT values for clusters with size one for the groups with different pixel designs of the module R9 at different bias voltages for the tuning of 1600 e 6 ToT at 20 ke. The module is annealed at 80 °C for 5 min (left) and 10 min (right).

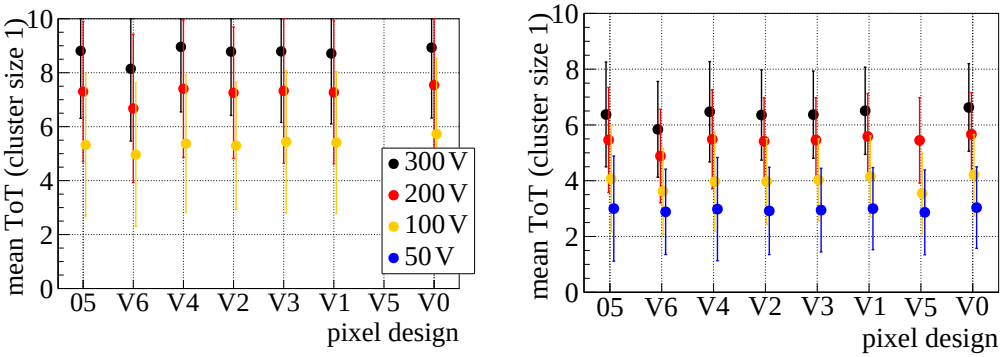

Figure E.10: Mean ToT values for clusters with size one for the groups with different pixel designs of the module R9 at different bias voltages for the tuning of 1000 e 10 ToT at 10 ke. The module is annealed at 80 °C for 5 min (left) and 10 min (right).

F New Sensor Designs REINER Mk II

Similar to REINER pixel sensors, the p-side of the new sensor is segmented by guard rings in six individual pixel groups while one of them is equipped with standard IBL pixels (V0). The other groups use modified pixel designs: Pixel design V7 features a minimal implant width of 8 µm and a metal width of 10 µm to investigate if further narrowing of the implantation would enhance the observed positive effects found in design V5. To investigate the influence of the metal layer width it is increased to 40 µm for pixel design V7M. Higher efficiencies and charge multiplication were observed at the edges of the n^+-implantation and doubling those edges could have a positive impact on the sensor performance. Consequently, pixel design V7D features two p-spray insulated strips of implant (8 µm width) and metal (10 µm width). Pixel design V8 consists of two implants with a size of 8 µm × 8 µm with a metal layer of 10 µm. These designs with a pitch of 50 µm are designed as a possible solution for the new RD53A readout chip. Finally, pixel design V8D features two rows of small n^+-implants each with 10 µm metal layer width similar to the ones used in V8.
In Figure F.1 the pixel designs of the new REINER Mk II sensor are schematically illustrated. The n-$^+$-implantation is indicated in red, the nitride openings as indication for regions with higher p-spray concentration in blue, metal in grey and the round opening in the outermost passivation layer in green.
Further studies will investigate if these new n^+-in-n sensors can improve the observed positive charge multiplication effects of pixel design V5. Furthermore, a new design with a possible adaption to smaller pixel sizes (50 µm × 50 µm) is tested since sensors with such pixel sizes will be used for the future ITk, the innermost detector of the upgraded ATLAS experiment (see Chapter 2.2.5).

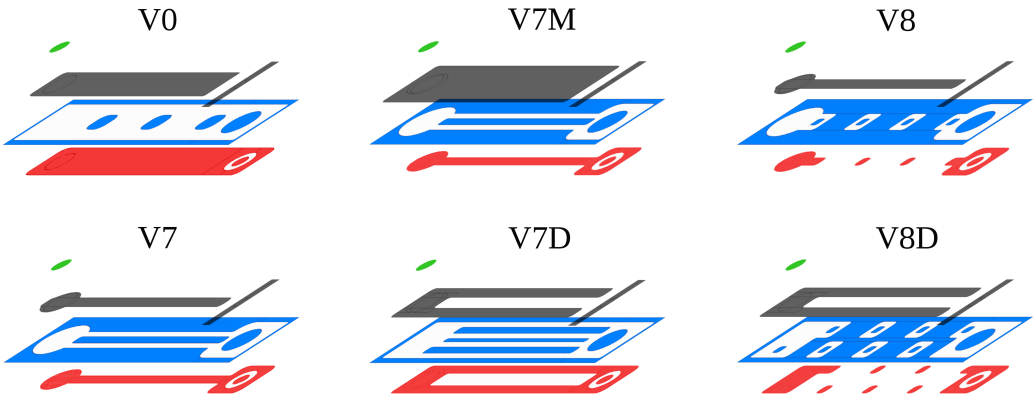

Figure F.1: Layer composition of the different pixel designs of the new REINER Mk II pixel sensor. The n^+-implantation is shown in red, openings in the nitride layer as indication for p-spray in blue, metal in grey and openings in the passivation layer in green.

In the test beam campaign March 2019 at DESY these new non-irradiated modules were tested. Table F.1 summarizes the module features, applied bias voltages and average efficiencies per module. Afterwards, all n^+-in-p modules were irradiated in Ljubljana to two different fluences, $1 \times 10^{15}\,n_{eq}/cm^2$ and $5 \times 10^{15}\,n_{eq}/cm^2$, and are now ready to be investigated.

Table F.1: Summary of the measurements for the new non-irradiated modules investigated in the DESY test beam campaign in March 2019. For all measurements the modules are tuned to a threshold of 1600 e, 6 ToT at 20 ke. The sensor features, bias voltage and mean efficiency over all pixel designs are indicated.

module name	sensor technology	sensor design	bias voltage	mean efficiency [%]
R20	n^+-in-n	REINER Mk II	170	87.07
R21	n^+-in-n	REINER Mk II	170	30.66
R22	n^+-in-n	REINER Mk II	120	45.23
R30	n^+-in-p	REINER	120	99.59
R31	n^+-in-p	REINER	120	99.53
R32	n^+-in-p	REINER	120	99.53
R40	n^+-in-p	REINER Mk II	100	98.92
R41	n^+-in-p	REINER Mk II	100	98.94
R42	n^+-in-p	REINER Mk II	90	96.50

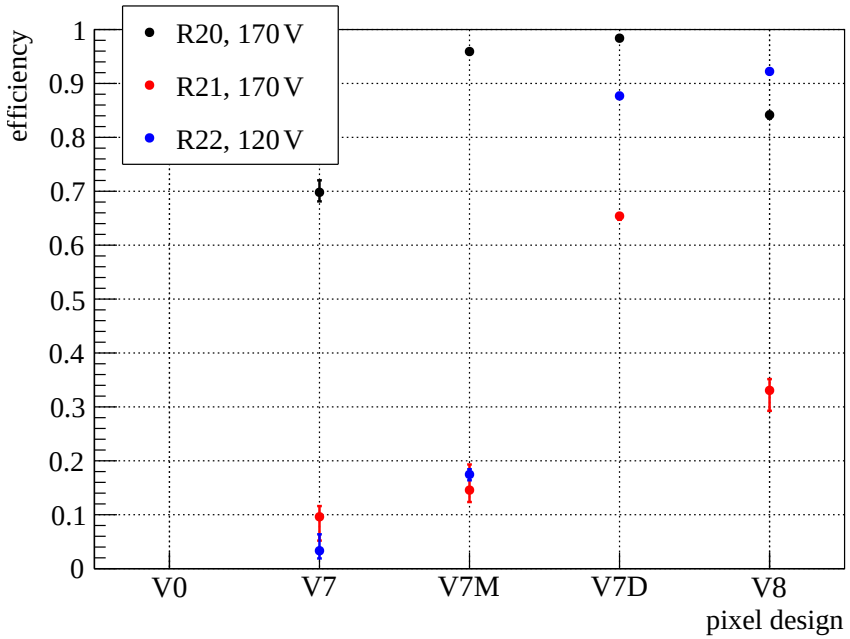

Figure F.2: Efficiencies of the different pixel design groups for the new designed n^+-in-n sensors R20, R21 and R22 measured at the DESY test beam facility in March 2019. The modules are tuned to 1600 e, 6 ToT at 20 ke and measured at different bias voltages. All pixels of the group with design V0 were disconnected in all three modules so that no efficiency data is available for this pixel design. In addition, the bump bond connection for the other designs is also not perfect causing a reduction in efficiency.

The new designed n$^+$-in-n REINER Mk II sensors R20, R21, R22, show lower hit detection efficiencies in the measurements presented in Figure F.2 resulting from bad bump bond connections between the sensors and the front-end. These bad connections are caused by a wrong UBM used by the vendor in the flip-chip process. After transporting the modules to DESY for the test beam measurements and back to Dortmund, the sensors and front-ends of modules R20 and R22 were completely disconnected. Consequently, all three modules were not sent to Ljubljana for neutron irradiations.

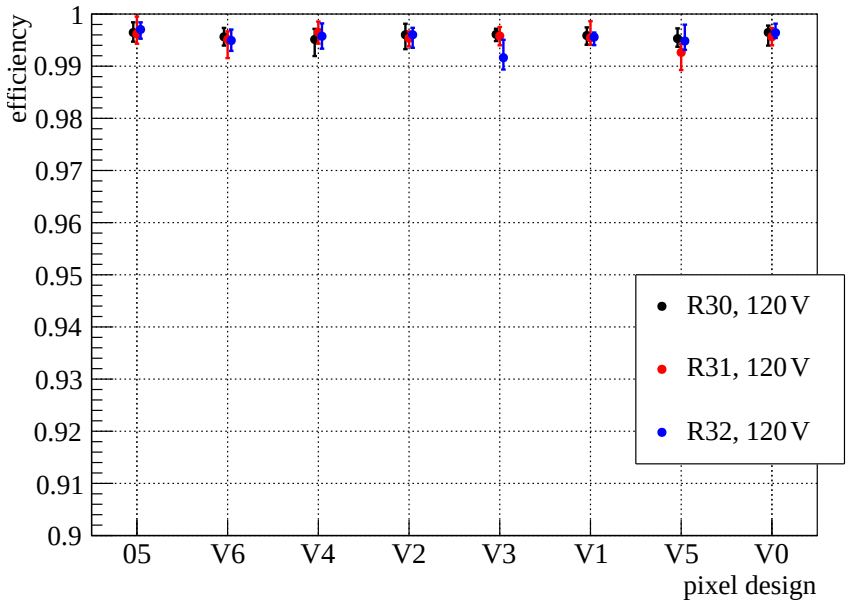

Figure F.3: Efficiencies of the different pixel design groups for the new designed n$^+$-in-p sensors R30, R31 and R32 measured at the DESY test beam facility in March 2019. The modules are tuned to 1600 e, 6 ToT at 20 ke and measured at 120 V.

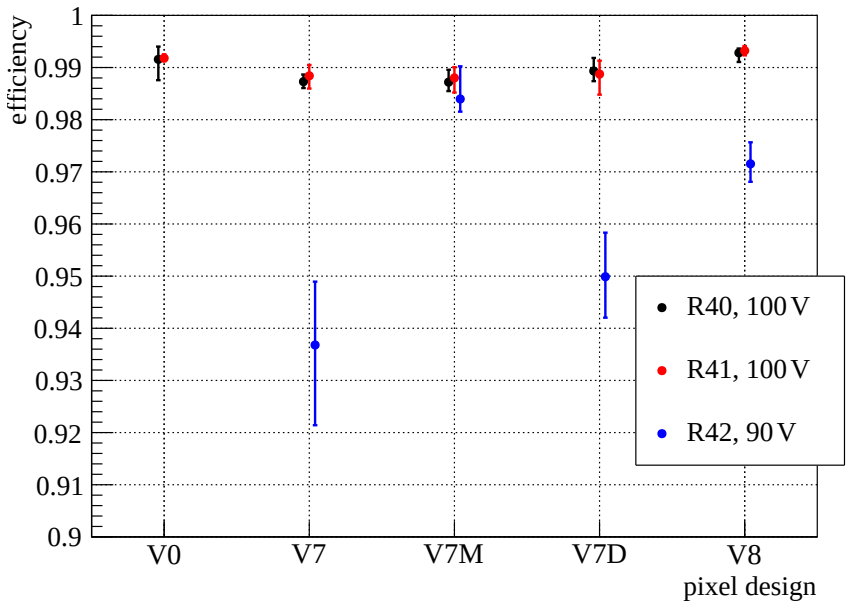

Figure F.4: Efficiencies of the different pixel design groups for the new designed n^+-in-p sensors R40, R41 and R42 measured at the DESY test beam facility in March 2019. The modules are tuned to 1600 e, 6 ToT at 20 ke and measured at different bias voltages.

G Summary of the Measurements and Test Beam Campaigns

Table G.1: Summary of the different test beam campaigns, the investigated modules and the performed measurements

date	TB facility	reco. method	inv. module	module condition	tuning	bias voltage [V]
Jul. 2019	DESY	GBL	R3	irr. an. 9h	1600 e, 6 ToT 20 ke	600, 400, 300, 200
Jul. 2019	DESY	GBL	R3	irr. an. 9h	1000 e, 10 ToT 10 ke	400, 300, 200, 100
Jul. 2019	DESY	GBL	R8	irr. an. 10min	1600 e, 6 ToT 20 ke	800, 600, 500
Jul. 2019	DESY	GBL	R8	irr. an. 10min	1000 e, 10 ToT 10 ke	800, 600, 500, 400
May 2019	DESY	GBL	R3	irr. an. 7h	1600 e, 6 ToT 20 ke	600, 400, 300, 200
May 2019	DESY	GBL	R3	irr. an. 7h	1000 e, 10 ToT 10 ke	400, 300, 200, 100
May 2019	DESY	GBL	R8	irr. an. 5min	1600 e, 6 ToT 20 ke	800, 600, 400
May 2019	DESY	GBL	R8	irr. an. 5min	1000 e, 10 ToT 10 ke	800, 700, 600, 500, 400
May 2019	DESY	GBL	R9	irr. an. 10min	1600 e, 6 ToT 20 ke	300, 200, 100, 50
May 2019	DESY	GBL	R9	irr. an. 10min	1000 e, 10 ToT 10 ke	300, 200, 100, 50
Mar. 2019	DESY	GBL	R3	irr. an. 5h	1600 e, 6 ToT 20 ke	600, 400, 300, 200
Mar. 2019	DESY	GBL	R3	irr. an. 5h	1000 e, 10 ToT 10 ke	400, 300, 200, 100
Mar. 2019	DESY	GBL	R9	irr. an. 5min	1600 e, 6 ToT 20 ke	300 200, 100
Mar. 2019	DESY	GBL	R9	irr. an. 5min	1000 e, 10 ToT 10 ke	300 200, 100
Mar. 2019	DESY	GBL	R20	non-irradiated	1600 e, 6 ToT 20 ke	170
Mar. 2019	DESY	GBL	R21	non-irradiated	1600 e, 6 ToT 20 ke	170
Mar. 2019	DESY	GBL	R22	non-irradiated	1600 e, 6 ToT 20 ke	120
Mar. 2019	DESY	GBL	R30	non-irradiated	1600 e, 6 ToT 20 ke	120
Mar. 2019	DESY	GBL	R31	non-irradiated	1600 e, 6 ToT 20 ke	120
Mar. 2019	DESY	GBL	R32	non-irradiated	1600 e, 6 ToT 20 ke	120
Mar. 2019	DESY	GBL	R40	non-irradiated	1600 e, 6 ToT 20 ke	100
Mar. 2019	DESY	GBL	R41	non-irradiated	1600 e, 6 ToT 20 ke	100
Mar. 2019	DESY	GBL	R42	non-irradiated	1600 e, 6 ToT 20 ke	90
Dec. 2018	DESY	GBL	R3	irr. an. 3h	1600 e, 6 ToT 20 ke	800, 600, 400, 300

Table G.1: Continuation: Summary of the different test beam campaigns, the investigated modules and the performed measurements

date	TB facility	reco. method	inv. module	condition	tuning	bias voltage [V]
Dec. 2018	DESY	GBL	R3	irr. an. 3h	1000 e, 10 ToT 10 ke	800, 600, 400, 300
Dec. 2018	DESY	GBL	R6	irradiated	1600 e, 6 ToT 20 ke	400
Dec. 2018	DESY	GBL	R6	irradiated	1000 e, 10 ToT 10 ke	340
Dec. 2018	DESY	GBL	R8	irradiated	1600 e, 6 ToT 20 ke	1000, 800, 600, 400
Dec. 2018	DESY	GBL	R8	irradiated	1000 e, 10 ToT 10 ke	1000, 800, 600, 400
Oct. 2018	CERN	daf	R12	irradiated	1600 e, 6 ToT 20 ke	600, 500, 400
Oct. 2018	CERN	daf	R12	irradiated	1000 e, 10 ToT 10 ke	600, 400
Aug. 2018	CERN	daf	R7	irradiated	1600 e, 6 ToT 20 ke	400, 300, 200, 150, 100
Aug. 2018	CERN	daf	R7	irradiated	1000 e, 10 ToT 10 ke	400, 300, 250, 200, 150, 100
Aug. 2018	CERN	daf	R9	irradiated	1600 e, 6 ToT 20 ke	400, 300, 200, 150, 100
Aug. 2018	CERN	daf	R9	irradiated	1000 e, 10 ToT 10 ke	400, 300, 250, 200, 150, 100
May 2018	CERN	daf	R3	irradiated	3200 e, 6 ToT 20 ke	1000, 800, 600, 400, 300
May 2018	CERN	daf	R3	irradiated	1600 e, 6 ToT 20 ke	800, 600, 400, 300
May 2018	CERN	daf	R5	irradiated	3200 e, 6 ToT 20 ke	1000, 800, 600, 400, 300
May 2018	CERN	daf	R5	irradiated	2000 e, 6 ToT 20 ke	1000, 800, 600, 400, 300
May 2018	CERN	daf	R7	irradiated	3200 e, 6 ToT 20 ke	800, 600, 500, 400, 300
May 2018	CERN	daf	R7	irradiated	1600 e, 6 ToT 20 ke	600, 400, 300
May 2018	CERN	daf	R9	irradiated	3200 e, 6 ToT 20 ke	900, 800, 600, 400, 300
May 2018	CERN	daf	R9	irradiated	1600 e, 6 ToT 20 ke	900, 800, 600, 400, 300
Dec. 2017	DESY	daf	R6	non-irradiated	3200 e, 6 ToT 20 ke	150, 120, 100
Dec. 2017	DESY	daf	R6	non-irradiated	1600 e, 10 ToT 10 ke	150, 120, 100
Dec. 2017	DESY	daf	R6	non-irradiated	1000 e, 10 ToT 10 ke	150, 120, 100
Dec. 2017	DESY	daf	R6	non-irradiated	1000 e, 7 ToT 14 ke	120
Dec. 2017	DESY	daf	R8	non-irradiated	1600 e, 10 ToT 10 ke	70, 60

Table G.1: Continuation: Summary of the different test beam campaigns, the investigated modules and the performed measurements

date	TB facility	reco. method	inv. module	condition	tuning	bias voltage [V]
Dec. 2017	DESY	daf	R8	non-irradiated	1000 e, 10 ToT 10 ke	70, 60
Oct. 2017	CERN	daf	R8	non-irradiated	1600 e, 8 ToT 16 ke	120
July 2017	CERN	daf	R2	irradiated	3200 e, 6 ToT 20 ke	1000, 800, 700, 600, 400
July 2017	CERN	daf	R2	irradiated	1600 e, 6 ToT 20 ke	1000, 800, 700, 600
July 2017	CERN	daf	R2	irradiated	1600 e, 6 ToT 6 ke	1000, 800, 700, 600, 500, 400
Aug. 2016	CERN	daf	R1	irradiated	3200 e, 6 ToT 20 ke	1000, 800, 600, 400
Aug. 2016	CERN	daf	R1	irradiated	1600 e, 6 ToT 20 ke	1000, 600
Aug. 2016	CERN	daf	R2	non-irradiated	3200 e, 6 ToT 20 ke	150, 120, 90, 50
Aug. 2016	CERN	daf	R2	non-irradiated	1600 e, 6 ToT 20 ke	120, 90
Nov. 2013	DESY	daf	R2	non-irradiated	3200 e, 8 ToT 16 ke	150
Nov. 2013	DESY	daf	R2	non-irradiated	1600 e, 8 ToT 16 ke	150

H Conference Contributions, Publications and Talks

Publications

M. Weers, S. Altenheiner, A. Gisen, M. Hötting, V. Hohm, K. Kröninger, J. Lönker, M. Muschak, A.-K. Raytarowski, J. Weingarten, F. Wizemann: *Lab and test beam results of irradiated silicon sensors with modified ATLAS pixel implantations.* JINST **13**, November 2018, C11004.

A. Gisen, S. Altenheiner, C. Gößling, M. Grothe, R. Klingenberg, K. Kröninger, J. Lönker, M. Weers, T. Wittig, F. Wizemann: *Investigation of modified ATLAS pixel implantations after irradiation with neutrons.* Nucl. Instr. Meth. A **924**, April 2019, pp. 203 - 207.

M. Wagner, A. Gisen, M. Hötting, V. Hohm, C. Krause, K. Kröninger, A. Kroner, J. Lönker, M. Muschak, J. Weingarten, F. Wizemann: *First annealing studies of irradiated silicon sensors with modified ATLAS pixel implantations.* JINST **14**, November 2019, C11003.

Conference Contributions and Talks

M. Weers: *Recent activities in Dortmund.* Talk at the "ATLAS ITk Week", June 2017, CERN, Geneva, Switzerland.

M. Weers: *Testbeammessungen an n^+-in-n-Silizium-Pixelsensoren mit verschiedenen Pixeldesigns für das ATLAS-Experiment.* Talk at the "49. Herbstschule für Hochenergiephysik", September 2017, Maria Laach, Germany.

M. Weers: *Recent activities in Dortmund.* Talk at the "ATLAS ITk Week", September 2017, CERN, Geneva, Switzerland.

M. Weers: *Test Beam Results of Sensors with Modified Pixel Implantations.* Talk at the "6th Beam Telescope and Test Beams Workshop", January 2018, Zurich, Switzerland.

M. Weers: *Testbeamergebnisse modifizierter Pixelimplantation.* Talk at the "Frühjahrstagung der DPG", March 2018, Würzburg, Germany.

M. Weers: *Lab and Test Beam Results of Irradiated Silicon Sensors with Modified ATLAS Pixel Implantations.* Talk at the "20th International Workshop on Radiation Imaging Detectors", June 2018, Sundsvall, Sweden.

M. Weers: *Test Beam Results of Irradiated Silicon Sensors with Modified ATLAS Pixel Implantations.* Talk at the "33rd RD50 Workshop", November 2018, CERN, Geneva, Switzerland.

M. Weers: *EUTelescope Workshop at DESY.* Software workshop at DESY, March 2019, DESY, Hamburg, Germany.

M. Weers: *Testbeam-Ergebnisse von bestrahlten Siliziumsensoren mit modifizierten ATLAS-Pixelimplantationen.* Talk at the "Frühjahrstagung der DPG", March 2019, Aachen, Germany.

M. Weers: *First Annealing Studies of Irradiated Silicon Sensors with Modified ATLAS Pixel Implantations.* Talk at the "21st International Workshop on Radiation Imaging Detectors", July 2019, Crete, Greece.

M. Wagner: *Test Beam and Lab Results of ATLAS Sensors with Modified Pixel Implantations.* Talk at the "8th Beam Telescope and Test Beams Workshop", January 2020, Tbilisi, Georgia.

I Supervised and Co-Supervised Theses

Alexander Kroner: *Entwicklung des DUT Config Checkers zur Verbesserung der Implementierung von Geometrien in TBMon2.* Bachelor thesis, TU Dortmund, July 2017.

Raphael Michallek: *Test Beam Studies of unirradiated Planar n^+-in-n Silicon Pixel Sensors with Modified Pixel Implantations for the ATLAS Experiment.* Master thesis, TU Dortmund, November 2017.

Anna-Katharina Raytarowski: *Comparison of Leakage Current Characteristics of the Pixel Designs of Irradiated and non-Irradiated REINER Pixel Sensors.* Master thesis, TU Dortmund, May 2018.

Marius Meinecke: *Labormessungen an bestrahlten und unbestrahlten REINER-Pixelsensoren.* Bachelor thesis, TU Dortmund, August 2018.

Valerie Vanessa Hohm: *Characterisation and Test Beam Measurements of Planar n^+-in-n Silicon Pixel Sensors with Modified Bias Grid Structures.* Master thesis, TU Dortmund, September 2018.

Alexander Kroner: *Simulation Studies of the Track Resolution at the ATLAS-ITk-Pixel Testbeam Setup at DESY.* Master thesis, TU Dortmund, November 2019.

Falko Barth: *Studies of the charge collection of silicon diodes and sensors with modified ATLAS Pixel implantations using Transient Current Technique.* Master thesis, TU Dortmund, February 2020.

Lars Bickehör: *Studien an neuartigen n-in-p Sensoren mit modifiziertem Pixellayout.* Bachelor thesis, TU Dortmund, February 2020.

Serena Di Pede: *Guard rings investigation of silicon sensors with modified pixel implant shapes in the context of the ATLAS experiment.* Master thesis, TU Dortmund, March 2020.

Sefa Aygün: *Untersuchung von Siliziumdioden und Sensoren nach partieller Entfernung der Metallschicht.* Bachelor thesis, TU Dortmund, January 2021.